Controlling Assembly and Activity of Biomimetic DNA Nanopores

Conor Joshua Lanphere

This dissertation is submitted for the degree of
Doctor of Philosophy

Supervisor: Prof. Stefan Howorka

Submitted: March 2021

Declaration

I, Conor Lanphere, confirm that the work presented in this Thesis is my own. Where information has been derived from other sources, I confirm that this has been indicated in the text.

Conor Lanphere
March 2021

Publications

A biomimetic DNA-based membrane gate for protein-controlled transport of cytotoxic drugs
C. Lanphere, P. M. Arnott, S. Fôn Jones, K. Korlova, S. Howorka
Angew. Chem. Int. Ed., 2021, **60**, 1903-1908

Design, assembly, and characterization of membrane-spanning DNA nanopores
C. Lanphere, D. Offenbartl-Stiegert, A. Dorey, G. Pugh, E. Georgiou, Y. Xing, J. R. Burns, S. Howorka
Nat. Protoc., 2021, **16**, 86-130

DNA Nanodevices with Selective Immune Cell Interaction and Function
N. Arulkumaran, **C. Lanphere**, C. Gaupp, J. R. Burns, M. Singer, S. Howorka
ACS Nano, 2021, **15**, 4393-4404

Triggered Assembly of a DNA-Based Membrane Channel
C. Lanphere, J. Ciccone, A. Dorey, N. Hagleitner, S. Haider, S. Howorka
J. Am. Chem. Soc., 2021 (submitted)

Conference Attendance and Contributions

16th Nucleic Acids Forum, Royal Society of Chemistry
29th of July 2020, London, United Kingdom (via Zoom)
Oral Presentation: A biomimetic DNA-based membrane gate for protein-controlled transport of cytotoxic drugs

Institute of Structural and Molecular Biology Postgraduate Lockdown Symposium
15th of June 2020, London, United Kingdom (via Zoom)
Oral Presentation: Building synthetic membrane pores with designed function

Chemical Biology Symposium 2020, Royal Society of Chemistry
11th of May 2020, London, United Kingdom
Poster Abstract accepted; cancelled due to COVID-19

London Interdisciplinary Doctoral Consortium retreat
10th-12th of September 2019, Yarnfield, Staffordshire, United Kingdom
Poster Presentation: Lipidated DNA nanobarrels controllably modulate human immune response

15th Nucleic Acids Forum, Royal Society of Chemistry
12th of July 2019, London, United Kingdom
Poster presentation: Lipidated DNA nanobarrels controllably modulate human immune response

Institute of Structural and Molecular Biology retreat
11th – 12th of July 2019, Cambridge, United Kingdom
Poster presentation: Lipidated DNA nanobarrels controllably modulate human immune response

London Interdisciplinary Doctoral Consortium retreat
18th-20th of September 2018, Yarnfield, Staffordshire, United Kingdom
Flash Talk

London Interdisciplinary Doctoral Consortium retreat
18th-20th of September 2017, Yarnfield, Staffordshire, United Kingdom

Institute of Structural and Molecular Biology retreat
27th – 29th of June 2017, Cambridge, United Kingdom

List of Abbreviations

3'	Three prime end of a DNA sequence – the end of a sequence
4HB	Four-helix bundle
5'	Five prime end of a DNA sequence – the start of a sequence
6HB	Six-helix bundle
A	Component monomer A or Adenine
A•B	The 4HB DNA nanopore assembled from component monomers A and B
Abs	Absorbance
AFM	Atomic Force Microscopy
α-HL	Alpha-Hemolysin
Apt	Aptamer
Avg	Average
B	Component monomer B
bp	Base Pair
C	Cytosine or cholesterol modification
CD	Circular Dichroism
Chol	Cholesterol
CLSM	Confocal Laser Scanning Microscopy
Δ	Delta, without, native conditions
ΔC	No cholesterol modifications, native conditions
d	Diameter
Da	Dalton
DOPC	1,2-dioleoyl-sn-glycero-3-phosphocholine
DOPE	1,2-dioleoyl-sn-glycero-3-phosphoethanolamine
DPhPC	1,2-diphytanoyl-sn-glycero-3-phosphocholine
DNA	Deoxyribonucleic Acid
dsDNA	Double-Stranded DNA
ext	Extension
F	Fluorescence Intensity
f	Femto ($1x10^{-15}$)
F_D	FRET Donor Intensity
F_{DA}	FRET Donor Intensity in the presence of the Acceptor
FRET	Förster Resonance Energy Transfer
G	Guanine
GUV	Giant Unilamellar Vesicle
h	Hours
HB	Helical Bundle

I	Intensity
k	Kilo (1x10³)
K_a	Association Equilibrium Constant
K^A	Key A, removes L^A and unlocks component A
K^B	Key B, removes L^B and unlocks component B
K_d	Dissociation Equilibrium Constant
K_M	Michaelis-Menten Constant
k_{obs}	Observed Rate Constant
k_{off}	Dissociation Rate Constant
k_{on}	Association Rate Constant
KCl	Potassium Chloride
L	Litre
L^A	Lock A, locks component A
L^B	Lock B, locks component B
LD	Linear Dichroism
LUV	Large Unilamellar Vesicle
μ	Micro (1x10⁻⁶)
M	Molar (mol/L⁻¹)
m	Milli (1x10⁻³)
min	Minute
MLV	Multi-Lamellar Vesicle
mol	Mole
n	Nano (1x10⁻⁹)
NA	Nucleic Acid
NP	Nanopore
nS	Nano Siemens
nt	Nucleotide
OH	Alcohol Functional Group
OMe	Methoxy Functional Group
OPOE	n-octyl-oligo-oxyethylene
π	Pi
p	Pico (1x10⁻¹²)
PAGE	Polyacrylamide Gel Electrophoresis
PBMC	Peripheral Blood Mononuclear Cells
PBS	Phosphate-Buffered Saline
pNP	Protein-gated Nanopore
pNP-L	Protein-gated Nanopore without the Lid Strand
pNP2	Protein-gated Nanopore with Alternative TBA Placement

pNP3	Protein-gated Nanopore without the TBA Sequence
POPC	1-palmitoyl-2-oleoyl-glycero-3-phosphocholine
PPT	Phosphorothioate
R	Receptor in the Model System
r	Radius
R_{SUV}	Receptor bound to the surface of SUVs in the Model System
R•S	Duplex of R and S
R•S_{NP}	Duplex of R and S_{NP}
R_{SUV}•S	Duplex of R and S tethered to the surface of a membrane
R_{SUV}•S_{NP}	Duplex of R and S_{NP} tethered to the surface of a membrane
r.t.	Room Temperature (typically 18-25 °C)
RMSD	Root-Means-Squared Deviation
RMSF	Root-Means-Squared Fluctuation
RNA	Ribonucleic Acid
S	Steric Element
s	Seconds
S_{NP}	Steric Element attached to a nanopore
T	Thymine or Thrombin
TAE	40 mM Tris, 20 mM acetic acid, 1 mM EDTA, pH 8.3
TBA	Thrombin Binding Aptamer
TBE	100 mM Tris, 90 mM boric acid, 1 mM EDTA, pH 8.3
TEG	Tri(ethylene glycol)
TEM	Transmission Electron Microscope
Temp	Temperature
T_m	Melting Temperature
Tris	Trisaminomethane
SDS	Sodium Dodecyl Sulfate
SRB	Sulforhodamine B
ssDNA	single-stranded DNA
Std. Dev.	Standard Deviation
SUV	Small Unilamellar Vesicle
UV	Ultraviolet
Vis	Visible Light

List of Figures

List of Tables

Table of Contents

Acknowledgements

Dan, Helena, Patrick, Katya and Elena. My time at UCL truly would not have been the same without you all.

I am eternally grateful to the Chickasaw Indian Nation for their support throughout the course of my time in Higher Education and particularly during my PhD. Their support allowed me focus on my research and make the most out of my PhD.

I would like to thank my parents and my family for their unconditional support, for their love and kindness and for making sure I was prepared to reach this stage. Thank you Mom, Skip, Clare, Katie, Quinn, Madi, Miranda, Mary, Blaise, Tristan, Noah, Grandma, Grandpa, Carol, Paul and Stan. Grandma, Grandpa, Art and Joan, I wish you could have all been with me until the end of this journey.

I would like to thank my Dad in particular for always pushing me to reach higher, to reach further.

Finally, I would like to thank my Fiancée, Amy. Thank you for your unwavering love and support, for always believing in me, supporting me and always being there to lend a hand when I needed it. I couldn't have done this without you.

1. Abstract

Biological channels control the transport of vital biomolecular cargo across the cellular membrane. Reflecting the channels' critical role, replicating their structure and improving on their function is of significant biomedical and scientific interest. However, *de novo* design of pores with the typical biological building material of polypeptides is challenging. DNA, by contrast, offers unrivalled structural control due to the simplicity and specificity of Watson-Crick base-pairing. Taking advantage of these properties, DNA membrane pores have been rationally designed with tuneable dimensions. The overall aim of this thesis is to advance on the simple barrel-like synthetic pores and create higher-order function to control pore formation and transport by means of exogenous triggers.

The first aim of this thesis was the development of a model system to probe DNA hybridisation under steric constraints. By exploring the effect of DNA hybridisation under steric constraints, such as at membranes and on DNA nanostructures, greater insight was provided for the design of DNA nanopore that assemble *in situ* and respond to exogenous triggers.

The second aim was to design a DNA nanopore that would mimic protein pore formation by undergoing triggered assembly. To transition the inactive pre-pore monomers to an active membrane-spanning oligomeric pore, the locked monomers can be unlocked in the presence of keys to trigger pore assembly. The pore advances functional DNA nanotechnology and synthetic biology by imparting targeted selectivity for pore activity and by serving as a synthetic mimic.

The third aim was to build a DNA nanopore that functions as a synthetic protein-gate, allowing the transport of molecular cargo only in the presence of a target exogenous trigger. To function as a protein-gate, a DNA nanopore was designed with a lid featuring an aptamer sequence. In the rational designed structure, the binding of a target protein to the aptamer actuates the lid to open the pore into a transport-active state. A pore with such selective control could then be used in targeted drug-delivery.

2. Impact Statement

The focus of this thesis was to advance small barrel-like DNA nanopores by creating higher-order biomimetic function, such as assembly on the surface of membranes or application in response to exogenous triggers for use as research tools or therapeutics as well as to advance DNA nanotechnology structural biology.

First, insight into DNA hybridisation under steric constraints. DNA hybridisation underpins all of DNA nanotechnology and hybridisation *in situ* is key to the development of dynamic structures, which have applications as biological mimics in sensing, therapeutics and as research tools. However, more and more applications necessitate hybridisation to large structures, at the membrane interface, or both. Therefore, insight gained into this process has the potential to impact research in biosensing, biophysics, and biomedicine within DNA nanotechnology and chemical and synthetic biology.

Second, the activity of a DNA nanopore that can undergo triggered assembly at the membrane interface can be controlled. Many proteins can only assemble or function under specific conditions on lipid bilayer membranes. This allows them to be used as targeted research and therapeutic tools. DNA nanopores, and nanostructures in general, are only just developing means of control over activity. Not only is biomimetic assembly on the membrane surface scientifically interesting, but it provides a means of control over activity and function. In addition, the insight gained can be applied to other biomimetic structures and processes advancing the development of new biomimetic DNA-based tools for targeted drug delivery, in biomedicine, or as research tools.

Third, the development of a synthetic protein-gate allows the transport of molecular cargo across lipid bilayers to be controlled. The protein-gated nanopore replicates natural function in a more versatile package that can be used outside of cellular membranes and has applications for targeted, controlled drug delivery. In addition, the modular design of this pore means that it would be straightforward to swap the DNA aptamer used to target a wide range of therapeutic targets. This technology need not be limited to DNA nanopores either. The principle is widely applicable to create any kind of functional dynamic change to a DNA based system.

Finally, this work led to the development of a unified set of protocols for the design, assembly and characterisation of membrane-spanning DNA nanopores. The field of DNA nanopores is now nearly a decade old and has begun to garner general scientific interest, but despite this, there is no unified set of protocols for the design, assembly and characterisation of new DNA nanopores and the field typically relies on protocols that were written for protein pores, which are not always applicable or relevant. DNA nanopores have recently generated success in protein detection, as synthetic enzymes and protein mimics as well as in drug delivery, among others. Therefore, this

protocol is expected to be of interest to those in the fields of biosensing, biophysics, biomedicine, DNA nanotechnology, chemical and synthetic biology as well as the scientific community at large.

3. Introduction

3.1. Lipid Bilayer Membranes

The lipid bilayer is the basis for all cell membrane structures.[1] While the cellular membrane is a complex structure containing vast amounts of critical cellular machinery, at least 50% of its mass comes from lipid molecules (there are ~10^9 lipids in an animal cellular membrane).[1] Lipids are amphipathic 'fatty' molecules that possess a polar and a hydrophobic end and are typically insoluble in water.[2] The most common lipids found in nature are phospholipids, sphingolipids, and sterols, with phospholipids being the most common components of the bilayer membrane.[1,2] Phospholipid molecules have a polar headgroup, a glycerol linker and two hydrophobic lipid tails (Fig. 1). Sphingolipids have a similar structure, but instead of a glycerol linker, they have a sphingosine that encompasses the linker and one of the lipid tails.[2] The other fatty acid lipid chain is attached to the sphingosine amine. The headgroup can be charged or zwitterionic resulting in a net neutral charge (see POPC in Fig. 1).[2] The length of the tails can vary from 14-24 carbon atoms and one of the tails usually has one or more *cis*-double bonds, while the other remains unsaturated.[1] The *cis*-double bond in the tail causes a 'kink' in the chain, which affects the packing properties of the lipid. Chain length and the degree of unsaturation are both important parameters that affect lipid packing and, therefore, the properties of the bilayer.[1,3,4]
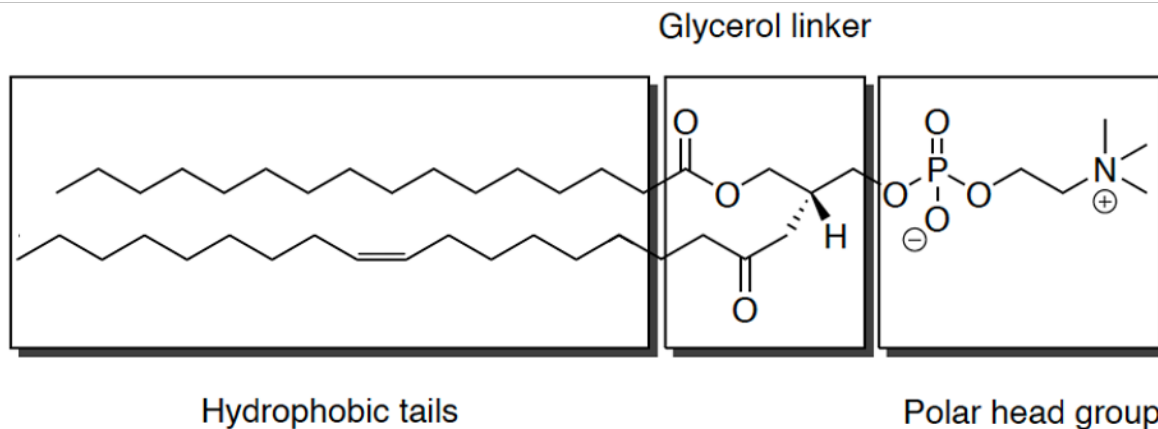
Figure 1. Chemical structure of 1-palmitoyl-2-oleoyl-sn-glycero-3-phosphocholine (POPC), a phospholipid in the phosphatidylcholine (PC) class of lipids. The zwitterionic choline headgroup, characteristic of PC lipids, has a net neutral charge. POPC has two tails, one 16 carbons long and the other that is 18 carbons long with a single *cis*-double bond. Adapted from Offenbartl-Stiegert.[5]

The amphipathic structure of phospholipids causes them to self-assemble into larger structures in aqueous environments in order to bury the hydrophobic tails while exposing the polar headgroups. The exact nature of the structure the lipids assemble into depends on the structure of the individual lipid molecules and their packing parameters (Fig. 2).[1,2] Lipid packing typically results in the

formation of two structures in aqueous environments: micelles, which typically result from wedge, or cone, shaped lipids with the tails oriented inwards, or lipid bilayers, which typically result from cylindrical shaped lipids, with the tails oriented towards each other between two lipid layers, known as leaflets (Fig. 2).[1,2]
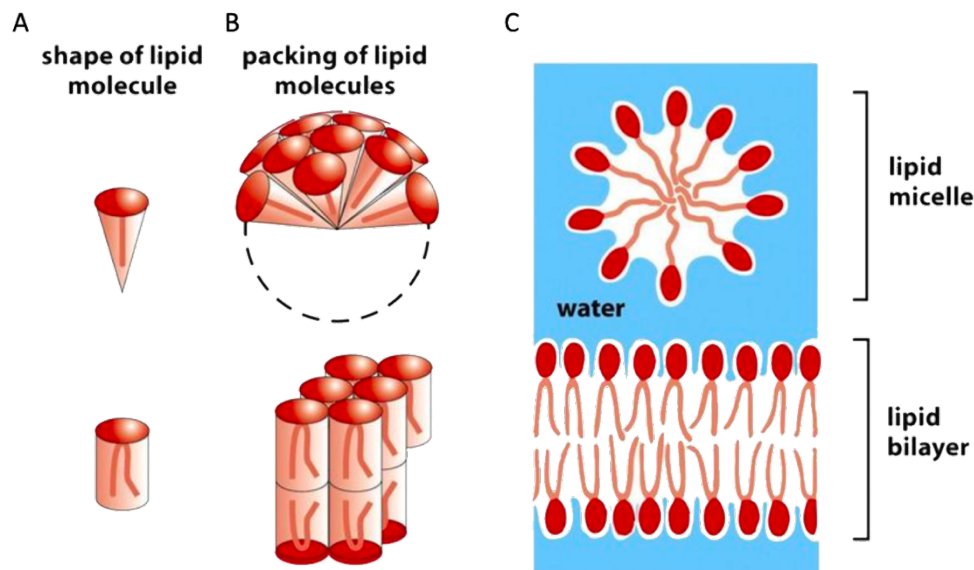
Figure 2. The structure of the lipid molecule affects its packing parameters and the structure the lipids adopt upon assembly. (A) There are two primary shapes of lipid molecules, wedge (top) and cylindrical (bottom). (B) Wedged shaped lipid pack into a spherical structure (top) while cylindrical shaped lipids form a planar structure. (C) This results in the formation of lipid micelles (wedge) and lipid bilayers (cylindrical).[1]

Phospholipids are cylindrical and spontaneously assemble into bilayer membranes in aqueous environments. The favourable energetics of bilayer formation also results in a self-healing mechanism. Any disruption to the bilayer structure (e.g., a tear) will expose the hydrophobic core to water and results in spontaneous membrane remodelling to minimise this effect. A result of this effect is an energetic drive to fold in on itself to create a spherical closed vesicle compartment. This property of the bilayer membrane directly contributes to the formation of living cells.[1] This property also allows liposomes, or vesicles, to be formed from dry lipid films.[2,6,7]

Synthetic vesicles, such as small unilamellar vesicles (SUVs) are important research tools as they serve as model membranes.[8–11] Lipid vesicles are easily formed simply by adding water or buffer to a dried lipid film and leaving it; however, this often results in multi-lamellar vesicles,[7,12,13] which can be desirable; however, as they are less representative of most cellular structures, they are less useful as model membranes. Unilamellar vesicles, such as SUVs, are normally formed via sonication or extrusion.[6,7] Extrusion can be a particularly useful method as it allows vesicles to be formed with an upper-size limit.[6] Giant unilamellar vesicles (GUVs), which are comparable to the size of cells, can be formed using current via a process known as electro-formation.[14] Formation from dry lipid films

is also a desirable property as it enables vesicles to be used to encapsulate molecular cargo, such as therapeutics, for drug delivery.[15,16] The exact properties of the vesicles formed will depend upon composition and preparation method and can be tailored for most research needs.

Lipid bilayers act as fluids with rapid lateral diffusion (neighbouring lipids swap places up to 10^7 times per second), but they are strictly two-dimensional fluids as exchange between leaflets happens less than once per month on average for any individual lipid.[1] However, a membranes fluidity depends on its composition and the structure of the individual lipids. Long saturated lipid tails result in a more tightly packed and less fluid membrane, while short lipid tails, which have reduced interaction with each other, result in greater membrane fluidity. In addition, unsaturation causes the lipid tail to have a 'kink', which further reduces interaction with its neighbours resulting in increased fluidity (see Fig. 3).[1,17] Increased fluidity is an important parameter for cellular membranes as this lowers the gel-phase transition temperature, which can affect many critical cellular processes.[1,18]

unsaturated
hydrocarbon chains
with *cis*-double bonds

saturated
hydrocarbon chains
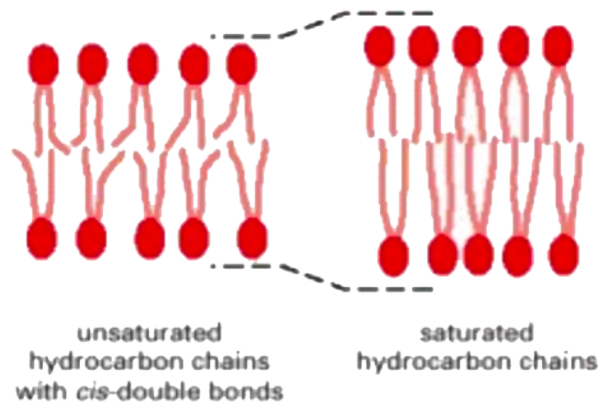
Figure 3. Packing properties of unsaturated hydrocarbon chains with a *cis*-double bond compared to saturated hydrocarbon chains. The increased packing density of saturated lipid tails results in a thicker bilayer membrane.[1]

While increased fluidity is a desirable property for cellular membranes, lipid bilayers with less densely packed lipids are also more permeable. The permeability of cellular membranes is closely regulated to optimise cellular processes.[1,19] To balance a low gel-phase transition temperature and membrane permeability, eukaryotic membranes often include a large number of sterols, cholesterol being the most common (see Fig. 4A). Cholesterol inserts in the empty space between phospholipids and orients parallel to the lipid chains with the hydroxyl headgroup sitting among the lipid headgroups. The rigid sterol rings have favourable interactions with the first few carbons of the lipid chains, which results in their partial immobilisation. This significantly reduces the mobility of the top of the lipid chains and subsequently, the headgroup, resulting in reduced fluidity and permeability (Fig 4B).[1,20] Some eukaryotic membranes have cholesterol concentrations as a high as one cholesterol for

every phospholipid. At these concentrations, permeability is significantly reduced, but the cholesterol also prevents lipid packing and so prevents gel-phase transitions.[1,20]
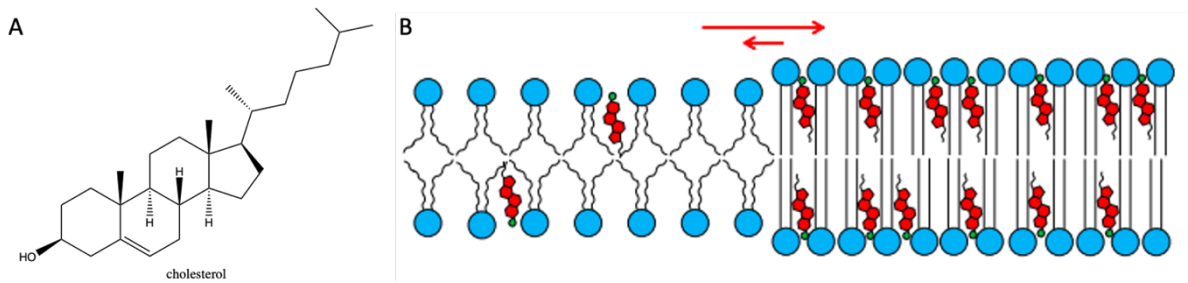
Figure 4. (A) The chemical structure of the sterol, cholesterol. Cholesterol has a small polar headgroup consisting of a single hydroxyl group. This is followed by a rigid ring structure and a short hydrophobic hydrocarbon chain. (B) The role of cholesterol in reducing the fluidity and permeability of a lipid membrane composed of unsaturated phospholipids. Adapted from Yang *et al.*[21]

While bacterial membranes are often predominantly composed of a single principal lipid type, eukaryotic membranes are usually composed of many different types of lipids. Indeed, even the different membrane leaflets have different lipid compositions. Lipid asymmetry is functionally important for many different cellular processes, such as signalling and positioning cellular machinery.[1] In addition to being composed of various different lipid types, cellular membranes are significantly more complex than model membranes and contain a host of proteins and other cellular apparatus (Fig. 5). The general structure, thermodynamic principles, and intra- and extracellular properties of the complex cellular membrane are usually described by the fluid mosaic model of membrane structure first proposed by Singer and Nicolson in 1972.[22,23]
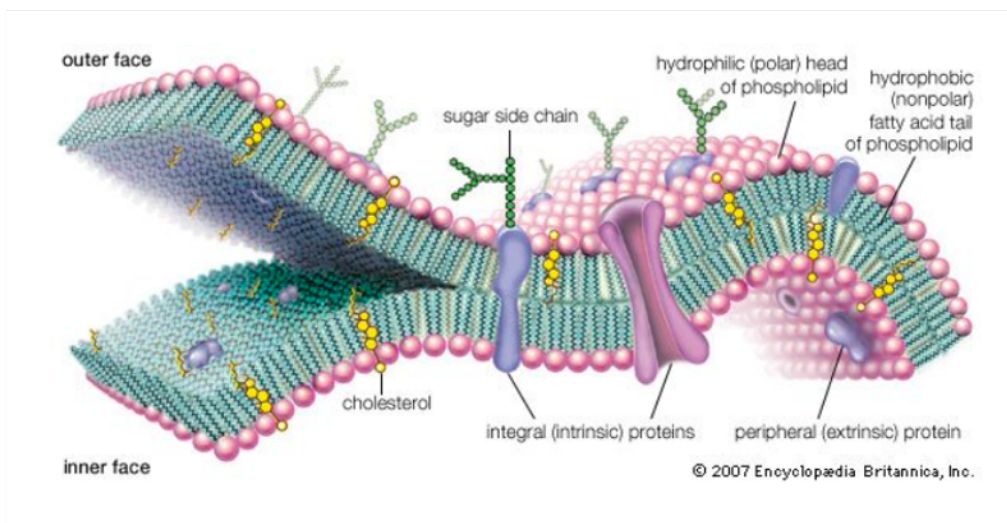
Figure 5. Model and composition of a eukaryotic cellular membrane.[24]

31

3.2. Protein Nanopores

Nanopores are ubiquitous in nature and fulfil a broad range of biological functions.[25] For example, protein pores act as channels that control the passage of ions and molecules into and out of cells and many subcellular entities. Comparably, nuclear membrane pores control the passage of messenger RNA from the nucleus.[26] Some protein pores are even responsible for controlling the passage of other proteins. Additionally, bacterial cells and viruses use protein pores offensively to kill other cells and or to facilitate infection by creating a means of inserting their own genomes into a host.[27]

The bacteria *Staphylococcus aureus* produces one such pore-forming cytotoxic protein, α-Hemolysin (α-HL, see Figure 6).[28] Other pores include cytolysin A (ClyA),[29] pneumolysin,[30] cytolysin K (CytK),[31] aerolysin (Aet),[32] as well as the class of cholesterol-dependent-cytolysins such as perfringolysin O (PFO) and binary agents such as anthrax toxin.[33] These pores have a range of targets and modes of action, making them scientifically interesting to study, but also medically important to understand. Given the efficacy of many of these pores, they have the potential to be used as a template to design synthetic variants that can be tailored for other targets.
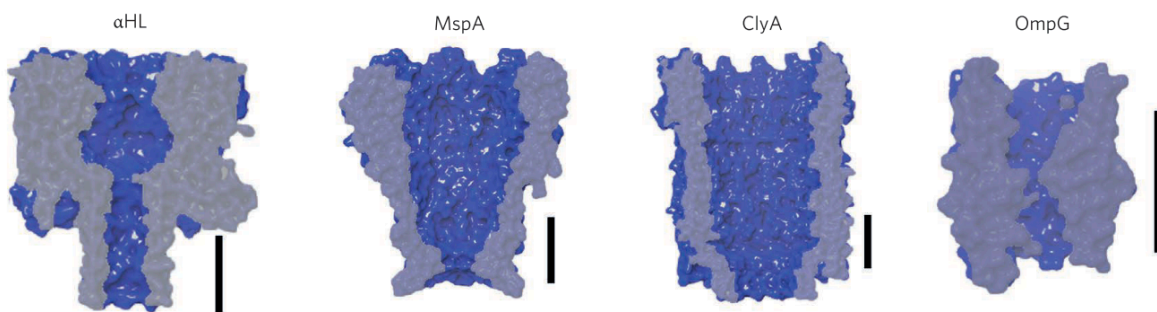
Figure 6. Cross-sections of X-ray crystal structures to show the lumen of four commonly used protein nanopores: α-HL, MspA, ClyA and OmpG. For scale, the lumen of α-HL is 1.4 nm in diameter at its narrowest point.[34] The scale bar = 3 nm. Adapted from Howorka.[35]

However, while cytotoxicity can be useful to harness in its own right, the pore-forming activity of proteins can be used for a host of other applications, principle among which is as molecular sensors. The ability to detect specific molecules in solution is both scientifically relevant and crucial to many processes, therapies, and devices. Protein nanopores have been used for nucleotide,[36] metal ion,[37] small molecule, [38,39] and protein detection,[40–42] as well as for DNA or RNA sequencing (Fig. 7).[43] α-HL is one of the most utilised protein nanopores, but it is not best suited for all applications. Some of the other common pores used for such applications are: OmpG, MspA, Aet, Phi29 Motor,

and ClyA.[34] Each of these protein nanopores have different structures and properties, such as different pore diameters, that make them more or less suitable for various applications.
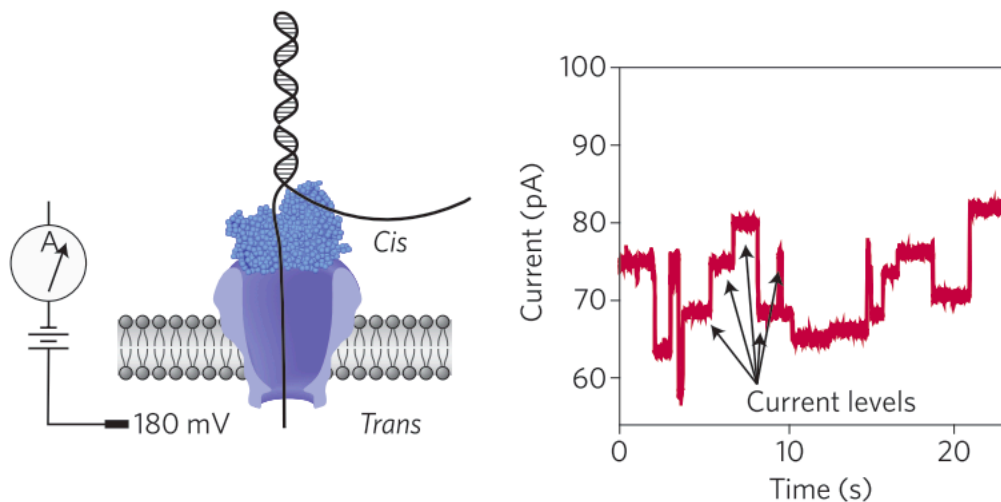
Figure 7. DNA sequencing using the protein pore, MpsA equipped with a DNA polymerase motor protein to controllably translocate the unzipped DNA through the pore allowing the sequence to be read from a current readout (right, red). Adapted from Howorka.[35]

Protein nanopores are highly stable in biological lipid bilayer membranes, reproducible and as they are produced by natural processes, they can be made in large quantities. However, protein pores are limited by the difficulties of large scale or *de novo* protein design.[44–46]

3.3. Solid State Nanopores

While protein nanopores have been highly successful as molecular detectors, there are several limitations. These include fixed pore sizes and geometries as well as the limited stability of the supporting lipid bilayers to adverse conditions such as changes in pH, salt concentrations and mechanical stress.[27,34] Some of these limitations have been addressed by research into solid-state nanopores (see Figure 8). Some of the advantages of solid-state nanopores are: they are highly stable; sub-nanometer precision has been achieved for pore size control and modifications; they can be more easily augmented with additional surface properties; and are easily manufactured and incorporated into other devises.[27,47] Common materials for solid-state nanopores have been SiN_x and SiO_2,[34] polymers,[48] as well as alumina.[49] In addition, there are a number of techniques for solid-state nanopore fabrications including: heavy-ion beam etching,[50,51] single heavy-metal ion etching,[52] electron beam etching,[53] asymmetric etching,[54] and track etching.[55] There have also been efforts to make ultra-thin solid-state nanopores to increase their sensitivity.[47,56] Solid-state nanopores have many of the same applications as protein nanopores and are similarly employed primarily as molecular detectors. Applications include: nucleic acid detection,[51] double stranded DNA

translocation,[57] direct protein detection,[58] detection of DNA bound proteins,[59] detection of protein-DNA interactions,[60] as well as for DNA sequencing.[61]
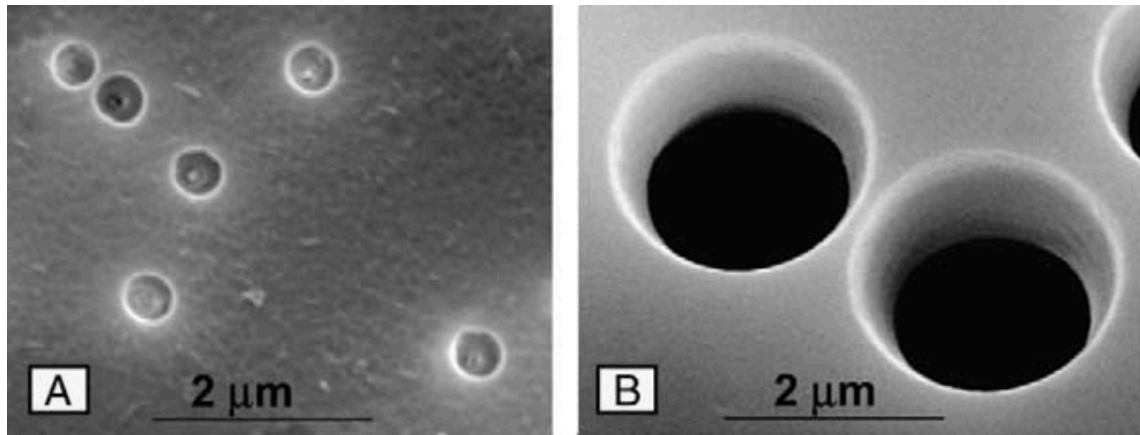
Figure 8. Scanning electron microscope images of conical poly(ethylene terephthalate) (PET) nanopores in (A) a 12 μm thick polyimide foil and (B) the large opening of a conical nanopore made via a track-etching technique.[62]

3.4. Protein vs solid-state nanopores

Despite the advances and success of solid-state nanopores, protein nanopores remain unrivalled for their atomic-level reproducibility.[34] In addition, advanced molecular biology techniques allow protein nanopores to be successfully modified and some control over their dimensions can be achieved. While this negates some of the advantages of solid-state pores, this is often offset by the intensive engineering effort that is required to do so.[44–46] The high stability of solid-state nanopores also makes them widely applicable in both biological and non-biological settings. While protein nanopores are generally more sensitive than solid-state pores, the instability of the lipid membranes they are inserted into, limits their application. In an effort to combine the advantages of both platforms hybrid pores have been created, such as that by Hall *et al.* where an α-HL nanopore was inserted and tethered within a solid-state nanopore.[63] Successful experiments proved that the structural integrity and functionality of the α-HL pore remained intact. Such systems could be used to integrate protein nanopores into other devices that have thus far only utilised solid state nanopores, as well as expanding the conditions under which protein nanopores can be used.

3.5. DNA Nanopores

3.5.1. Structure and Chemical Properties of DNA

Deoxyribonucleic acid, or DNA, is a large bio-macromolecule composed of two chains of poly-nucleic acids that coil around an axis to create a double helix.[64–66] Each DNA chain is composed of four bases: adenine (A), cytosine (C), guanine (G), and thymine (T). Each base is attached to a deoxyribose sugar that is linked to its neighbour via a phosphodiester linker to create a chain (Fig. 9). The four DNA bases fall into two categories: purine bases (adenine and guanine) and pyrimidine bases (cytosine and thymine). In classical DNA (B-form DNA), the two chains, or strands, of DNA are held together via hydrogen bonding between bases on opposite strands. This hydrogen bonding occurs between a purine and pyrimidine base and is highly specific between two base-pairs: A-T and C-G (Fig. 9). This specific association is the basis of the 1953 discovery of Watson-Crick base-pairing and is responsible for DNA's high sequence specificity that underpins transfer of genetic material and much of life.[64,66] This was a landmark discovery that effectively set-the-scene for the next half-century of biological research.[64,67,68]
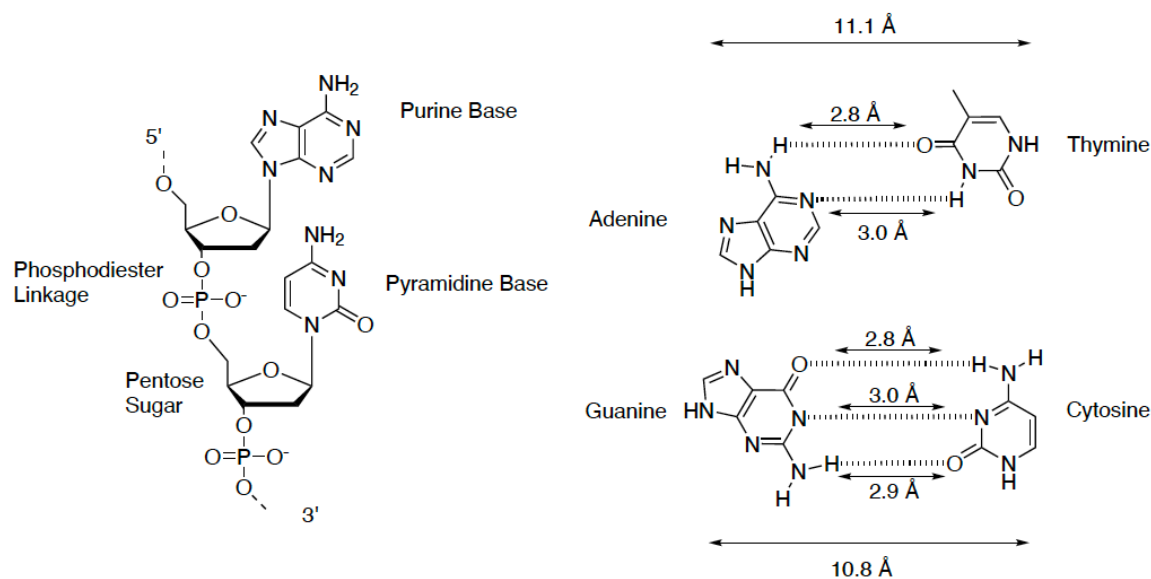
Figure 9. Chemical structure of DNA and Watson-Crick base-pairing in B-form DNA.[64]

Watson-Crick base-pairing facilitates the sequence-specific interaction of two strands and the formation of the antiparallel double helix structure. As indicated by Figure 9, the two sets of base-pairs are not equal. The G-C base-pair is stabilised by three hydrogen bonds, while the A-T is stabilised by two, making the G-C pair more stable. This is reflected by the higher than average melting temperatures (T_m) of G-C rich DNA and the lower than average T_m of A-T rich sequences.[64,69,70] Nevertheless, these base-pairs are more stable than any other combination of the

bases.[64]   In B-form DNA, the Watson-Crick base-pairs are held almost perpendicular to the phosphodiester backbone creating a flat plane. Each of these planes sits almost directly over the next base-pair in the chain.[64] This base-stacking occurs to maximise π-π interactions above and below the aromatic bases-pairs. Base-stacking, and hydrophobic burying in general, are a major driver of DNA strand assembly into the double helix structure.[64] Indeed, base-pairing is not the major driver of the formation of the DNA double helix. In fact, the hydrogen bonds stabilising the base-pairs are more easily stabilised by water. Rather base-pairing is responsible for the specificity.[66] DNA-DNA interactions are driven by hydrophobic burying, which is best achieved through base-stacking. To maximise base-stacking the bases must be held rigidly to allow for more than transient π-π overlap to occur, which is achieved through base-pairing. The specificity is imparted by the greatest stability imparted by A-T and C-G pairing.[64] Furthermore, as π-π interactions are most favourable when the bases are slightly offset, this promotes the formation of the right-handed antiparallel double-helix (Fig. 10).[64] This means that one strand of the double helix will run from the 5' to 3' end of the strand while the other strand will run from the 3' to the 5' in the same direction.
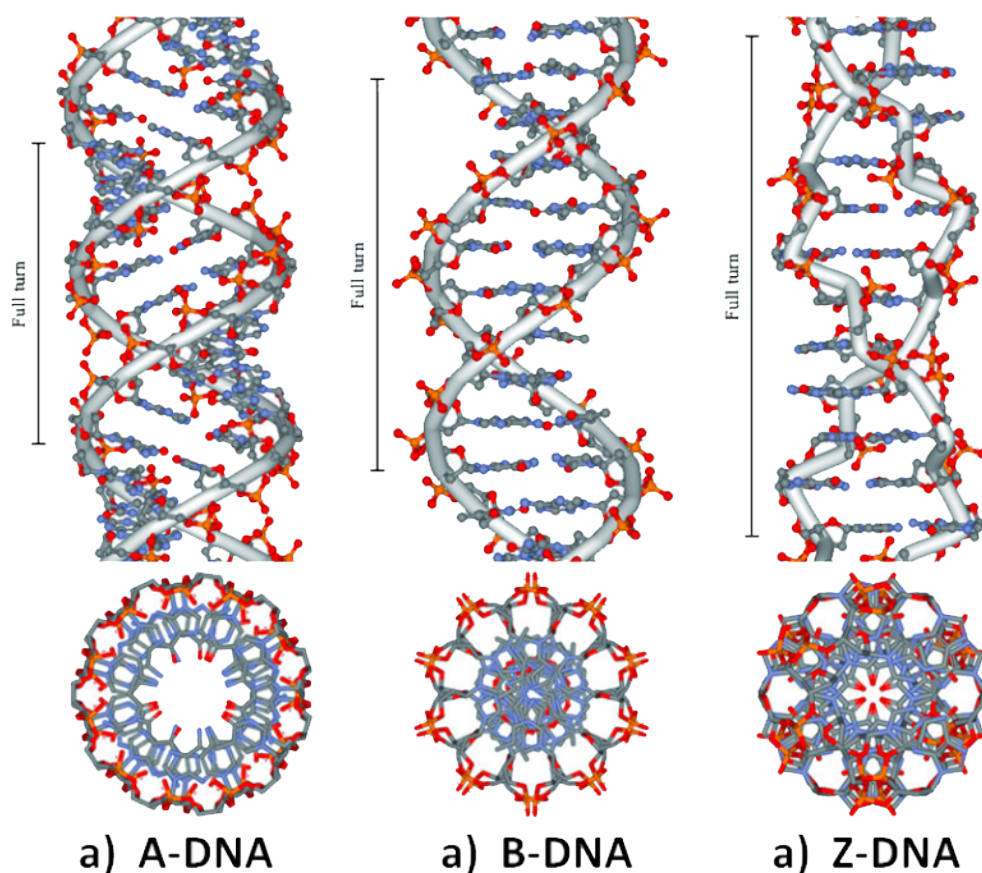
Figure 10. Top-down and side-on views of the three most common types of DNA tertiary structure. Adapted from Garcia-Ramos *et al*.[71]

The classical form of DNA, now known as B-form DNA (Fig. 10), was first described in 1953 by James Watson and Sir Francis Crick as a double helix with residues spaced 3.4 Å apart, a helical radius of 10 Å and a full turn every 10 residues.[66] It has now been shown that a full turn of B-form DNA occurs every 10.4-10.5 residues rather than 10.[64] B-form has a major and minor groove, which are 12 and 6 Å wide and 8.5 and 7.5 Å deep, respectively.[64,72] B-form DNA is the classical form of DNA because it is the most stable under physiological conditions and therefore the most biologically relevant. However, there are myriad different tertiary structures than can be adopted by DNA, which are driven by the energetics of base-stacking and the degree of hydration under different conditions. For example, the A-form of DNA (Fig. 10) is favoured in conditions of high salt and low humidity.[64] As shown in Figure 10, in A-form DNA the bases tilt to form a more compact structure.[64,66,71] Compared to B-form DNA, A-form has residues spaced 2.56 Å apart, 11 residues per turn and a helical radius of 12 Å. Moreover, A-form has a hollow core 3 Å in diameter, in contrast to the filled core of B-form.[64] This more compact structure leads to a shorter, but wider double helix with the major and minor grooves being more equivalent in size, but deeper than in B-form DNA. Another common form of DNA is Z-form DNA (Fig. 10). Unlike A- and B-form DNA, Z-form is left-handed, has comparable major and minor grooves, and repeats every two residues. Indeed, the left-handed structure necessitates a nucleoside *syn*-conformation of the glycosylic bond; however, this is not possible for pyrimidine bases, which causes them to adopt the *anti*-confirmation. This regular *syn-anti* alteration leads to a zig-zag shape and hence the name: Z-form.[64] A-, B- and Z-form are the most common and biologically relevant forms of DNA. Their different structures are shown in Figure 10. However, not all DNA tertiary structures adopt a helical structure, are necessarily a linear structure (e.g., G-quadruplex), or involve only two strands (e.g., triple-stranded DNA, G-tetrads, i-motifs, holiday junctions, etc.).[64,73–75] More than a simple carrier of genetic information, this range of possible structures and conformations makes DNA a highly versatile material.

3.5.2. DNA Nanotechnology

DNA nanotechnology is a 'bottom-up' fabrication approach that makes use of the highly specific Watson-Crick DNA base pairing,[66] structural regularity and flexibility.[67,68,76] While DNA molecules are principally found as primarily linear helical structures in nature, they can adopt a wide variety of structures, both permanent and transient. For example, during cellular meiosis when chromosomes share information in a process known as recombination, DNA molecules change into a transient migratory branched structure.[73] However, if maximum Watson-Crick base-pairing is achieved, it is possible to generate migrationally immobilised junctions (Fig. 11B).[76,77] Between three and eight DNA double helices may emanate from these junctions, which are known as Holliday Junctions after their discovery by Robin Holliday in 1963.[73] With the ability to incorporate permanent junctions, branched structures were created that self-assemble into pre-determined structures. DNA has other appealing features as a 'building-block' for nanotechnology. DNA is relatively small

compared to other macromolecules: with the previously described 2 nm helical diameter and 3.4 per-residue helical pitch. DNA is relatively stiff with a persistence length of approximately 50 nm, which makes it an ideal structural scaffold. In addition to these characteristics, there are 4^n possible base-pair combinations for a strand of length n, which allows for highly specific structures without the risk of miscoding, meaning structures are more likely to correctly assemble.[68]
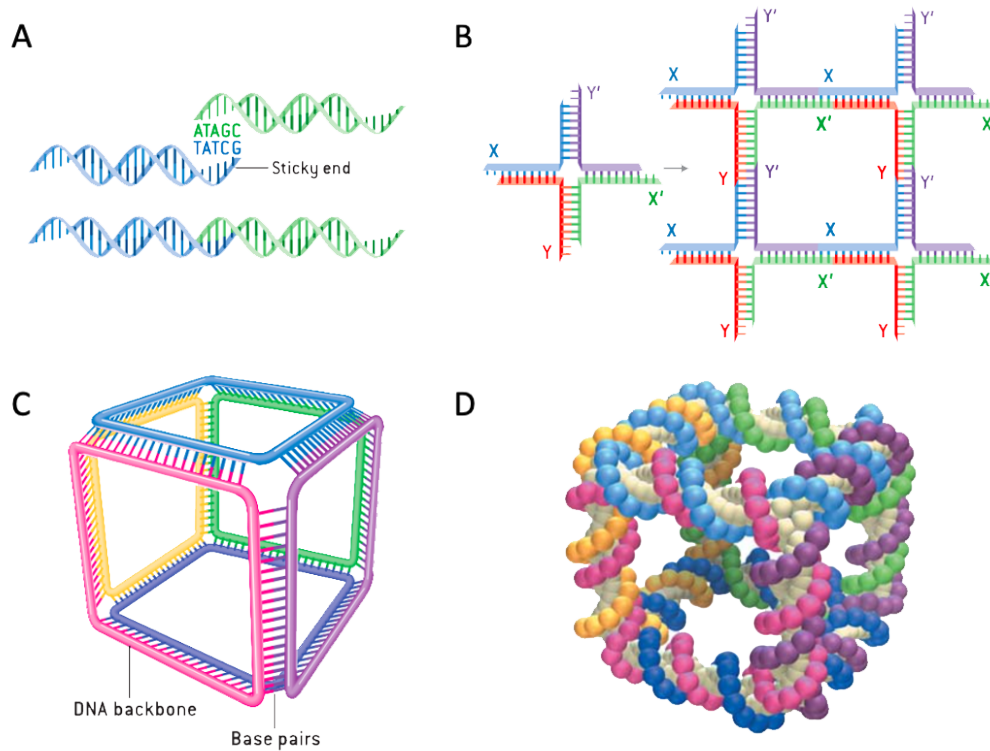
Figure 11. Construction of the 1991 Seeman Cube, the first DNA nanostructure.[78] (A) Illustration of the method of 'sticky ends', which allows two separate DNA helices to be connected. (B) The method of 'sticky ends' employed to connect immobilised DNA Holliday junctions to form a square face of the DNA cube. (C) 3D cartoon schematic representation of the DNA cube outlining its DNA structure in simplified form. (D) 3D structural representation of the DNA cube. (A)-(C) were adapted form Seeman[67] and (D) was adapted from Chen *et al.*[78]

The theoretical possibilities of using DNA as a building material were first theorised by Nadrian Seeman in the 1980s,[76,77] but it would take until 1991 for the first DNA nanostructure to be successfully constructed. This was a DNA cube[78] created by Junghuei Chen and Nadrian Seeman (see Figure 11C & D). Ten DNA oligonucleotides were used to construct two-dimensional (2D) squares, which were then ligated together to create the 3D cube. Shortly thereafter in 1994, Yuwen Zhang and Nadrian Seeman constructed a 'truncated octahedron' using an only slightly modified method, but with an expanded 49 individual DNA strands.[79] The construction of these original DNA nanostructures was laborious and time-consuming as they were reliant on precise stoichiometries between a large number of small DNA oligonucleotides. After each step, any excess

strands had to be removed and the assembled structure ligated together.[80] Even for a structure as simple as the cube there were a minimum of four of these steps. This original method quickly achieved an upper size limit due to the complexity of designing larger more complicated structures and the challenges associated with their assembly.

In 2006 Paul Rothemund published a paper in *Nature*, which outlined a new technique capable of creating much larger structures known as DNA origami.[80] Instead of many small equally sized oligonucleotides that were required in precise stoichiometries, this new method relied on a long scaffold strand that was then folded into the desired shape and secured by numerous short 'staple strands'. Rothemund's first structures were created using a scaffold strand with a length of 7,176 nucleotides, which was obtained from the genome of the *m13mp18* virus, and over 200 staple strands with lengths an average of 32 nucleotides (nt) in length. The staple strands were added in a 100-fold excess and then removed following purification. The DNA origami method is illustrated in Figure 12.
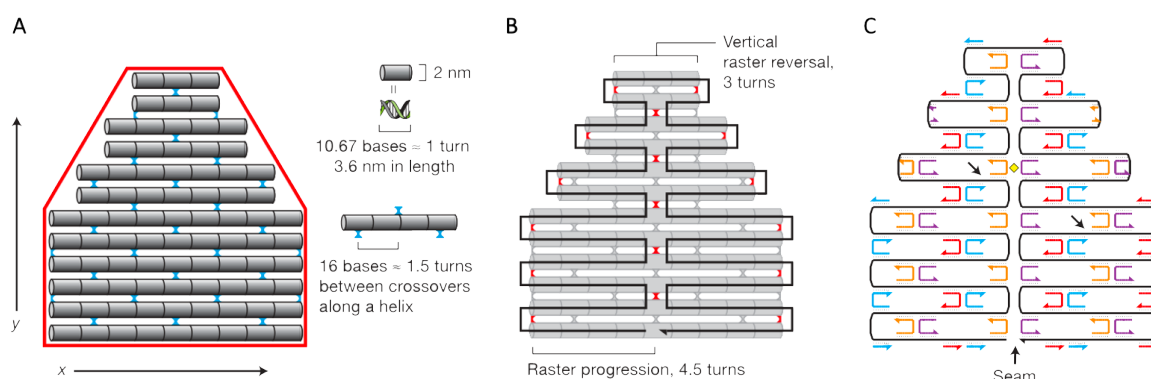
Figure 12. Schematic 2D diagrams illustrating the design of a relatively simple 2D structure composed of 12 inter-linked helices using the DNA Origami method. (A) 2D structural schematic indicating the 12 inter-linked helices that comprise the DNA nanostructure and the location of their connections. (B) Same as (A) with the scaffold strand overlain to indicate its use as the structural scaffold. (C) Reduced presentation of (A) and (B) indicating the locations of the staple strands (multiple colors) and how they are used to secure the scaffold strand (black) into the desired structure. Adapted from Rothemund.[80]

The structure shown in Figure 12 was only a relatively simple 2D structure composed of 12 helices, but at 200+ strands and dimensions of 34 x 36 nm it was already significantly larger and more complex than any previously designed structures. The DNA origami method demonstrated clear potential for the design and assembly of much larger, complex structures. The promise of the method was further demonstrated by the design of additional relatively simple shapes and demonstrating their successful assembly via transmission electron microscopy (TEM, Fig. 13).

Despite their relative simplicity, the TEM images clearly demonstrated fine structural control over a variety of large shapes with both external and internal definition, which was previously only the realm of top-down fabrication techniques. There have been numerous efforts since the publication of this paper to use DNA origami to create three-dimensional structures, with varying success. One of the most successful techniques was developed by E. Benson *et al*.[81] Their method utilised polyhedral meshes, which could be easily generated using computer software and then replicated using DNA origami. Structures varying in complexity have been constructed using this method. Some examples are provided in Figure 13B including a waving stickman, a bottle and a version of the Stanford bunny.
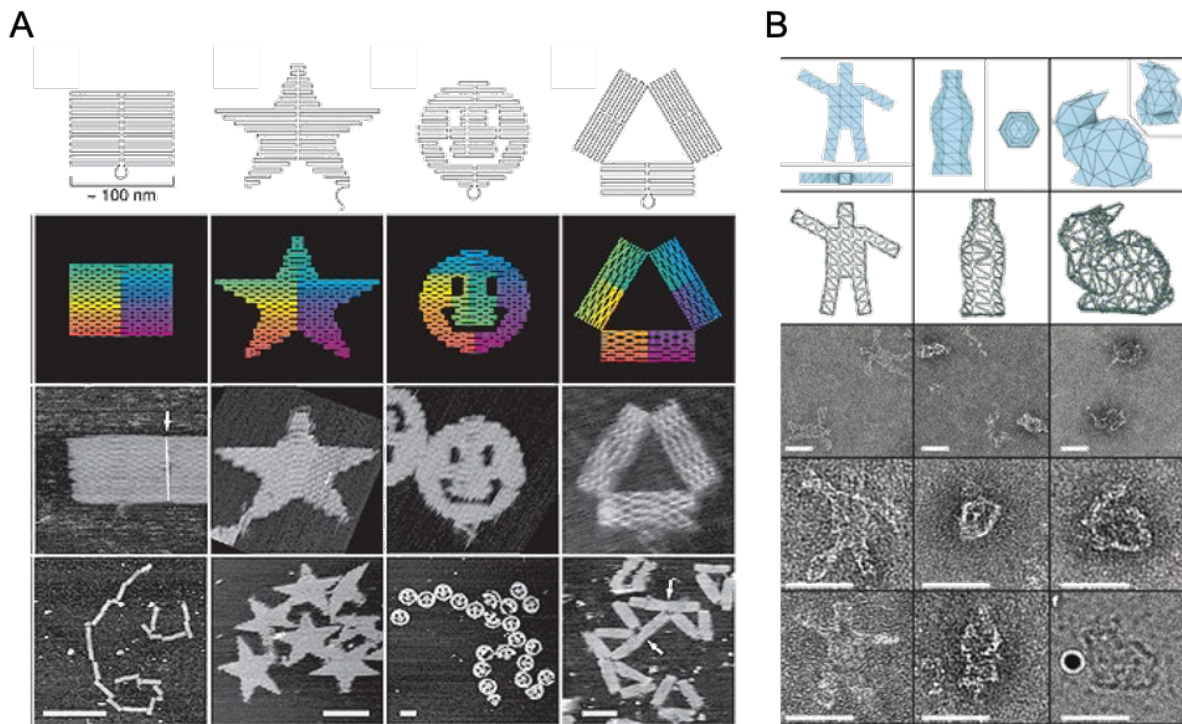
Figure 13. 2 and 3D structures designed and assembled using DNA origami and imaged using TEM. (A) 2D DNA origami shapes designed by Paul Rothemund. The first row depicts the folding paths: rectangle, star, smiley face, triangle with rectangular domains. The second row shows the blend of helices at crossovers and colours represent the base-pair index – red represents the 1st base and purple the 7000th; bottom two rows depict TEM images. (B) Examples of 3D DNA origami shapes designed using polyhedral mesh: a waving stickman, a bottle and a version of the Stanford bunny. The first row shows the computer-generated meshes; the second the idealised mesh transposed into DNA helices. The bottom three rows show TEM images to confirm their assembly. (A) was adapted from Rothemund[80] and (B) was adapted from Benson *et al*.[81]

Another important discovery was toehold-mediated strand displacement.[82–84] Toehold-mediated strand displacement is based on a biological process known as branch migration wherein a complementary strand replaces another strand in a duplex. This process was first applied to DNA nanotechnology in 2000 by Yurke *et al.* who used it to create a DNA-fuelled molecular machine.[83] Toehold-mediated strand displacement makes use of a short ssDNA overhang (known as a toehold) at the end of a duplex. A complementary strand then binds to this toehold and due to more favourable energetics, displaces the old strand. An example of this process has been reproduced in Figure 14. Toehold mediated strand displacement is a powerful technique that allows DNA to be used as part of dynamic systems. In particular this method has been employed in the development of DNA nanorobotics (such as a cartwheeling DNA acrobat[85] and a cargo-sorting DNA nanorobot[86]) and DNA smart devices and nanocomputing.[87,88]
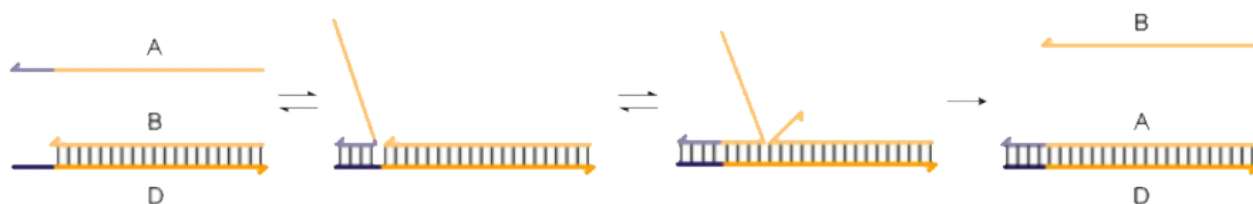
Figure 14. Example of toehold-mediated strand displacement. Strand A binds to the 4-nt toehold region of strand D to displace strand B due to the greater thermodynamic stability of the longer duplex and loss of the destabilising ssDNA region. Adapted from Haley *et al.*.[82]

DNA nanotechnology is a high precision technique that allows complete control over the special arrangement of different components in a given system (Fig. 15). This has made it a highly versatile technique that has seen wide ranging applications. In addition, to the previously mentioned examples of DNA robotics, smart devices and nanocomputing, DNA nanotechnology has also been used to engineer an autonomous DNA nanowalker,[89] and as a smart robot to delivery therapeutic cargo.[90] In recent years, DNA nanotechnology has increasingly been used to deliver therapeutic cargo,[15,91–96] or act as a therapeutic itself.[97–101] It has also been used for molecular detection.[102–105] In addition, DNA nanotechnology has also been used to mimic the function of naturally occurring proteins such as by artificial DNA-based SNARE proteins,[106,107] replicating the function of protein molecular motors;[108,109] creating a platform to facilitate and speed-up multi-enzyme cascades,[110] replicating the antibodies by creating a polyvalent DNA nanostructure[111] or through the use of DNA aptamers,[112,113] or by replicating the function of protein channels.[15,101,114–116] The potential applications for DNA nanotechnology are vast and rapid development is ongoing.
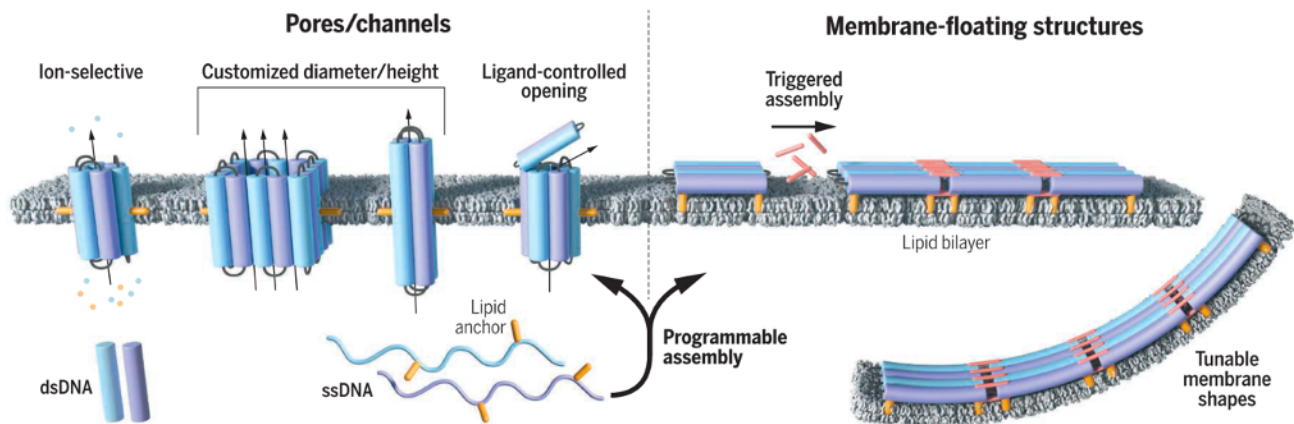
Figure 15. The interaction of various DNA nanostructures and nanopores with biological membranes demonstrating the power and precision of DNA nanotechnology to create customised biomimetic nanostructures and nanopores with various functions. Adapted from Howorka.[117]

3.5.3. DNA Nanopores

DNA is an ideal building material for the construction of synthetic biomimetic nanopores. As described in the previous section, DNA nanotechnology allows angstrom-level control of the shape and structural characteristics of DNA nanostructures.[117] In addition, the predictable and reliable nature of Watson-Crick base-pairing allows DNA nanopores to self-assemble quickly and reliably to make billions of identical structures with every fold, most of which are done in less than one day.[118] DNA nanopores can be designed with a wide variety of dimensions ranging from a single duplex[119] to pores with lumen diameters of >20 nm.[42,102] The design of some small DNA nanopores can even be done by hand,[118] while the design of large, complex pores is relatively straightforward with the aid of computer-assisted design using programs such as CaDNAno,[120] Perdix[121] or Adenita.[122] A few examples of DNA nanopores that have been published are summarised in Figure 16. In addition, because DNA nanopore structures can be predicted with great accuracy, functional groups, such as lipid anchors and fluorophores, can be placed on the structure with nanometer or even angstrom level precision without disrupting the overall structure.[123]
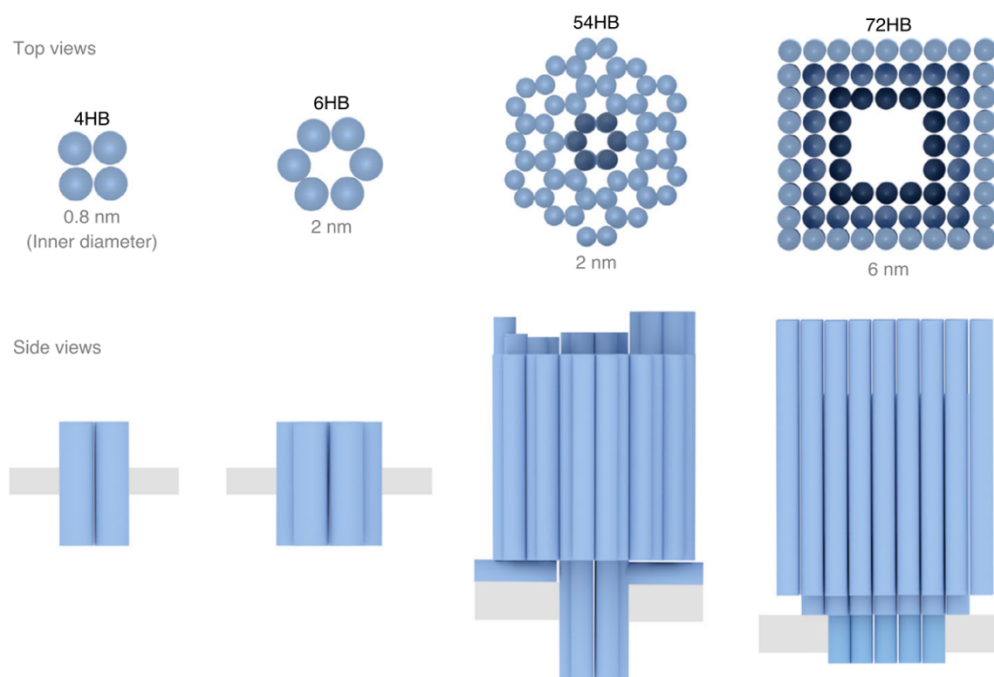
Figure 16. Overview of the designs of several existing DNA nanopores to highlight the range of possible designs and dimensions. The pores are arranged in order of pore lumen diameter from left to right and each blue cylinder represents a single DNA duplex, while the grey bar represents a lipid bilayer membrane. Adapted from Lanphere *et al.*[118]

3.5.3.1. DNA Nanopore Interactions with Lipid Bilayer Membranes.

Unlike protein or peptide pores, which have hydrophobic residues that allow them to insert into bilayers, the negatively charged DNA nanopores cannot insert into membranes on their own. To overcome this shortcoming, lipid anchors are used. There are several strategies that have been employed successfully in the literature. The first effectively mimics the hydrophobic belt of protein nanopores by masking the negative charge on the DNA backbone. This method involves using phosphorothioate modified DNA where the negatively charged phosphate oxygen is replaced by a thiol. An ethyl group can then be coupled to the thiol to make an ethyl phosphorothioate (ethyl PPT) hydrophobic belt around the nanopore.[101,114,124] The pore can then insert in the same manner as a protein without disturbing the lipid bilayer (Fig. 17B, Type I).[118,124]

By far the most common strategy was to use cholesterol (Fig. 17A).[11,15,42,97,102,115,125–127] Cholesterol is more efficient and cholesterol-modified DNA can be purchased commercially,[118] which makes it an appealing choice. Fewer cholesterol lipid anchors were required than ethyl PPT modifications to achieve successful anchoring (Burns *et al.*[114] used 72 ethyl PPT compared to 3 cholesterol modifications[115] to anchor comparably sized pores.). However, unlike with ethyl PPT, the use of a cholesterol lipid anchor does not mask the negatively charged DNA and results in the formation of

a toroidal lipid pore (Fig. 17B, Type II), which leaves small water filled gaps between the pore and the walls of the membrane.[118,119,128] Other lipid anchors have also been reported such as tocopherol (Fig. 17A),[129] and porphyrin (Fig. 17A),[119,130] which had the benefit of being fluorescent enabling label free monitoring of insertion.[119,130] The high affinity biotin-streptavidin interaction has also been exploited to anchor a DNA nanopore.[129]
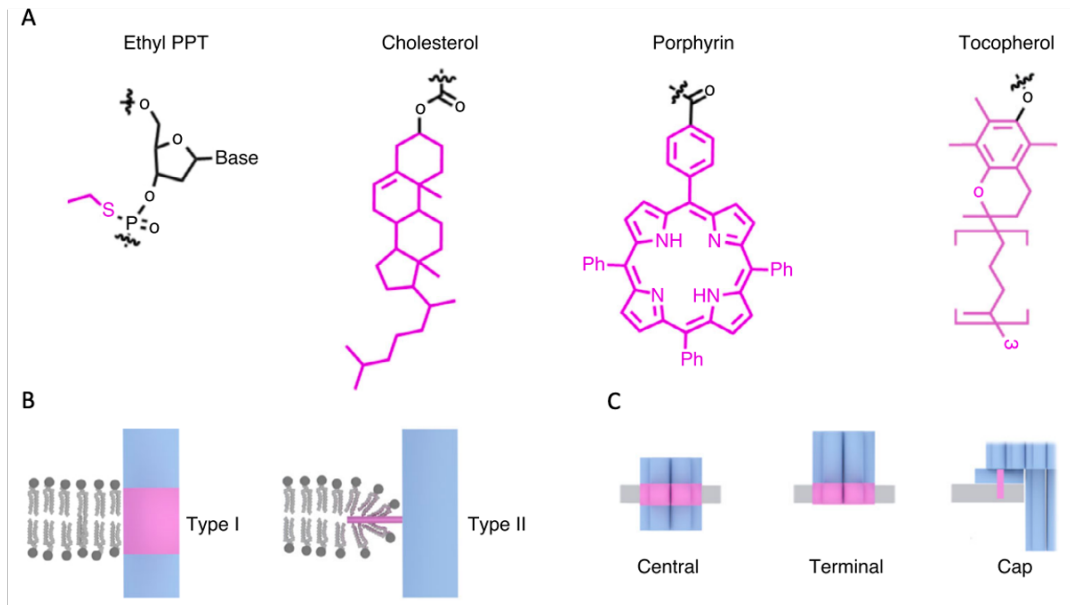
Figure 17. (A) Lipid anchors (purple) used to insert negatively charged DNA nanopores into hydrophobic lipid bilayer membranes including the charge masking ethyl-PPT, and lipid anchors: cholesterol, porphyrin and tocopherol. (B) The choice of lipid anchor affects the interaction of the pore with the lipid bilayer membrane. Type I is achieved using a hydrophobic belt such as by multiple ethyl PPT. The pore remains flush with the membrane. Type II results in the formation of a toroidal pore and occurs when a lipid anchor such as cholesterol is used. (C) The possible locations of lipid anchors. Central is the most common for small nanopores while terminal can be used by small and large pores. Cap is the most common for large DNA origami pores. Adapted from Lanphere *et al.*[118]

The mechanism for insertion of a cholesterol modified archetypal 6HB DNA nanopore recently published by Burns *et al.*[115] was recently investigated by Birkholz *et al.*[131] and Burns *et al.*[11]. Birkholz *et al.* used single molecule fluorescence to monitor the interaction of 6HB DNA nanopores with a lipid membrane when they were modified with one cholesterol lipid anchor (1C) or with three (3C). The authors observed rapid membrane tethering and diffusion along the lipid bilayer with the 6HB-1C. The same behaviour was initially observed for 6HB-3C, but after 60 min the pores demonstrated an 80% drop in mobility with most immobilised, while 6HB-1C remained mobile. The authors interpreted this change as 6HB-3C inserting into the lipid bilayer, which was not possible for 6HB-1C. This led to the proposed mechanism of rapid initial tethering the membrane followed by slower reorientation and insertion into the lipid bilayer (Fig. 18A). The proposed mechanism was supported

by Burns *et al.* who used a nuclease digestion assay to demonstrate that the 6HB-1C remains only tethered to the membrane, while the 6HB-3C inserts into the membrane. In a tethered state the strand nicks were exposed to the nuclease and digestion was observed; however, in the transmembrane orientation, the nicks were buried in the lipid bilayer and no digestion was observed (Fig. 18B).

In addition to corroborating the proposed mechanism of nanopore insertion, Burns *et al.* were able to use the same Bal-31 digestion assay to also demonstrate that the archetypal 6HB with centrally located cholesterol modifications (Fig. 17C) preferentially inserted into bilayers with a high degree of curvature (Fig. 18C). This matched a finding by Birkholz *et al.* who observed that particle immobilisation occurred more quickly when curvature was introduced to the bilayer (Fig. 19A). Furthermore, the authors also observed that in addition to inserting into bilayers, the 6HB-3C nanopores acted as a membrane exoskeleton and remodelled planar lipid bilayers into curved lipid nanotubes (Fig. 19B).
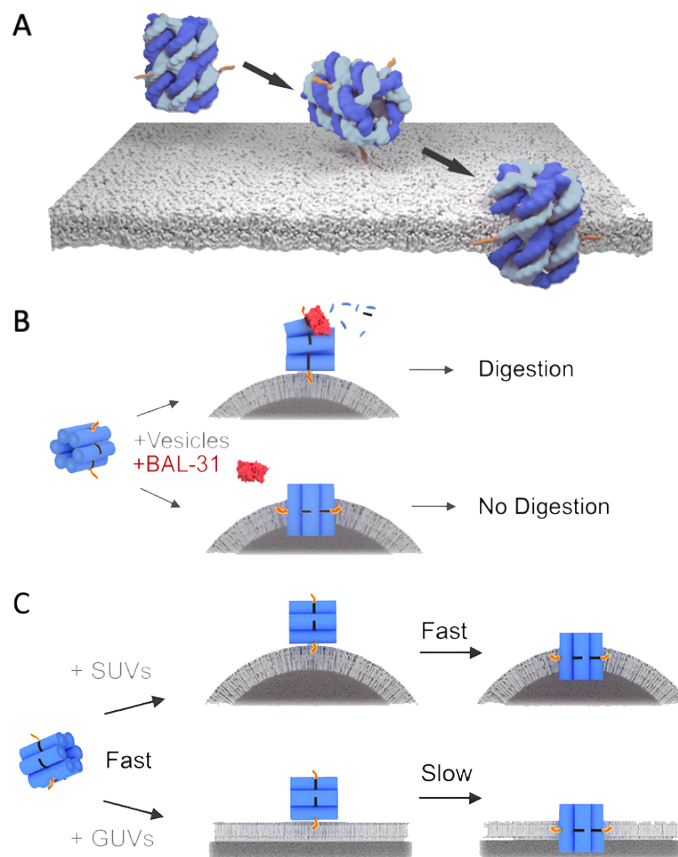
Figure 18. (A) Proposed mechanism of insertion for a small 6HB DNA nanopore functionalised with three cholesterol lipid anchors (orange) into lipid bilayer membranes by first tethering to the surface, then inserting into the bilayer and adopting a transmembrane orientation. Adapted from Birkholz *et al.*[131] (B) The insertion of a 6HB DNA nanopore into the membrane was confirmed

using a nuclease digestion assay. Membrane-tethered nanopores were digested, while membrane-spanning nanopores were not. (C) Following the proposed mechanism from (A) DNA nanopores functionalised with cholesterol lipid anchors insert more readily and at a faster rate into bilayers with higher degrees of curvature, such as SUVs. (B) and (C) were adapted from Burns *et al.*[11]
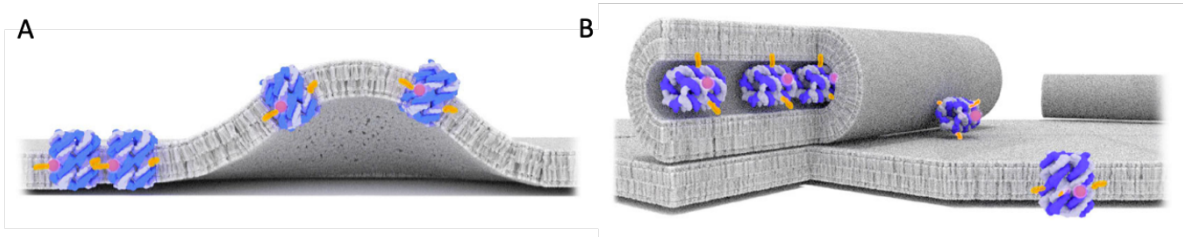
Figure 19. DNA nanopores remodelling lipid bilayer membranes. (A) Nanopores interacting with each other in a transmembrane orientation. (B) Nanopores causing the formation of lipid nanotubes. Adapted from Birkholz *et al.*[131]

While cholesterol has proven to be a highly effective lipid anchor, it has also been reported to cause DNA nanostructures to aggregate.[97,131–136] Cholesterol on its own has a critical micelle concentration (CMC) of ~30 nM[137] and maximum solubility in aqueous environments of 4.7 μM.[134] Banchelli *et al.*[134] observed that the critical aggregation concentration (CAC) of ssDNA modified with a single cholesterol was 10 μM; however, when four cholesterols were present this dropped to 0.2 μM. These values are close to the concentrations typically used to assemble DNA nanopores. It was therefore of fundamental importance to assess the stability of the DNA nanopores under various conditions to determine whether they existed in a free, available state, or an aggregated, and, therefore, unavailable state. Burns *et al.*[138] investigated the stability of the archetypal 6HB with up to three cholesterol modifications is various buffer conditions. The authors found that the 6HB was successfully assembled in all buffer conditions, including foetal bovine serum (FBS) and that the pores remained predominantly water-soluble even after 48 h, although some aggregation was observed, especially in FBS. The authors also assessed the cholesterol modified 6HB's ability to bind to vesicles in the various media. Membrane interaction was successfully observed in all media, with the exception of FBS, which observed significant loss of membrane interaction after as little as 20 min and almost no interaction after 1 h. The authors proposed that the cholesterol lipid anchors complex with serum proteins in FBS. This was later corroborated by Arulkumaran *et al.*[97] who observed the same behaviour in human serum. These findings present a significant challenge for the future application of lipidated DNA nanostructures in biological environments. Nevertheless, the pores demonstrated successful activity in all other conditions. The authors also noted that addition of a mild detergent, n-octyl-oligo-oxyethylene (OPOE), during the assembly process in all conditions, including FBS, resulted in significantly reduced aggregation. In addition, Arulkumaran *et al.* found that serum proteins did not interfere with vesicle binding that occurred prior to addition

of serum media. These findings present possible solutions for the use of lipidated DNA nanostructures in biological media.
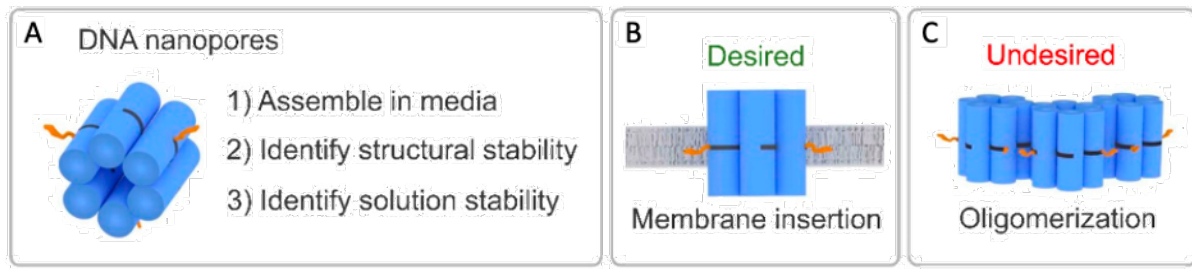
Figure 20. An investigation into the use of DNA nanopores in different media and their off-target effects, such as aggregation. (A) DNA nanopore assembly in different media. (B) Desired interaction between DNA nanopores and lipid membranes. (C) Undesired aggregation behaviour between DNA nanopores modified with cholesterol lipid anchors. Adapted from Burns *et al.*[138]

3.5.3.2. Large DNA Nanopores

The archetypal 6HB nanopore[115] discussed in the previous section is a minimal DNA nanopore that consists only of a transmembrane stem and has nominal dimensions of 9 x 5 nm with a pore lumen of ~2 nm. One of the major drivers for the inception of DNA nanopores was a desire to overcome the size and structural limitations imposed by protein nanopores.[118] In particular, it was of interest to develop synthetic nanopores for use in sensing.[35,42,102,116,117,139] To this end, a number of large DNA origami pore have been designed.[42,102,103,116,139]

Bell *et al.*[103] designed the first DNA nanopore, which was published in 2012. It was actually a hybrid nanopore composed of a large DNA origami nanofunnel modelled after the protein pore α-HL, which was inserted into a solid-state nanopore. This was conceptually very similar to the hybrid nanopore using α-HL published by Hall *et al.* in 2010.[63] The DNA funnel featured a 23 kbp long DNA double helix to help guide the pore into the solid-state support. This modification allowed the funnel to be easily trapped in the correct orientation and unlike in its α-HL counterpart, the strong negative charge of the DNA backbone allowed the DNA nanofunnel to be easily displaced by reversing the polarity of the current that was used to direct the pores insertion in the first instance. This pore was able successful translocate 15 kbp λ-DNA to successfully demonstrate that DNA nanopores can be used for DNA detection in addition to protein and solid state nanopores.

Also in 2012, the first membrane-spanning DNA nanopore was published by Langecker *et al.*[116] This pore was also modelled on the design of α-HL and featured a large membrane cap and a small transmembrane stem. The extra-membrane cap featured a thick outer shell of multiple layers of

DNA, which housed 26 cholesterol lipid anchors to insert the pore into the membrane (Fig. 21). This pore was used successfully to detect single-stranded DNA (ssDNA) and the electrophysiological measurements were comparable to those reported for α-HL indicating that the pore had successfully mimicked both the shape and function of α-HL. α-HL is an important benchmark for DNA nanopores as it often represents the gold-standard for activity due to its well-known structure, activity and reliable assembly.[102,115,116,140]
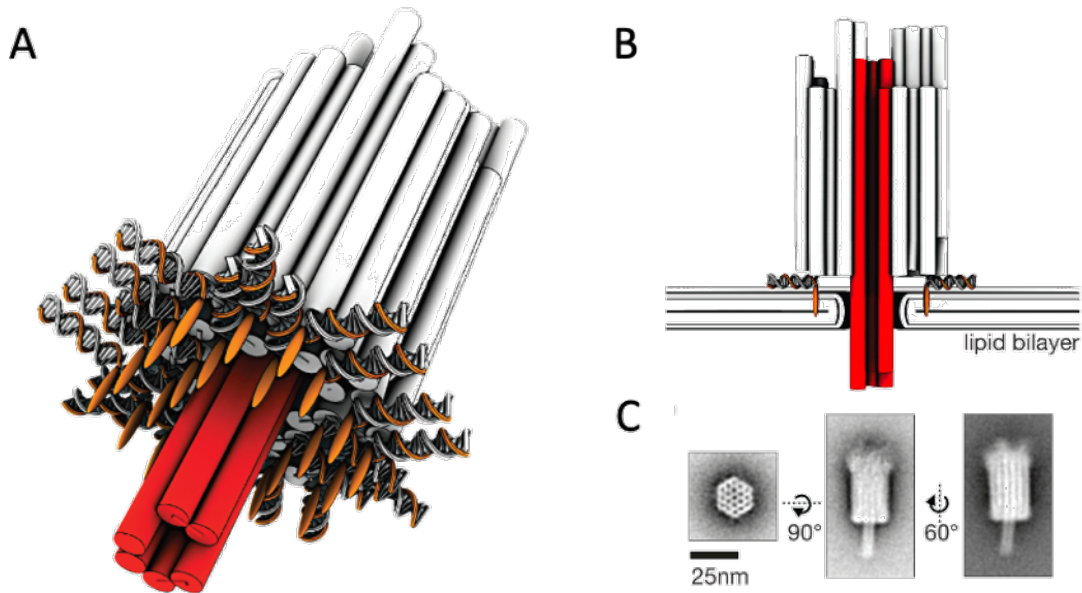
Figure 21. (A) The first published membrane spanning DNA nanopore featuring a large membrane cap region (white) modified with 26 cholesterol lipid anchors (orange) and a smaller transmembrane stem (red). (B) The pore inserted into a lipid bilayer. The pore is 42 nm long with a lumen diameter of 2 nm. (C) TEM images of the pore confirming assembly. Adapted from Langecker *et al.*[116]

Krishnan *et al.*[129] designed a DNA origami nanopore that featured the same basic elements of the Langecker *et al.* pore, a large extra-membrane cap region and a small transmembrane stem (Fig. 22A, red); however, unlike the Langecker *et al.* pore, the extra-membrane cap was a flat 51x46 nm rectangular DNA origami plate (Fig. 22). The benefit of this design was that it was able to accommodate significantly more membrane anchors and space them further apart (Fig. 22B). Instead of cholesterol, Krishnan *et al.* used two different strategies. The first, deployed 54 tocopherol lipid anchors. The second used 54 biotin modified anchors to bind to biotinylated lipids via streptavidin bridges. Both strategies proved successful to anchor the pore to membranes (Fig. 22C). Despite the superior binding of the biotin/streptavidin method, the drawback is the requirement of biotinylated lipids. Current recording analysis indicated ohmic behaviour and a large conductance of 3 nS, which was consistent with the size of the 4 x 4 nm lumen. In addition, this pore was able to translocate dsDNA across a membrane, which was previously only the remit of protein and solid state

nanopores. The T-shaped pore also demonstrated superior detection properties to the hybrid pore from Bell *et al.*[103] with a significantly improved signal to noise ratio. In another significant step, the T-shaped pore was able to spontaneously insert into GUVs without an applied current.
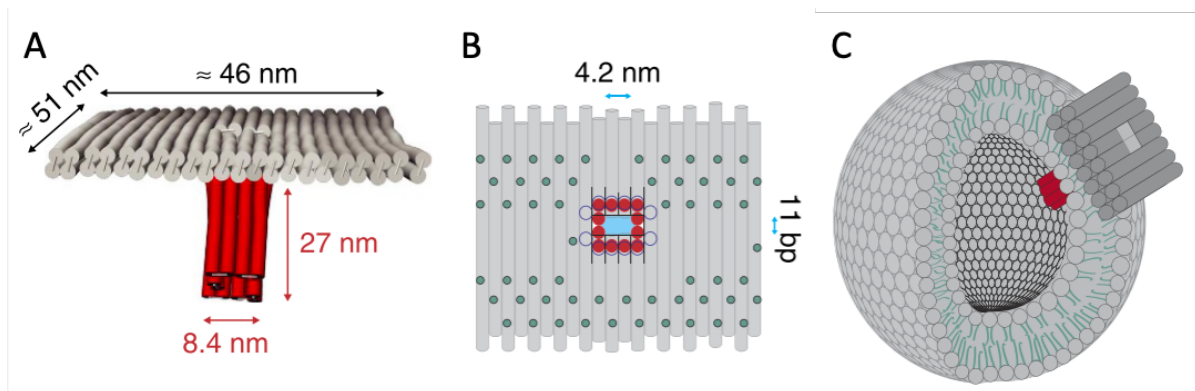
Figure 22. A large diameter DNA origami nanopore with a large flat rectangular membrane cap region and a square transmembrane stem (red). (B) The underside of the pore indicating the 57 possible tocopherol or biotin anchoring points to insert the 4.2 nm wide pore into the membrane. (C) The pore inserted into an SUV. Adapted from Krishnan *et al.*[139]

In 2016 Göpfrich *et al.*[42] published the largest DNA nanopore to date with a molecular weight of ~5 MDa (Fig. 23A). This 54 x 22 nm DNA origami pore further demonstrated the power of DNA origami to generate structures of comparable size and complexity to natural proteins. Most importantly this was the first DNA nanopore to have a >5 nm lumen, which at 6 nm was larger than most natural proteins. In addition, it is the largest DNA nanopore to be freely inserted into a lipid bilayer and not as a hybrid DNA pore into a solid-state support (this design was very similar to that used by Bell *et al.*[42] for the hybrid solid state nanopore). This pore also made use of the α-HL structure of a large extra-membrane cap region and a smaller transmembrane stem; however, unlike the Langecker *et al.* and Krishnan *et al.* pores, this pore adopted a funnel shaped lumen starting at 18 nm and narrowing to 6 nm (Fig. 23B). Furthermore, only 19 cholesterol lipid anchors were required to insert this much larger structure, compared to the 26 required to insert the pore developed by Langecker *et al.* or the 54 used by Krishnan *et al.* for their T-shaped pore. Supplementary to the achievement of inserting the largest DNA nanopore into a lipid membrane, the group also report a conductance of 30 nS, which was approximately 10x larger than the conductance reported by Krishnan *et al.* for their T-shaped pore and the conductance observed for α-HL.
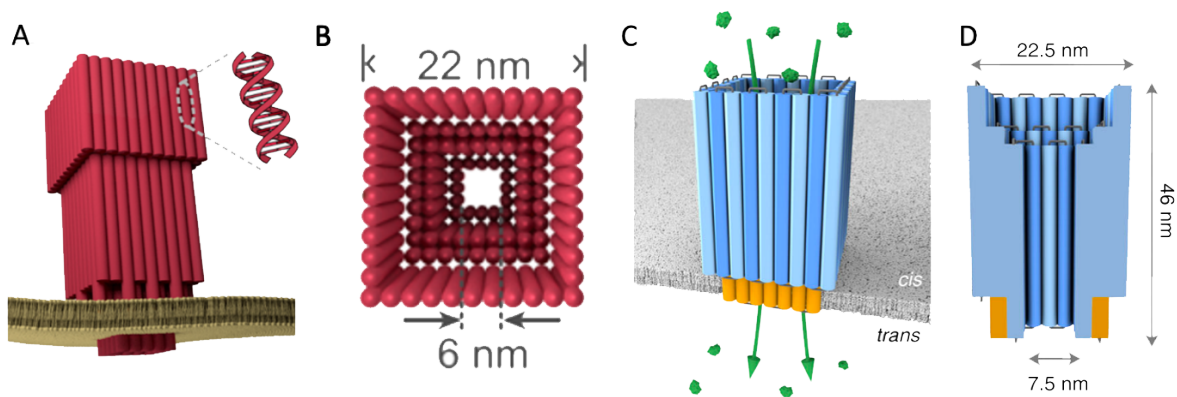
Figure 23. Two large diameter DNA origami nanopores with funnel shaped lumen.(A) The side-on and (B) down-down view of the 5 MDa DNA origami nanopore from Göpfrich *et al.*[42]. The pore has dimensions of 54 x 22 nm with a pore lumen of 6 nm at its narrowest extent. (C) Side-on view of the DNA origami nanopore from Diederichs *et al.*[102] that was able to translocate and discriminate between proteins. (D) Pore cross-section indicating pore dimensions (46 x 22.5 nm with a lumen of 7.5 nm) and lumen shape.

Another DNA origami nanofunnel was designed by Diederichs *et al.*[102] This pore was slightly smaller at 4.87 MDa than the 5 MDa pore from Göpfrich *et al.*; however, this nanopore achieved an even larger pore lumen of a remarkable 7.5 nm. In an important step for DNA nanopores, this pore demonstrated the translocation of folded proteins. The authors analysed protein translocation via single channel current recordings as well as single molecule fluorescent read-outs. By monitoring the kinetics of translocation, the authors were able to observe effects of nanoconfinement. This was the first instance of protein translocation through a membrane spanning nanopore and demonstrated the power of DNA nanotechnology to exceed the capabilities of protein pores. In addition, this study opened the door to membrane-spanning nanopore based protein-detection.

3.5.3.3. Small DNA Nanopores

While large DNA nanopores have been used to demonstrate the potential of DNA origami by replicating protein design and function (and in some cases, even surpassed it), they are time-intensive, costly and can only be produced at low concentrations.[118] This makes large DNA origami pores unsuited to many applications. In many cases, the large extra-membrane cap is superfluous to the intended application and can be removed leaving only the small transmembrane step. This was the approach that formed the basis of the archetypal 6HB bundle from Burns *et al.*[115] that was discussed in previous sections.

The Howorka group have produced several iterations of 6HB DNA nanopores. The first was produced in early 2013 using a DNA-origami based approach of scaffold and staple strands and so

was directly comparable to the Langecker *et al.* pore. However, unlike that pore which was 42 nm tall with a 2 nm wide lumen, this pore was only 15.5 nm tall and also achieved a lumen width of 2 nm. In addition, this was the first DNA nanopore to pioneer the use of the ethyl PPT hydrophobic belt to facilitate insertion into the lipid bilayer (Fig. 24A). The measured conductance was relatively low at 0.4 nS; however, this was only 55% lower than the conductance of 0.87 nS observed by Langecker *et al.* for this significantly larger pore. Subsequent iterations of this pores design experimented with different lipid anchor positions (central[114,124] vs terminal[101,123,130]) as well as different lipid anchors, such as the aforementioned ethyl-PPT, as well as porphyrin (Fig. 24B),[123,130] and cholesterol.[124] This pore design also pioneered the use of single channel current recordings on planar lipid bilayers for small DNA nanopores. This technique produced a conductance of 1.6 nS, which was more in line with expectations[123] and in excess of the larger DNA origami pores with a comparable pore lumen.[116] This technique also revealed channel-gating behaviour at high voltages.[123]
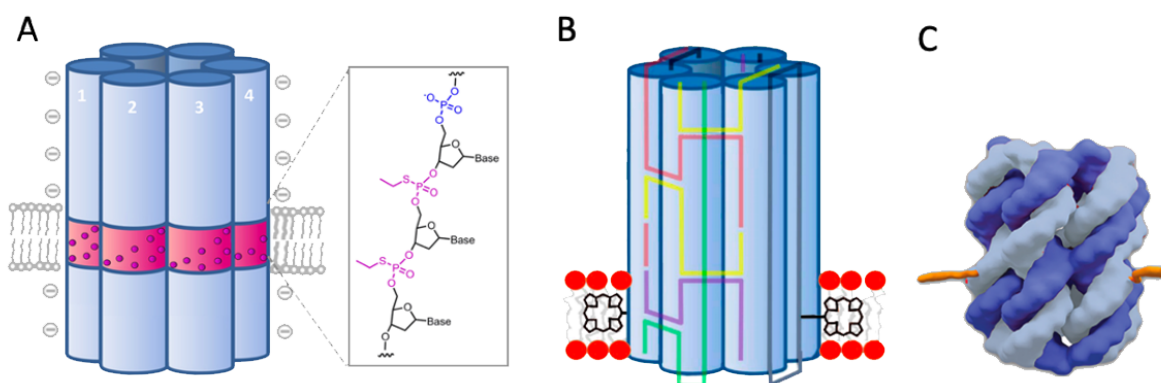
Figure 24. Different iterations of a 6HB DNA nanopore design from the Howorka group. (A) A DNA origami based 6HB nanopore with nominal dimensions of 15.5 x 5.5 nm with a 2 nm lumen and a centrally located belt of 72 ethyl-PPT lipid anchors.[114] (B) A pore with a design nearly identical to that of (A), but featuring duel terminal porphyrin lipid anchors.[123,130] (C) A 6HB DNA nanopore based on a terminal cross-over design. The pore is smaller than (A) and (B) at 9 x 5 nm with a lumen of 2 nm. The pore was modified with three evenly spaced central cholesterol lipid anchors.[115]

In a departure from DNA origami, in 2016 Burns *et al.*[115] developed a 6HB with a simplified terminal cross-over design (Fig, 24C).[118] Rather than the scaffold-staples technique, this pore relied on a classical approach of equimolar concentrations of strands of equal length. This new technique also allowed the pore dimensions to be further reduced to 9 x 5 nm, while maintaining a 2 nm wide lumen. In addition, this pore also demonstrated a conductance of 1.6 nS, which was in line with the larger design. This pore also used cholesterol lipid anchors, which would be used for nearly all pore future pore designs.

The Keyser group have developed extremely minimal nanopore designs. In 2016, Göpfrich *et al.*[119] developed a DNA nanopore based on a single duplex (Fig. 25A). The nanopore was 5 nm and only

20 kDa making it the smallest DNA nanopore ever developed by a significant margin. The conductance measured for this pore was extremely low at approximately 0.08 nS; however, this pore confirmed the formation of the toroidal lipid pore and that current, even if only in very small quantities, can traverse the membrane through the gaps between the walls of the membrane and the DNA.

The Keyser group also developed a 4HB DNA nanopore based on a single-crossover DNA tile design (Fig. 25B).[118,127] The benefit of the DNA tile design was that it made the pore easily scalable and allowed for rapid assembly – a 10 min folding protocol resulted in 85% and a 10 min incubation at r.t. resulted in a yield of 76%. However, the DNA tile designed 4HB resulted in a minimal conductance of 0.3 nS and demonstrated significant gating behaviour at high voltages.
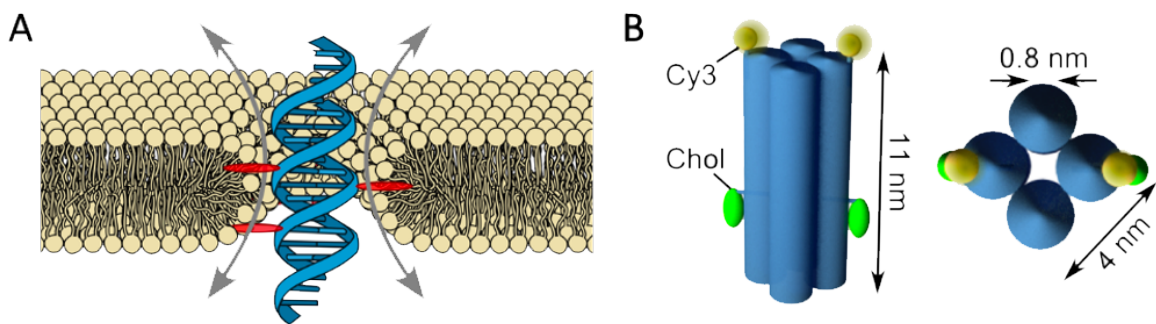
Figure 25. Minimal DNA nanopore designs form the Keyser group. (A) A DNA nanopore based on a single 5 nm long duplex.[119] The duplex uses six porphyrin anchors to sit in the membrane and current was observed translocating through the toroidal lipid pore and DNA helix. (B) A 4HB DNA nanopore based on a single-crossover DNA tile design.[127] This pore was 11 x 4 nm with a lumen of 0.8 nm and features two cholesterol lipid anchors.

In another significant deviation from the standard helical-bundle-based pore, Chidchob *et al.*[133] developed a wireframe DNA nanocube that features four dsDNA pillars that are connected by ssDNA regions (Fig. 26). This design feature allows the pore to be modified with up with eight cholesterol lipid anchors by addition of short 14-nt cholesterol modified ssDNA conjugates (Fig. 26). Using this design, the authors were able to successful demonstrate that cholesterol tags on at least two faces is key for a transmembrane orientation by successful transport of small molecule dyes across a bilayer membrane. The design and structure were also confirmed by molecular dynamics (MD) simulations, which also confirmed the formation of a toroidal lipid pore.
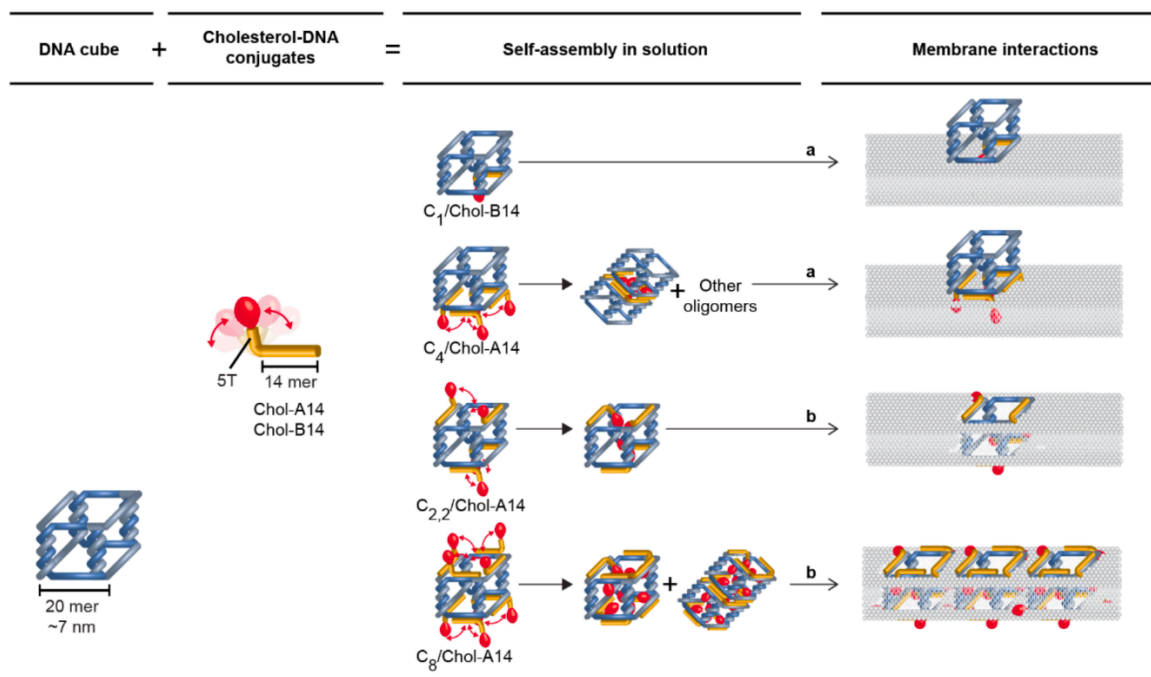
Figure 26. Wireframe DNA nanocube pore designed by Chidchob *et al.*[133] The design features four dsDNA pillars connected by ssDNA docking regions, which can be decorated with up to 8 cholesterol lipid anchors via conjugation to cholesterol modified ssDNA strands. The nanocubes are nominally 7 x 7 nm and successful demonstrated molecular transport across a bilayer.

3.5.3.4. Applications of DNA Nanopores

Over the course of the past decade, DNA nanopores have advanced from the proof-of-concept and design stages to demonstrating viable applications in their own right. Some of these applications have been previously described, such as a cholesterol modified DNA nanopore functioning as a cytoskeleton to remodel planar lipid bilayers,[131] or folded protein translocation through a large aperture pore for protein sensing,[102] but there are also other, equally varied applications.

In 2014, Burns *et al.* successfully inserted a 6HB DNA nanopore modified with a terminal band of 72 ethyl-PPT modification into HeLa cervical cancer cells.[101] This demonstrated the first instance of a DNA nanopore interacting with cells. In addition, the authors demonstrated a cytotoxic effect as a 20% decrease in cell viability was observed, with cytotoxicity observed after one hour or interaction and lasting for up to 72 hours. While significantly lower than what can be achieved by natural pore forming cytotoxins, such as α-HL,[141] the effect was comparable to small synthetic peptides.[142]

Then in 2016, Burns *et al.*[115] demonstrated that DNA nanopores can be used to mimic another cellular function: that of ligand gated channels (see Figure 27).[115] This pore was a modified version of the archetypal 6HB design shown in the same paper to include two loops extending form the top

of the pore allowing for a lid strand to be introduced that blocks the pore lumen. The authors demonstrated that the lid could be removed by addition of a ligand in the form of a complementary strand to the lid (Fig. 27). In addition, the authors were able to demonstrate that the lid prevented the passage of any molecular cargo across the bilayer and that transport was only restored upon addition of the key. Furthermore, the authors demonstrated charge selectivity allowing only a fluorophore with a net -1 charge to traverse the membrane and preventing the passage of a fluorophore with a net -3 charge. The transport activity was directly compared with the activity of α-HL using the same molecular cargo. While α-HL was a better transporter overall, it did not demonstrate any selectivity between the different charged cargos.
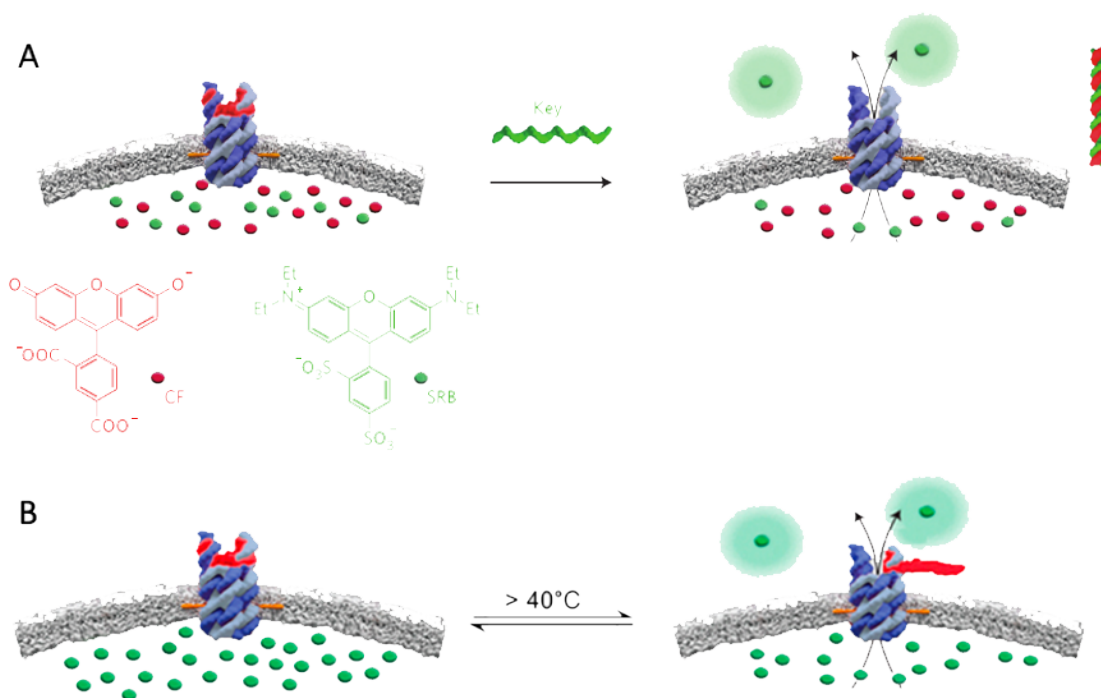
Figure 27. Scheme illustration of DNA nanopores able to function as synthetic gates that can be opened upon addition of a ligand[115] (A) or upon a change in temperature[125] (B) to transport molecular cargo across lipid bilayers. The ligand-gated pore in (A) was also shown to be able to discriminate between molecular cargo based on charge.

A pore using the same construction was designed by Arnott *et al.*[125] in 2019, except that instead of a ligand-gated pore, the authors designed a lid that was sensitive to temperature (Fig. 27B). The authors demonstrate that when the temperature increased to above 40 °C, the lid would dissociate from the docking loops to open (becoming fully open once the temperature reached 50 °C) and allow the transport of molecular cargo across the bilayer. The authors were also able to demonstrate that if the temperature then fell back below 40 °C, that the lid, which remained tethered to the pore, would close again demonstrating true reversibility.

DNA nanopores have also been used to form nanocontainers that function as a part of a hybrid nanoreactor.[143] The first DNA nanocontainer was developed by Andersen *et al.* in 2009 and featured a controllable lid that could release cargo;[144] however, Messager *et al.* were the first to design a nanocontainer that can also function as a nanoreactor. The nanocontainer was a hybrid structure made up of the archetypal 6HB DNA nanopore from Burns [115] and a synthetic polymersome (Fig. 28). The authors compared the synthetic vesicles to natural membrane compartment and organelles, but with added stability. The hybrid structure was large enough to encapsulate large enzymes on the order of 5 nm, while retaining their catalytic activity. It was also demonstrated that the enzyme substrate could be transported into the nanoreactor, undergo reaction and then the product could be transported out of the nanoreactor.
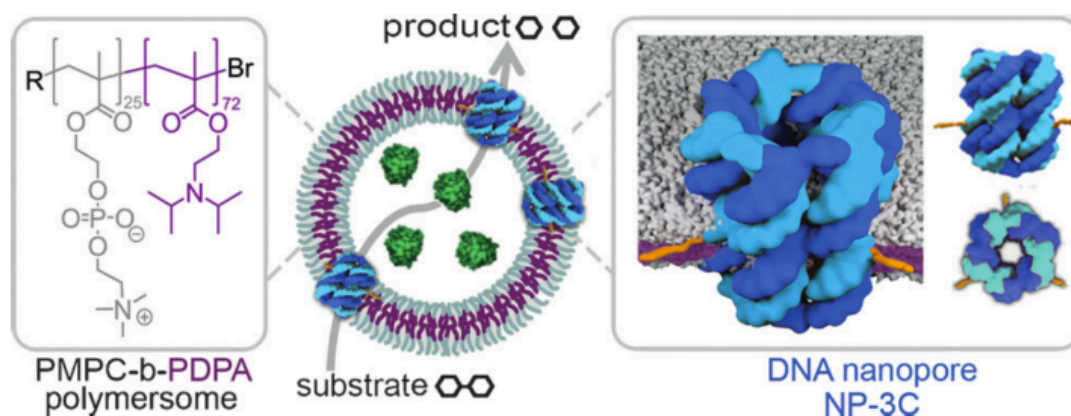
Figure 28. A synthetic nanoreactor designed by Messager *et al.*[143] and made from a hybrid of a DNA nanopore and synthetic polymersome. The DNA nanopore used as part of the nanoreactor was the 6HB DNA nanopore from Burns *et al.*[115] and features three cholesterol lipid anchors. The polymersomes were constructed using amphiphilic block co-polymers. The enzyme used was trypsin and the substrate was the fluorescent molecule B-NAR-AMC.

Ohmann *et al.*[126] design and built a synthetic biomimetic enzyme that replicates and outperforms the function of biological lipid scramblases (Fig. 29). This synthetic lipid scramblase was built from a 4HB DNA nanopore composed of eight strands using a double crossover design and two cholesterol lipid anchors. The authors demonstrate that insertion of the pore results in the formation of a toroidal lipid pore that connects the upper and lower membrane leaflets. This then leads to the rapid movement of lipids between the leaflets (the authors note a rate in excess of 10^7 lipids/s). Furthermore, the authors noted that this was a unique feature of pores that form toroidal lipid pores. Scramblase activity was not observed when pores were anchored via a hydrophobic belt, such as PPT-ethyl (Fig. 17A, Type I), which mimics protein insertion, instead of cholesterol lipid anchors. Indeed, the authors used a dithionite reduction assays to demonstrate scramblase activity using

GUVs and an annexin V-based assay to demonstrate scramblase activity on the surface of HeLa cervical cancer cells by scrambling the negatively charged PS lipids from the inner leaflet to the outer leaflet.
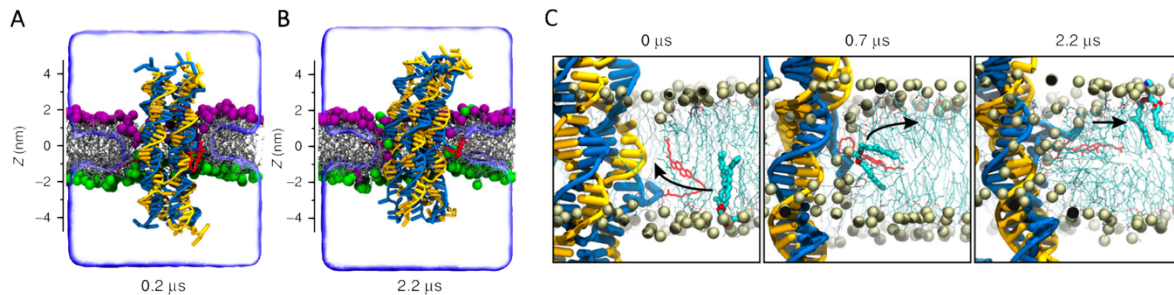
Figure 29. Synthetic lipid scramblase enzyme based on a 4HB DNA nanopore with two cholesterol lipid anchors designed by Ohmann *et al.*[126] (A) Initial parameters for an MD simulation demonstrating scramblase activity. The two leaflets are shown in different colors. (B) 2.2 μs into the MD simulation demonstrating mixing of the leaflets. (C) MD simulation demonstrating the chaperone activity of the cholesterol lipid anchor to flip a lipid from the inner leaflet to the outer leaflet.

Recently, DNA nanopores with cholesterol lipid anchors have been demonstrated to have a selective interaction with human immune cells (Fig. 30).[97] The pores demonstrated no interaction with red blood cells (RBCs) and demonstrated selectivity for white blood cells (WBCs) with an approximately 4-fold selectivity for granulocytes over peripheral blood mononuclear cells (PBMCs). The pores demonstrated no significant interaction with any other circulating cells. In addition, the authors demonstrated that the pores had no significant impact on WBC viability. Furthermore, it was shown that if WBCs were pre-incubated with the pores and then challenged with an endotoxin, such as lipopolysaccharide (LPS), the pores demonstrated a cholesterol dependent inhibitory effect by lowering the immune response.
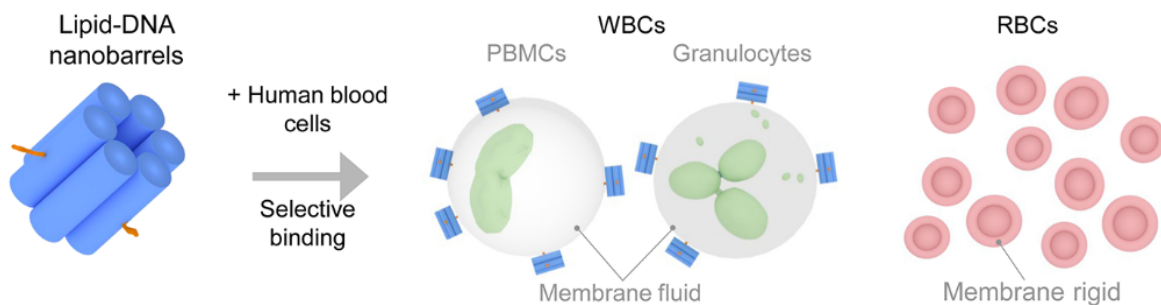
Figure 30. DNA nanopores with cholesterol modifications interact selectively with WBCs and demonstrate so significant interaction with other circulating cells.[97]

DNA nanopores are only a decade old and are still in a relatively early stage of research. Nevertheless, even at this early stage, DNA nanopores have demonstrated applications that are able to mimic and, in some cases, even surpass natural functions. DNA nanopores can demonstrate precise control of their geometries, their interactions with lipid bilayer membranes as well their interaction with molecular cargo. Together with the ease with which DNA nanopores can be designed and assembled, these characteristics make DNA an ideal material to construct nanopores with advanced functions and applications.

3.6. Nucleic Acid Aptamers

An aptamer is a short oligonucleotide of DNA or RNA (15-80 nucleotides in length) that folds into a unique 3D structure that is capable of binding to a specific target structure with high affinity (normally between 1 pM and 1 μM)[145] and specificity.[146–149] The term "aptamer" was coined in 1990 by Ellington and Szostak and was derived from the Latin "aptus" meaning "to fit" and the Greek "meros" meaning "part".[150] Nucleic acid aptamers are capable of binding to an extensive range of different targets from heavy metal ions[151–153] to small molecules,[154–160] proteins,[161–166] such as thrombin,[74,167–170] and even parasites,[171] viruses,[172–178] bacteria,[179–182] and whole cells.[183–190] Aptamers mimic the function of antibodies, as both bind targets with high affinity and selectivity;[156] however, aptamers (~10-15 kDa) are substantially smaller than antibodies (>150 kDa).[92,191] Aptamers can be so specific that they can differentiate between enantiomers or targets that differ by a single functional group[156] or even between proteins that have undergone post-translational modifications.[192,193] Aptamer-target binding occurs through a variety of non-covalent interactions such as electrostatics, Van der Waals forces, and hydrophobic interactions (such as base stacking) as well as induced fitting.[159,194–198] There are two primary regions of an aptamer: essential and supporting nucleotides.[160] The essential nucleotides are those that contribute directly to the binding of the target molecule or structure; removing or substituting any of these bases will lead to a loss of affinity. Supporting nucleotides are those that support the aptamer's secondary structure.

3.6.1. Aptamer Development

Aptamers are selected for their target using a technique known as SELEX (systematic evolution of ligands by exponential enrichment).[150,161] Starting from a large initial library of sequences (10^{14}-10^{15} unique oligonucleotides), over the course of several selection stages (each increasing the selection pressure) an aptamer can theoretically be selected for any target in a matter of days with minimal, if any, discrepancy between batches (Fig. 31).[147,156,174,199,200] The SELEX process can now be largely automated, selecting targets on nanomole scales and even incorporating post-selection modifications to further improve affinity.[147,148,156,201,202] The SELEX process has advantages over antibody

development as it can be performed *in vitro*, unlike antibodies, which require costly and time-consuming *in vivo* experiments for development.[174,203] In addition, aptamers can also be selected for a wider array of targets, including small non-toxic and non-immunogenic ones, unlike antibodies which require an immunogenic target.[153,156,204] Furthermore, as short single stranded oligonucleotides they are thermally stable, have reversible denaturisation, can be stored for months at room temperature and possess minimal immunogenicity or toxicity.[147,149,186,205] Both antibodies and aptamers bind to targets with extremely high affinity; however, due to the SELEX process, it is possible to tune the binding affinity of an aptamer by selecting for an aptamer with a dissociation constant (K_d) that falls within a desired range.[206]
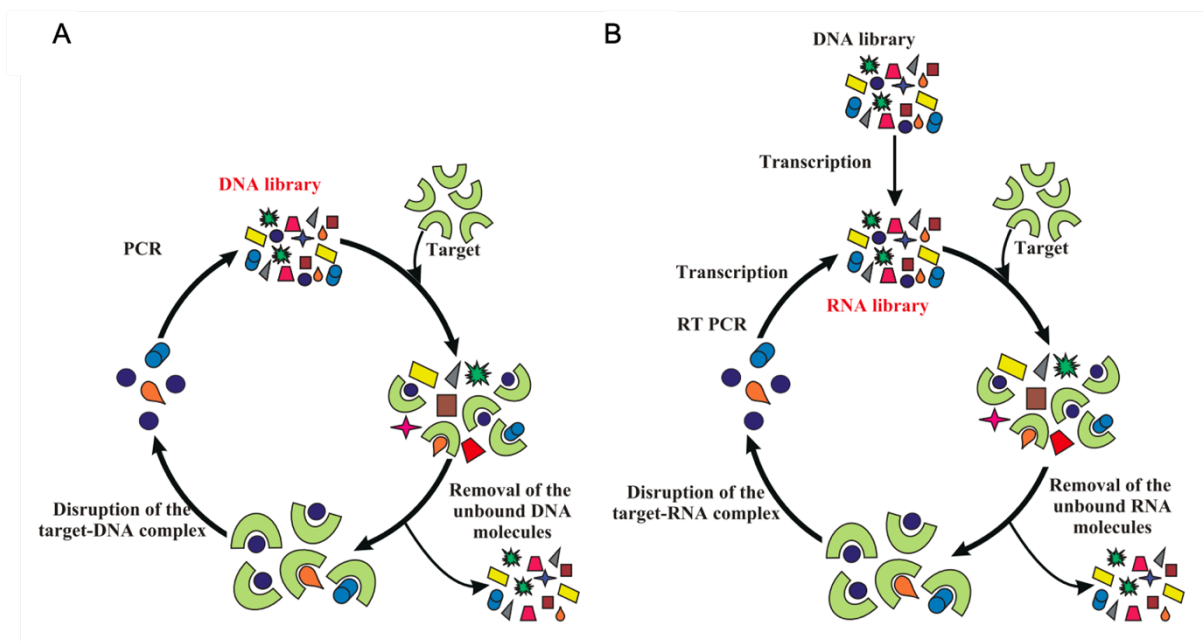
Figure 31. General scheme for the systematic evolution of ligands by exponential enrichment (SELEX) for DNA (A) and RNA (B) aptamers. Adapted from Davydova *et al.*.[204]

A major drawback to many common SELEX methods is that they require purified, immobilised targets.[112,151,166,183,207] First, not all targets can be immobilised as they may be too small (e.g. an ion) or they may require a membrane for stability. Second, an aptamer selected for a certain binding site on a purified protein may not bind to the target in its natural environment (e.g., the surface of a cell). To overcome these shortcomings the SELEX process needs to be adapted.

Cell-SELEX selects for targets in their natural environment.[173,208–211] This can be particularly potent when the desired target is a cell surface protein.[173,209,212] This removes the chance that the selected aptamer binds to a part of the protein that is now inaccessible or that has changed due to post-translation modifications.[149,208,213] Cell-SELEX works exactly the same way as traditional SELEX, except that whole cells are used in place of a purified product. To ensure that the correct target is selected for, negative selection steps are employed using either a cell derivative or cell line that does

not possess the target surface protein. [148,174,210,214] A further advantage is that this method allows an aptamer to be selected without any prior structural knowledge of the target.[208,213,215] Cell-SELEX has opened the doors for numerous applications including the detection of cancer cells.[186,207,209]

In vivo SELEX allows aptamers to be selected to target tissues and circulating species.[149,183,216] Furthermore, aptamers selected via this method have the advantage of being nuclease resistant, nor will they bind to non-target circulating cells or cell surface proteins, which prevents them from being removed from circulation. In this way, *in vivo* SELEX can be used to combat the major challenges posed to aptamers as therapeutics: namely the rapid degradation by nuclease, poor bio-distribution and rapid renal clearance.[147,149,217,218]

While *in vivo* SELEX can be a potent tool to develop nuclease resistant aptamers, it is not a universal method. By far the more common method is to use modified DNA and RNA. These can be modifications of either the nucleobases themselves or the sugar backbones (Fig. 32).[200,203,208] The most common modifications are modification of the sugar 3' position with an amine, methoxy or fluorine functional group, capping the 3'-end of the oligonucleotide with an inverted thymidine residue or replacement of the phosphate backbone with phosphorothioate.[146,147,208] Other modifications are also used such as incorporating nuclease resistant secondary structures (such as hairpins) or via ligation.[146,149,168] Another solution is the use of spiegelmers or "mirror aptamers", which are entirely composed of the *L-* rather than *D-* form of the oligonucleotide and are unaffected by nucleases.[146,147,149,203,208] A further strategy is to eliminate the aptamer entirely using "aptamer displacement screening" to replace the selected aptamer with an inhibitory low molecular-weight molecule instead.[176,177,219,220] While these modifications may improve nuclease resistance, it should be noted that the inclusion of any modification has the potential to impact the aptamer's affinity or specificity for its target.[149,208]

Being relatively small has distinct advantages for aptamers; unfortunately, a major disadvantage is that they are readily cleared by the kidneys, which can severely limit their efficacy as a therapeutic.[149] A common solution to this problem is to conjugate the aptamer to a larger, bulkier structure (e.g. PEG). This is a common solution for many low-molecular weight substances to increase their circulation time, including oligonucleotides, proteins, peptides, and small molecules.[149,221] PEG is a common choice,[147,207,208,216,222,223] but other molecules such as cholesterol,[224,225] proteins[226,227] and liposomes[225] have also been used. Some conjugates can also improve uptake into the desired tissues, such as the liver via conjugation to N-acetylgalactosamine (GalNAc).[228] The exact choice will depend on the desired properties.
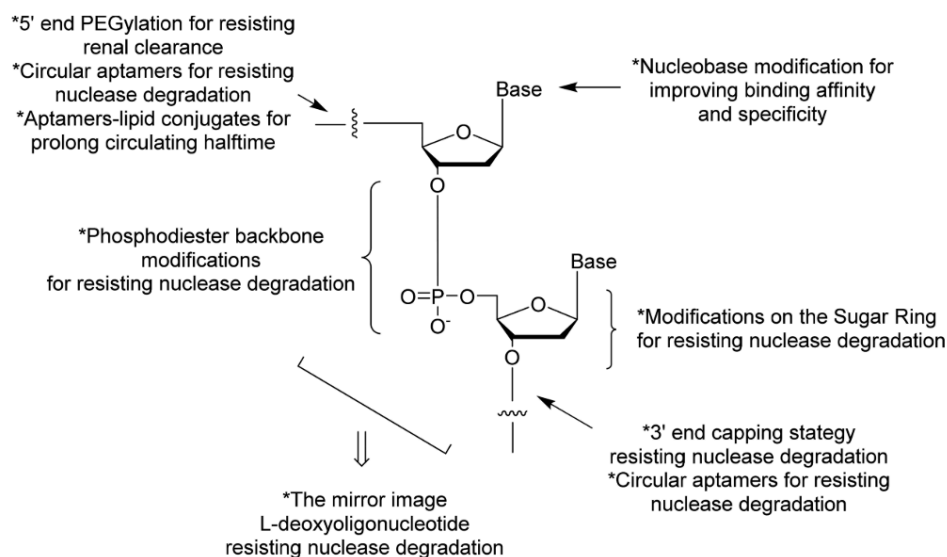
Figure 32. Schematic illustrating the common chemical modifications made to aptamers and the strategies behind them. Adapted from S. Ni, *et al.*.[228]

Aptamer modification can not only increase the stability, retention and structural diversity of aptamers and, therefore, the number of targets, but can also lead to stronger binding and control over the mode of action. One example are SOMAmers (slow off-rate modified aptamers), which contain deoxyuracil bases modified with various hydrophobic functional groups.[156,208,229] Or the creation of activated aptamers, which can be activated to transform from an inactive to an active conformation such as by incorporating a photosensitive moiety, such as o-nitrophenylethyl (NPE), into the nucleic acid backbone.[230]

Despite their potential, the hurdles faced by aptamers have limited their application as direct therapeutic agents and antibodies, which are well characterised and face fewer obstacles to *in vivo* applications, continue to dominate. Nevertheless, significant strides are being made to address these issues and increase aptamers viability as therapeutic agents while also making aptamers increasingly versatile.

3.6.2. Applications using Aptamers

Aptamers have been developed that fulfil a wide variety of biomedical applications from the therapeutic and diagnostic, to incorporation into smart-devices and technology. The ability to select an aptamer for any target with high binding affinity makes aptamers ideal candidates for detection and imaging. Aptamers, or "Aptasensors", have been developed to detect a wide array of targets ranging from small molecules,[231–234] viral[235–238] and bacterial[239–241] pathogens, as well as detecting various types of cancer[105,216,242–246] at extremely low levels. For example, when MCF-7 breast cancer

cells were plated at a concentration of 10^5 cells, an aptamer (AS 1411) was able to detect these cells with a detection limit of only 10 cells.[105] Aptamers can also be used to distinguish between types of closely related cells, such as between mature and immature dendritic cells[247] or between morphologically similar myeloid leukemia cells.[148,209] Aptamer-based sensing has been further improved through the development of smart functionality such as off/on activation, which not only improves the signal to noise ratio, but also allows different concentrations to be determined.[248] The same techniques used for sensing can be extended to provide the same degree of selectivity and sensitivity for live cell bioimaging.[94,98,182,248–251] The strong binding affinities allow less material to be used, which can limit toxicity of, for example, radiolabels. In addition, the fast renal clearance rates can be useful in this case to prevent build-up and improve detection limits.

Another development that recommends aptamers as therapeutic agents as well as imaging agents has been the development of aptamer antidotes. Antidotes allow the duration of action to be controlled by allowing aptamers to be "turned off". This can be achieved by employing the aptamer's complementary sequence[252,253] or, more universally, by polycationic biopolymers which bind the highly anionic oligonucleotides.[254] The efficacy of the antidote approach is highlighted by aptamers that act as anticoagulants, such as pegnivacogin,[255] an RNA aptamer that targets coagulation Factor IXa, where the reversal of aptamer action can be used to modulate or end the response, which may be necessary in the event of surgery or emergency.

Despite their potential, aptamers have not yet seen widespread use as therapeutic agents. There is currently one aptamer-based drug approved for use by the FDA: pegaptanib (trade name: Macugen, Fig. 33). Pegaptanib is an anti-VEGF-A (vascular endothelial growth factor A) RNA aptamer composed of 28 nucleotides, which is an anti-angiogenic drug used for the treatment of age-related macular degeneration (AMD).[222,256] Pegaptanib is a heavily modified aptamer with modifications including: inverted 3' thymidine cap, 12x 2'-OMe- and 13x 2'-F-modifications and a branched 40 kDa PEG – each branch is 20 kDa (Fig 33). The extent of the required modifications in order for pegaptanib to be a viable therapeutic highlight the challenges posed to the development of additional therapeutic aptamers. A good review that examines the path of pegaptanib from conception to FDA approval is provided by E. Ng *et al.*.[257]
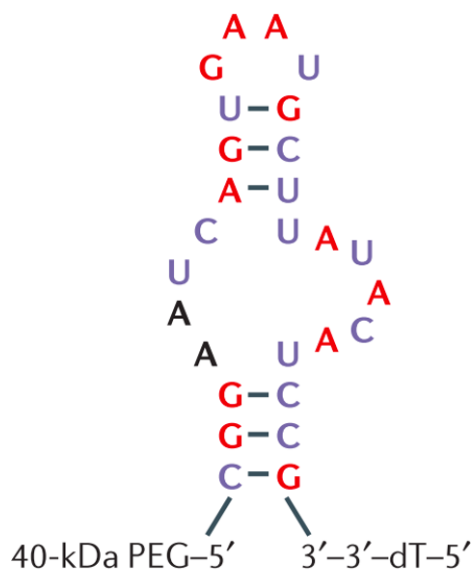
Figure 33. Structure and predicted secondary structure of Pegaptanib (Macugen) featuring the structural modifications. Purine bases with 2'-OMe-modifications are shown in red, pyrimidine bases with 2'-F-modifications are shown in purple and unmodified ribonucleotides are shown in black. The inverted thymidine (dT) is indicated at the bottom right and the dual 20 kDa PEG entity is indicated at the bottom left. Adapted from E. Ng. *et al.*.[257]

While only pegaptanib has been approved thus far, there are an additional 10 aptamer-based therapeutics currently undergoing clinical trials with various targets to treat a range of maladies, such as: nucleolin binding to treat leukemia,[258,259] hepcidin inhibition to treat anemia of chronic inflammation,[260] CCL2 inhibition to treat inflammatory diseases,[261,262] CXCL12 inhibition to promote T-Cell mediate cancer therapy,[100] thrombin inhibition for anti-thrombosis,[263] inhibition of the von Willebrand factor for anti-thrombosis,[264,265] inhibition of the C5 component to reduce imflammation,[266] inhibition of the tissue factor pathway inhibitor (TFPI) to treat hemophilia A and B,[267] direct coagulation factor IXa inhibition to treat acute coronary syndrome,[268] and another to treat age-related macular degeneration by targeting the platelet derived growth factor (PDGF).[269] In addition to the challenges already described, the modifications made to aptamers to overcome these challenges can cause problems themselves during development and clinical trials. This was the case with pegnivacogin, which was recently withdrawn from phase III clinical trials due to PEG allergies in a few candidates.[270,271] Additional hurdles are posed by the regulatory process itself. One example being the difficulty posed by pre-clinical evaluation in other species due to aptamers sensitivity to post-translational modifications.[147,224]

The application potential of aptamers does not end with therapeutics. Aptamer's small size (~2 nm and ~6-30 kDa), especially compared to antibodies (~15 nm, 150-180 kDa),[208] gives them excellent tissue penetration and also makes them easy to incorporate as part of larger biotechnological systems

and devices. A further advantage is aptamer stability outside of biological environments and their long shelf-lives making them ideal for long-term use or devices whose remit falls outside of the biological environment. One such application is the creation of a new type of stochastic protein detection devices. For example, by adding a thrombin binding aptamer to the protein nanopore alpha-hemolysin in order to detect thrombin concentrations.[272] Another is a multifunctional DNA nanodevice (termed nanoflower) that uses an aptamer to target the overexpression of PTK7 receptors on the surface of HeLa cells to image the cells and also deliver a cytotoxic payload of doxorubicin.[98] A further example is a DNA nanorobot that employs a nucleolin binding aptamer to target cancer cells and specifically deliver a thrombin payload to tumour-associated endothelial cells as a targeted cancer treatment *in vivo*.[90] For the reverse, a logical smart circuit for the programmable autonomous detection and regulation of proteins has been developed to detect local levels of thrombin and sequester thrombin when the levels are over the threshold.[206] This device takes advantage of two aptamers that bind to thrombin. One is used purely for concentration detection and binds to the heparin binding site (exosite II), which does not interfere with anticoagulation. The other is a true anti-thrombin aptamer and binds to the thrombin active site, the fibrinogen exosite (exosite I), to arrest thrombin anticoagulation activity. This smart circuit has now been incorporated into an intelligent autonomous DNA nanorobot that can monitor and control coagulation in human plasma.[87] These devices highlight the role aptamers can play as part of next-generation smart devices for personalised medicine and bio-computers.

While aptamers have not yet lived up to their potential as direct therapeutics, there has been an explosion of aptamer research in the last 30 years and development continues apace. Indeed, aptamer utilisation for detection and imaging purposes as well as increasingly part of nanodevices indicates that aptamers have a bright future as part of next-generation targeted therapies and diagnostics as well as part of smart technologies such as bio-computing.

4. Model System to Explore DNA Hybridisation Under Steric Constraints

4.1. Aims

The aim of this chapter was the design of a model system to explore DNA hybridisation under steric constraints. The major focus of this thesis was the development of DNA nanopores with higher-order function that respond to exogenous triggers. In order for those nanopores to be effective, it was important to understand the effect on hybridisation at the membrane surface as well as on a DNA nanostructure itself. DNA hybridisation on surfaces has been previously explored[273–280] as has the interaction of DNA tethered to surfaces[10,131,134–136]; however, these studies have generally focused on the interaction of small DNA oligonucleotides and the effect of density. These are important properties, but less relevant for constructing a system that will assemble into a larger nanostructure or open in response to a trigger. Indeed, the explicit effect of sterics on the biophysical properties of DNA hybridisation on the membrane surface when one of the ssDNA strands is attached to a bulky nanostructure has not been sufficiently explored. This was vital for pore assembly on the surface and unlocking pore formation and function on the membrane surface. To this end, a model system comprising four hybridisation conditions was conceived. A control system was designed as a baseline that consisted of simple DNA hybridisation in solution between two 20-nt ssDNA strands: a receptor and a steric element. The other three conditions were hybridisation at the membrane surface as well as hybridisation in solution and at the membrane surface when the steric element was attached to a DNA nanopore. The aim was to extract biophysical data about hybridisation under these steric constraints to inform the design of the nanopore that can undergo triggered assembly on the surface of a membrane as well as the protein-gated nanopore.
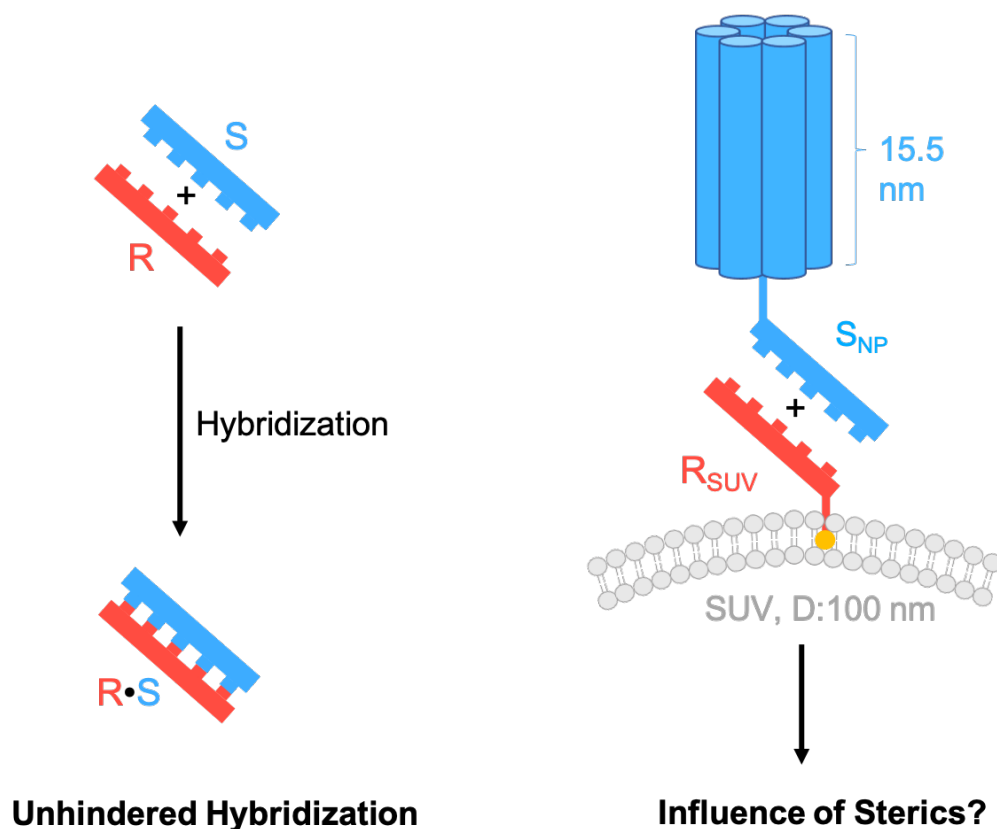
Figure 34. Schematic illustrating the purpose of the model system and how it is used to probe the influence of sterics on DNA hybridisation on the surface of a lipid membrane. The simplest of the four conditions, hybridisation of the receptor (R, red) and the steric element (S, blue) is shown on the left. This is the baseline condition. The most sterically hindered of the four conditions is shown on the right, hybridisation of the vesicle anchored receptor (R_{SUV}, red) and the ligand attached to the nanopore, (S_{NP}, blue). The cholesterol lipid anchor used to anchor R to the SUV is shown in orange inserted into the grey lipid bilayer. The SUVs used were composed of DOPC and DOPE in a 7:3 mole ratio and extruded to be ~100 nm in diameter. The other two conditions are implied as a mixture of the two shown.

4.2. Results and Discussion

I conceived of the project under the guidance of Prof. Stefan Howorka. All experiments for the model system were carried out by me, except for the TEM, which was carried out by Dr. Yongzheng Xing. Dr. Yongzheng Xing also assisted with confocal laser scanning microscopy and the formation of GUVs. In addition, Dr. Christoph Salzmann was consulted for the kinetic analysis. All data analysis was carried out by me, unless the assay was performed with or by someone else, in which case analysis was done with or by them. Prof. Stefan Howorka supervised all stages of the project.

4.2.1. Design and Assembly of the Model System

The main requirement of the model system was simplicity. For this reason, a simple receptor-ligand model was selected with the binding region composed of 20-nucleotides (20-nt). For the receptor, a 20-nt ssDNA strand was selected. In addition, when used to bind to vesicles, this strand would carry a cholesterol lipid anchor modification attached to the 3' end via a triethyleneglycol (TEG) linker. The receptor was designated, R, or R_{SUV} when carrying a lipid anchor and bound to vesicles (Fig, 34). The sequence of R is:

R (5'→3'): TAGTCGATTTTATCCATGCA

Two ligands were then designed. The first was simply the 20-nt complementary sequence to R on its own. This was designated, S, for steric element. The second was again the 20-nt complementary sequence to R but with a DNA nanopore composed of six-helical bundles (6HB) attached to it. This was designated S_{NP} (Fig. 34). The sequence of S is:

S (5'→3'): TGCATGGATAAAATCGACTA

The next step was the selection of the DNA nanopore to act as a scaffold for the 20-nt extension to make S_{NP}. Variants of the nanopore designed by Burns et al.[115] were initially selected featuring a range of locations for the 20-nt S extension (Fig. 35).
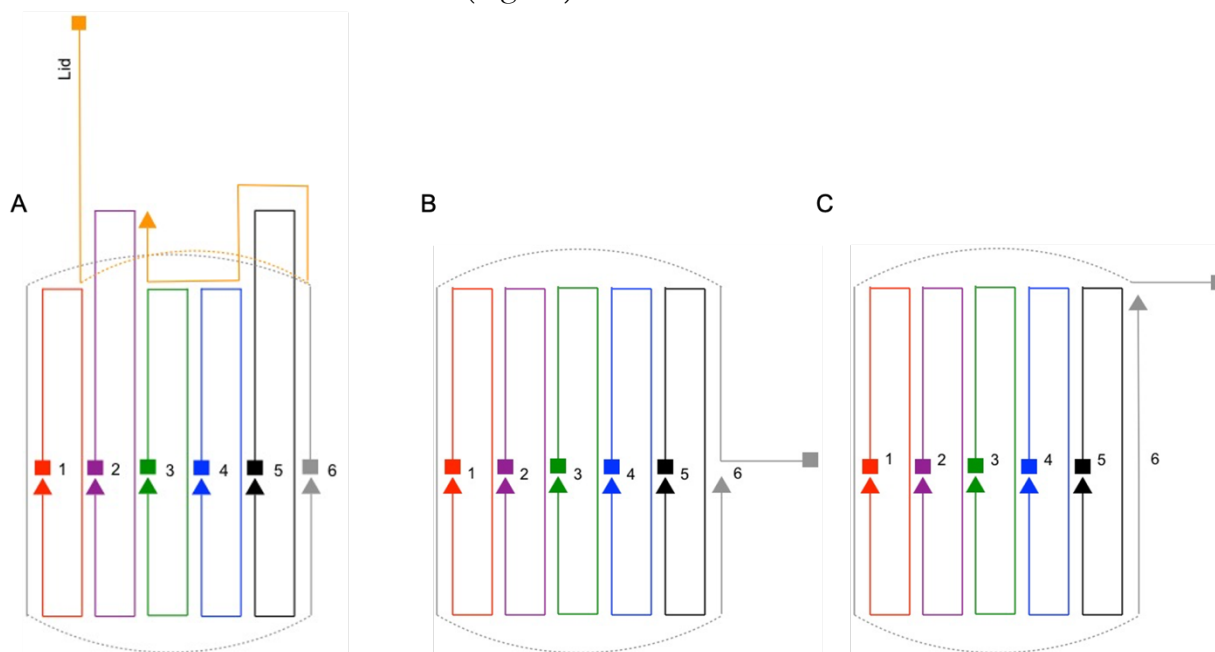
Figure 35. 2D maps of the DNA nanopore designs from Burns et al.[115] adapted for use as the initial scaffolds to hold the 20-nt extension. (A) An adaptation of NP-C from Burns et al. with Lock II removed and the 3' end of the lid shortened for stability. The extended 5' end of the lid contained

the sequence for S. (B) An adaptation of NP from Burns et al. with a 20-nt extension containing the sequence for S at the 5' end of strand 6. (C) Same as (B) except that the nick of strand 6 was shifted from near the center of the pore to the top.

Unfortunately, none of these pores proved to be suitable scaffolds for S_{NP}. The pore featured in Figure 35A proved difficult to fold as the lid tended to spontaneously dissociate. A single band in gel electrophoresis was only observed when it was folded with R. In order for the interaction between R and S_{NP} to be characterised, S_{NP} must be a stable entity, therefore, this design was dismissed. The pore featured in Figure 35B was successfully folded, but it too was dismissed as no binding between the pore and R was observed. A hypothesis is that the extension tended to be folded facing the pore lumen rather than the exterior of the pore. This is suspected because even when folded with R, only a very small fraction bound to SUVs. Only a very small fraction of the pore depicted in Figure 35C was successfully folded. The fraction that was folded appears to interact well with R; however, this was dismissed like the other two as the successful folding of only a small fraction was unacceptable. Each of the scaffolds was folded in 300 mM KCl, 15 mM Tris-HCl, pH 7.8 and two different folding protocols (1) the fast-folding protocol as described in Burns *et al.*, which involved heating to 95 °C followed by cooling to r.t. at a rate of 5 °C/min and (2) the 2.5 h folding protocol that involves heating to 95 °C then cooling to 70 °C at a rate of 2.5 °C/min followed by cooling to 4 °C at a rate of 0.5 °C/min. The two protocols were used to ensure that a scaffold was unsuitable before being discarded.

A major limitation posed by the scaffold designs modelled on the pores from Burns *et al.* was their simplicity. Unlike other DNA nanostructures, there are no crossovers, or linkages between each of the six DNA duplexes other than the poly-T loops at the top and bottom. As was demonstrated by the pore featured in Figure 35C destabilising one of these crossovers will destabilise the structure. This was also a contributing factor behind spontaneous lid dissociation in the pore featured in Figure 35A. Clearly, the 20-nt extension was a destabilising element. This was not unexpected considering that the 20-nt extension is an asymmetric ssDNA region. Therefore, a design that features enhanced core stability was desired, such as a design that incorporates inter-helical cross-linkages that would stabilise any modifications. The older 6HB nanopore design from the Howorka group was selected as an ideal candidate.[101,114,123,124,130] There are three published variants of this scaffold featuring 12 (Ref.[114]), 8 (Ref.[124]), and 6 strands,[101] respectively. The 8 strand variant published by Maingi *et al.*[124] (Fig. 36) was selected as this provided a desirable mix of short (42-nt) and long strands (88-nt) allowing the most stable variant to be selected.

This nanopore design, in its several variants, has been folded in a range of KCl-based buffers ranging from 0.3-1.85 M KCl,[101,114,123,124,130] with 1 M KCl, 50 mM Tris-HCl, pH 8 being a common choice. To deduce the most appropriate buffer, the pore was folded in three different KCl-based buffers of

different ionic strengths: 3 M KCl, 150 mM Tris-HCl, pH 8.3 (3 M), 1 M KCl, 50 mM Tris-HCl, pH 8 (1 M), 0.3 M KCl, 15 mM Tris-HCl, pH 7.8 (0.3 M). The 2.5 h folding protocol outlined previously was selected for consistency with the literature on this pore. To aid in characterisation, the nanopore, NP, designed by Burns et al.[115] was folded in 0.3 M KCl to be used as a reference. This pore is commonly used as a reference in the Howorka lab due to its high reproducibility and availability of the strands.

All strand sequences used to fold both pores are listed in the Appendix A, Section 9.2.1.
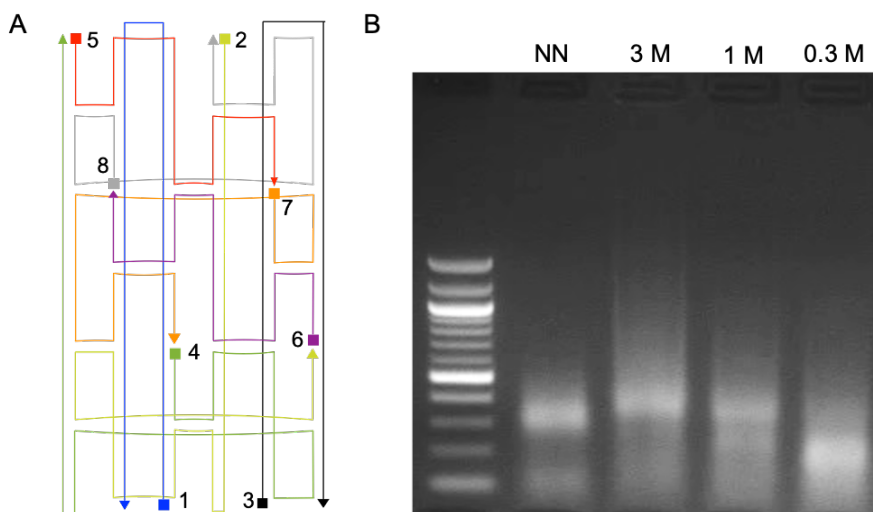
Figure 36. (A) 2D DNA strand map of the cross-linked nanopore published by Maingi et al.[124]. Each strand is numbered and shown in a unique colour. Squares represent the 5' end and triangles the 3' end of a DNA oligonucleotide. (B) Electrophoretic characterisation of the nanopore folded in KCl-based buffers of different ionic strengths: 3 M KCl, 150 mM Tris-HCl, pH 8.3 (3 M), 1 M KCl, 50 mM Tris-HCl, pH 8 (1 M), 0.3 M KCl, 15 mM Tris-HCl, pH 7.8 (0.3 M). The nanopore from Burns et al.[115] (NN) was used as a reference. 2% agarose gel run in 1x TAE buffer at 60V for 100min. At left is a 100 bp DNA ladder.

The 8-stranded Maingi et al. nanopore has dimensions of ~15 x 5.5 nm compared to 9 x 5 nm for the NP from Burns et al.; therefore, of the two, the Maingi et al. pore was expected to have slower mobility through the gel. The control NP from Burns et al. ran to approximately the 300 bp marker, while in 3 M and 1 M KCl, the Maingi et al. nanopore ran to roughly the 400 bp marker, indicating a successful fold. However, while the pore folded in 3 M KCl had a single band, two bands were apparent for the 1 M KCl, one matching the 3 M and the other matching the 0.3 M KCl fold, which does not appear to have folded successfully and runs to around the 200 bp marker. To corroborate the results of the gel, the pore folded in each of the three conditions was imaged using transmission electron microscopy (TEM, Fig. 37).[118]

Nanopores are clearly visible in both 3 M and 1 M KCl confirming that the pore has successfully folded in both of these buffers. Indeed, the pore lumen is clearly visible, and it is nearly possible to distinguish the individual helices. No pores were visible when folded in 0.3 M KCl, which corroborates the electrophoretic results (Fig. 35). Beyond helping to characterise the successful folding of the nanopore, these images are striking as they were the first TEM images successfully obtained for any nanopore constructed in the Howorka group. It is hypothesised that the added height and rigidity of this pore compared to other designs, such as the NP from Burns *et al.*, aided in successful imaging.
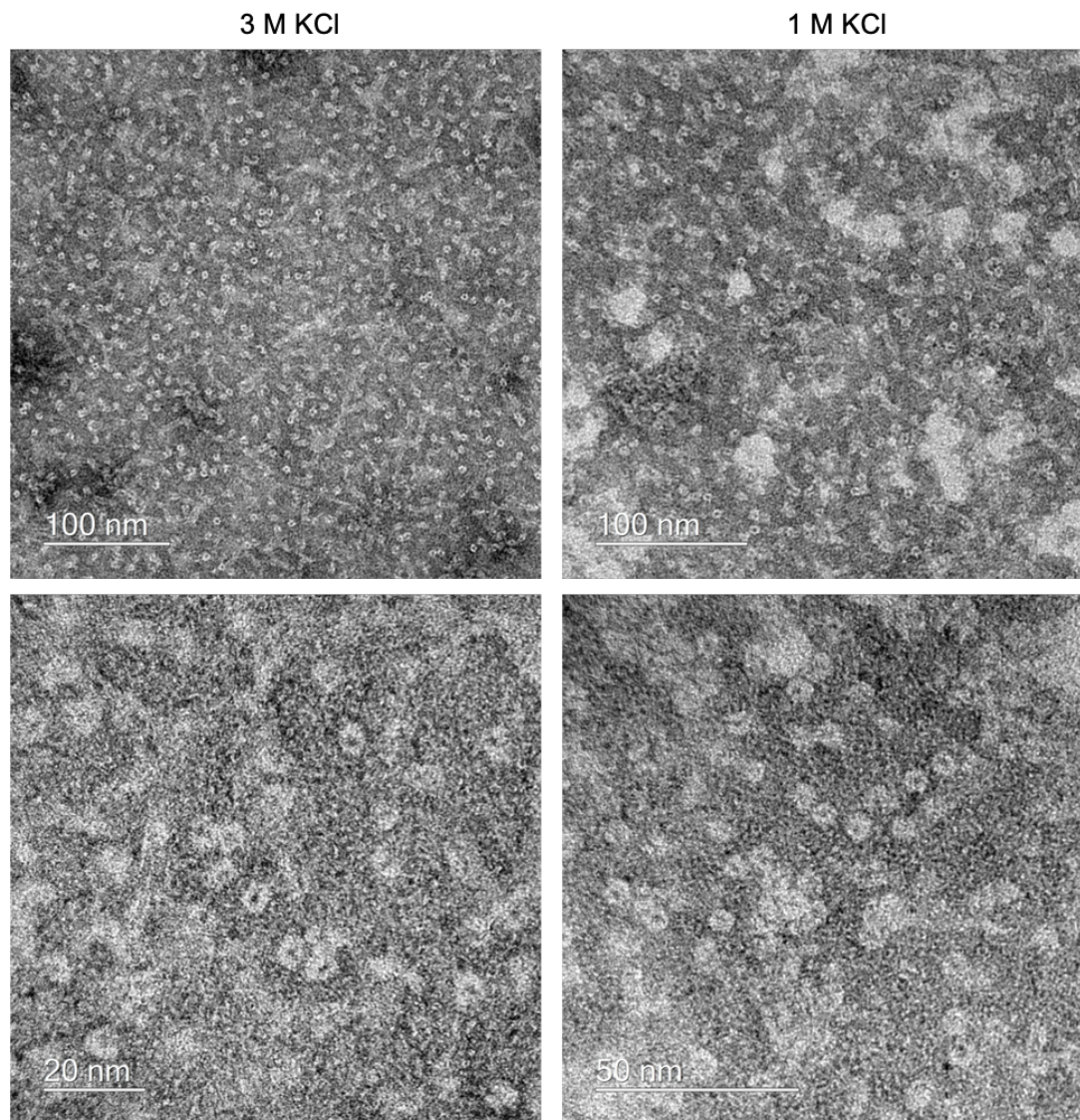
Figure 37. Transmission electron microscopy images of the nanopore by Maingi *et al.*[124] folded in either 3 M (3 M KCl, 150 mM Tris-HCl, pH 8.3, left) or 1 M KCl (1 M KCl, 50 mM Tris-HCl, pH 8, right).

Following successful characterisation of the scaffold, three strands were selected for extensions. Strands 1, 2 and 5. Strands 1 and 2 are long, 88-nt strands. The expectation was that these would

confer the most stability. Two long strands were selected as they have different inter-strand connectivity. Strand 5 was selected as being representative of the shorter, 42-nt, strands. All three variants were extended from the 5' end of the oligonucleotide with the 20-nt sequence of S plus a 4-nt spacer composed of thymine bases. The sequence of each of the extended strands are shown below (5' → 3') with red indicating the binding region and **bold** the spacer. The original sequence is shown in black.

Strand s1-ext:

TGCATGGATAAAATCGACTA**TTTT**ACAGGATTTTCGCCTGCTGGGGCAAACCAGCGTGGACCGCTTTTTTGGCTATTCTTTTGATTTATAAGGGATTTTGCCATTTCGGAA

Strand s2-ext:

TGCATGGATAAAATCGACTA**TTTT**CAACTCTCTCAGGGCCAGGCGGTGAAGGGCAATCAGCTGTTGTTTTCAACAGCATCCTGTTTCCGAAATCGGCATTAAAGACCAGCTG

Strand s5-ext:

TGCATGGATAAAATCGACTA**TTTT**TGTTCCAAATAGCCAAGCGGTCCACGCTCCCTGAGGGGCGCC

From here onwards, the scaffold featuring the extended strand 1 will be referred to as $S_{NP}1$, for strand 2: $S_{NP}2$ and for strand 5: $S_{NP}5$. 2D DNA strand maps for $S_{NP}1$, $S_{NP}2$, and $S_{NP}5$ indicating the 20-nt strand extension are shown in Figure 38.
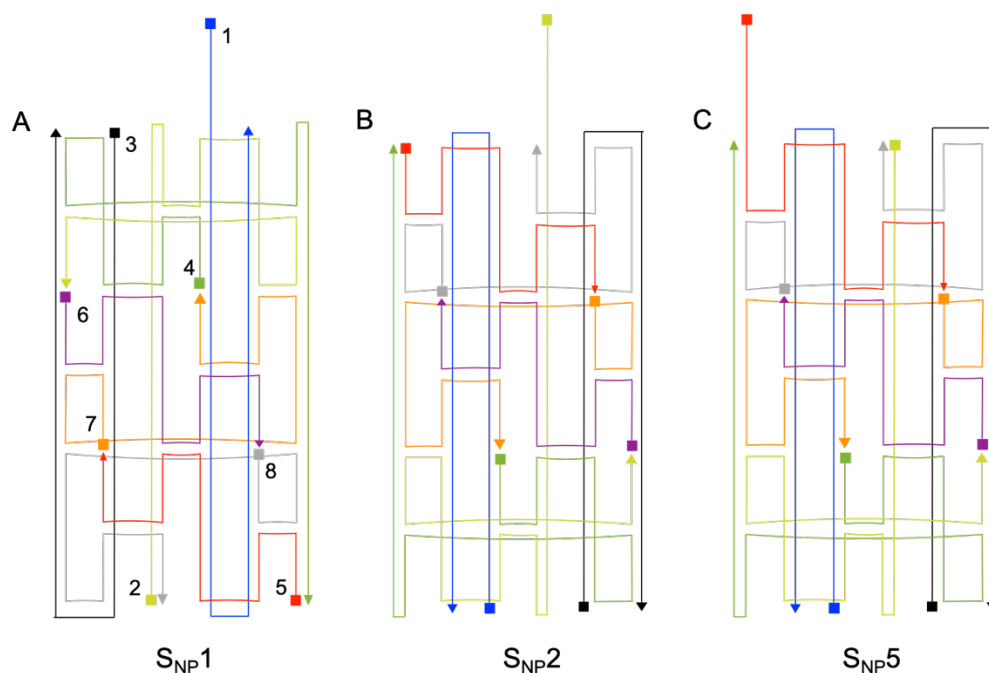
Figure 38. 2D DNA strand maps for the nanopore scaffold adapted from Maingi *et al*.[124] featuring the 20-nt extension and four thymine spacer: A) $S_{NP}1$ with strand 1 (blue) extended from the 5' end with a four thymine spacer and the 20-nt sequence of S. b) $S_{NP}2$ with strand 2 (yellow) extended from the 5' end with a four thymine spacer and the 20-nt sequence of S.; c) $S_{NP}5$ with strand 5 (red) extended from the 5' end with a four thymine spacer and the 20-nt sequence of S. Strands are indicated with unique colours and are numbered from the 5' end.

Based on both the gel and the TEM images, 0.3 M KCl was deemed to be insufficient and so was discarded. 3 M KCl appeared to be the best choice; however, as the salt concentration was high, the folding of $S_{NP}1$, $S_{NP}2$ and $S_{NP}5$ was investigated in both 3 M and 1 M KCl (Fig. 39). In addition, the ability of the S_{NP} variants to bind to R and form R•S_{NP} was also assayed (Fig. 39).
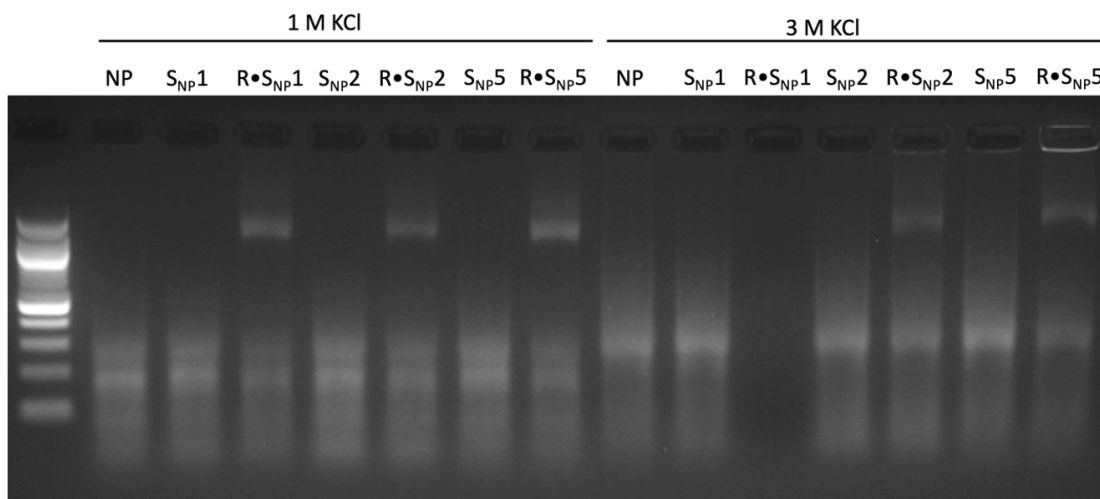
Figure 39. Gel electrophoretic characterisation of the success of folding the S_{NP} variants $S_{NP}1$, $S_{NP}2$ and $S_{NP}5$ in either 1 M or 3 M KCl buffers as well as their ability to bind to R and form R•S_{NP}. NP

is the original scaffold nanopore by Maingi *et al.*, which is used as a control for both folding buffers. 2% agarose gel run in 1x TAE buffer at 60 V for 110min. A 100 bp DNA ladder appears at the left of the gel. R•S_{NP}1 was mistakenly cut out.

The results for all three S_{NP} variants were very consistent and mirror what was obtained for the original scaffold on its own in Figure 39. When folded in 1 M KCl, two bands were apparent for all three S_{NP} variants. In contrast, a single band was obtained when they were folded in 3 M. In addition, all three S_{NP} variants formed a definitive band when R was added; however, the main S_{NP} band did not disappear indicating incomplete binding. The S_{NP}s were only incubated with R for five minutes at room temperature. A longer incubation period was likely required for full binding to occur. What was evident however, was that all variants of the nanopores show consistency. As there was no folding improvement for the S_{NP} in 1 M KCl compared to the scaffold, 3 M KCl was selected as optimal folding buffer.

Next, the binding of the three S_{NP} variants with R_{SUV} was assayed (Fig. 40). To determine the optimal binding conditions, titrations with increasing concentrations of R_{SUV} were performed for each S_{NP} variant. For this assay, a gel electrophoretic mobility shift assay was used. A gel electrophoretic mobility shift assay is a common technique to monitor nucleic acid binding be it simple hybridisation,[10] interaction with a protein[15,170,281] or with lipid vesicles.[118] The principle underpinning the technique is fairly simple: larger structures have reduced mobility through the gel matrix and will, therefore, appear higher up the gel. This allows binding to be easily monitored as long as there is a change in size. Furthermore, only one species needs to be able to be visualised as the presence of the other is implied by the band shift on the gel.

R was added to SUVs composed of DOPC & DOPE in a 7:3 mole ratio and incubated at 30 °C for 30 min to ensure complete interaction. Each of the three S_{NP} variants was then added and incubated for a further 30 min at 30 °C in increasing R:S_{NP} ratio from 0 to 20:1 representing a change in the concentration of R from 0 to 5 µM. The concentration of SUVs used was determined using equation (1) (Ref.[118]):

$$C_{SUV} = \frac{A_l C_l}{2SA} \qquad (1)$$

Where C_{SUV} = SUV concentration; A_l = the lipid headgroup area; C_l = lipid concentration; SA = surface area of a sphere ($4\pi r^2$) and the two is to account for the bilayer leaflet.

The lipid headgroup area for DOPC is ~69 Å^2 and for DOPE it is ~ 64 Å^2 (Ref.[17]). Dynamic light scattering indicated that the average SUV diameter was ~ 136 nm. This yielded an SUV concentration of 5.87 nM.
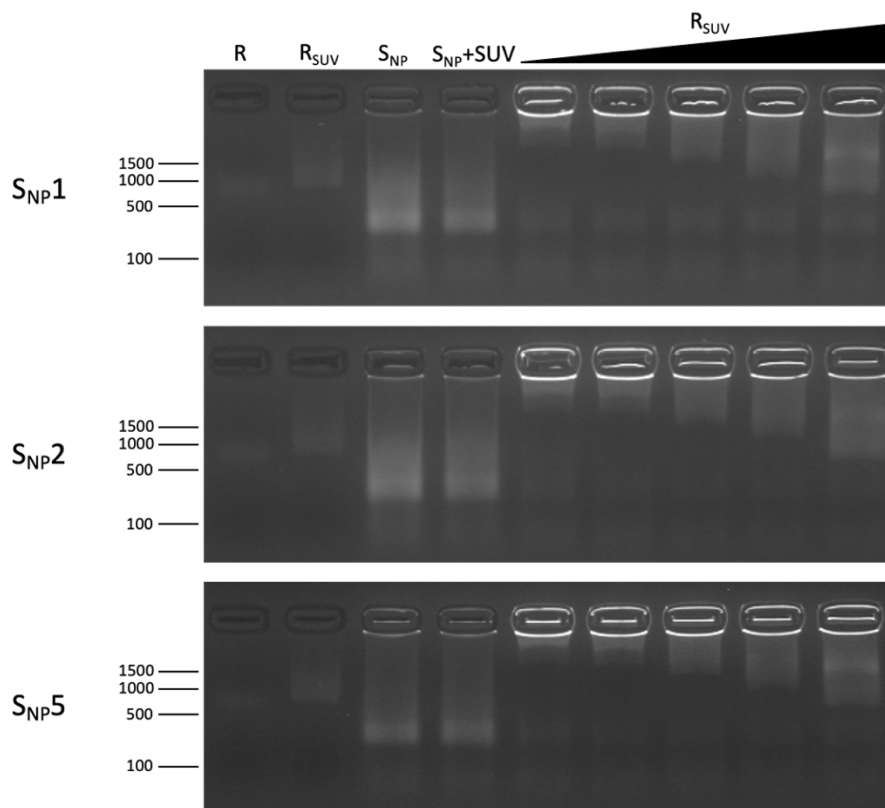
Figure 40. Electrophoretic gel shift assay to assess the binding of each of the three S_{NP} variants with R_{SUV}. 2% agarose gels run in 1x TAE buffer at 60 V for 60 min. S_{NP} concentration was 0.25 μM and concentrations of R ranged from 0 to 0.5 μM for a maximum R:S_{NP} ratio of 20:1. The final SUV concentration was 1.5 nM resulting in an approximate R to SUV ratio of 17:1 at the lowest loading and 340:1 at the highest. In all three cases an R•S_{NP} band emerged at around the 1500 bp marker.

The titrations suggest very similar binding properties for all three S_{NP} variants. In all three cases, successful binding was observed; however, there is faint evidence of the S_{NP} band remaining indicating that not all is bound in all three cases. The intensity of this band was, nevertheless, fairly constant even as the concentration of R increased, which may suggest that there is a small proportion of the S_{NP} that is unavailable for binding or it could equally be an artifact of the gel. Either way, the band was not significant and did not interfere with binding. It was anticipated when the model system was designed that the binding between R and S would occur in a 1:1 stoichiometry; however, it was unclear if the added steric bulk of (a) the nanopore or (b) the SUV would cause this ratio to change. The titrations for all three variants indicated that the binding stoichiometry remained 1:1. At the highest R:SUV loading of 3400:1, a band around the 1500 bp marker is visible for all three variants. This appeared to correspond to the R•S_{NP} band in Figure 38. This may indicate that the

SUVs cannot readily accommodate so many Rs and some remained free in solution. In addition, the titrations indicated that all 3 variants yielded similar results and any of the three could be used. Of these, $S_{NP}5$ was the best candidate. Strand 5 was the shortest by over 50%, making it much more cost effective. In addition, the long lengths of strands 1 and 2 meant that certain modifications were unavailable, such as fluorophores, which would significantly limit characterisation. $S_{NP}5$ will now be referred to simply as: S_{NP}.

While the electrophoretic mobility shift assays are convincing, the interaction of the R•S_{NP} complex remained only implied. Confocal laser scanning microscopy (CLSM) was used to visualise and confirm interaction with the membrane as well as binding on the membrane surface. The 5' end of R was modified with a Cy3 fluorophore while an additional thymine carrying a Cy5 fluorophore was added to the four T spacer preceding the 20-nt S extension of strand s5 on the S_{NP}. This location was chosen so that the two fluorophores would be separated by four nucleotides, resulting in a distance of ~3.5-4 nm upon hybridisation to maximise Förster resonance energy transfer (FRET). A FRET pair was used in the place of two non-interacting fluorophores as the FRET pair offers the ability to discern whether binding has occurred in real-time, which will be discussed later. The sequence for ^{Cy3}R and s5-ext^{Cy5} are shown below (5'$\rightarrow$3').

^{Cy3}R:

Cy3-TAGTCGATTTTATCCATGCA-TEG-Chol

Strand s5-ext^{Cy5} (red represents the binding portion and **bold** the Cy5 modified base):

TGCATGGATAAAATCGACTATTTT**T^{Cy5}**GTTCCAAATAGCCAAGCGGTCCACGCTCCC TGAGGGGCGCC

Giant unilamellar vesicles (GUVs) composed of POPC lipids were formed and used for the CLSM binding experiments (Fig. 41). GUVs, which are >1 μm in diameter, were used in place of SUVs because SUVs, which are on the order of 100 nm in diameter, are too small to be successfully visualised by the 96x objective of the confocal microscope.

Three conditions were explored: (A) ^{Cy3}R tethering to the surface of the GUVs in the absence of S_{NP}. This control was used to ensure that fluorescence was only observed in the Cy3 exciting green channel. (B) ^{Cy5}S_{NP} binding to ^{Cy3}R_{SUV} and observed fluorescence in both the red and green channels. (C) ^{Cy5}S_{NP} and GUVs only as a control to demonstrate that without lipid anchors S_{NP} can only interact with the GUVs via hybridisation with R.
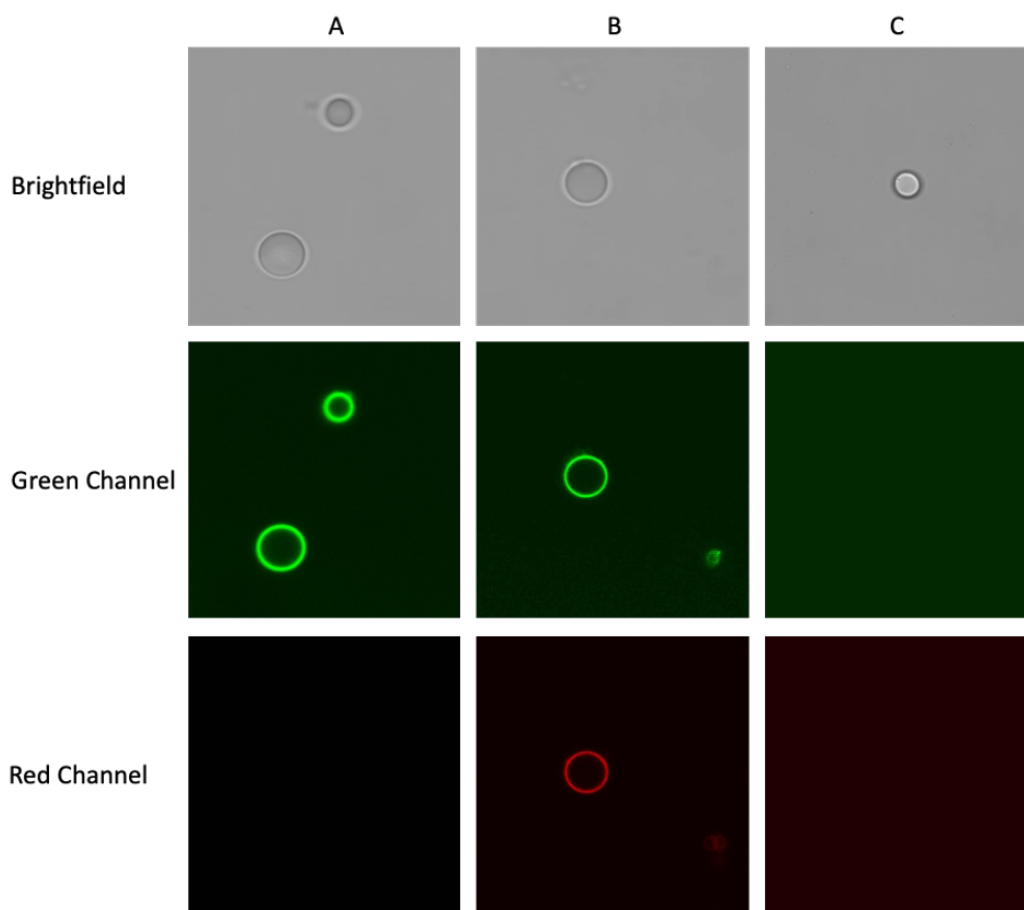
Figure 41. Confocal laser scanning microscopy images of the binding of $^{Cy3}R_{GUV}$ and $^{Cy5}S_{NP}$ on the surface of giant unilamellar vesicles (GUVs) composed of POPC lipids. Three channels are shown: the brightfield in the top row confirms the presence of GUV's; the second row shows the green channel exciting the Cy3 fluorophore on R; the third row shows the red channel exciting the Cy5 on S_{NP}. A) Fluorescent green halos around the GUVs confirm insertion and tethering of ^{Cy3}R into the bilayer. B) Both green and red fluorescent halos around the GUVs reaffirm (A) as well as successful hybridisation of $^{Cy5}S_{NP}$ with $^{Cy3}R_{GUV}$. C) The absence of any fluorescent halos confirms that without the presence of ^{Cy3}R on the membrane surface $^{Cy5}S_{NP}$ does not interact with the GUVs.

CLSM successfully demonstrated that (A) ^{Cy3}R interacts with the GUVs, (B) that $^{Cy5}S_{NP}$ successfully hybridised with ^{Cy3}R on the surface of the GUVs and (C) that in the absence of ^{Cy3}R, $^{Cy5}S_{NP}$, which does not carry any cholesterol modifications, cannot interact with the GUV's lipid bilayer. These results confirmed that the model system is fit for purpose.

Using these four entities, four different conditions can be probed to determine the effect of sterics on DNA hybridisation on the surface of a membrane: S vs R, S vs R_{SUV}, S_{NP} vs R and S_{NP} vs R_{SUV}.

4.2.2. Biophysical Data – Thermodynamic Binding Measurements

Following the establishment of the four components of the model system, the kinetics and thermodynamics of their hybridisation were investigated. The first parameter to be investigated was the steric effect on binding affinity. Binding affinity is commonly measured by determination of the dissociation constant (K_d), due to the fact that it is relatively straightforward to determine the K_d by titration from one of the unbound components, in this case: R or S. As above, gel mobility shift assays were used to monitor hybridisation. In order to first establish a baseline, R was titrated against S in solution. S was kept constant at a concentration of 250 nM, while R was titrated in at ratios of 0.1:1, 0.2:1, 0.5:1, 1:1 and 2:1 representing concentrations of 25 to 500 nM (Fig. 42A). The amount of bound R•S complex formed was quantified from normalised band intensities according to equation (2):

$$B = 1 - \left(I_{DNA} - I_{background}\right) \qquad (2)$$

B = bound, and I=band intensity.[10,15,118]

The normalised band intensities were then plot against the concentration of R and fit to a Michaelis-Menten curve to determine the Michaelis-Menten constant (K_M), which is formally equivalent to K_d as determined by the Langmuir-Hill equation when ligand binding is noncooperative (i.e., n=1).[118] This is a convenient method of analysis as the fitting parameters for Michaelis-Menten are built into many fitting programs, such as OriginLab.

ssDNA is poorly resolved when stained with ethidium bromide (EtBr), a common nucleic acid stain, due to the fact that EtBr is a DNA intercalator. Therefore, to improve resolution, [Cy5]S was used and imaged using a fluorescence gel scanner. This allowed nM concentrations to be used, whereas, with EtBr, ssDNA is generally limited to μM concentrations. S_{NP} was stained with EtBr as this offers excellent resolution with the compact 6HB and is much more cost-effective (Fig. 42B). Sufficient band separation between R•S_{NP} and R could not be achieved so the cholesterol modified version of R was used for titrations against S_{NP}.
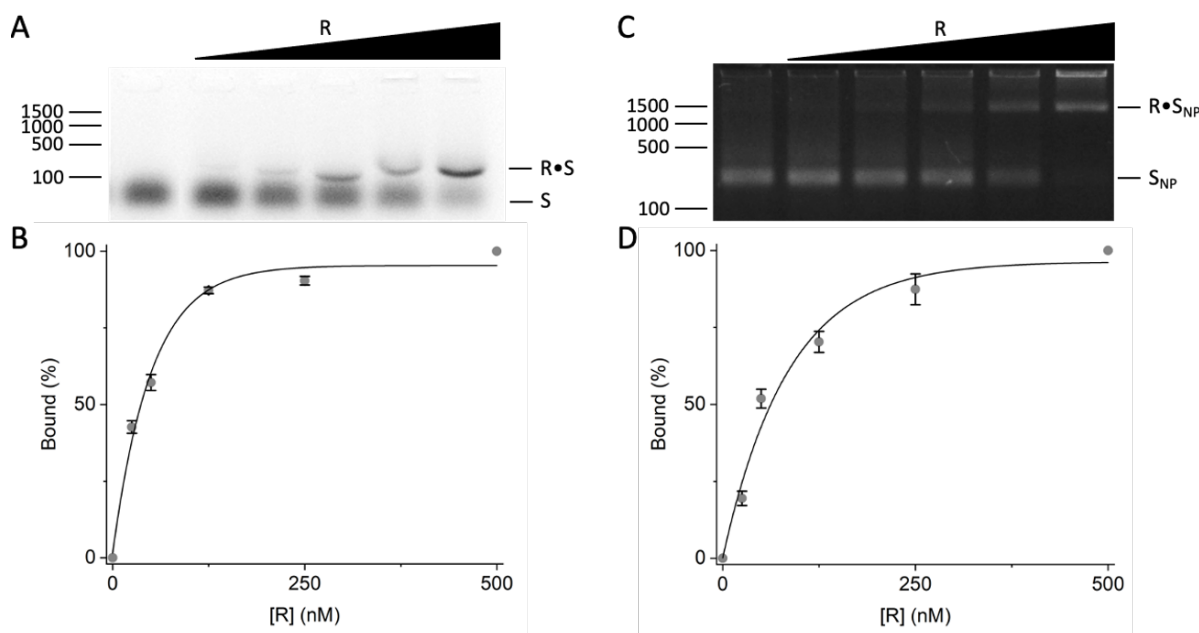
Figure 42. Gel electrophoretic mobility shift assay to assess the binding of the receptor (R) to the ssDNA steric element (S) or nanopore-bound steric element (S_{NP}). (A) A 3% agarose gel shift assay: increasing the concentration of R results in the formation of the R•S dsDNA complex, which is visualised by the formation of a tighter more slowly migrating band in the gel representing the larger duplex. S carries a Cy5 fluorophore to improve resolution at low concentrations. The gel was imaged using a fluorescence gel scanner. (B) Binding curve of R•S complexation displayed as percent bound. The data were fit with a Langmuir-Hill binding curve and represent averages and standard deviations from 3 independent experiments. The curves were fit to the data with an average R^2 of 0.99 from the three repeats. (C) A 2% agarose gel shift assay measuring the formation of the R•S_{NP} complex. While the S_{NP} is significantly more massive than R, the cholesterol modification interacts with the gel matrix resulting in significantly reduced R•S_{NP} mobility. (D) Binding curve of R•S_{NP} complexation displayed as percent bound. The data were fit with a Langmuir-Hill binding curve and represent averages and standard deviations from 3 independent experiments. The curves were fit to the data with an average R^2 of 0.98 from the three repeats. All gels were run in 1x TAE buffer at 60 V for 60 min. The major markers of a 100 bp DNA ladder are indicated on the left.

Both titrations revealed successful formation of the bound complex. Titrations with R_{SUV} were then considered. The conditions used for the initial titrations to determine the most suitable variant of S_{NP} were replicated. SUVs were made from DOPC and DOPE in a 7:3 ratio. The average diameter was revealed to be 122 nm, which following equation (1) yielded an SUV concentration of 7.22 nM. The final SUV concentration used in the titrations was 1.80 nM, which results in R:SUV loadings of 14:1 at the lowest point and 278:1 at the highest loading. In all other ways the conditions of the titrations in solution were replicated for those against R_{SUV} (Fig. 43).
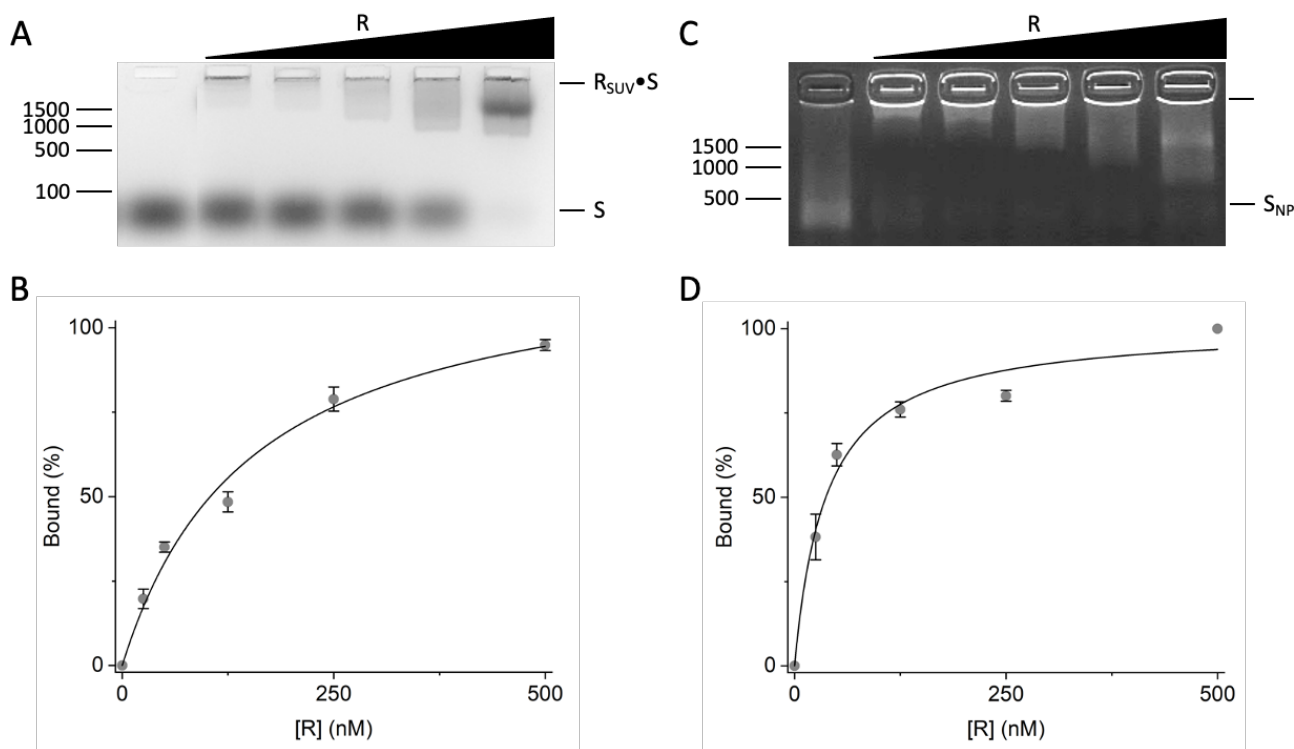
Figure 43. Gel electrophoretic mobility shift assay to assess the binding of the ssDNA steric element (S) or nanopore-bound steric element (S_{NP}) to the receptor (R), which is tethered to the surface of SUVs. (A) A 3% agarose gel shift assay: increasing the concentration of R results in the formation of the R_{SUV}•S membrane-bound dsDNA complex, which is unable to migrate into the gel matrix and remains in the well. S carries a Cy5 fluorophore to improve resolution at low concentrations. The gel was imaged using a fluorescence gel scanner. (B) Binding curve of R_{SUV}•S complexation displayed as percent bound. The data were fit with a Langmuir-Hill binding curve and represent averages and standard deviations from 3 independent experiments. The curves were fit to the data with an average R^2 of 0.97 from the three repeats. (C) A 2% agarose gel shift assay: increasing the concentration of R results in the formation of the R_{SUV}•S_{NP} membrane-bound complex, which is unable to migrate into the gel matrix and remains in the well. (D) Binding curve of R_{SUV}•S_{NP} complexation displayed as percent bound. The data were fit with a Langmuir-Hill binding curve and represent averages and standard deviations from 3 independent experiments. The curves were fit to the data with an average R^2 of 0.98 from the three repeats. All gels were run in 1x TAE buffer at 60 V for 60 min. The major markers of a 100 bp DNA ladder are indicated on the left.

Successful binding was also observed on the surface of SUVs, between both S and S_{NP} vs R. Following this success, the dissociation equilibrium constant, K_d, was determined for each of the four conditions by fitting the data to a Langmuir-Hill plot. These results are summarised in Table 1. As expected, S vs R displays the strongest binding with a K_d of 40.5±3.60 nM. The hybridisation of short DNA oligonucleotides typically results in a K_d between 1×10^{-7} 1×10^{-9}, or the nM range[277,282–284] so this is in good agreement with the literature. DNA hybridisation is largely controlled by the

ionic strength of the buffer, the base composition of their sequences and temperature,[275,282] but the formation of secondary structures also has a significant effect.[285] All titrations were performed in 1 M KCl, 50 mM Tris-HCl at the slightly basic pH 8.0. The attachment of the nanopore to S results in an almost exactly 50% reduction in binding strength, but of the same order of magnitude. A weaker K_d was expected, but it was unclear how large of a decrease would be observed. Both R vs S and R vs S_{NP} only achieve around 90% binding at a 1:1 stoichiometric ratio (250 nM) and tend to level off asymptotically from here. Only at a stoichiometric ratio of 1:2 R:S and R:S_{NP} does binding approach 100%. This was also observed by Zhang *et al.* who observe that most of their observed hybridisation reactions do not reach yields of more than 90%,[285] which is consistent with my findings from the gel titrations. They hypothesise that the cause is likely due to misaligned hybridisation or other non-specific interactions. This may explain the faint band present in all titration gels. Nevertheless, it is interesting that the asymptotic yield is consistent between S and S_{NP}. Furthermore, this observation extends to titrations against R_{SUV}; however, rather than 90%, the yield is closer to 80%. S vs R_{SUV} is approximately three-fold weaker than S vs R in solution. It was expected that hybridisation on the surface would be weaker than in solution based on the literature.[134,135,273,275–277,280,286–288]

Table 1: Summary of thermodynamic and kinetic data obtained for the four conditions of the model system. In solution: R vs S and R and S_{NP} as well as with R bound to SUVs composed of DOPC:DOPE in a 7:3 mole ratio: R_{SUV} vs S; and R_{SUV} vs S_{NP}. n equals the number of repeats used to obtain the average and standard deviation for each condition and parameter.

Parameter	Name	Avg ± Std. Dev.	n	Ratio (norm. % vs R)
K_d (M)	S vs R	$4.05 \pm 0.36 \times 10^{-8}$	3	100
	S_{NP} vs R	$8.01 \pm 0.33 \times 10^{-8}$	3	51
	S vs R_{SUV}	$15.4 \pm 2.36 \times 10^{-8}$	3	26
	S_{NP} vs R_{SUV}	$7.86 \pm 1.91 \times 10^{-8}$	3	52
k_{on} ($M^{-1}s^{-1}$)	S vs R	$10.7 \pm 0.87 \times 10^{5}$	3	100
	S_{NP} vs R	$4.79 \pm 0.24 \times 10^{5}$	3	45
	S vs R_{SUV}	$9.16 \pm 0.89 \times 10^{5}$	3	86
	S_{NP} vs R_{SUV}	$3.88 \pm 0.44 \times 10^{5}$	3	36
k_{off} (s^{-1}) implied	S vs R	$4.33 \pm 0.53 \times 10^{-2}$	Derived	100
	S_{NP} vs R	$3.84 \pm 0.25 \times 10^{-2}$	Derived	113
	S vs R_{SUV}	$14.1 \pm 2.60 \times 10^{-2}$	Derived	31
	S_{NP} vs R_{SUV}	$3.05 \pm 0.82 \times 10^{-2}$	Derived	142

DNA hybridisation on surfaces and interfaces is governed primarily by probe density, which in turn is affected by the ionic strength of the buffer and surface charge. Here, the zwitterionic lipids DOPC and DOPE were used in 1 M KCl so surface charge should not be an important factor. DNA oligonucleotides bound to the surface adopt three conformational regimes based on probe density: a mushroom-like state, a cross-over state and a brush-like state[289,290] (Fig. 44). When strand density is low, part or all of each strand may interact with either itself or the surface, which makes it less available for hybridisation. As strand density increases to the point that the inter-strand distance is roughly equivalent to strand length, the strands adopt a cross-over state, which is ideal for hybridisation. As strand density approaches saturation, the strands adopt a rigid polymer brush-like state to maximise inter-strand distances and minimise electrostatic repulsion.[10,135,289,290] Ravin et al.[289] found that hybridisation efficiency was reduced to only 10% at high strand densities and similar results have been achieved by other groups.[275,291] The ionic strength of the buffer can also have a significant effect. It has been observed that at low salt concentrations, while hybridisation took place in solution, it was not observed on surfaces.[289] While high ionic strengths can help stabilise the immobilised strands by effectively screening the negatively charged phosphate backbone, this can also result in increased packing density, which can further reduce hybridisation.[286,291]

Mushroom-like state   Crossover state   Brush-like state
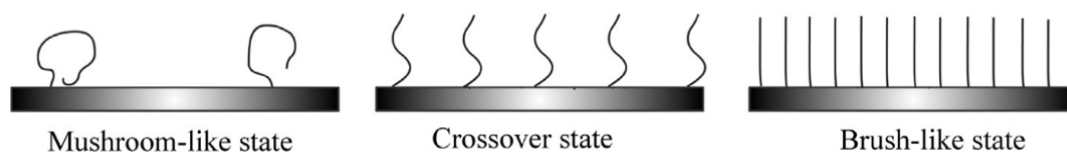
Figure 44. The three conformational regimes adopted by DNA probes attached to surfaces. At low density, DNA adopts a mushroom-like state to maximise interaction with itself and the surface. As probe density increases and the distance between probes is roughly the length of the probes, electrostatic repulsion causes them to adopt a more erect orientation away from the surface. As probe density nears saturation, electrostatic repulsion causes probes to adopt a brush-like state to maximise inter-probe distances. Adapted from Ravan et al.[289]

These states were investigated for the current system. Using an approximation of 10.3 nm for the length of R in the ssDNA state plus the TEG linker (derived from Banchelli et al.[135]) the crossover state will be reached at an R:SUV loading of 140:1 based on the definition above. At a loading of R:SUV of 278:1, the case at 500 nM R, the anchored strands will be ~ 5.3 nm apart, which may be approaching conditions for the brush-like state. Gambinossi et al.[136] found that probe density will reach saturation on a supported lipid bilayer at a lipid:strand ratio of 80:1 and at ~ 60:1 with vesicles of ~30 nm diameter, which suggests that this must be close to the required density for the formation of the brush-like state. 30 nm vesicles will allow significantly closer packing than 122 nm vesicles, so this ratio is likely higher. However, even at 500 nM R, the lipid:R ratio is 500:1, which is likely

sufficiently high to prevent adoption of the brush-like state. At the lowest concentration of R, 25 nM, the lipid:R ratio is 10,000:1 or 14:1 R:SUV, which suggests it may adopt the mushroom-like state. This could account for the weak binding and why at a 1:1 ratio only 78% of S is bound to R. This is also the case for S_{NP} where at 1:1 only 80% is bound to R. However, the K_d for $R_{SUV} \cdot S_{NP}$ binding (78.6 ± 19.1 nM) is nearly two-fold stronger than $R_{SUV} \cdot S$ (154 ± 23.6 nM) and indeed, is equivalent to the K_d obtained for $R \cdot S_{NP}$ binding (80.1 ± 3.3 nM). It is unclear why the added steric bulk of the nanopore would result in a stronger K_d. One hypothesis is that the attachment to the NP results in a more ordered system by reducing the number of degrees of freedom for S both sterically and due to electrostatic repulsion. This leads to better orientation and, therefore, more successful binding than S in solution, which can adopt a range of conformations (Fig. 45). It is also possible that this results in more energetically favourable binding due to the previously observed instability imparted to the NP by the ssDNA 20-nt extended S. Thus, while hybridisation between S and R may be faster than between S_{NP} and R overall, the individual hybridisation step itself occurs more quickly resulting in stronger binding.[276] This hypothesis was supported by the slow off-rate for $R_{SUV} \cdot S_{NP}$. This will be discussed in more detail later.
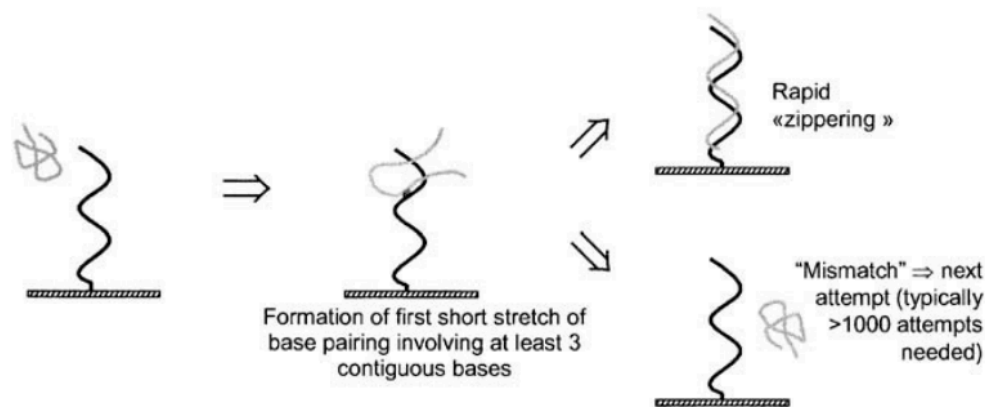
Figure 45. Schematic illustration for DNA hybridisation between a surface immobilised strand and strand in solution. Adapted from Pappaert *et al.*.[276]

In the presence of SUVs, the band for S and S_{NP} appeared to have completely disappeared at 500 nM R unlike in solution where a faint band is visible for both S and S_{NP}; however, a band around the 1500 bp marker does appear in both gels. For the S_{NP} vs R_{SUV} titration this corresponds to the $R \cdot S_{NP}$ band in Figure 42C, which suggests that the band in Figure 43A is also $R \cdot S$ with a cholesterol modified R. The appearance of this band implies that either not all of R has inserted into the SUVs or that upon complexation, the cholesterol lipid anchor was ripped out of the bilayer. If the previous calculation is correct, the density of R on the SUV surface could be sufficient to prevent some R from inserting, which would leave them free for hybridisation. The resulting complex would be even larger and less able to insert. Nevertheless, as this only occurred at the highest concentration of R, it is unlikely to be a concern.

4.2.3. Biophysical Data – Hybridisation Kinetics Measurements

To explore the model system further, the kinetics of hybridisation were investigated. This was monitored via FRET using fluorescence spectroscopy and the fluorophore labelled R (^{Cy3}R), S (^{Cy5}S) and S_{NP} ($^{Cy5}S_{NP}$) were again used. As R and S (or S_{NP}) hybridise, the fluorophores will be 5-nt apart. As the 4-T spacer is an ssDNA region this placement positioned them at a distance of ~3.5-4 nm.[292] This distance is well within the Förster distance (R_0) of ~6 nm for the Cy3-Cy5 FRET pair,[91,293,294] which should ensure a strong fluorescence response. The Förster distance (R_0) is the distance at which a FRET pair will have 50% transfer efficiency[295] so this distance is expected to give a FRET efficiency of closer to 75%. In the presence of an acceptor (Cy5), which has an excitation that overlaps with the emission of a donor (Cy3), excitation of the donor allows energy, which would normally be given off as fluorescent emission, to be transferred to the acceptor. In this way, the hybridisation of the two strands can be monitored in real-time. Further specifics of FRET pair interactions will not be described here as it is a well characterised process. The fluorophores were previously tested using CLSM; however, a FRET interaction was not investigated so the FRET interaction was first assayed using ensemble fluorescence and a pre-folded ^{Cy3}R•$^{Cy5}S_{NP}$ (Fig. 46A) and then kinetic fluorescence to monitor the hybridisation in real-time (Fig. 46B).
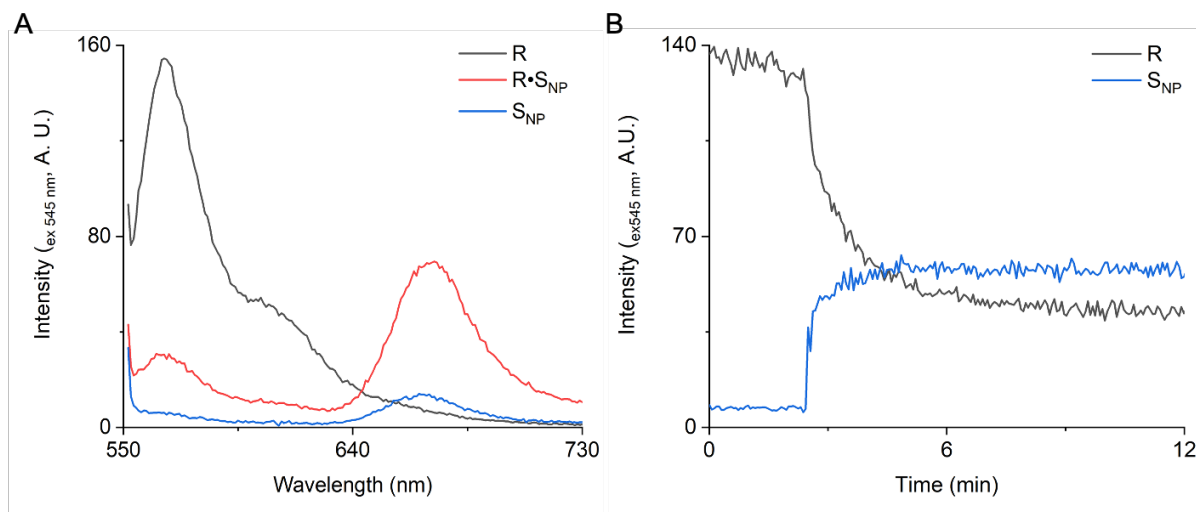
Figure 46. Fluorescence analysis of the interaction of R and S_{NP} labelled with the FRET pair, Cy3 and Cy5, respectively. (A) Ensemble fluorescence measurement of the change in intensity of the Cy3 and Cy5 peaks on their own and when hybridised. (B) Kinetic fluorescence measurement of the change in intensity of the Cy3 and Cy5 signals upon ^{Cy3}R and $^{Cy5}S_{NP}$ hybridisation over time. ^{Cy3}R was added and the signal allowed to stabilise for 2.5 min before $^{Cy5}S_{NP}$ was rapidly added and hybridisation monitored. In both cases ^{Cy3}R and $^{Cy5}S_{NP}$ were assayed in a 1:1 stoichiometry at 33.3 nM in 1 M KCl, 50 mM Tris-HCl, pH 8.0.

A strong FRET interaction was observed using ensemble kinetics with both the Cy3 and Cy5 signals undergoing a significant change in intensity from the free, unbound state to the bound state. The kinetic measurement confirmed that the change in signal intensity also occurs when hybridisation is monitored *in situ* and the signals underwent the same overlap observed in the ensemble experiment.

FRET interaction confirmed, kinetic analysis was then undertaken to determine the rate constant, k, for each of the four modes in the model system. DNA hybridisation is a second order kinetic reaction; however, it is difficult to determine the second order rate constant, so a pseudo-1st order system was constructed[296,297] by using a large excess of S and S_{NP} using the relationship outlined in equations (3) and (4) below:

$$\text{rate} = k_{obs}[\text{R}] \qquad (3)$$

$$k_{obs} = k[\text{S}] \qquad (4)$$

to give the 2nd-order rate equation (5):

$$\text{rate} = k[\text{R}][\text{S}] \qquad (5)$$

Hybridisation was monitored via the change in donor (Cy3) intensity. The donor, R, was selected to monitor over the acceptor since in the case of R_{SUV}, the addition of SUVs was required, and it was necessary to account for the vesicle light scattering as well as to ensure SUV stability. By monitoring the change in fluorescence intensity of R, the SUVs could be added gently to ensure stability. In the absence of SUVs, R was added for a final concentration of 1.25 nM in 1 M KCl, 50 mM Tris-HCl, pH 8.0 and the signal allowed to stabilise, the run was then started and after 30 seconds a 100-fold excess of S or S_{NP} was added (125 nM) and rapidly mixed. To monitor the kinetics of hybridisation with R_{SUV} it was found that scattering prevented 1.25 nM from being an adequate concentration and 5 nM was used instead. In addition, to get adequate signal, a 20-fold excess was used instead of 100-fold; nevertheless, this was determined to still be a suitable excess. 100 nm SUVs were added at a concentration of 22.2 pM for an R:SUV loading of 225:1 based on results from the gel mobility shift binding assays. Traces were averaged and normalised from the point of S or S_{NP} addition; however, the initial vertical drop following acceptor addition, which is due to dilution was removed prior to normalisation. The combined kinetic traces are displayed in Figure 47.
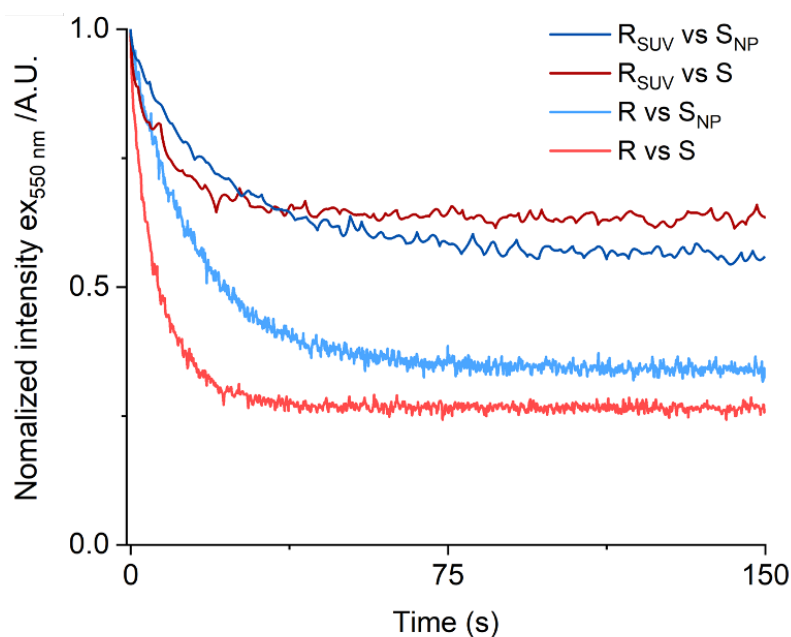
Figure 47. Kinetic fluorescence analysis of the four conditions of the model system. The fluorescence signal was normalised as F/F_0 from the point of S or S_{NP} addition. For R vs S (red) and R vs S_{NP} (blue), R was added at 1.25 nM and S and S_{NP} were added in a 100-fold excess at 125 nM. R_{SUV} vs S (dark red) and R_{SUV} vs S_{NP} (dark blue), R was added at 5 to nM and S and S_{NP} were added in a 20-fold excess at 100 nM. SUVs (100 nm) were added at a concentration of 22.2 pM for an R:SUV loading of 225:1 or a lipid:R ratio of 1167:1.

Kinetic traces for hybridisation were successfully obtained for all four conditions of the model system. The observed pseudo-1st-order rate constant, k_{obs}, was then calculated by fitting the curves to the integrated 1st-order rate equation (6):

$$Rate = Ae^{-kt} \qquad (6)$$

The traces were fit with average root-means-squares values of 0.98, 0.96, 0.91 and 0.96 for R vs S, R vs S_{NP}, R_{SUV} vs S, and R_{SUV} vs S_{NP}, respectively. The lower root-means squared value for R_{SUV} vs S_{NP} is reflected by the fact that this is also the trace with the greatest amount of noise, particularly over the crucial first 30 seconds. (Fig. 47, dark red). The calculated observed pseudo-1st-order rate constant, k_{obs}, was then used to determine the 2nd-order rate constant, k, for each condition via rearrangement of equation (4).

The calculated 2nd-order rate constants for hybridisation, k_{on}, are summarised in Table 1 along with the binding data (K_d) obtained from the electrophoretic mobility shift assays. From these results the dissociation rate constant, k_{off}, was derived following rearrangement of equation (7). The derived k_{off} are summarised in Table 1.

$$K_d = \frac{k_{off}}{k_{on}} \qquad (7)$$

The kinetics of DNA hybridisation in solution have been explored using a range of techniques, including FRET,[273,275,297,298] and reported 2nd-order rate constants, k, range from 10^2-10^7 $M^{-1}s^{-1}$ depending on the length of the sequences and technique used.[282,285,299,300] Although they typically fall between 10^5-10^7 $M^{-1}s^{-1}$.[282,285,299] A good summary of rate constants found in the literature for complementary sequences ranging from 6-25-nt in length is provided by Wyer *et al.*[299]. DNA hybridisation can be very sequence dependent with variation of even a few bp resulting in remarkably different rate constants, which can make direct comparison challenging.[299,300] One of the reasons for this is that sequences that tend to form more secondary structures typically present slower kinetics.[285,299,300] The most comparable condition is R vs S, which with a rate constant of 1.07 ± 0.09 $\times 10^6$ $M^{-1}s^{-1}$ is in good agreement with the literature.

The kinetics of DNA hybridisation on surfaces have typically been found to be slower than in solution[135,273,275–277,291] by up to two orders of magnitude.[275] However, this has been found to be highly dependent upon the surface density. Of particular interest for this system, Banchelli *et al.*[135] measured the kinetics of hybridisation between a cholesterol modified 18-nt strand and its compliment on the surface of POPC SUVs. Similarly, to what was discussed previously regarding binding and probe density, they found in the brush state (i.e., average distance between probes is $\leq$ 55 Å) that the rate constant was approximately 1×10^5 $M^{-1}s^{-1}$, whereas when probe density decreases the rate constant becomes equal to or even faster (3-5.2 $\times 10^5$ $M^{-1}s^{-1}$) than the rate constant for hybridisation in solution (3×10^5 $M^{-1}s^{-1}$). This is highly comparable to the model system as the values between hybridisation in solution and on the surface are very similar. While the rate constant for R_{SUV} vs S was lower than for R vs S, it was within error. The effect of the membrane was larger for S_{NP}, but only slightly at 4.79 ± 0.24 $\times 10^5$ $M^{-1}s^{-1}$ in solution compared to 3.88 ± 0.44 $\times 10^5$ $M^{-1}s^{-1}$ on the membrane. For both S and S_{NP}, the difference in rate between solution and on the surface differed by ~ 1.5 $\times 10^5$ $M^{-1}s^{-1}$, which is a difference of only 14.4 and 19.0% for S and S_{NP}, respectively. Based on the results from Banchelli *et al.* and the results obtained here, it can be concluded the surface of the membrane is not a significant factor unless the surface density is high.

The most significant factor was the addition of the nanopore. The hybridisation of R and S_{NP} was 55.2% lower than R and S, which is significant compared to the 14.4% difference between R and S in solution and on the membrane surface. Remarkably, this difference was consistent for hybridisation on the membrane surface as well with S_{NP} vs R_{SUV} 57.6% lower than S vs R_{SUV}. Varying by only 2.4%, this was a surprisingly conserved difference.

In general, the kinetics followed the expected trend of S hybridising with R faster than S_{NP} with R. Indeed, the results even matched the general trend from binding data, with one significant exception: S vs R_{SUV} has significantly faster kinetics than would be implied based on the binding data alone. However, oligonucleotides adopt a range of conformations and Pappaert *et al.*.[276] suggest that at least four base-pairs must form for hybridisation to proceed and that when one strand is immobilised on a surface, the steric factor can significantly reduce the rate of this individual step. As hypothesised earlier, the added steric bulk of the nanopore may have made the individual hybridisation step faster even if the bulk rate remained slower. It was also noted that binding on the surface reached a limit of ~80% compared to 90% in solution. In Figure 47, it is notable that hybridisation with R_{SUV} finished with a significantly higher normalised intensity than the corresponding condition in solution. Indeed, the observed trend is in line with the binding data as S vs R_{SUV} ends with a higher normalised intensity than S_{NP} vs R_{SUV}. The different endpoints suggest that not all of the reactions went to completion, despite levelling off. To investigate this further, the FRET efficiency, E, was calculated for each condition using equation (8) (Ref.[301]):

$$E = 1 - \frac{I_{DA}}{I_D} \qquad (8)$$

I_{DA} = donor intensity in the presence of the acceptor, I_D = donor intensity only.

As I_{DA}/I_D was used for normalisation, E was easily calculated by 1 – the endpoint of each trace. The calculated FRET efficiencies are summarised in Table 2. A control for maximum expected FRET Efficiency was calculated using the folded R•S_{NP} and the ensemble FRET scans. This was used to determine the extent that each of the four conditions went to completion.

Table 2. Summarised FRET efficiencies derived from the hybridisation kinetics between the four components of the model system. Averages and standard deviations were calculated from at least three independent repeats.

Condition	FRET Efficiency, E Avg. ± Std. Dev.	Extent of reaction (norm. % vs control)
Control	0.80	100
S vs R	0.74 ± 0.01	92.6
S_{NP} vs R	0.66 ± 0.05	82.8
S vs R_{SUV}	0.37 ± 0.02	46.1
S_{NP} vs R_{SUV}	0.45 ± 0.06	55.8

The calculated extent of reaction for S vs R matches well with the ~ 90% threshold from the binding data and the similar observation from Zhang *et al.*[285]. In general, the trend matches what was observed from the binding data. The notable exception in this case was that S_{NP} vs R_{SUV} only reached 55.8% completion. However, this was still nearly 10% more than S vs R_{SUV}. Nevertheless, both cases are much lower than expected. There are a few possible explanations. One is that the binding titrations were incubated at 30 °C for 30 min before being loaded onto the gel while the kinetic data was obtained in December when the temperature of the lab was ~ 18 °C. Another factor is that the samples were not mixed except upon addition of S or S_{NP}, which limited the extent of reaction. A final consideration is related to the surface crowding. The SUVs used for this experiment were ~100 nm, which is nearly 3x larger than used by Banchelli *et al.*[135], this may have reduced the packing extent and caused the R:SUV ratio to approach a brush-like state limiting hybridisation. Similarly, the R:SUV ratio was 225:1, which was not too far away from the 278:1 used with the binding experiments where a band for the unanchored complex was observed. Indeed, those SUVs were 122 nm in diameter and able to accommodate a higher R:SUV ratio. The dissociation rate constant, k_{off}, for S vs R_{SUV} was also an order of magnitude higher than the others; however, all of the k_{off} rate constants are 6-7 orders of magnitude slower than the k_{on} rate constants meaning it is unlikely this was the cause of the lower extent of reaction at surfaces.

4.3. Conclusion

A model system was constructed with four conditions featuring varying degrees of steric hindrance to probe the effect of sterics on DNA hybridisation. This system was constructed to guide the design of a DNA nanopore that is able to assemble from component monomers at the membrane surface. The four conditions were: hybridisation between a 20-nt unmodified receptor oligonucleotide, R, and its complement, S, in solution and when R was bound to the membrane surface of SUVs. These conditions were replicated when S was attached to a 15.5 x 5.5 nm DNA nanopore to make: S_{NP}. Biophysical experiments were used to probe the effect of sterics on DNA hybridisation. The binding of S vs R behaved as expected, demonstrating both the fastest and the strongest binding. S vs R_{SUV} demonstrated the weakest binding, but kinetically was very similar to S vs R. Attachment of the nanopore to S mitigated the effect of the membrane on the binding strength, which suggested that the added steric bulk was advantageous for hybridisation at the membrane interface. However, kinetically, addition of the nanopore resulted in a nearly 60% decrease in the hybridisation kinetics. Nevertheless, the extent of reaction was higher with S_{NP} than with S vs R_{SUV}.

The model system demonstrated that as long as surface crowing is not too dense, hybridisation on the membrane surface can occur with minimal loss to binding strength and kinetics even if the ssDNA is attached a larger nanostructure.

4.4. Future Work

In the future, it would be of interest to investigate the effect of sterics on DNA hybridisation using different positions for S along the pore. For example, it would be interesting to investigate the effect of hybridisation when S extends from the middle of the pore. In theory, this would create a much larger steric object, especially for hybridisation at the membrane interface. Using the same side-emanating position for S on the nanopore, it would be interesting to assess the effect on DNA hybridisation if the pore were inserted into the bilayer. This would significantly reduce the number of degrees of freedom experience by S. In addition, the effect of surface crowding would be a potent factor. An additional application of such a system could be to use these side-emanating strands to dock other pores on the membrane. Such a system would have a variety of potential applications, including building larger transmembrane structures on the surface of the membrane.

In addition, it would also be interesting to assess the effect on hybridisation when the receptor contains a tertiary structure, such as a G-quadruplex, an i-motif or a hairpin. This would introduce an additional steric element as the receptor would be less available for hybridisation; however, it may also have the effect of reducing interactions with the membrane. This would be of interest to investigate as it would allow such tertiary structures to be used on the membrane surface, but also to be controlled by use of an antidote.

Finally, it would be of interest to investigate the effect of the shape of the nanostructure attached to S on hybridisation. Compared to the barrel shape of the nanopore, it would be interesting to assess the effect when S emanates from the point of a tetrahedron, or when it extends from a concave or bowl-shaped system. A bowl-shaped system would limit potential trajectories of R from the size; however, it may also serve to funnel trajectories coming directly on, but off target.

5. DNA Nanopore with Biomimetic Triggered Assembly

5.1. Aims

The aim of this project was to design and build a synthetic nanopore composed of DNA capable of mimicking the assembly of natural protein pores by transitioning from an inactive pre-pore monomer state to an active pore state on the surface of a membrane. A DNA nanopore composed of a bundle of four DNA-helices (4HB) was designed that could easily be cleaved into two component parts (A and B, Fig. 48). On their own, the components were designed to be inactive and have no function. When both components come together, they spontaneously self-assemble into the 4HB DNA nanopore (A•B, Fig. 48). Assembly can take place in solution, while one component is tethered to a membrane and while both components are attached to the membrane surface for a flexible approach. A lock strand was also designed that, if added to the components, would prevent spontaneously self-assembly (AL^A and BL^B, Fig. 1). In this way, the pore can be kept in an inactive state until activity is desired. When desired, pore assembly can be triggered by addition of keys (K^A and K^B, Fig. 48) that remove the locks via a toehold mediated strand-displacement mechanism to yield the active 4HB. Only upon pore assembly can molecular cargo, or ions, be transported across the lipid bilayer. A further aim of this project was to use molecular dynamics simulations to investigate the active structure of A, B and A•B and the effect of the bilayer on assembly. In addition, it was of interest to investigate the effect that the components and nanopore have on the membrane. The pore lumen was also modelled to gain a better understanding of the transport ability of A•B, such as to function as a synthetic ion channel.
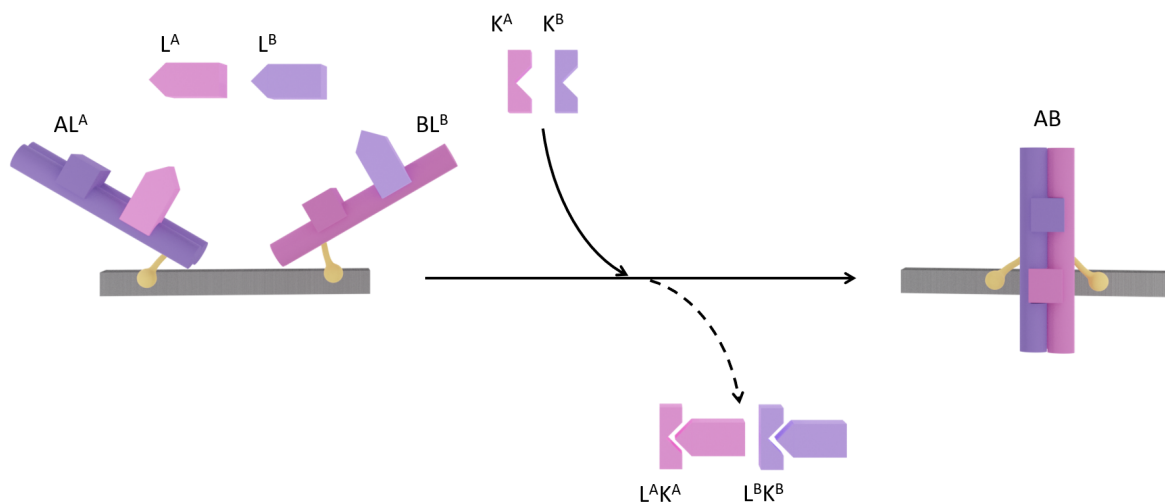
Figure 48. Schematic to illustrate the design and function of the triggered assembly of monomer components into an active synthetic DNA-based ion channel on the membrane surface. The membrane-tethered components, AL^A and BL^B, are locked and cannot self-assemble into the active

pore (A•B). However, upon addition of the keys (K^A and K^B) the locks are removed causing A and B to spontaneously assemble into the active membrane spanning A•B.

5.2. Results and Discussion

I conceived of and designed the project under the guidance of Prof. Stefan Howorka. I carried out the CLSM GUV-binding experiments with the help of Dr. Yongzheng Xing. Single molecule FRET and single particle tracking was performed by Dr. Jonathan Shewring from Oxford Nanoimaging and assisted by Dr. Yongzheng Xing and me. Linear dichroism spectroscopy was performed by Dr. Jascindra Ravi from the National Physical Laboratory and assisted by me. SRB dye flux assays were performed by me with assistance from Jonah Ciccone. Nora Hagleitner and Dr. Adam Dorey carried out the single-channel current recordings. All molecular dynamics simulations were carried out by Jonah Ciccone with guidance from Dr. Katya Ahmad and Prof. Shozeb Haider. All other experiments were designed and performed by me. All data analysis was carried out by me, unless the assay was performed with or by someone else, in which case analysis was done with or by them. Prof. Stefan Howorka supervised all stages of the project.

5.2.1. DNA Nanopore and Component Design

The architecture of the six-helical bundle originally published by Burns *et al*.[115] was used as the basis for the design of the DNA nanopore used in this chapter. Two of the helices were removed to reduce the pore from a six- to a four-helical bundle to simplify the structure and reduce the complexity of the system. The 4HB nanopore, A•B, was then divided in half resulting in two components: A and B. Each component was composed of two strands of 50-nucleotides (nt) each that formed a central dsDNA backbone with an ssDNA loop attached to the top and bottom of the duplex. Opposite the loops were two ssDNA 'arms' of 14- and 7-nt. To assemble into a pore, the two ssDNA arms were required to hybridise with the loop of the other component (see 2D maps in Fig. 49). Each component would, therefore, have two loose ssDNA regions and one immobilised one to create a mechanism reminiscent of a hook and loop. This was also a more stable design than having four free ssDNA regions while also reducing the likelihood of non-target multimerization.
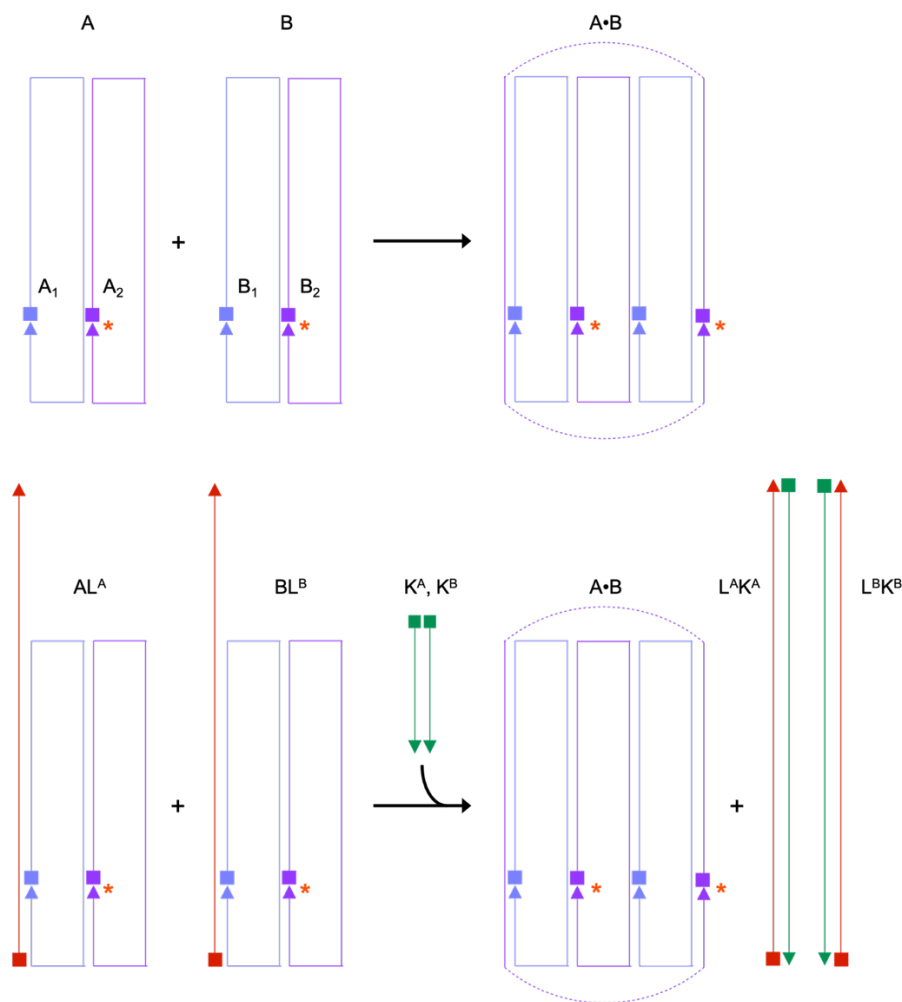
Figure 49. 2D strand maps and naming scheme of all nanopore components. (Top) 2D strand maps of the components A and B and how they assemble to form the 4HB nanopore, A•B. (Bottom) 2D strand maps of the locked components AL^A and BL^B and how, upon addition of the keys: K^A and K^B (green), the locks (red) are removed to form A•B. The resultant duplexes are indicated at the right. Squares represent the 5' and triangles the 3' end of DNA, orange asterisks represent cholesterol modifications attached to the 3' end of the indicated strand via a tri(ethylene glycol) (TEG) linker. Strands that make up the pore are shown in alternating blue and purple. The crossovers at the top and bottom of each strand consist of four thymine bases each.

A locked version was also conceived that would prevent pore assembly unless triggered by a key. The lock consisted of another DNA oligonucleotide that bound the two ssDNA arms. In the locked version, each component consisted of two duplexes and an ssDNA loop (see Fig. 49, bottom). The additional duplex was expected to make the locked components more stable than the unlocked version. The lock was designed to be removed with a key strand (see Fig. 49, bottom, green), which was the complementary sequence to the lock, via toehold strand displacement. It has been reported that the reaction rate of toehold mediated strand displacement saturates with toeholds of 6-10-

nt;[82,84,298,302] therefore, to maximise efficiency, an overhang of 10-nt was implemented for each lock. The sequences and composition of all structures can be found in Appendix A (Section 9.4.1).

The simplicity of the Burns *et al.* scaffold was an important feature, as was the fact that the pore was small and could be assembled using a simple folding protocol. In addition, the lack of inter-duplex connectivity throughout the body of the pore was a desired characteristic for *in situ* assembly of the two components. While double-crossover designs, such as the 6HB nanopore from Maingi *et al.*[303] used in Chapter 4, and single-crossover designs, such as the 4HB from Göpfrich *et al.,*[127] have advantages, they are also larger, require longer, more complex folding protocols and have a larger number of inter-duplex linkages. Additional crossovers add rigidity and stability, but if divided in half for *in situ* assembly, the strands would either be short reducing binding strength or too long, reducing component stability. In the Burns *et al.* scaffold, the central portion of the strand forms part of the duplex, which was hypothesised to impart the desired level of stability while maintaining appropriate binding strength and rate of hybridisation.

Nevertheless, while the Burns *et al.* scaffold had a number of advantages, there were drawbacks. The location and length of the arms made them somewhat unwieldly. They have a number of degrees of freedom and are minimally sterically hindered. While this was considered advantageous for hybridisation, the drawback was that the arms were free to interact with each other, the loop as well as other components. In addition, the single duplex with a nick has a point of high flexibility further imparting degrees of freedom and instability to the system. The many degrees of freedom of the structure and the many ssDNA regions were likely to drive hydrophobic burying via secondary structure formation. This made it likely that the conformations adopted by components would be far from the idealised structure, which was likely to have an impact on the binding strength and rate of hybridisation. However, the locked version was a more stable and rigid structure and so was expected to be closer to the idealised structure than the unlocked components. Nevertheless, it was unclear if the unlocking mechanism would prevent subsequent adoption of the hypothesised contorted free component conformation before assembly.

5.2.2. Assembly and Structural Characterisation

With the overall design finalised, it was necessary to optimise the folding conditions. The pore and components were first assembled using the fast-folding protocol from Burns *et al.*[115] that involved heating to 95 °C then cooling to r.t. at a rate of ~2.5 °C/min. Generally, this provided good results; however, the quality of the fold was not consistent and often additional bands in the lanes of A, B AL^A and BL^B were apparent. To overcome this the longer 2.5 h folding protocol was used instead. This protocol involves heating to 95 °C then cooling to 70 °C at a rate of 2.5 °C/min followed by cooling to 4 °C at a rate of 0.5 °C/min. In addition, while PBS appeared to be a successful buffer

for the pore and components, they were also folded in 300 mM KCl, 15 mM Tris-HCl, pH 7.4. In addition to the success of the fold, it was of interest to ascertain the degree to which the lock strand on each of A and B would prevent pore formation. All folding protocols are described in full in Appendix A, Section 9.2.
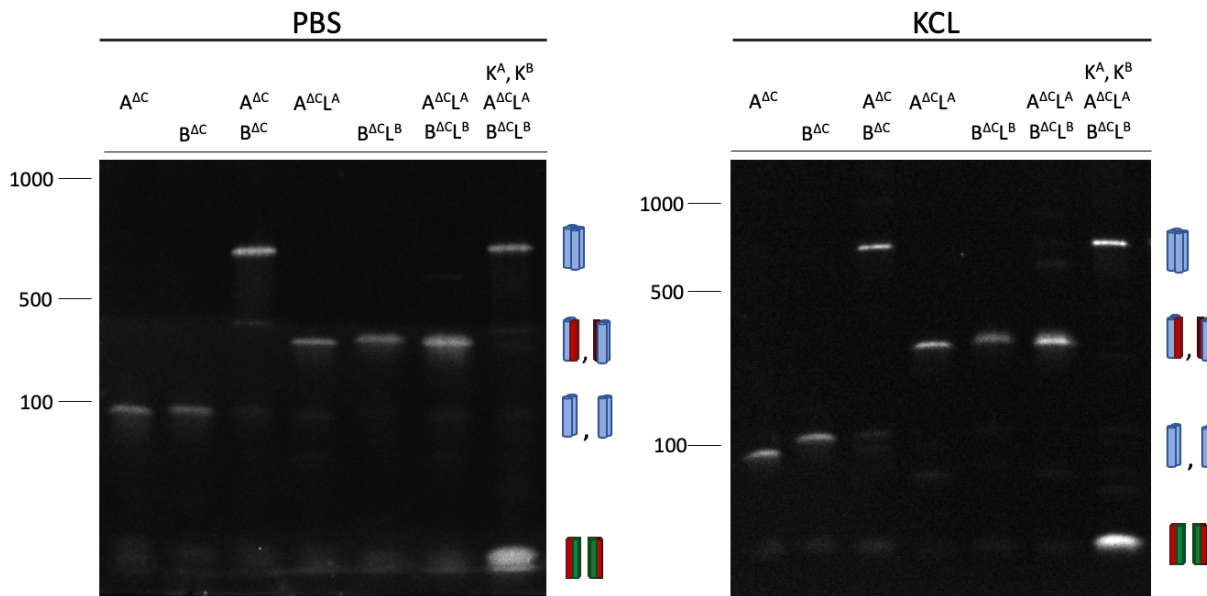
Figure 50. Confirmation of the assembly of the native nanopore without cholesterols (A•B$^{\Delta C}$) from component parts and the efficacy of the locking mechanism to control and trigger pore assembly in PBS (left) and KCl (300 mM KCl, 15 mM Tris-HCl, pH 7.4; right) was assessed by native PAGE. Addition of A$^{\Delta C}$ and B$^{\Delta C}$ in a 1:1 stoichiometric ratio results in the assembly of (A•B)$^{\Delta C}$ (Lanes 1-3). Addition of A$^{\Delta C}$L^A and B$^{\Delta C}$L^B together show no interaction and remain in their constituent parts (Lanes 4-6); however, if the keys, K^A and K^B are added, the locks are removed and (A•B)$^{\Delta C}$ forms in a 1:1 stoichiometric ratio (Lanes 4,5,7). Addition of keys in a 1:1 ratio with the components was also sufficient for complete removal of the corresponding lock (Lane 7). Samples were incubated at 30 °C for 30 min before being loaded onto the gel. 10% (left) and 12% (right) native PAGE were run in 1x TBE buffer at 90 V for 115 min at 4 °C.

The 2.5 h folding protocol was more reliable and led to enhanced stability for all components, with and without the locks. In both buffers, addition of A$^{\Delta C}$ and B$^{\Delta C}$ resulted in efficient formation of A•B with no other significant bands. The lock strand also effectively prevented formation of A•B. Addition of the keys, K^A and K^B, to AL^A and BL^B in a 1:1 stoichiometric ratio further resulted in very efficient pore formation, which was entirely comparable to the band resultant from the unlocked A and B as well as the control (not shown). These results indicate that not only are the locks effective in preventing formation of the pore, but following addition of the keys are in no way

a hindrance to the formation of $(A \cdot B)^{\Delta C}$. There does not appear to be any observable difference in assembly in either PBS or the KCl-based buffers.

UV-thermal denaturing melts were used to further characterise the pore and assess its structural integrity by measurement of the melting temperature (T_m). In addition, a further goal was to compare the T_m of the pore assembled *in situ* from $A^{\Delta C}$ and $B^{\Delta C}$ to a control $A \cdot B$ that was folded directly as the 4HB structure. UV thermal melts are a common technique used to assess the stability of structures composed of DNA from simple duplex[135,184,300,304] to larger, more intricate DNA nanostructures.[101,115,124,125,127,130,305,306] The principle of UV melts relies on DNA hyperchromicity.[301,307] As DNA denatures from a duplex to ssDNA, base stacking is disrupted, changing the dipole moment of the stacked bases, which results in a significant increase in UV intensity.[307] For a single structure composed of linked dsDNA duplexes, a single, sharp transition is expected. Multiple transitions are indicative of multiple structures. Similarly, a broad transition can be indicative of multiple structures with similar melting temperatures. This can also be the result when large structures with multiple domains, such as DNA origami structures, are assayed as these may denature at different temperatures. The inclusion of hydrophobic lipid anchors often leads to multiple or broad transitions due to aggregation. In this case UV melts are not always useful as the true structural transition may be masked. The average melting profile for $A \cdot B$ assembled from both conditions and the resultant 1st derivatives are shown in Figure 51.
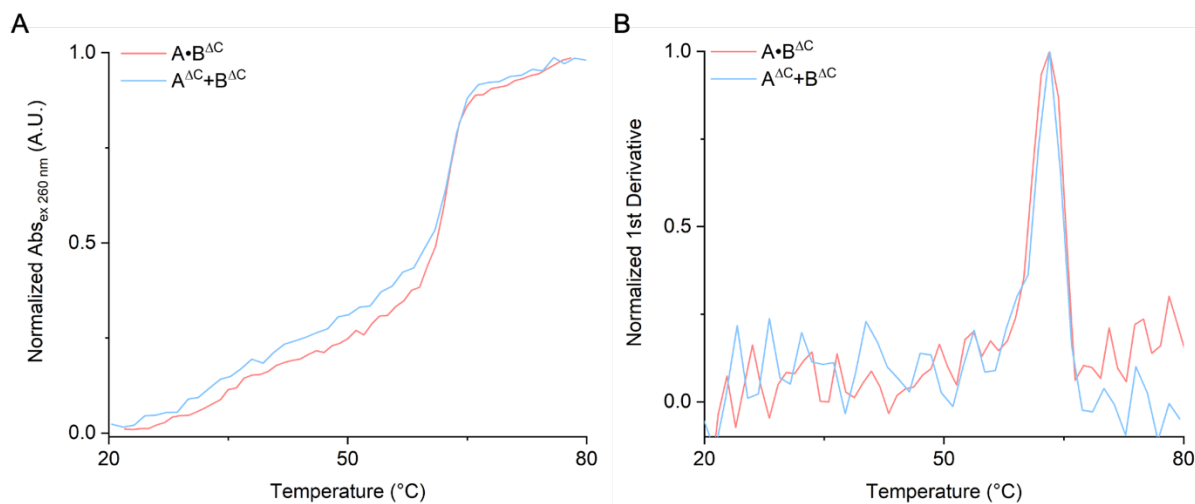
Figure 51. (A) UV-melting profiles of $(A \cdot B)^{\Delta C}$ when folded directly or assembled in situ from $A^{\Delta C}$ and $B^{\Delta C}$ to assess structural stability and structural similarity. $(A \cdot B)^{\Delta C}$ was assessed at 0.2 μM in 150 μL of PBS buffer. Samples were melted using a temperature ramp of 1 °C/min between 20 and 80 °C. Each trace represents an average from three independent repeats. (B) 1st derivative of the melting profiles used to identify the melting temperature (T_m) of each structure.

The average melting profile of $(A \bullet B)^{\Delta C}$ folded *in situ* from $A^{\Delta C}$ and $B^{\Delta C}$ shows excellent overlap at the transition point with the control, folded $A \bullet B$. This was corroborated by the 1st derivative, which indicated identical average T_m of 63.1 ± 0.2 °C and 63.1 ± 0.1 °C for the folded $A \bullet B^{\Delta C}$ and $A \bullet B^{\Delta C}$ assembled *in situ* from $A^{\Delta C}$ and $B^{\Delta C}$, respectively. Taken together, the PAGE and T_m strongly suggested an identical 4HB structure. Both melting profiles demonstrate a fairly linear increase in UV intensity from 20 to ~57-60 °C before undergoing to sharp transition at 63 °C. The melting profiles were typical for DNA nanostructures of this size.[127,305]

Before modifications were added, it was of interest to qualitatively assess the kinetics of pore assembly. In particular, it was of interest to determine if the locks had a significant impact on the kinetics of assembly. The toehold mechanism should be fast, and it was hypothesised that the rate-limiting-step would be the rate of mass transport at these concentrations;[273,308–310] however, the locked components required two reactions steps: (1) unlocking and (2) pore formation. This also meant that there would be two mass transport steps. Nevertheless, the small size of the locks should ensure that the first step was faster than the second. For this assay, all components, and keys (where applicable), were added in a 1:1 stoichiometric ratio, incubated at 30 °C for 1, 5, 10, 15, 20, 25 and 30 min. Samples were prepared in reverse time order and at each time point the sample was crashed in ice to quench pore formation. Samples were then immediately loaded onto the gel and the gel run (Fig. 52).
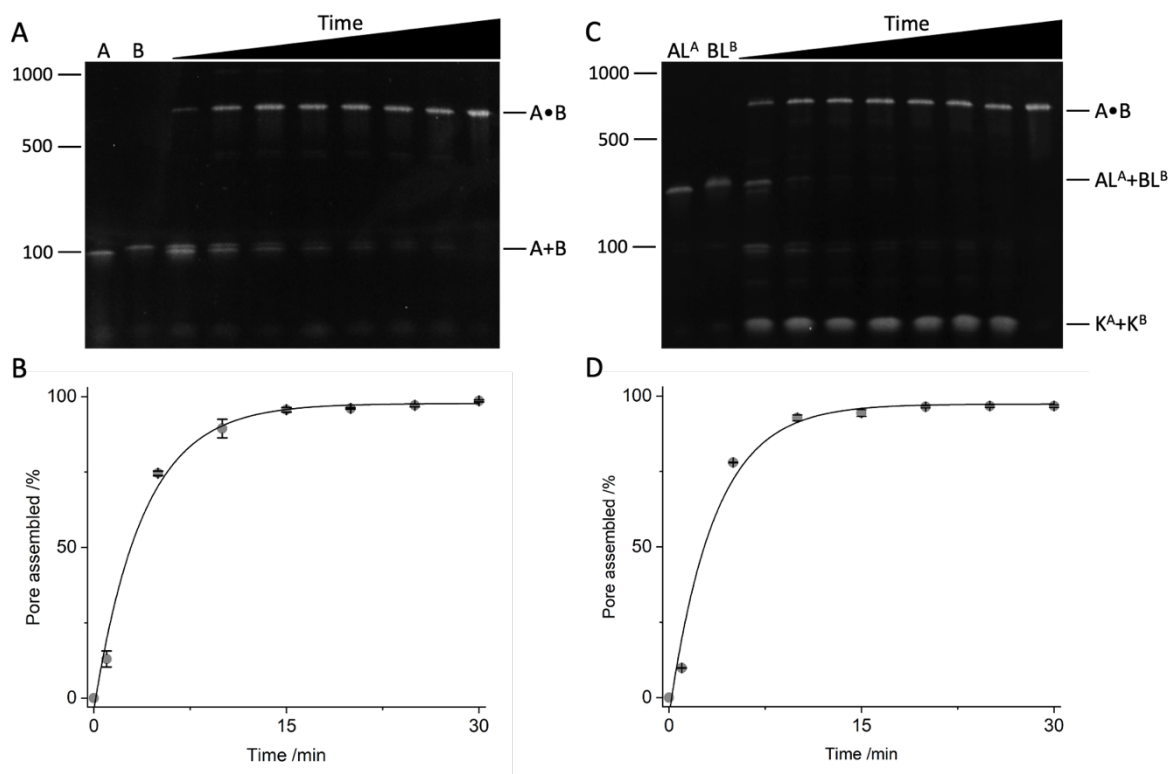
Figure 52. Qualitative PAGE time titration to assess the time required for pore assembly and the effect of the locks. (A) PAGE titration to assess the time required for $A \bullet B$ assembly from free A+B.

(B) Plot of the data from (A) using normalised band brightness from equation (2). (C) PAGE titration to assess the time required for A•B assembly upon addition of keys to the locked AL^A+BL^B. (D) Plot of the data from (A) using normalised band brightness from equation (2). 12% native PAGE run in 1x TBE buffer at 115 V for 90 min at 4 °C. Time points are 1, 5, 10, 15, 20, 25, and 30 min. Each trace represents data from three independent repeats. The major markers of a 100 bp DNA ladder are indicated at the left.

Pore assembly progressed at an approximately equal rate from the unlocked A and B and the locked components. The minimal influence suggested that the initial hypothesis was correct and that the toehold unlocking mechanism was suitably fast to have no observable impact on the rate. Indeed, investigating the assembly from locked components (Fig. 52C), there was evidence of four bands after 1 min. One for the locked components AL^A and BL^B, one for the keys, K^A and K^B, one for the pore A•B, and one that corresponds to the A, B band in panel A. The presence of this band indicated that the unlocking toehold-mediated strand displacement was indeed faster than pore assembly. However, beyond the assertion that the unlocking requirement did not appear to significantly affect the rate, further claims on the kinetics could not be made with any accuracy. Nevertheless, the combination of the results from the gel in Figure 50 and the results of these gels indicate that the locked components can be employed successfully.

After confirming general assembly and structural integrity for the native pore, assembly in the presence of cholesterol lipid anchors was investigated. A and B were each modified with one cholesterol lipid anchor at the 3' end of strand A_2 and B_2, respectively (see Fig. 49). This location positioned the cholesterol anchor on the most stable point of the component. It also minimised potential steric effects, such as tangling that were a risk if the anchor was located on the 3' end of strand A_1 or B1. In addition, this would add the membrane as a significant steric element in a required rearrangement on the membrane surface. Placement on the duplex left the membrane as a steric element, but no rearrangement would be required, which was preferable. A cholesterol lipid anchor on each component resulted in a symmetrical arrangement of lipid anchors on either side of the pore.

To assess the effect of cholesterol modification on pore assembly and pore structure, A, B, AL^A and BL^B were folded in 300 mM KCl, 15 mM Tris-HCl, pH 7.4 and the conditions used for the PAGE in Figure 50 were replicated (see Fig. 53).
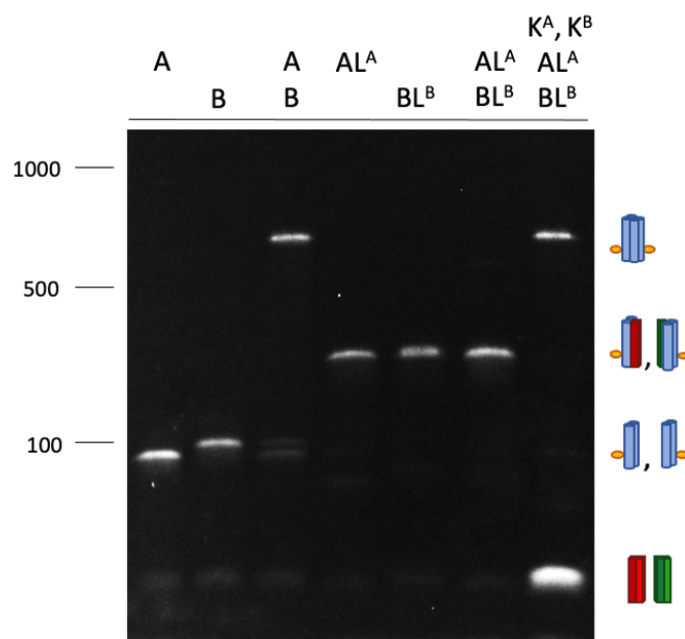
Figure 53. Confirmation of the assembly of the nanopore (A•B) from unlocked components and the efficacy of the locking mechanism to control and trigger pore assembly was assessed by native PAGE in KCl (300 mM KCl, 15 mM Tris-HCl, pH 7.4). Addition of A and B in a 1:1 stoichiometric ratio results in the assembly of A•B (Lanes 1-3). No interaction is observed upon addition of AL^A and BL^B and they remain in their constituent parts (Lanes 4-6); however, if the keys, K^A and K^B are added, the locks are removed and A•B forms in a 1:1 stoichiometric ratio (Lanes 4,5,7). A 1:1 ratio for keys to components is also sufficient for complete removal of the corresponding lock (Lane 7). Samples were incubated at 30 °C for 30 min before being loaded onto the gel. 12% native PAGE were run in 1x TBE buffer at 90 V for 115 min at 4 °C.

The PAGE obtained with cholesterol modified components matched the PAGE for the unmodified ones indicating that cholesterol modification did not impact pore stability or successful pore assembly. A very faint band was visible in the A+B lane around the 100 bp marker. This corresponded to the individual components and likely indicated a minimal concentration discrepancy when loading onto the gel as this was not apparent in $AL^A + BL^B + K^A, K^B$. Otherwise, the gels were nearly identical.

The PAGE indicated that the structure had been successfully assembled; however, it remained important to confirm that the cholesterol lipid anchors had been (a) successfully incorporated and (b) that they were available for membrane anchoring. To visualise this CLSM was used and component A was modified with a Cy3 fluorophore on the 5' end of strand A_1 and $B^{\Delta C}$ was modified with a Cy5 fluorophore on the 5' end of strand B_1. The sequences of both strands (5' $\rightarrow$ 3') are listed below. The dyes are labelled in red. The sequences of all strands and compositions of all structures used can be found in the Appendix A (Section 9.4.1).

^{Cy3}A₁: Cy3ATT AGC GAA CGT GGA TTT TGT CCG ACA TCG GCA AGC TCA CTT TTT CGA CT

^{Cy5}B₁: Cy5AGG CGA AGA TCG TTC TTT TCC TGC ACG TCC AAC TGG TCA GTT TTC GCA GC

^{Cy3}A was added to GUVs composed of POPC in a FluoroDish and mixed. After 10 min ^{Cy5}B$^{\Delta C}$ was added, and the solution was thoroughly mixed. Brightfield was used to identify GUVs, which were then visualised in the green and red channels to observe the Cy3 and Cy5 fluorophores respectively. The observation of a halo surrounding the GUVs was indicative of interaction with the membrane (Fig. 54). Successful tethering of A to the GUVs was observed by a resultant halo and A halo was also detected in the red channel indicating that B was also tethered to the membrane. Without a cholesterol lipid anchor, B$^{\Delta C}$ can only interact with a membrane by binding to A, which has a cholesterol lipid anchor. Therefore, the presence of a halo indicated that B was successfully bound to A. To confirm this observation, the two channels were overlain to reveal a yellow halo around the GUVs (Fig. 54). Rather than simply labelling the formed A•B pore with a fluorophore and visualising membrane interaction, labelling both A and B with a fluorophore allowed pore formation to be visualised on the membrane surface in addition to membrane tethering. B$^{\Delta C}$ was not modified with a cholesterol lipid anchor to allow pore assembly to be differentiated from both components binding to the membrane, which would not have confirmed assembly.
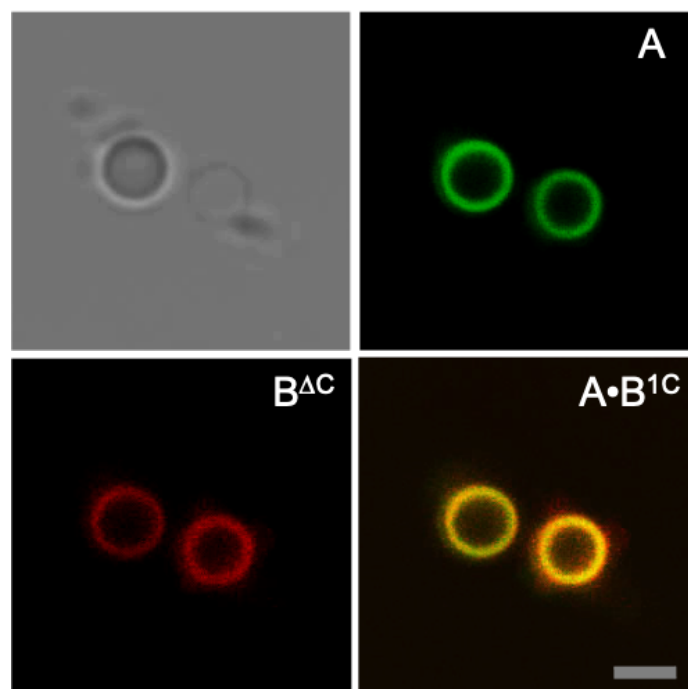
Figure 54. Confirmation of cholesterol-mediated anchoring to the lipid bilayer of GUVs composed of POPC and pore assembly on the surface of a membrane. A was modified with a Cy3 fluorophore and B with a Cy5 fluorophore. CLSM images were obtained using a 96x oil objective. Top left: brightfield image of two GUVs of approximately 5 μm diameter. Top right: green channel shows a ring around the GUVs demonstrating the Cy3-tagged A tethering to the membrane. Bottom left: red channel shows the Cy5-tagged B$^{\Delta C}$, which cannot interact with the membrane on its own, has bound to the membrane tethered A. Bottom right: overlay of the red and green channels demonstrating (A•B)^{1C} formation

The UV-thermal denaturing assay was repeated to probe the nature of the interaction of A•B with lipid vesicles (Fig. 55). It has been previously observed that insertion into the membrane has a stabilising effect on the nanopore, which results in a sharper transition and as an increase in T_m by as much as 5 °C.[115,127] The sharper transition is likely due to minimisation of thermal fluctuations in the DNA that would otherwise occur. The experimental set-up was identical to the unmodified pore, except that DPhPC lipid vesicles were added at a lipid concentration of 200 μM. To avoid undesired transitions for tethered A and B alone, these were first mixed and incubated at 30 °C for 10 min before being added to the SUVs.
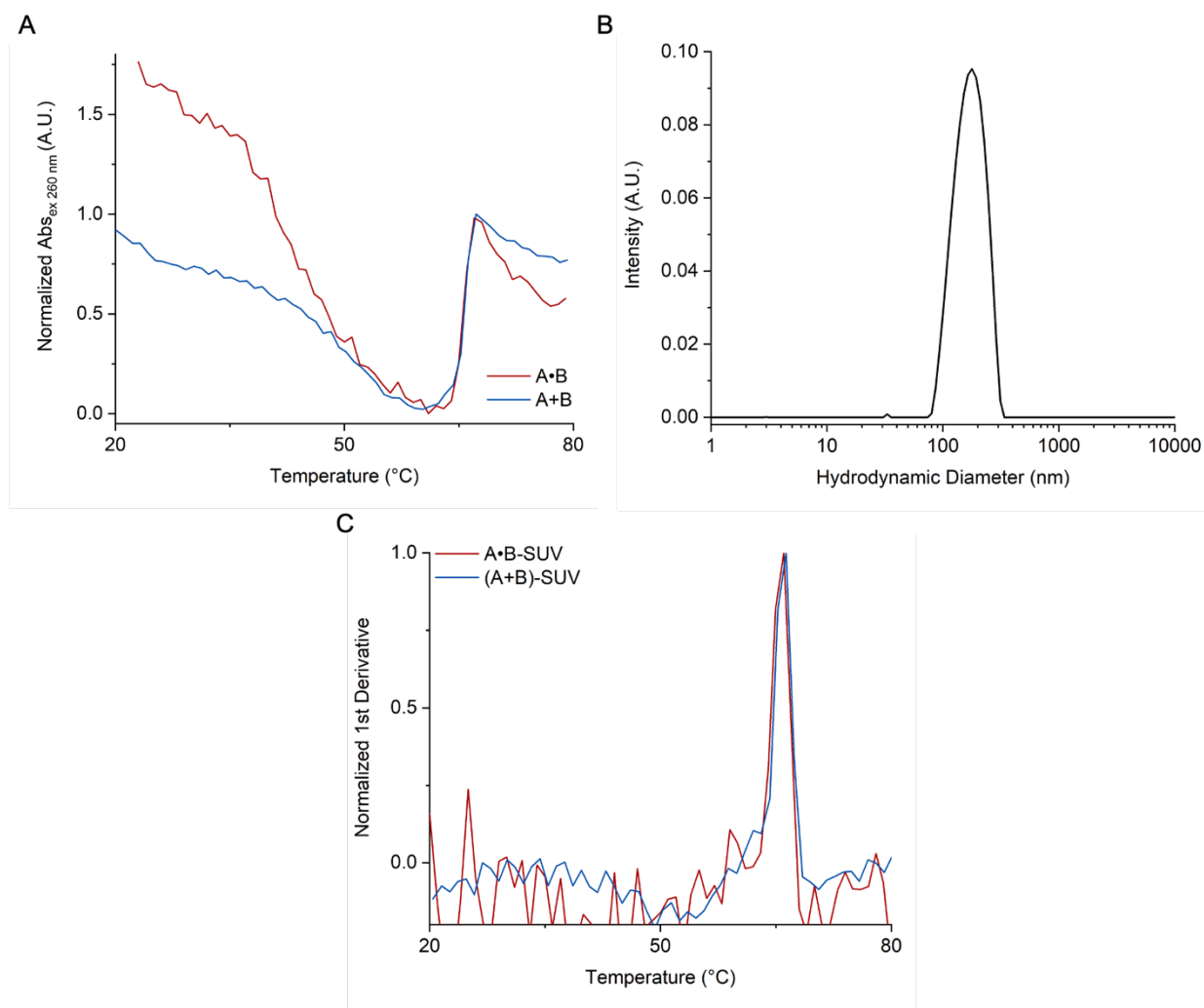
Figure 55. (A) UV-melting profiles of A•B inserted into SUVs composed of DPhPC with an average diameter of 170 nm when folded directly or assembled *in situ* from A and B to assess structural stability and confirm structural similarity. A•B was assessed at 0.2 µM with 200 µM DPhPC lipid in 150 µL of PBS buffer. Samples were melted using a temperature ramp of 1 °C/min between 20 and 80 °C. Each trace represents an average from three independent repeats. (B) Dynamic light scattering trace of SUVs composed of DPhPC lipids in PBS buffer. (C) 1st derivative of the melting profiles used to identify the melting temperature (T_m) of each structure.

Three observations were apparent upon investigation of the melting profiles of A•B in the presence of SUVs. The first was the change in shape compared to the melting profiles in the absence of SUVs. Rather than the expected sigmoidal curve associated with UV melts as was the case with the unmodified (A•B)$^{\Delta C}$, in the presence of SUVs, the melting profiles display what was closer to an inverted bell-curve. A decrease in UV intensity as the temperature increases is sometimes observed when nanostructures are modified with lipid anchors, such as cholesterol, due to the breaking up of aggregates as the temperature increases; however, this effect is normally relatively minor unless significant aggregation is present. If this were the case, the transition would likely be much broader.

The more likely explanation relates to the SUVs. Lipid vesicles are well known to scatter light.[311] Of particular interest to this experiment was that as the size of the vesicle approaches the wavelength of light, the scattering results in elevated absorbance readout.[312] For these experiments, vesicles of DPhPC lipids were selected due to the lack of gel transition phase change over the desired temperature range.[313–315] The vesicles were sonicated for 20 min at 30 °C which resulted in vesicles with a hydrodynamic radius of ~170 nm (Fig. 55B). 170 nm is close enough to the 260 nm DNA absorptions wavelength to cause significant scattering, which likely explains the elevated absorbance. With regards to the ~1.5x difference in intensity between the A•B-SUV and (A+B)-SUV experiments, A•B-SUV was performed a day later than the (A+B)-SUV experiments, which may have resulted in the formation of a less homogenous sample either via the formation of some multilamellar vesicles, which results in increased scattering[311] or an increase in size, e.g., via vesicle fusion, increasing scattering compared to the smaller vesicles. The scattering effect was significantly reduced as the temperature increased resulting in a trough at ~60 °C, right before the DNA melting transition. DPhPC does not have a transition at this temperature so this is not the cause. The increasing temperature likely increased membrane fluidisation, which resulted in reduced scattering.

The second observation was that the transition was very sharp, especially compared to the transition for A•B$^{\Delta C}$. This has been previously observed in the literature with the explanation that insertion into the lipid bilayer confers an increase in stability.[115,127] In the presence of vesicles, the strand termini were expected to be located within the membrane so no change as a result of strand fraying was expected.[118] This was more clearly observed in Figure 56A where the traces were overlain. The other effect of an increase in stability conferred by insertion into the lipid bilayer leads to the third observation: an increased T_m. Both A•B formed from folding and *in situ* formation from A and B demonstrated excellent overlap at the transition point (Fig. 55A). The 1st derivative demonstrates highly comparable overlap, which indicates that the two species were identical. The resultant T_m were 66.1 ± 0.1 and 66.2 ± 0.2 °C for A•B-SUV and (A+B)-SUV, respectively. An overlay of the 1st derivatives obtained with and without SUVs highlights the shift in T_m (Fig. 56B). The combination of a sharper transition and increased T_m was indicative of pores in a membrane-spanning orientation.[115,127] Burns *et al.*[115] and Göpfrich *et al.*[127] both observed a shift of approximately 5 °C when cholesterol modified pores were incubated with lipid vesicles. A small shift was observed here; however, the T_m even of the unmodified (A•B)$^{\Delta C}$ was at least 10 °C higher than for either of those pores. It may be that A•B was already sufficiently stable that the additional stability conferred by the membrane has a reduced effect compared to the pores from Burns *et al.* and Göpfrich *et al.*
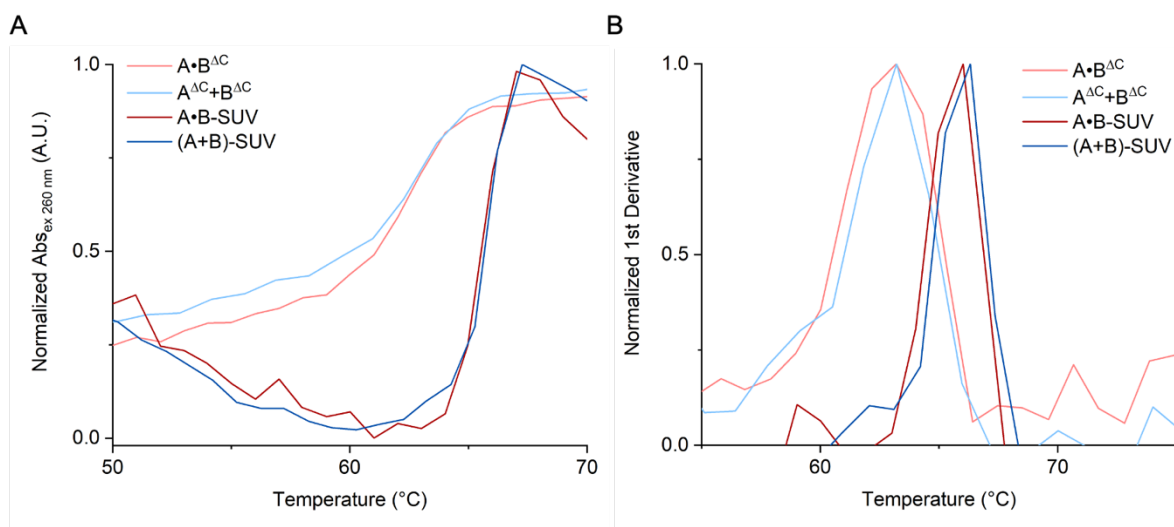
Figure 56. (A) Comparison of the (A•B)$^{\Delta C}$ and A•B-SUV UV melting profiles. (B) Comparison of the 1st derivatives from the melting profiles in (A).

5.2.3. Pore Assembly – Electrophoretic Gel Mobility Shift Assay

Following successful assembly of the pore and all components (free and locked) as well as the pore and component interaction with vesicles, the next step was to probe the binding properties of A and B. The first step was to investigate the binding of A$^{\Delta C}$ and B$^{\Delta C}$ in solution. It was clear from the model system that only 90% hybridisation was observed even in solution and that this fell to approximately 80% for hybridisation on the membrane surface. The data acquired in the previous section (5.2.2.) indicated that A and B bind in a 1:1 stoichiometric ratio and no other bands were present in any of the gels, which was not the case for the model system. However, there was an important difference between hybridisation in the model system and assembly of the 4HB nanopore. In the model system hybridisation occurred between two complementary strands. Here, the pore was formed via four hybridisation events: one for the two arms on each of the two components. This provided the advantage that if hybridisation between any one of the arms and the corresponding loop on the other component was successful, hybridisation between the other arms and loops would then be intramolecular and correspondingly fast. It also meant that because there were four opportunities for hybridisation, it was expected that pore formation would go to completion. Nevertheless, the presence of a loop and two arms on each component may also have provided greater scope for the formation of secondary structures. While the formation of hairpins and other secondary structures was a risk, the location of the arms on either end of the duplex meant that there was also the risk of significant dimer or chain formation.

The conditions used for the electrophoretic mobility shift titration assays for the model system (Section 4.2.2.), both with and without SUVs, were replicated here. However, in place of SUVs composed of DOPC and DOPE, SUVs were made with DPhPC with an average diameter of 119

nm. This resulted in an SUV concentration of 7.53 nM and a maximum A:SUV loading of 265:1. The 500:1 lipid:A ratio from the model system was also conserved here.
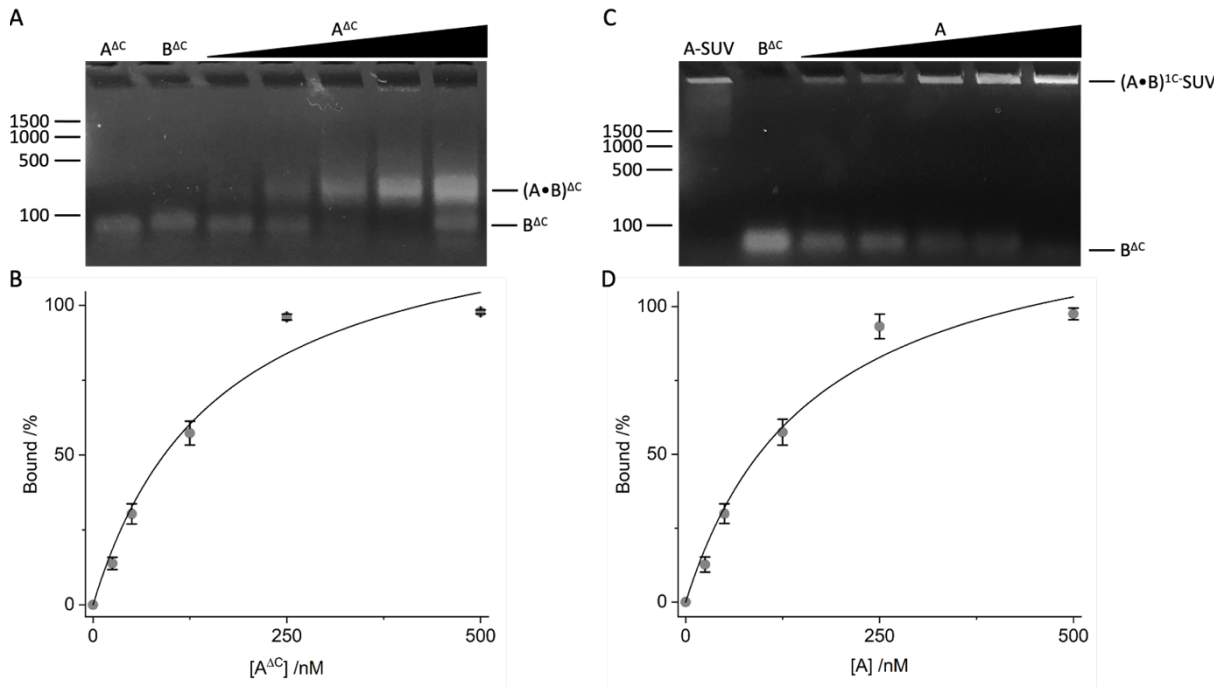
Figure 57. Gel electrophoretic mobility shift assay to assess the binding properties of $A^{\Delta C}$ and $B^{\Delta C}$, both in solution and when A is tethered to the surface of SUVs. (A) A representative 3% agarose gel shift assay: increasing the concentration of $A^{\Delta C}$ results in the formation of the $(A \bullet B)^{\Delta C}$ nanopore complex, which is larger than the individual components and migrates through the gel more slowly. (B) Binding curve of $(A \bullet B)^{\Delta C}$ complexation displayed as percent bound revealed a K_d of 1.54 ± 0.23 x 10^{-7} M. The data represent averages and standard deviations from three independent experiments. The curves were fit to the data with an average R^2 of 0.97 from the three repeats. (C) A representative 2% agarose gel shift assay: increasing the concentration of A results in the formation of the $(A \bullet B)^{1C}$ membrane-bound complex, which is unable to migrate into the gel matrix and remains in the well. (D) Binding curve of $(A \bullet B)^{1C}$ complexation displayed as percent bound revealed a K_d of 1.64 ± 0.14 x 10^{-7} M. The data represent averages and standard deviations from three independent experiments. The curves were fit to the data with an average R^2 of 0.97 from the three repeats. All gels were run in 1x TAE buffer at 60 V for 60 min. The major markers of a 100 bp DNA ladder are indicated on the left of each gel. Bands are identified at the top and right.

The electrophoretic mobility shift assays indicated successful binding both in solution and on the membrane surface. In both cases, a definitive band shift was observed, which indicated the successful formation of the A•B nanopore complex. In addition, the titration for hybridisation in solution confirmed that A and B underwent complete complexation at a 1:1 stoichiometric ratio as only one band was evident in this lane of the gel (Fig. 57A, second from the right). This corroborated

the results obtained previously, which implied a 1:1 stoichiometry. For hybridisation on the surface, a very faint band was observed at the same stoichiometry, but, nevertheless, this still represented $95.3 \pm 1.9\%$ hybridisation, which was an increase in hybridisation of ~15% compared to the same conditions in the model system. This also suggested that the proposed hypothesis relating to multiple points of hybridisation to tie the structure together was correct. In addition, no other bands were observed in either gel, which implied no other structures were present. This belied the concern about the formation of dimers or chains as these would most likely have been evident at either the lower stoichiometries or the 2:1.

Both conditions resulted in a very similar K_d: $1.54 \pm 0.23 \times 10^{-7}$ and $1.64 \pm 0.14 \times 10^{-7}$ M for solution and surface, respectively. These results mirrored those obtained for S_{NP}, which also demonstrated very similar binding (within error) both in solution and on the membrane surface. However, the K_d obtained here were two-fold weaker than those obtained for S_{NP} in the model system and were very similar to the K_d obtained for S vs R_{SUV}. As previously discussed, A and B are more complex structures than the simple 20-nt complementary duplexes of S and R or the simple strand extension of S_{NP} and this was likely to be reflected in the binding strength. Another potential explanation may be related to the means by which the gels were imaged. In the model system S was modified with a Cy5 fluorophore, which was used for imaging. Whether as ssDNA or dsDNA, the intensity was unlikely to change. Similarly, S_{NP} was primarily imaged via EtBr in between the 252-bp of the six 15 nm long helices of the NP. Both of these are very constant. By contrast, the components, A and B, are composed of a single, 21-bp duplex and three ssDNA regions, which bind EtBr only weakly. Upon formation of A•B this changes to four 21-bp duplexes, effectively quadrupling EtBr staining. This may have affected the normalisation process, implying weaker binding at the lower stoichiometries than was in fact the case. Nevertheless, K_d in the nanomolar range represent strong and satisfactory binding.

5.2.4. Pore Assembly Monitored via Förster Resonance Energy Transfer

The confirmation of binding in solution and on the membrane surface when one component is tethered was an important step; however, in order to mimic the formation of protein pores, assembly on the membrane surface when both components were tethered needed to be investigated. Gel binding titrations using electrophoretic mobility shift assays are a simple and powerful technique to assess binding. Unfortunately, in the case of this project, they have a significant drawback in that it cannot be used to assess membrane surface binding between two anchored components. Gels cannot discriminate between different membrane bound entities as they all remain in the well. Therefore, a different technique was required.

Förster resonance energy transfer (FRET), which was previously used to monitor the hybridisation kinetics of the model system in Section 4.2.3, was an ideal technique because the signal change is based on distance allowing the independent monomer components, A and B, to be differentiated from the assembled nanopore, A•B. For FRET to be observed, the two dyes must be within 1-10 nm of each other. [Cy3]A and [Cy5]B, which were used in Section 5.2.2. were again used here. The location of the fluorophores positions the dyes on opposite duplexes in the nanopore (Fig. 58). Upon assembly, the two dyes were anticipated to be ~5-6 nm apart, which is very similar to the Förster radius for Cy3-Cy5 of ~6 nm[99,293,294,316–318] and, therefore, should result in a strong FRET signal.
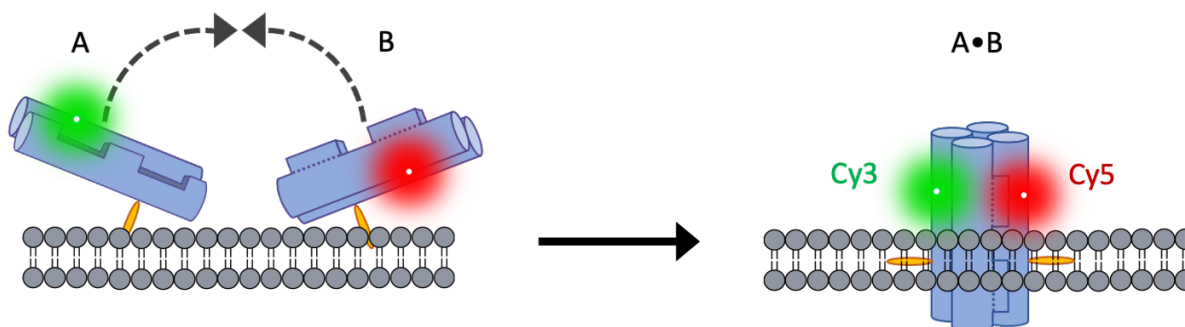
Figure 58. Schematic illustration of the FRET pore assembly on the membrane surface. The left-hand side indicates the location of the FRET pair, Cy3 on A and Cy5 on B, in the monomer component state, independently tethered to the membrane. The right-hand side indicates the change in proximity of the fluorophores following assembly into the nanopore, A•B, and insertion into the membrane. The schematic is for visualisation purposes only and the location of the dyes is not representative.

As a fluorescence-based technique, FRET was also much more sensitive than gel electrophoresis, which allowed lower concentrations to be assayed. For example, in Section 4.2.3., 1.25 nM (150 fmol) DNA was used. The lower concentrations should allow a more sensitive K_d for A and B binding to be determined. Therefore, the conditions previously assayed by the gel mobility shift assays (binding in solution and when one component was tethered to the membrane) were repeated. These conditions would also function as controls to ensure reliability of the system. As was the case with the hybridisation kinetics in Section 4.2.3., the Cy3 signal, and therefore [Cy3]A, was monitored. The concentration of A was held constant at 100 nM and B was titrated in at concentrations of 10-100 nM. SUVs composed of DPhPC were used again for reproducibility with the gel mobility shift titrations. DLS was unavailable due to COVID-19 restrictions, so an accurate determination of the diameter was not possible; however, the three previous batches of SUVs, which were all extruded 25 times though a 100 nm polycarbonate membrane and subjected to DLS, yielded diameters of 119, 122 and 123, therefore a diameter of 122 was assumed. This resulted in a final SUV concentration of 0.37 pM and, therefore, an A:SUV loading of 270:1, which is comparable to the maximum loading

used for the gel mobility shift assays. As a band for A•B was not observed at this loading in the gel this was considered a suitable loading to maximise signal and binding efficiency. The FRET pore assembly titrations for all three conditions are shown in Figure 59.
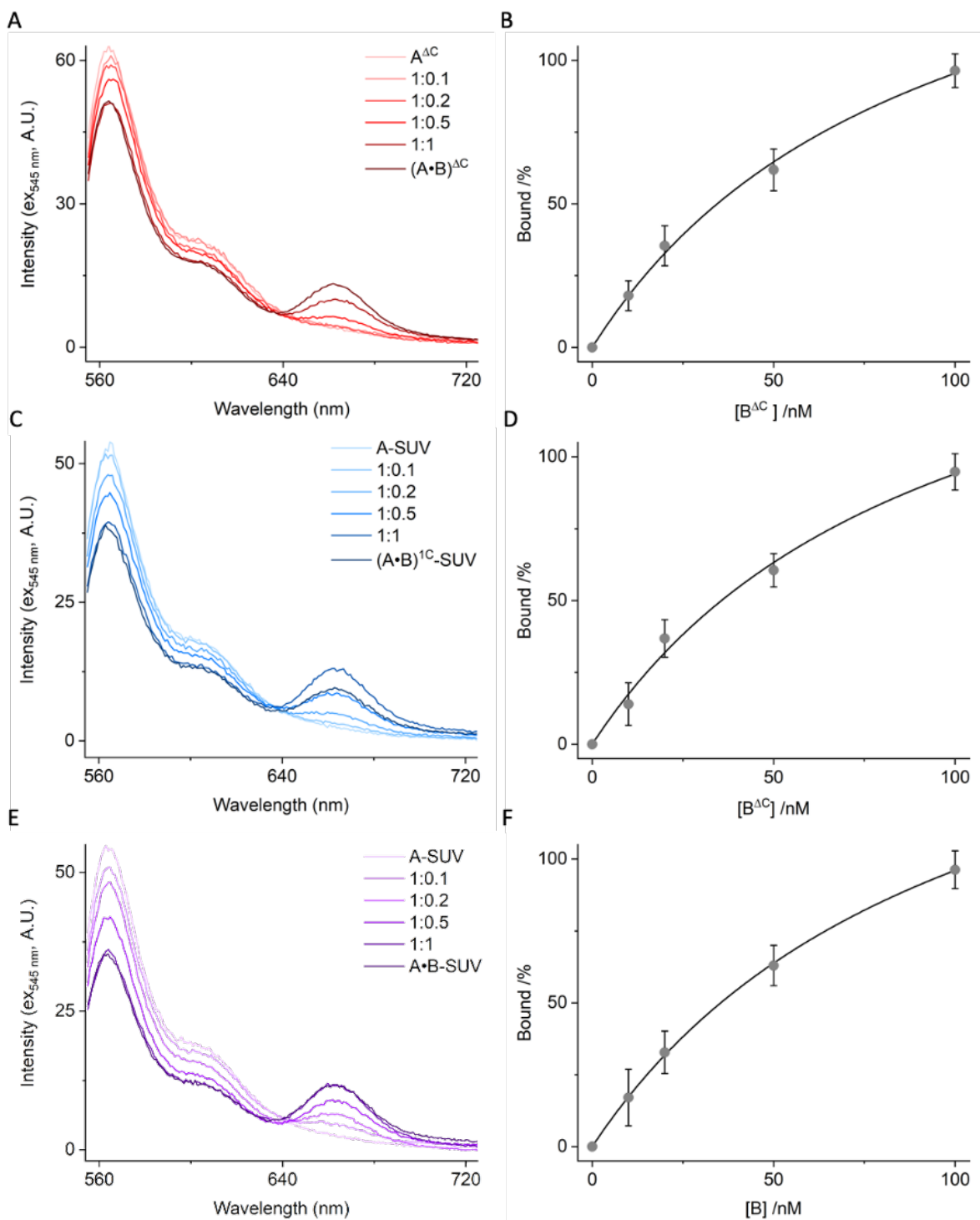
Figure 59. FRET pore assembly assays. A carries a Cy3 fluorophore and FRET donor and B carries a Cy5 fluorophore and FRET acceptor. When separate, the fluorescence intensity of Cy3 emission

will be high and Cy5 emission will be low. As A and B assemble into A•B the two fluorophores will come into close proximity, observed as a decrease in Cy3 emission and an increase in Cy5 emission. (A) Pore assembly titration of $A^{\Delta C}$ vs $B^{\Delta C}$ in solution. (B) Binding curves of A•B pore assembly based on (A) displayed as percent bound. The data represent averages and standard deviations from three independent experiments. The curves were fit to the data with an average R^2 of 0.98 from the three repeats (C) Pore assembly titration of the membrane tethered A-SUV vs $B^{\Delta C}$. (D) Binding curves of A•B pore assembly based on (C) displayed as percent bound. The data represent averages and standard deviations from three independent experiments. The curves were fit to the data with an average R^2 of 0.97 from the three repeats. (E) Pore assembly titration of A vs B on the surface of membrane surface. (F) Binding curves of A•B pore assembly based on (E) displayed as percent bound. The data represent averages and standard deviations from three independent experiments. The curves were fit to the data with an average R^2 of 0.98 from the three repeats

Successful titrations were achieved for all three conditions. The results are summarised in Table 3. A gradual elongation of the distance between the curves for A on its own and the A•B control was observed when moving from pore formation in solution (Fig. 60A) to pore formation on the membrane (Fig. 60C & E). This indicated a change in the inter-dye distance in solution compared to when bound to the membrane (this will be discussed in more detail later). Nevertheless, all three conditions resulted in highly comparable binding curves Fig. 60B, D, &F) with derived K_d all within error of each other (Table 3). Indeed, the degree of similarity between the three curves was unexpected. However, the electrophoretic mobility shift assays for this system (Fig. 57) were effectively mirrored here, which instilled confidence in the technique. The K_d derived from the model system (Fig. 42 & 43) also corroborated this similarity, which indicated that the presence of the SUVs had limited impact on pore assembly. The results suggest that the addition of some degree of steric bulk to the membrane bound species mitigated the effect of the membrane. Despite their similarities, the K_d obtained from the FRET titrations were ~30% lower than those obtained from the gel mobility shift assays, which was in line with the increased FRET sensitivity. While FRET is a more sensitive technique, the K_d remained higher than those obtained using gel mobility shift assays for the simple hybridisation in the model system. This may indicate that those K_d would also be lowered if assayed via FRET. However, as previously discussed, the biomimetic pore assembly is a more complex system than the model system and so weaker binding was expected.

Table 3. Summary of thermodynamic and kinetic data obtained using FRET for the assembly of the nanopore, A•B, in solution, when A only is tethered to the membrane and when both A and B are tethered to the membrane. Averages and standard deviations were calculated form at least three independent repeats.

Parameter	Condition	Value ± Std. Dev.	Ratio (norm. % against $A^{\Delta C}$ vs $B^{\Delta C}$
K_d (M)	$A^{\Delta C}$ vs $B^{\Delta C}$	$9.15 \pm 2.35 \times 10^{-8}$	100
	A-SUV vs $B^{\Delta C}$	$9.53 \pm 2.90 \times 10^{-8}$	95.9
	A-SUV vs B	$1.02 \pm 0.23 \times 10^{-7}$	88.4
k_{on} (M^{-1} s^{-1})	$A^{\Delta C}$ + $B^{\Delta C}$	$1.19 \pm 0.29 \times 10^{4}$	100
	A-SUV + $B^{\Delta C}$	$5.86 \pm 0.57 \times 10^{3}$	49.2
	A-SUV + B	[a] $3.39 \pm 0.56 \times 10^{3}$	32.8
		[b] $1.90 \pm 0.39 \times 10^{3}$	16.0
k_{off} (s^{-1})	$A^{\Delta C}$ + $B^{\Delta C}$	1.09×10^{-3}	100
	A-SUV + $B^{\Delta C}$	5.58×10^{-4}	51.3
	A-SUV + B	[a] 3.99×10^{-4}	36.6
		[b] 1.94×10^{-4}	17.8

[a] Including the rapid initial drop observed for A-SUV vs B (Fig. 62A).
[b] Removing the rapid initial drop observed for A-SUV vs B (Fig. 62B).

Unlike assembly from $A^{\Delta C}$ and $B^{\Delta C}$ in solution or A-SUV and $B^{\Delta C}$ when only one component was tethered to the membrane, the FRET observed for assembly on the membrane surface between A and B could be due to unbound components tethered within 10 nm of each other. To assess this, the locked components, AL^A and BL^B were used. Gel electrophoresis has confirmed that the locked components are unable to assemble into A•B in the absence of the keys, K^A and K^B (Fig. 50 & 53), so any observed FRET signal could be attributed to proximity on the membrane surface rather than assembly (Fig. 60).
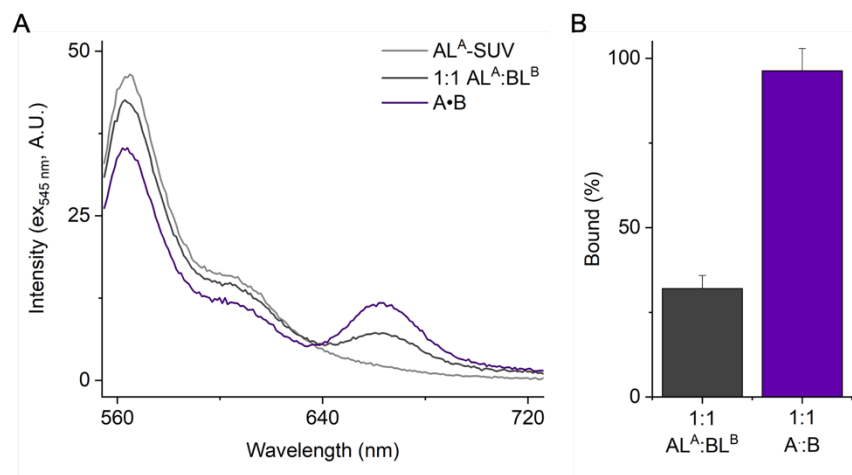
Figure 60. (A) Fluorescence spectra of the locked components AL^A and BL^B used as a control to assess the effect that donor and acceptor tethering on the surface has on the observed FRET signal for pore assembly on the membrane surface. (B) Normalised bar graph comparing the FRET signal observed from 1:1 stoichiometric ratios of the interaction of locked components, AL^A and BL^B, on the surface to that following pore formation from A and B. Each trace is an average of three independent repeats, the standard deviation of which are shown by the error bars in the bar chart.

A small change in the FRET signal was observed when a 1:1 stoichiometric amount of AL^A and BL^B were both present on the membrane compared to AL^A on its own. Upon normalisation with the folded A•B, this equated to $32.0 \pm 3.89\%$ binding, which was equivalent to the 1:0.2 ratio of A:B at $32.8 \pm 7.40\%$. By contrast, a 1:1 stoichiometric ratio of A:B yielded $96.3 \pm 6.59\%$ binding. The bar graph (Fig. 60B), where these are directly compared, makes it clear that the strong change in the A:B FRET signal cannot be accounted for by proximity alone. This indicated that in order for a change in the FRET signal of that magnitude the components must have been closer together, which could only be accounted for by pore assembly.

As an additional control, single molecule FRET (smFRET) was used to probe pore assembly and confirm that pores were indeed formed. The assembly of A•B from $^{Cy3}A+^{Cy5}B$ was compared to a control of pre-mixed $^{Cy3}A•B^{Cy5}$ on supported planar lipid bilayers at a concentration of 62.6 pM (Fig. 61, left). The successfully formed pores were visualised as small green dots (see grey box), which are present in both images. The formation of individual pores was also monitored over time via single particle tracking to confirm assembly from smFRET. The smFRET experiments corroborates the AL^A:BL^B control and successfully confirms pore assembly on the membrane surface from two anchored components.
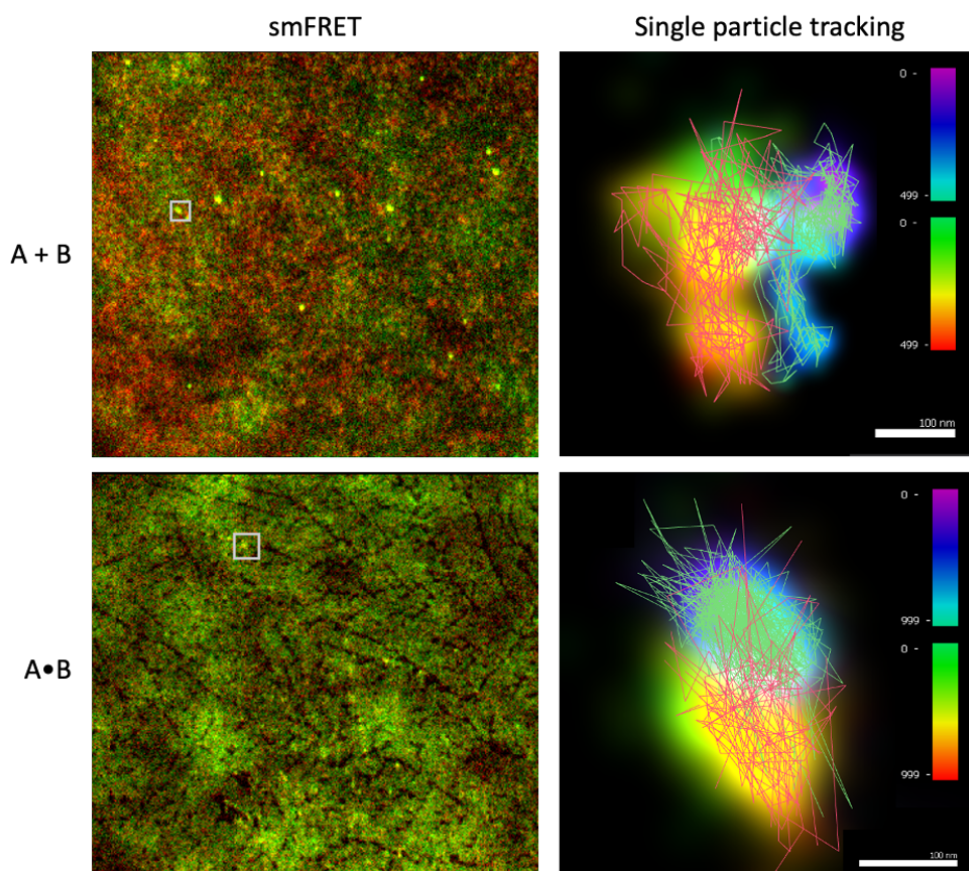
Figure 61. Single-molecule FRET and single particle tracking images confirm pore assembly from the monomer components: A and B (top) in comparison to a control, pre-mixed A•B (bottom). Bright green spots indicate the formation of A•B in the smFRET pictographs (e.g., grey boxes). A carries a Cy3 fluorophore at the 5' end of strand A_1 and B carries a Cy5 fluorophore at the 5' end of strand B_1. Pore assembly from A and B was monitored on the supported lipid bilayer membrane at 62.5 pM for 500 s.

Following confirmation of pore assembly under all three conditions and investigated the thermodynamics of component binding, the next step was to investigate pore assembly kinetically. Following the success of the pseudo-1st order kinetics method, this was repeated here. This was determined to be acceptable, despite the more complicated system involving multiple hybridisation steps. At nanomolar concentrations it was expected that the laws of mass transport kinetics[273,308–310] would be the predominant factor. Following the initial hybridisation step, the other three will all be intramolecular and therefore should be fast. In the case of hybridisation between membrane anchored A and B, the rate limiting step is expected to be diffusion along the membrane, which is likely to be slower than mass transport kinetics in solution.[131]

While the overall method was repeated from Section 4.2.3., two changes were made. To accommodate for the likely slower kinetics, pore assembly was monitored for 1 h instead of 13 min. The other change was an ~10-fold increase in the concentration of the donor (Cy3) from 1.25 nM to 16.67 nM. This was done to ensure adequate signal strength and to minimise the effect of vesicle scattering. In addition, as the 20-fold excess of the acceptor provided good results with the model system, this ratio was used over the 100-fold excess. This provided a substantial cost-savings and allowed the higher concentrations to be used. For consistency with the other experiments performed in this section, DPhPC vesicles were again used. Unfortunately, DLS was also unavailable for these experiments due to COVID-19 restrictions so as previously, a vesicle diameter for 122 nm and concentration of 7.22 nM was assumed (Section 4.2.3.). The 500:1 lipid:A ratio that had been successful previously was maintained. This resulted in a final SUV concentration of 60.17 pM and an A:SUV ratio of 277:1. The normalised and averaged results for all three conditions are shown in Figure 62. In addition to the three conditions, an $A^{\Delta C}$ and buffer only control was also run to demonstrate that the resultant curves were not the result of dilution.
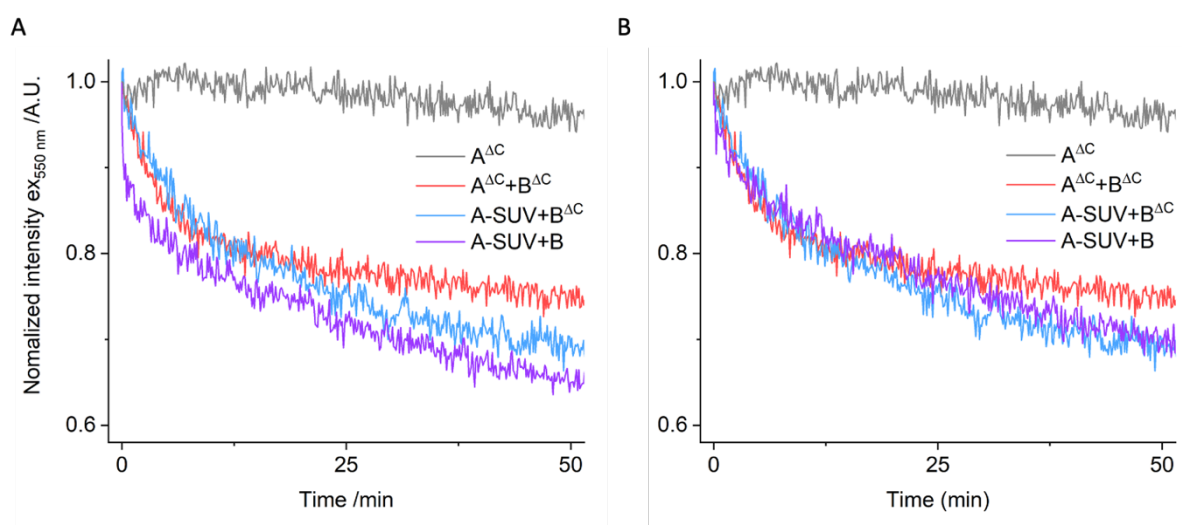
Figure 62. (A) Kinetic fluorescence analysis of pore assembly over time in solution ($A^{\Delta C}+B^{\Delta C}$, red), when one component is tethered to the membrane (A-SUV+$B^{\Delta C}$, blue), and on the surface of the membrane (A-SUV+B, purple). A control trace (grey) was also added using $A^{\Delta C}$ and buffer only. (B) The same as (A), but the initial rapid decline of A-SUV+B (purple) has been removed. Each trace is an average of three independent repeats.

Successful kinetics traces were obtained for all three conditions and the $A^{\Delta C}$+buffer control. There was a significant gap between the species hybridising in solution and those hybridising on the membrane surface in the model system, but the traces for all three pore assembly conditions (Fig. 62, red, blue, purple) were fairly closely grouped together. Indeed, assembly in solution (blue) was actually higher than the those with the membrane; however, this was likely a result of a wider pore diameter in solution due to swelling compared to when bound to the membrane (this will be

111

discussed in more detail later). The order of the traces effectively mirrored the increased separation between the F_D only and F_{DA} traces from the FRET binding titrations. This was a good sign as it indicated the same trend with regards to FRET efficiency (to be discussed in more detail later). The kinetic traces for each condition were fit using Equation (6), the integrated 1st-order rate equation, and the value for k_{on} was then determined as in Section 4.2.3. from Equations (3)-(5). The results are summarised in Table 3.

Unlike the K_d, which were all within error, the derived k_{on} differ more significantly. In the model system, hybridisation in solution occurred ~18% faster than hybridisation on the membrane surface. Here, pore assembly in solution occurred over 50% faster. Pore assembly between A and B on the membrane surface was nearly an order of magnitude slower than in solution. However, the major difference was the rate of pore assembly, which was 1-2-orders of magnitude slower than hybridisation in the model system. Pore assembly has a number of additional parameters. In addition to the steric element posed by the four arms, the four sequences were likely to confound hybridisation by presenting additional targets, significantly slowing down the assembly process.

In general, the shape of the three curves in Figure 62A followed the anticipated trend: $A^{\Delta C}+B^{\Delta C}$ faster than A-SUV+$B^{\Delta C}$, which was faster than A-SUV+B. However, a rapid initial decline was observed for A-SUV+B, which was a unique factor that was only present when both components carried a cholesterol lipid anchor and did not influence the hybridisation of A-SUV+$B^{\Delta C}$ or $A^{\Delta C}+B^{\Delta C}$. The initial rapid decrease to 0.912 on average was equivalent to the normalised F/F_0 change of 0.916 observed in the presence of AL^A:BL^B (Fig. 60). This equivalency suggested that this was likely a result of the rapid membrane association of B. The similarity of the normalised value to that of the locked components indicated an effect of proximity rather than assembly. When this initial rapid drop was removed (Fig. 62B), the resultant k_{on} was $1.90 \pm 0.39 \times 10^3$, which represented a decrease of 44% from $3.39 \pm 0.56 \times 10^3$ when the drop was present (Fig. 62A). However, despite the near perfect overlap of this drop with the FRET signal caused by the proximity of AL^A and BL^B on the membrane surface, it could not be said with certainty that this was entirely caused by proximity alone. Therefore, both values have been included in Table 3, as well as their effect on the derived k_{off}. Removing the drop also affected the extent of reaction and implied that the extent of A•B formed on the surface was lower than measured (Table 4).

As was the case for the model system in Section 4.2.3., the measured values for K_d and k_{on} allowed the dissociation rate, k_{off} to be calculated using Equation (7). The derived k_{off} were summarised in Table 3. As expected form the results for k_{on}, the derived k_{off} values followed the same trend of assembly in solution being faster than assembly on the membrane surface. However, notably, these k_{off} values were two orders of magnitude slower than the equivalent values for the model system. This was an anticipated result. A simple duplex dissociates from a single element; however, the

nanopore, A•B, would require dissociation from at least four points. The likelihood of concurrent dissociation was very low, which was reflected by the extremely low rates for k_{off}.

As with the model system, it was of interest to determine the yield of pore formation for each of the three conditions. The extent of reaction for all conditions was investigated via calculation of the FRET efficiencies (E) using Equation (8). FRET is based on an ensemble average so a lower experimental E than the control can be converted to a percentage used to calculate the extent of reaction, or yield. The control FRET efficiency was calculated from the ensemble FRET titrations using the folded A•B control for each of the three conditions as F_{DA}. The experimental E was then calculated from both binding and kinetic data. The results were summarised in Table 4.

Table 4. Summarised FRET efficiencies (E) for pore assembly derived from the pore assembly binding titrations and pore assembly kinetics between A, labelled with a Cy3 fluorophore, and B, labelled with a Cy5 fluorophore, in solution, when A is tethered to the membrane and when both A and B are tethered to the membrane. Averages and standard deviations were calculated from at least three independent repeats.

Condition	Control: FRET Efficiency (E)	Binding: FRET Efficiency (E)	Extent of reaction: Binding	Kinetics: FRET Efficiency (E)	Extent of reaction: Kinetics
$A^{\Delta C} + B^{\Delta C}$	0.27 ± 0.07	0.26 ± 0.07	96.3	0.26 ± 0.02	95.6
A-SUV + $B^{\Delta C}$	0.28 ± 0.02	0.26 ± 0.03	94.8	0.31 ± 0.05	113
A-SUV + B	0.36 ± 0.03	0.34 ± 0.03	96.3	[a] 0.35 ± 0.02 [b] 0.31 ± 0.04	98.7 87.2

[a] Based-on kinetics for A-SUV vs B including rapid initial drop (Table 3, Fig. 62A).
[b] Based-on kinetics for A-SUV vs B excluding rapid initial drop (Table 3, Fig. 62B).

The control FRET efficiencies indicate a high degree of structural similarity between the nanopore formed in solution from $A^{\Delta C} + B^{\Delta C}$ and the nanopore that tethers to the surface from A-SUV + $B^{\Delta C}$. However, the FRET efficiency then increases by 33% to 0.36 for the nanopore formed from A and B on the membrane surface. The FRET efficiency of 0.36 from A+B assembly on the SUV surface was corroborated by a FRET efficiency of 0.38 obtained using smFRET. This indicates a closer Cy3-Cy5 distance, which suggests that the pore may be in a transmembrane-spanning orientation. This will be investigated further later. To determine the extent of reaction, or yield, of pore assembly, the E value was calculated for each condition from the binding titrations and kinetics. The yield for pore assembly in solution between $A^{\Delta C} + B^{\Delta C}$ (96.3%) and on the membrane between

A-SUV + B$^{\Delta C}$ (94.8%) closely matched the yields obtained from the gel mobility shift (97.7 and 95.3%, respectively) and FRET titrations (96.4 and 94.8%, respectively), which validated the method. Even assembly on the surface from A and B resulted in a high yield of 96.3%. There was a concern that pore assembly on the surface would be too sterically hindered to proceed in high yield. However, as was previously discussed, adding AL^A and BL^B to SUVs also resulted in a mild FRET interaction equivalent to 32.0 ± 3.89% of the total binding, which may have partially masked the true yield. This was investigated more accurately from the kinetics traces, as previously discussed. The yield for pore assembly in solution obtained from the kinetics was within error of the yield obtained from the binding assay.

The kinetic FRET efficiency for the pore formed from A-SUV + B$^{\Delta C}$, however, was higher than the control and resulted in a 113% yield. Nevertheless, the error for the FRET efficiency was relatively high and the control E value was within error. An investigation of the kinetic trace for A-SUV + B$^{\Delta C}$ shown in Figure 62 shows that the trace has a general linear decline from approximately 25 min, which may indicate that some of the SUVs have sunk to the bottom of the cuvette, artificially increasing the E value. This linear decrease from ~25min was also observed for A-SUV + B but was absent for A$^{\Delta C}$ + B$^{\Delta C}$ suggesting this may be an SUV induced effect. The fluorescence spectrometer used to monitor the kinetics did not have stirring functionality and the system was not perturbed once B$^{\Delta C}$ or B was added to avoid influencing the kinetics in an uncontrolled manner. A decrease in fluorescence signal has been observed on occasion for other fluorescence experiments involving vesicles. The kinetics measurements for the model system were only monitored for 800 s, which was likely not enough time for SUVs to sink in any meaningful capacity. Another possibility is that due to the high dilution some membrane bound A bound two B$^{\Delta C}$. There may also have been some slight compression onto the membrane resulting in increased dye proximity. Nevertheless, as the kinetically derived value for E was within value of the control and this is the only observed outlier, it was not of significant concern.

Two FRET efficiency values were included for the kinetics of A+B formation on the membrane surface. The first value, footnote (^{a}), was based on the entire observed kinetic trace. The second value, footnote (^{b}), was based on the trace with the rapid initial drop that corresponded well with the AL^A + BL^B trace and was believed to be a result of rapid membrane anchoring of B leading to rapid <10 nm proximity rather than assembly. If the entire trace was used, footnote (^{a}), then the reaction proceeded with a yield of 98.7%. However, even if the rapid initial drop was removed, footnote (^{b}), the yield was still 87.2%, which was still satisfactory. Indeed, this represented a 30-40% increase compared to the results from S and S$_{NP}$ vs R$_{SUV}$ in the model system (46.1 and 55.8%, respectively). The true result was likely somewhere in between these two values. In general, these results indicated that pore assembly occurred with a high degree of success whether in solution or tethered or bound to the membrane surface, which was a positive result.

From the FRET efficiencies it was possible to calculate the approximate Cy3-Cy5 distance, which is a good approximation for the average diameter of the pore in each of the three conditions. However, in order to calculate this distance, the Förster radius (R_0) for the FRET pair must be known. Values of R_0 for the Cy3-Cy5 FRET pair used here have been found in the literature ranging from 5.2-6 nm.[99,132,293,294,318–321] In addition, it has been observed that moving from an ssDNA to a dsDNA environment can also have an effect on fluorescence quantum yields and, as a result, R_0.[11,132,322] R_0 is also dependent on the orientation of the fluorophores relative to each other and the overlap of their dipole moments.[294] Therefore, considering these dependences, the calculated Cy3-Cy5 distances were likely only approximations; nevertheless, they were still useful to understand the effect of the environment on the nanopore, A•B, as well as elucidating its final state. The Cy3-Cy5 distance can be calculated from the FRET efficiency, E, and R_0 using Equation (9). The Cy3-Cy5 distances were calculated using the FRET efficiency values of the control to eliminate the effect of unformed pores. The calculated distances are summarised in Table 5.

$$E = \frac{1}{1 - (\frac{r}{R_0})^6} \qquad (9)$$

E= FRET efficiency, r = donor-acceptor separation distance, R_0 = Förster distance where E = 50%.

Table 5. Calculated Cy3-Cy5 distances as an approximation for the average diameter of the nanopore, A•B, in each condition: solution, $(A•B)^{\Delta C}$; tethered to the membrane, $(A•B)^{1C}$-SUV; and tethered/spanning, A•B-SUV. Distances were calculated using the control FRET efficiency values in Table 4 and using three literature values for R_0.

Condition	Cy3-Cy5 Distance /nm		
	$R_0 = 5.2$	$R_0 = 5.6$	$R_0 = 6.0$
$(A•B)^{\Delta C}$	6.15 ± 0.43	6.63 ± 0.47	7.10 ± 0.50
$(A•B)^{1C}$-SUV	6.11 ± 0.12	6.58 ± 0.13	7.05 ± 0.14
A•B-SUV	5.74 ± 0.13	6.19 ± 0.14	6.63 ± 0.15

The different literature values for R_0 result in Cy3-Cy5 distances that vary by nearly 1 nm or ~14% for each condition. Nevertheless, the difference between $(A•B)^{\Delta C}$ in solution and A•B bound to SUVs was reasonably consistent at 0.44 nm, on average across the three conditions. However, the

error for $(A•B)^{\Delta C}$ is significantly larger than for the other two conditions and means that the variation with A•B-SUV may be over 1 nm. There was very little variation between $(A•B)^{\Delta C}$ and $(A•B)^{1C}$-SUV and what little variation was observed may be explained by compression on the membrane surface or the large error associated with $(A•B)^{\Delta C}$. The contraction of A•B in the presence of the membrane implies that this is due to the membrane and as this effect was not observed for $(A•B)^{1C}$, it can be inferred that this was unique to A•B. With two cholesterol lipid anchors, A•B should be able to adopt a transmembrane orientation. The UV-melts (Fig. 55 & 56) previously demonstrated additional stability for A•B in the presence of SUVs, which was interpreted as the pore adopting a membrane-spanning orientation in the bilayers. The contraction observed here would appear to corroborate that. However, additional data was required to confirm.

The 4HB from Göpfrich *et al.*[127] was found to have a hydrodynamic radius of 5.1 nm and an inner lumen diameter of 0.8 nm. This pore design is more rigid than the more open structure used here so this can be used as a baseline. In solution, this results in an increase of 21, 30 and 39% when R_0 = 5.2, 5.6 and 6, respectively. As there are no inter-duplex crossovers, except for the poly-T loop at the top and bottom, the nanopore was expected to swell in solution; however, to what extent was unknown. To assess the validity of the calculated Cy3-Cy5 distances for A•B, the Cy3-Cy5 distance for the model system was calculated (Section 4.2.3.). The fluorophores are separated by 4-nt, and for $R•S_{NP}$ both fluorophores are attached to a double helix. Therefore, the Cy3-Cy5 distance should be ~3.5-4.1 nm. Using the value of E for the control (Table 2), the Cy3-Cy5 distance was calculated as 4.13, 4.44 and 4.76 nm for R_0 = 52., 5.6 and 6, respectively. The distances calculated at R_0 = 5.2 and 5.6 show good agreement with the theoretical estimation, while 4.76 nm at R_0 = 6 appeared to be outside of the possible dimensions for the model system. This suggests that R_0 = 5.2 or 5.6 are more accurate values for R_0 in the environment of this system, which would also bring them more in line with the hydrodynamic radius calculated by Göprich *et al.*

5.2.5. Linear Dichroism Spectroscopy

To assess the orientation of A•B in the presence of the membrane, linear dichroism experiments were conducted. Linear dichroism (LD) spectroscopy measures the difference in absorbance of polarised-light parallel and perpendicular to an orientation axis according to Equation (10).[323,324]

$$LD = A_\parallel - A_\perp \qquad (10)$$

Therefore, an LD spectrum can be obtained for any molecule or macromolecule that can be oriented along an axis. This allows structural changes to large macromolecules, such as the binding of a drug to DNA (>200 bp), to be observed.[324] However, a particularly potent use of LD is to probe the orientation of membrane bound species, such as proteins and peptides.[324,325] Vesicles, or liposomes,

can be used as model membranes and then oriented using shear-flow to deform the membrane from an unoriented spherical to an oriented ellipsoidal structure (Fig. 63) allowing the orientation of the membrane bound structure to be deduced.[325] As DNA is not a naturally-occurring membrane bound species, few studies have been performed investigating the orientation of membrane tethered-DNA.[135,326] Both the study by Banchelli *et al.* and Lundberg *et al.* investigated the orientation of relatively simple duplexes bound to the membrane surface via cholesterol lipid anchors. No studies have yet been published investigating the orientation of a transmembrane DNA nanostructure.

Liposome   Shear deformed liposome   Model of a deformed liposome
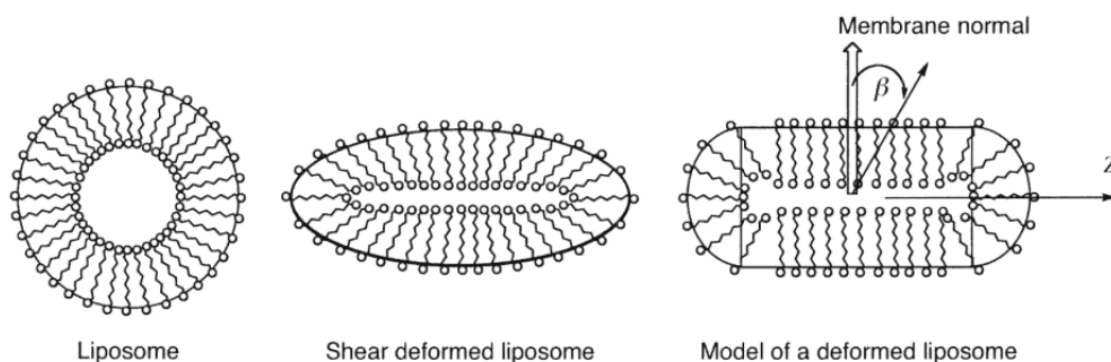
Figure 63. Schematic illustration of a liposome and a shear deformed liposome after undergoing shear-flow orientation. Adapted from B. Nórden *et al.*.[325]

The orientation of A•B on the membrane surface was assessed using POPC SUVs. The size of the components, as well as their loose arms and the loops, were judged to be too small and not sufficiently uniform to provide an interpretable signal so $(A•B)^{1C}$ was used as a control in place of A. $(A•B)^{\Delta C}$ was also used to control for the effect of nanopores in solution. SUVs composed of DPhPC were initially assessed, but these tended to crash-out and denature under shear-flow and so POPC was used. Some evidence of wispy lipid strands was evident following shear-flow even with POPC on a few occasions; however, it was significantly reduced. It was not possible to perform DLS on the vesicles before use, but they were extruded through a 100 nm polycarbonate membrane and so were expected to be consistent in size with SUVs used previously. To obtain LD spectra, the sample is first shear-flow oriented and then allowed to relax to obtain the isotropic spectra, which is then subtracted from the oriented spectra to allow orientation to be measured. The resultant LD spectra are shown in Figure 64.
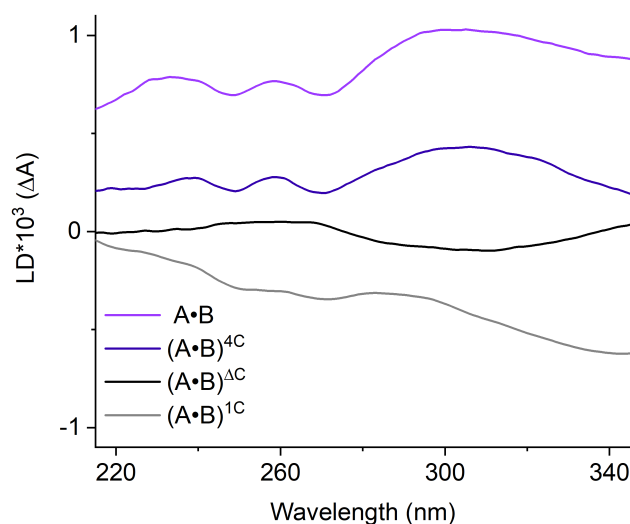
Figure 64. Representative linear dichroism spectra of A•B (purple) interacting with SUVs composed of POPC and control pores: $(A•B)^{4C}$ (dark purple), which was expected to insert into the bilayer; $(A•B)^{1C}$ (grey), which was expected only to tether to the membrane; and $(A•B)^{\Delta C}$ (black), which was expected to have no interaction with the membrane.

The spectra for A•B and the control $(A•B)^{4C}$ demonstrate positive peaks at 259 nm. A positive peak at the DNA absorption wavelength indicated that the bases were parallel to the direction of orientation and perpendicular to the membrane normal. As the bases are perpendicular to the direction of the double helix, this indicates that A•B is perpendicular to the membrane.[135,326] This also explains the negative peak over 260 nm for $(A•B)^{1C}$, which was expected to only tether and be oriented parallel to the membrane. However, as indicated by the calculated Cy3-Cy5 distances, the dyes are further apart for the tethered pore than for the spanning pore, which mean that the pore has expanded creating a variety of different angles to the membrane. This may explain the large very broad flat peak. $(A•B)^{\Delta C}$ resulted in a very flat trace, which was expected as it has no membrane interaction.

Conversely, the peak at 260 nm for A•B and the control $(A•B)^{4C}$ were comparatively very sharp and narrow. It was possible that scattering was the cause of the apparent peak at 234 nm in the A•B spectra and at 237 nm in the $(A•B)^{4C}$, which may have overlain part of the peak at 259 nm. Vesicle scattering is a well-documented problem for LD, especially below 250 nm.[323,324,326] The broad peak stretching from approximately 280-340 nm, however, was unlikely to be caused by scattering and cannot be readily explained. It does not appear in the spectra from either Lundberg *et al.* or Banchelli *et al.*, which tend to 0 over this region; however, in both cases, simple DNA duplex were assessed compared to the more complex 4HB nanopores assessed here. In addition, another key difference is that those duplexes were tethered to the membrane via a single cholesterol lipid anchor, while A•B carries two cholesterol lipid anchors on either side of the pore (the control $(A•B)^{4C}$ carries four) and was expected to span the bilayer. Furthermore, DNA nanopores with cholesterol lipid anchors are

known to result in toroidal membrane pores.[118,126] The possible effect of these pores on the LD spectra is unknown. While the spectra for A•B and (A•B)[4C] were very similar, it was unclear why A•B resulted in a stronger signal. Additionally, the spectra represent an ensemble average of the states that are present in the system, including pores that are perpendicular and parallel to the membrane. The stronger signal may indicate that A•B had more pores oriented perpendicularly. If this was the case, it may indicate that two cholesterols tethered to the membrane requires an additional energy input in order to achieve insertion. An alternative explanation could be related to pore stacking on the surface of the membrane.[131] This would stabilise the pore parallel to the membrane. Nevertheless, there were cases for both A•B and (A•B)[4C] where the spectra resembled that of (A•B)[1C] indicating that both states were likely present; however, the shear-flow orientation process may have also had an effect.

The aim of the LD experiments was to ascertain the relative orientation of A•B on the membrane only, so quantitative analysis was not undertaken. The approximate angle of each of the four duplexes was unknown nor were they expected to be homogeneous. In addition, it was unclear what effect the toroidal pore would have on the LD spectra. It would be of interest in the future to investigate a DNA nanopore using LD as it does provide valuable insight into interactions with the membrane. For A•B, the LD measurements indicate a perpendicular orientation when at least two cholesterol lipid anchors are present. A perpendicular orientation could only be achieved by A•B in a membrane spanning orientation. The pore was designed such that maximum cholesterol hydrophobic burying in the membrane would necessarily position the pore in a transmembrane orientation. While when only one cholesterol anchor was present, (A•B)[1C] adopts a membrane tethered orientation parallel to the membrane as there was no cholesterol opposite to allow for pore insertion. This understanding was then used to guide molecular dynamics simulations.

5.2.6. Molecular Dynamics Simulations

To aid this investigation, molecular dynamics simulations were conducted on the monomer component, A, and the pore, A•B, in solution and when tethered or spanning the membrane. First, root-mean squared fluctuation (RMSF) analysis was conducted to assess how the structure of A and A•B differ (a) from the idealised structure and (b) how the membrane affects the structure. The results are displayed pictographically in Figure 65 and the data itself is shown in Figure 66. It is important to note that the simulations performed in solution used A•B and not (A•B)[ΔC]; however, this is unlikely to affect the pores behaviour significantly as the pores were not simulated to aggregate, which would be the major influence of the lipid anchor.
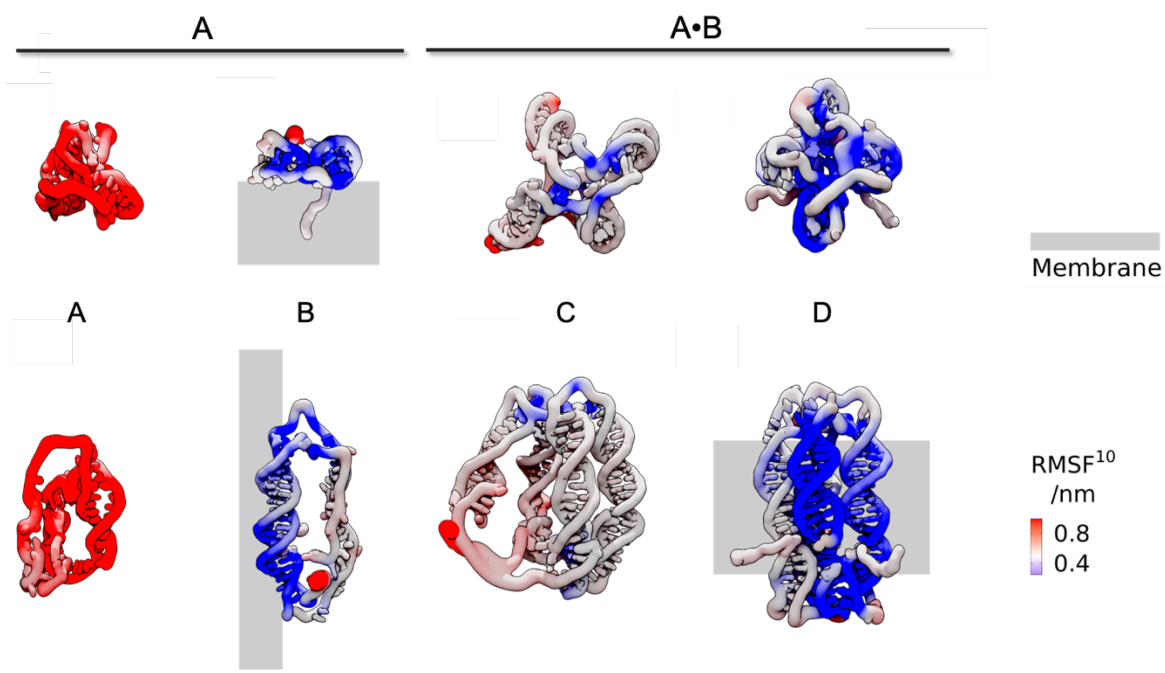
Figure 65. Top-down and side-on views of representative structures from simulated trajectories for the monomer component, A, in solution (A) and tethered to a membrane (B) and the nanopore, A•B, in solution (C) and spanning a membrane (D). The membrane was simulated as a POPC bilayer (represented by a grey bar). The colour of the structure is representative of their per-residue $RMSF^{10}$ to indicate structural flexibility (red=high, blue=low).
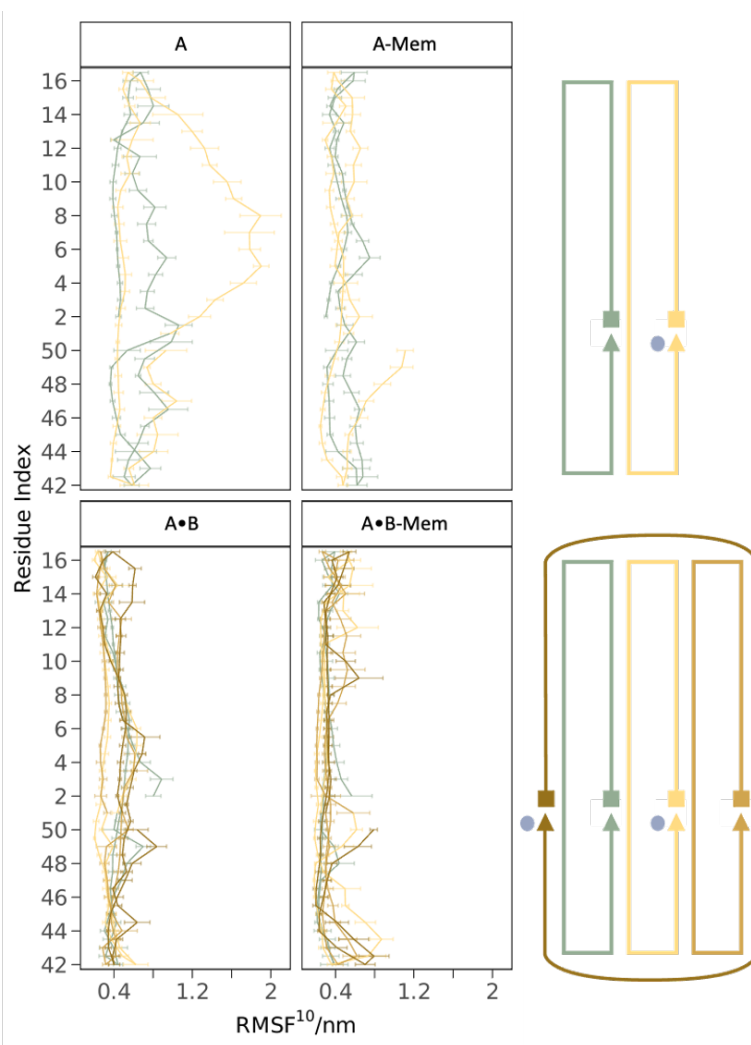
Figure 66. Per residue RMSF[10] values and standard deviations plotted against the residue index for each of the four simulated trajectories. Top: A and A-bound to the membrane. Bottom: A•B and A•B spanning the membrane. The residue index has been ordered to match the associated strand map (Top: A; Bottom: A•B). Squares represent the 5' and triangles the 3' end of each DNA strand. The grey circle indicates a cholesterol modification attached to the 3' end of the DNA strand via tri(ethylene glycol) (TEG) linker.

A in solution demonstrates significantly higher variability than any of the other conditions. This was expected, because, as has been previously discussed, the three ssDNA regions are unstructured and are, therefore, likely to adopt a wide variety of structures. Indeed, looking at Fig. 66 it is clear that the variability of the ssDNA arms has an RMSF of nearly 2 nm. Even the loop fluctuates by nearly 1 nm compared to the central helix, which is comparatively extremely rigid. Looking at the structure of A (solution) in Fig. 65 it was easy to see the effect of the highly contorted structure on the binding strength and kinetics. While a high degree of variation was observed, the arms and loop were also generally bound and contorted into a structure that made them significantly less available for binding. However, the low variation of the central duplex also implied that as soon as one of the arms (or the

loop) underwent hybridisation the structure would become significantly more rigid, and the other arm(s) and loop would be more available for hybridisation. This suggested that the initial supposition that the intra-structural hybridisation steps would be fast was likely correct.

The addition of the bilayer significantly stabilised A, and it adopted a structure more similar to the anticipated idealised structure. The membrane appeared to stabilise the duplex significantly, which rather than an RMSF of 0.6-0.8 had an RMSF of 0.2-0.4. This appeared to be partly due to sterics (the duplex now adopted a rigid rod conformation rather than bending at the nick as it did in solution) and partly due to adsorption to the surface. Indeed, the top-down view in Fig. 65B suggested that the duplex, arms and loop were all adsorbed to the surface. It is important to note that the simulations were conducted in high salt conditions (1 M KCl, the same conditions used for the model system). The high salt conditions mask the negatively charged DNA phosphate backbone allowing the different strand regions to interact more closely and also increases interactions with the zwitterionic membrane. The FRET assembly and kinetics experiments were conducted in lower salt conditions using 300 mM KCl instead, therefore, this effect may have been less prevalent. Nevertheless, the effect of the membrane may help explain why the K_d for A-SUV vs B$^{\Delta C}$ was as comparable to A$^{\Delta C}$ vs B$^{\Delta C}$ in the absence of the membrane. While the membrane presents a steric hinderance, it also significantly ordered the structure. This likely had a more significant effect for A-SUV vs B binding as the two species can only interact side-on as both are bound to the membrane. The increased structural order likely helped to compensate for the steric effect of the membrane. Nevertheless, it was also clear how this would impact the kinetics. While the increased order reduced the number of conformations and subsequent intra-structural interactions, adsorption to the membrane meant that the rate of interaction would be significantly reduced, as was evident from the lower kinetics for A-SUV vs B$^{\Delta C}$ and A-SUV vs B.

In general, A•B was more stable in solution and had less structural variation than the monomer A. This was expected considering the lack of ssDNA regions (excluding the poly-T loops) and the presence of a continuous structure. The addition of the membrane also had a more muted effect than for the monomer. Nevertheless, a comparison of the top-down views in Figure 65C and D indicated different pore diameters in solution compared to when the pore was inserted in the membrane corroborating the Cy3-Cy5 distances. The fluorophores were located at the 5' end of the non-cholesterol modified duplex. Figure 65A and Figure 65C indicated that the duplexes of both A and A•B were flexible at the nick. Figure 65A indicated a sharp angle for the unsupported duplex of the monomer. It was also clear from Figure 66 that the strand termini generally experienced the highest fluctuations. This suggested that some unzipping at the strand termini may occur, which would further increase the Cy3-Cy5 distance. This may be partly responsible for the large error associated with the value for E and subsequent Cy3-Cy5 distance calculated for A$^{\Delta C}$ vs B$^{\Delta C}$. However, this does not appear to be limited to solution. The strand termini for A•B in the membrane

(Fig. 66) also appear to fluctuate significantly, especially compared the increased stability of the rest of the pore. For the strands with a cholesterol lipid anchor this may be due to the cholesterol pulling those strands towards the bilayer; however, fluctuations for the non-cholesterol modified strands are also apparent. If unzipping at the termini is indeed present, this may help account for the larger than expected Cy3-Cy5 values predicted from the FRET efficiencies.

If the degree of monomer adsorption to the membrane surface was comparable for $(A \bullet B)^{1C}$ this may have resulted in increased Cy3-Cy5 separation in analogy to swelling in solution. The conformation adopted by A on the membrane surface indicated that the location of the fluorophores on the duplex flanking the cholesterol lipid anchors would likely result in structural flattening to maximise interactions with the membrane. Surface adsorption may also be affected by temperature, which could explain the different FRET efficiencies observed from binding and kinetics experiments. The components were incubated at 30 °C for 30 min before being scanned while the kinetics assays were conducted at r.t. (which in January was approximately 18 °C). It was likely that more surface interactions would be observed at lower temperatures and the absorption to the surface may result in a slight reduction into Cy3-Cy5 distance resulting in a higher FRET efficiency. This may explain the similar Cy3-Cy5 distance calculated for $(A \bullet B)^{\Delta C}$ and $(A \bullet B)^{1C}$-SUV in the binding assays.

The most notable observation from these simulations was the significantly enhanced rigidity of the pore in the membrane. This structure was much closer to the ideal confirmation of the nanopore. In comparison, the structure of A•B in solution cannot accurately be considered a pore. Indeed, the close inter-duplex geometry induced by the membrane was critical for pore channel function. An examination of A•B in solution and A•B in the membrane made it relatively straightforward to determine the cause of the shorter Cy3-Cy5 distance calculated for A•B-SUV. The average idealised structure began with a diameter of ~5.4 nm at the nick, which was slightly larger than the pore from Göpfrich *et al*. From Figure 66, the average RMSF around the nick for A•B in solution was ~0.5 nm. The additional 0.5 nm to each duplex would account for the calculated Cy3-Cy5 distances of ~6.4 nm for $(A \bullet B)\Delta C$ (Table 5). Comparatively, the average RMSF around the nick for A•B in the membrane falls to ~0.25, which again, accounts for the calculated Cy3-Cy5 distances for A•B in the membrane of 5.7-6 (Table 5). Indeed, these values were in remarkably good agreement with the calculated Cy3-Cy5 distances. Furthermore, this also corroborated the finding that an R_0 of 5.2 or 5.6 nm was a better fit for the data than 6 nm based on the calculation of the Cy3-Cy5 distance for $R \bullet S_{NP}$.

In solution, the cholesterol lipid anchors appeared to retreat into the pore structure and interact with the hydrophobic core of the duplex. The open structure in solution, posed the risk that the cholesterol lipid anchor may not be as available for insertion into the bilayer as anticipated. This was unlikely to be the case upon direct contact with the membrane; however, the method of insertion

postulated by Birkholz *et al.*[131] indicated the pore first tethered parallel to the membrane before interaction of the other lipid anchor pulled the pore perpendicular into a transmembrane orientation. If the anchor was buried, this would likely slow the rate of pore insertion. Furthermore, it was possible that assembly of A•B from A and B made this more likely as the anchor had more degrees of freedom on the monomer. Nevertheless, this was unlikely to be a factor when A and B assembled on the surface of the membrane as both cholesterol anchors would already be buried in the membrane. However, it should be noted that the anchors in Figure 65C appeared to have rotated to an inter-duplex location rather than being on the edge of the duplex. In addition, they were both on the same relative side of the pore. This may make it more favourable for both anchors to insert in the membrane without adopting a transmembrane orientation. Nevertheless, this was always a risk when only two anchors were used.

The next simulation investigated the effect of the pore and cholesterol lipid anchors on the membrane itself (Fig. 67A & B). A tethered to the membrane was used as a control (Fig. 67C & D). The snapshot in Figure 67A confirmed the formation of the toroidal pore.[118,126,327] A snapshot of the initial parameters (Fig. 67A, inset) shows the pore and membrane in their ideal initialised states and the toroidal membrane pore is absent. A toroidal pore forms to maximise hydrophobic burying of the hydrophobic lipid chains and the electrostatic interactions between the charged phosphate DNA backbone and the zwitterionic lipid headgroups. The toroidal pore connects the upper and lower bilayer leaflets to create an uninterrupted continuous bilayer with a water filled pore stabilised by the charged DNA nanopore and cholesterol anchors. In addition, the formation of the toroidal lipid pore positions the cholesterol lipid anchors in their preferred orientation parallel to the lipid chains.[20] The formation of the toroidal pore and the remodelling of the membrane results in the cholesterol adopting a more contracted position relative to A•B. This can be seen from Figure 67A (and inset) but is more clearly indicated in Figure 67B. The contraction of the cholesterol lipid anchor was also observed in the simulations by Ohmann *et al.*[126] who also employ a 4HB with two cholesterol lipid anchors. The formation of the toroidal lipid pore also results in the expected contraction of the membrane to maximise points of contact between the lipid headgroups and the pore while positioning the cholesterol lipid anchor in the center of the bilayer leaflets. The contraction of the cholesterol lipid anchor and the membrane as well as the formation of a toroidal pore was also observed in the simulations by Ohmann *et al.*[126] who also employ a 4HB with two cholesterol lipid anchors.
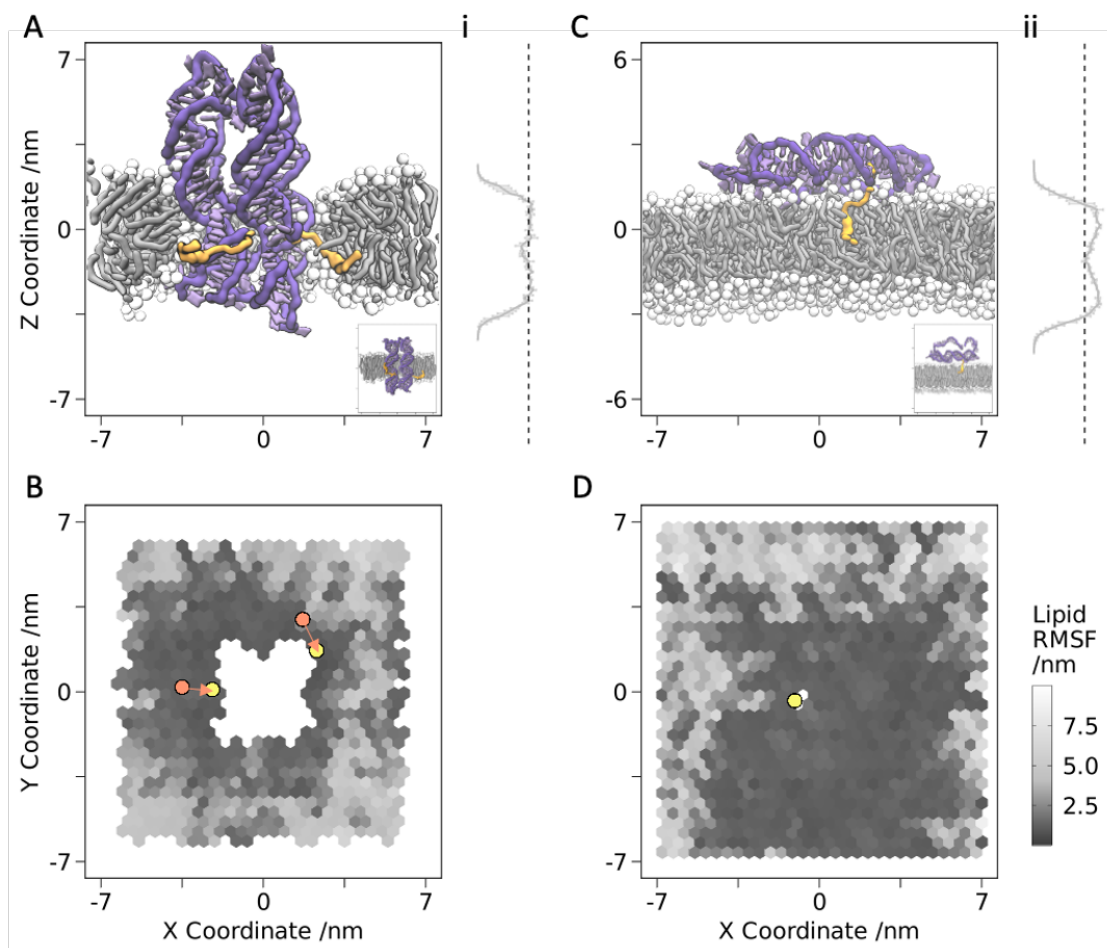
Figure 67. Representative snapshots of the equilibrated regions of the membrane bound A•B (A) and A (C) trajectories. The insets show the initial configurations. The DNA is coloured purple and cholesterol modified residues are gold. The headgroups of the POPC bilayer are shown in white and the lipid tails are shown in grey. The bilayer density from the A•B (i) and A (ii) trajectories are plotted at the right of each snapshot, with a dashed line indicating 0.425 g/mol/A³. Top-down views of the POPC bilayer for the transmembrane A•B (B) and membrane tethered A (D), with the DNA omitted for clarity. The hexagons represent the per molecule lipid RMSF (black = low, white = high). The locations of the cholesterol lipid anchors are shown for the start (orange) and end (yellow) of the trajectory.

In contrast to the significant effects on the bilayer that result from insertion of A•B, the tethering of A has a more muted effect on the bilayer. The only notable effect was that A flattens against the membrane, presumably to maximise the electrostatic interactions with the lipid headgroups. This was previously noted in Figure 65B. The high RMSF of the lipid headgroups observed in Figures 67B and D are likely artifacts due to the effect of the boundary conditions imposed on the simulations.

5.2.7. Molecular Transport

Following the investigation into, and confirmation of, pore assembly, it was necessary to investigate the ability of A•B to function as a pore. To assess this functionality, a dye flux assay was used.[15,118] The principle of this assay relies on the fact that at high concentrations (50 mM), the fluorophore sulforhodamine B (SRB) is contact-quenched resulting in low fluorescence emission. Thus, if SRB is encapsulated in lipid vesicles, transport across the lipid bilayer will abolish contact-quenching resulting in a large increase in fluorescence intensity. As SRB has a net charge of -1, it cannot traverse the membrane on its own. SRB transport has been previously demonstrated through DNA nanopores;[15,115,125] however, those pores were larger 6HB with lumens ~2 nm in diameter, while A•B was a 4HB with a lumen ~0.8-1 nm. SRB is ~0.7 nm in diameter[115] so transport through A•B was anticipated, but with reduced transport properties. There was, however, a chance that the similarity in pore and SRB diameter would result in pore blockage, which may reduce observed transport.

Before transport was assessed, it was necessary to confirm encapsulation. SUVs composed of DPhPC were used in place of the 7:3 mole mixture of DOPC and DOPE lipids previously used in the literature.[15,115,118,125] DLS was again unavailable due to COVID-19 restrictions, but the SUVs were extruded through 100 nm polycarbonate membranes and so were expected to be of a similar size to previously characterised SUVs and a diameter of 122 nm (7.22 nM) was assumed (as in Section 5.2.4.). Following purification, the SUVs were then assessed to confirm successful encapsulation by scanning before and after addition of Triton X-100 (TX-100, Fig. 68A). Low emission intensity was observed for the SUVs with encapsulated SRB, but upon addition of TX-100 emission increased 10-fold indicating dye release and, therefore, successful encapsulation.

The transport properties of A•B formed from A+B were assessed. It was also of interest to monitor the effect of the locks and the unlocking mechanism on dye transport. Due to the slow rate of pore assembly, the high nanopore concentrations required and the low overall extent of release, it was not possible to assess release from A•B formed by pore assembly directly on the membrane. Instead, the components (or the locked components plus the keys) were mixed together, incubated for 30 min and then added to the vesicles. The key results are shown in Figure 68B.
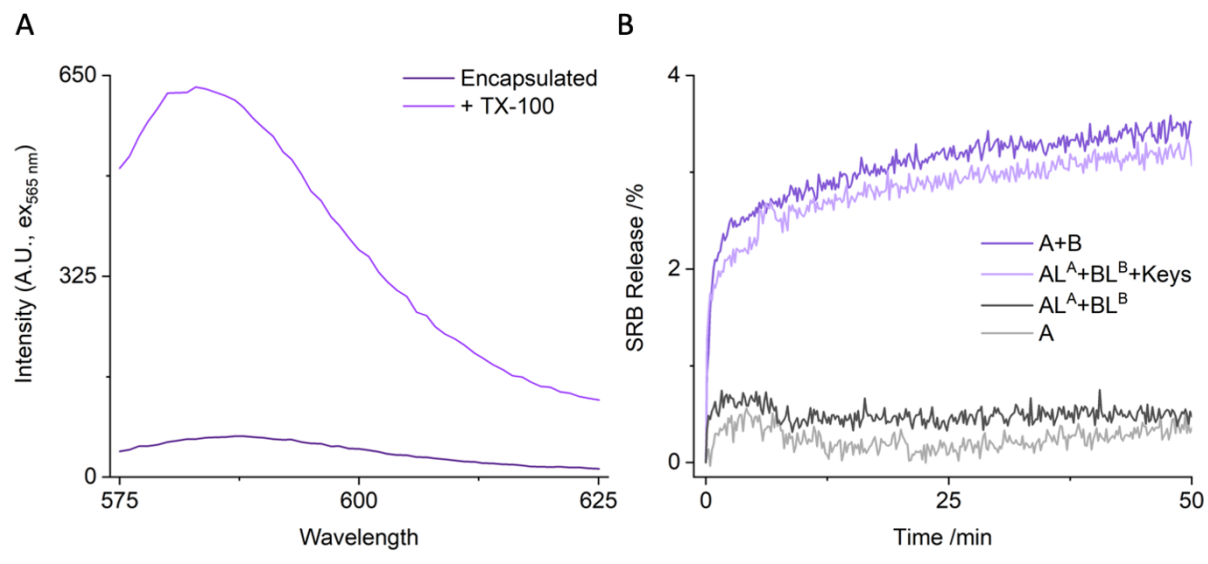
Figure 68. (A) Fluorescence scan of purified small unilamellar vesicles (SUVs) with encapsulated fluorophore: sulforhodamine B (SRB). At 50 mM the dye is contact quenched inside the vesicle and due to its charge of -1 it cannot traverse the lipid membrane resulting in low fluorescence emission. Upon addition of the detergent, TX-100, the vesicles are lysed releasing the SRB into the ambient. Contact-quenching is eliminated resulting in a strong 10-fold increase in the intensity of SRB's fluorescence emission (B) Kinetic fluorescence traces of SRB dye transport from SUVs in the presence of the nanopore components (black and grey) or formed pores (light and dark purple). In each, dye flux was assayed at 400 nM. Neither the membrane-tethered component: A, nor the locked AL^A and BL^B, span the membrane and no significant dye flux is observed. Only when both components are present, or upon addition of the keys. can the membrane-spanning active pore (A•B) form and initiate transport. As the dye flows into the ambient, the concentration is lowered, which abolishes contact-quenching and results in an increase in fluorescence intensity. 100% release was obtained by addition of TX-100 to rupture the vesicles and release all encapsulated dye into the ambient. Each trace is an average of three independent repeats.

SRB transport was successfully achieved upon addition of A+B (3.57 $\pm$ 0.14%). In addition, comparable transport was also achieved from AL^A+BL^B + keys (3.33 $\pm$ 0.26%) corroborating the results from gel electrophoresis and indicating that the unlocking mechanism has no significant effect on the ability of the pore to transport molecular cargo. In contrast, the efficacy of the locking mechanism was reconfirmed. In the absence of keys, the locked AL^A+BL^B resulted in net release of only 0.47 $\pm$ 0.3%, which was comparable to the release generated by buffer (0.81 $\pm$ 0.27%, Fig. 69C, light grey). For comparison, addition of A on its own also resulted in minimal dye transport (0.43 $\pm$ 0.5%), as expected. Indeed, the component controls resulted in less release than the buffer only control. Some fluorophore leakage is almost always observed when vesicles are monitored on their own over time. However, leakage is significantly reduced when negatively charged DNA is tethered to the surface or a negatively charged lipid, such as DOPG, is used. Considering that leakage is

reduced in both conditions, it is likely that electrostatic repulsion reduces vesicle-vesicle interactions that may result in the escape of some dye to the ambient. Dye leakage is also reduced when the internal and external solutions are properly osmotically balanced.

To gain a more thorough understanding of the dye transport properties of A•B, dye flux was also assessed for A+B and AL^A+BL^B at 200 nM as well as from pre-folded A•B. The traces for each of these three conditions are shown in Figure 69A-C. The resultant net fluorescence for each of the three conditions at each concentration were summarised in a bar chart in Figure 69D.
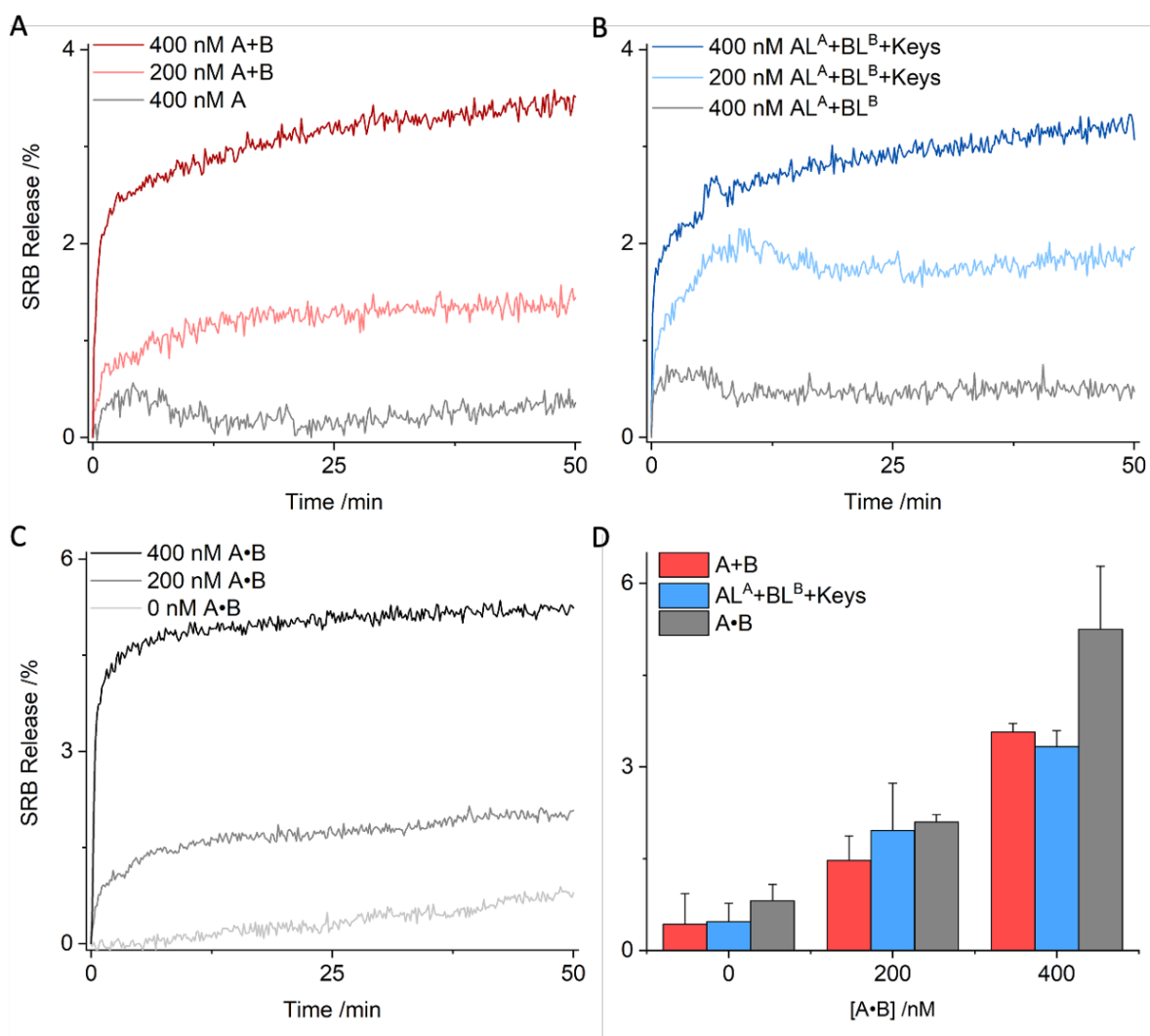
Figure 69. A•B concentration dependent SRB release from SUVs. Concentration dependence when A•B was formed from unlocked components A+B (A), from locked components AL^A+BL^B upon addition of keys (B) and when A•B was pre-folded (C). (D) Bar chart of net fluorescence increase summarising the results from (A)-(C). 0 nM A•B represents the controls: 400 nM A only (red), 400 nM (AL^A+BL^B) (blue) and buffer (grey). The data represent averages and standard deviations from three independent repeats.

The release obtained for A•B formed under each of the three conditions was highly comparable and generally within error. However, pre-folded A•B at 400 nM resulted in release of 5.25 ± 1.03%, which was nearly 2% more net release than either A+B and AL^A+BL^B+keys -- an increase of 47% from A+B and 58% from AL^A+BL^B+keys. This was a slightly surprising result given the similarity at 200 nM. The only significant difference at 200 nM was the slightly odd behaviour of the AL^A+BL^B+keys trace, which was not a smooth curve like the others. The A•B:SUV loading at 200 nM was 415:1, which was a higher A•B:SUV loading than was used previously for any of the binding or kinetic assays; however, 200 nM was demonstrated to be a successful nanopore concentration for monitoring dye transport through a 6HB nanopore.[15] However, at 400 nM the loading was 830:1, which while high, still represented a lipid:pore ratio of 166.67:1 and remained below the theoretical maximum A•B:SUV loading of 1200:1. Nevertheless, it was possible that at such high A•B:SUV loadings the effect of unbound components may have an observable steric effect. Even in solution, the binding titrations and kinetic assembly (Section 5.2.4.), indicated a yield of ~95%. In addition, it was possible that not all pores were fully assembled before addition to the system. At such high concentrations and A•B:SUV loadings the reduced mobility on the membrane surface due to steric effects may further reduce the chances of the remaining unbound components assembling. Furthermore, any unbound tethered component monomers would increase steric hindrance on the surface as well as electrostatic repulsion, which may have limited the number of pores able to insert into the membrane. This effect would not have been observed for pre-folded A•B. However, additional experiments and modelling would be required to assess this. Due to the 10-fold increase in fluorescence observed upon lysis, it was not possible to significantly increase SUV concentration. In addition, the low overall extent of release at the lower 200 nM concentration of A•B, and in general, would have necessitated prohibitively high A•B concentrations, without any gain in the A•B:SUV loading.

As expected, the dye transport capabilities of the 4HB A•B were inferior compared to the 6HB pNP assessed in Chapter 6 (Section 6.3.6.). At 400 nM, 5.25 ± 1.05% represents a 60% reduction from the 13.12 ± 0.47% release achieved by pNP at 400 nM. The 3.57 ± 0.14% generated by A+B represents a 73% reduction. However, considering the significant difference in the size of the respective lumen, this was anticipated. At 2 nm, the lumen of the pNP is ~4x larger than that of A•B and can accommodate two SRB end-to-end with nearly space enough for a third. In contrast, the 0.8-1 nm lumen of A•B is barely able to accommodate one. The near overlap of the size of SRB and the lumen of A•B means that A•B may be prone to fouling by SRB. The fact that the size of the lumen approached the size of small molecules makes A•B less well suited for molecular transport than larger pores. Nevertheless, the SRB transport assay was sufficient to probe the transport properties of A•B formed under the three conditions and was able to successfully demonstrate pore activity resulting from monomer assembly.

5.2.8. Ion Channel Activity and Lumen Analysis

Pore activity confirmed, the capacity of A•B to function as an ion channel was then investigated. This was first probed using single-channel current recordings (SCCR)[118] to assay the ability of A•B to allow a current of solvated K^+ to flux across a membrane and characterise the channel lumen. SCCR is a powerful technique because it allows label-free activity to be monitored from an individual pore. This allows the behaviour of the channel to be investigated, such as its unitary and voltage-dependent conductance.[102,114,115,118,119,123,127]
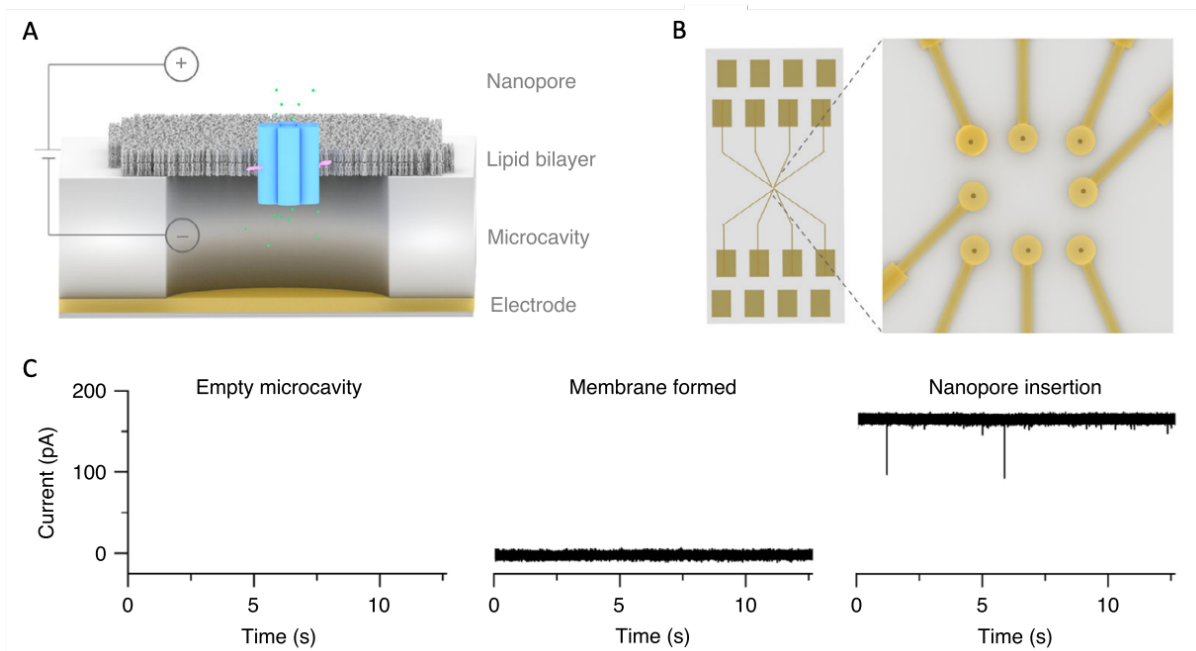
Figure 70. Single-channel current analysis of a representative 6HB DNA nanopore using planar lipid bilayer recordings. (A) Schematic illustration of a 6HB DNA nanopore (blue) embedded in a planar lipid bilayer (grey) formed over a microcavity on a MECA16 chip (B). The two electrolytic chambers are indicated by the positive and negative ends of the cell. (C) Current recordings obtained from an empty cavity (left), a cavity with a DPhPC planar lipid bilayer spanning the cavity (middle), and a DNA nanopore spanning the bilayer (right). Adapted from Lanphere *et al.*.[118]

To obtain SCCR measurements, a planar lipid bilayer is formed over a small aperture, which separates two chambers that are filled with electrolyte (Fig. 70A).[118] In this case, 1 M KCl, 10 mM HEPES, pH 7.4 was used, which is a common electrolytic buffer that facilitates comparison between different nanopores.[102,115,118] A potential is then applied across the membrane to induce the flow of electrolyte ions; however as the membrane is impermeable to ions, no current is observed (Fig. 70C, middle).[115] Nanopore insertion can then be monitored via the resultant current as the ions are able to flux across the membrane through the pore (Fig. 70C, right). As DNA nanopores do not insert efficiently into planar lipid bilayers,[11] they are often added with a mild detergent (such as OPOE) in

a 2:1 pore:detergent ratio to improve the rate of insertion.[118] The current-voltage relationship can then be investigated by measuring the current at different positive and negative voltages. This in turn allows the behaviour of the pore to be characterised. For example, a symmetrical pore, such as A•B, is anticipated to display a linear current-voltage relationship, known as ohmic behaviour.[42,55,115,116,119,123,127,130,328,329] The slope of this relationship can then be used to calculate the pore conductance.[118] If the predicted or actual dimensions of the pore are known then this can be compared to the theoretical conductance using Equation (11):

$$G = \kappa \frac{\pi d^2}{4L + \pi d} \qquad (11)$$

κ = the electrical conductivity (equal to 10.86 Sm^{-1} for 1 M KCl at 25 °C), d = pore diameter and L = pore length.[118]

Using an anticipated lumen diameter of 0.8 or 1 nm and a pore height of 7.5 nm, the theoretical conductance was calculated as 0.67 or 1.03 nS for pore diameters of 0.8 and 1 nm, respectively. The results for single-channel current recordings from A•B are summarised in Figure 71.

Single-channel current analysis revealed that A•B formed stable transmembrane channels. Figure 71A shows an example trace with an observed current of -54.0 pA at a membrane potential of -50 mV. In addition, investigation of the current-voltage relationship at different membrane potentials revealed the expected linear-ohmic behaviour (Fig. 71B). This was also observed for the 6HB from Burns *et al.*[115] with the same architecture; however, NP-O, which has two ssDNA loops extending form the top of the pore (analogous to pNP from Chapter 6) shows non-ohmic behaviour and gating at high positive potentials, which likely drives the loops together blocking the lumen. The corresponding conductance distribution from 17 independent A•B insertions revealed an average conductance of 0.70 ± 0.27 nS (Fig. 71C). This was consistent with a small pore lumen. For comparison, the 4HB from Göpfrich *et al.*[127] has a comparable conductance of 0.47 nS, while the 6HB from Burns *et al.* had an average conductance of 1.62 ± 0.09 nS, which is consistent with the lumen of the 6HB being approximately 4x larger than the 4HB. In addition, a conductance of 0.7 nS was in excellent agreement with the theoretical conductance of 0.67 nS, which suggests the pore lumen was likely closer to 0.8 nm than 1 nm in diameter.
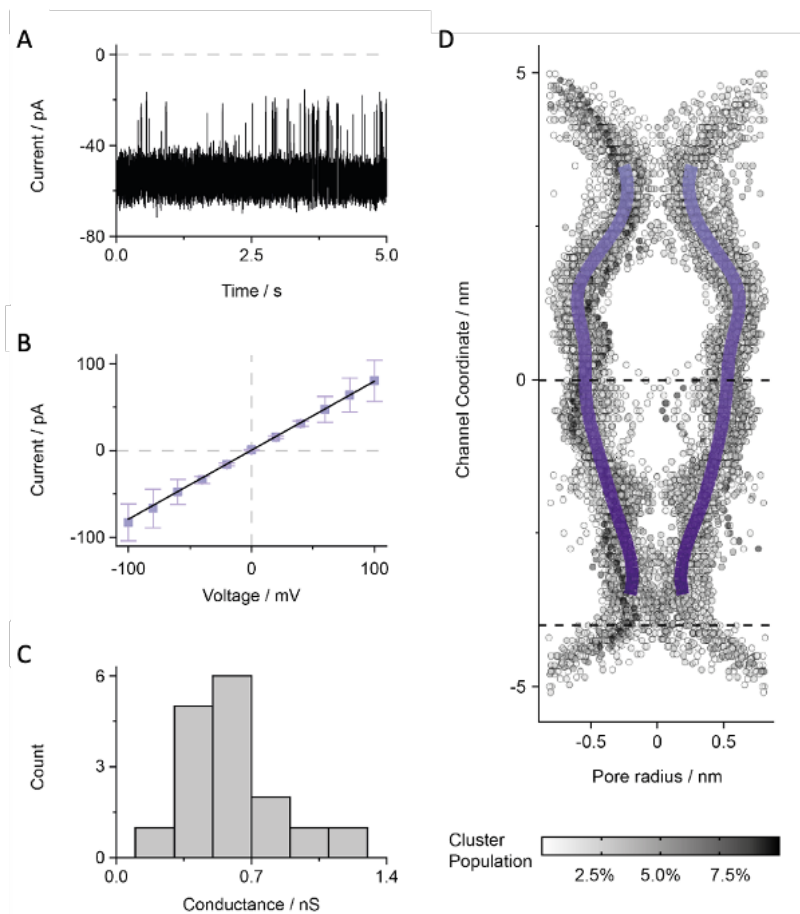
Figure 71. Characterisation of the A•B channel using single channel current recordings and molecular dynamics. (a) Representative ionic current traces from a single A•B nanopore inserted in a planar lipid bilayer composed of DPhPC lipids in 1 M KCl, 10 mM HEPES, pH 7.4 at a membrane potential of -50 mV. (b) IV curve for voltage ramp from -100 to 100 mV showing ohmic properties of the A•B channel and displaying averages ± SEM from 17 independent NP insertions. (c) Histogram of channel conductance obtained from 17 independent single-channel recordings at membrane potentials ranging from +20 mV to +50 mV. (d) Simulated mapping of the channel lumen using HOLE analysis on a series of clustered snapshots of the A•B channel in a POPC bilayer in 1 M KCl. The proportion of the trajectory represented by each cluster is indicated by the alpha, and a trend line has been plotted to estimate the average channel shape.

To further investigate the pore lumen and compliment this analysis, molecular dynamics simulations were used to model the channel lumen. The results are summarised in Figure 71D. These simulations revealed that the lumen has a highly non-uniform structure. The lumen narrows at both ends of the pore, which was expected as these are the only two locations where the duplexes are connected. The top and bottom of the pore have approximate lumen diameters of 0.6 and 0.4 nm, respectively; however, the trajectories imply significant variation ranging from contracted, extremely narrow nearly closed states to expanded states of over ~1.2 nm. This level of variation was present throughout the lumen which implied a dynamic structure. This corroborated the results of the RMSF

analysis from Figures 65 and 66, which indicated fluctuations of 0.2-0.6 nm for each duplex in the membrane. The portion of the pore outside the membrane, just below the top of the pore, had the widest diameter. This was also consistent with the significant swelling that was observed in solution from the RMSF analysis and the FRET efficiencies. The lower portion of the lumen, which would be the portion inserted in the bilayer, appeared much more constricted than the top half of the pore. This was consistent with the stabilising effect of the membrane observed previously. Indeed, the approximate location of the fluorophores on the pore had a lumen diameter of ~0.9 nm. If this was compared to the RMSF data in Figures 65 and 66 it clearly indicated that in solution, the same area of the pore transitioned from being one of the narrowest points to the widest. In solution, A•B had an RMSF ~0.25 nm larger than when in the membrane, which would result in a correspondingly ~0.5 nm larger pore lumen. The difference of ~0.5 was also consistent with the 0.41-0.44 nm difference between the Cy3-Cy5 distances of $(A•B)^{ΔC}$ and A•B-SUV.

The small lumen diameters indicated by SCCR and lumen analysis corroborate the finding from the SRB dye flux assay that A•B is poorly suited for molecular transport; however, the dimensions of the pore recommend it as an ion channel. Indeed, single-channel current analysis already proved the capacity of A•B to function as an ion channel by measuring the current of ions through the pore across the membrane. However, SCCR measures the flux of ions in the presence of an applied potential. It was of interest to assess A•B's capacity for passive ion flux. Ca^{2+} was selected as an ideal candidate for ion transport as it does not feature in any commonly used buffers, a number of Ca^{2+} sensitive dyes exist and it has been previously used to assess ion transport.[329–338] In addition, Ca^{2+} is similar in size to K^+,[337,339] which was successfully transported using the SCCR assay. Of the various Ca^{2+} sensitive dyes, the ratiometric dye Fura-2 was selected. Fura-2 has among the highest K_d for Ca^{2+} at 134 nM,[333] it is relatively inexpensive, and has been previously used for Ca^{2+} influx into vesicles.[332,338] Fura-2 is a ratiometric dye with variable excitation wavelengths and a constant emission at 510 nm. At low Ca^{2+} concentrations, the excitation maximum is 380 nm. As the concentration of Ca^{2+} increases the excitation maximum shifts to 340 nm around the isosbestic point (360 nm).[340] Therefore, the Ca^{2+} concentration can be monitored via the 340/380 nm ratio.

The method for Ca^{2+} influx was adapted from Berendes *et al.*[338] and Hugonin *et al.*.[332] Fura-2 was encapsulated at 100 μM in SUVs composed of POPC. Following purification, it was necessary to confirm that Fura-2 had been successfully encapsulated and that the membrane was impermeable to Ca^{2+}. The SUVs were scanned on their own, in the presence of 250 μM $CaCl_2$ and following addition of TX-100 as a control (Fig. 72A). The 340/380 nm ratio for the SUVs in the absence of Ca^{2+} was 0.95. Addition of 250 μM $CaCl_2$ resulted in a slight shift of the excitation spectrum and a slight increase in the 340/380 nm ratio to 1.13; however, the increase was likely due to small quantities of Fura-2 bound to the surface of the vesicles that was not removed during purification.[332] Addition of TX-100 resulted in vesicle lysis and a significant shift in the excitation spectrum resulting in a

significant increase in the 340/380 nm ratio to 5.62, which was consistent with literature.[332] These results confirmed the successful encapsulation of the Fura-2 and the impermeability of the membrane to Ca^{2+} as well as Fura-2.

Following confirmation of encapsulation, SUVs were subjected to DLS (Fig. 72B). As an additional control, SUVs were assays on their own and in the presence of 250 μM Ca^{2+} to determine if the Ca^{2+} had any effect on the vesicles. DLS revealed an average diameter of 186 $\pm$ 9 nm for the SUVs on their own and 178 $\pm$ 10 nm with added Ca^{2+}. Vesicles were extruded 25 times through a 100 nm polycarbonate membrane, so these diameters were higher than expected; however, vesicles extruded through 100 nm membranes have previously had similarly high diameters (e.g., see Section 4.2.2.). However, these values were within error. The slight contraction in diameter upon addition of Ca^{2+} is consistent with Ca^{2+} induced membrane compression.[341–343]

Fura-2 successfully encapsulated, and vesicle characterisation confirmed, Ca^{2+} influx was then monitored at three (A•B)[4C] concentrations: 75, 38 and 25 nM to give A•B:SUV loadings of 97.3:1, 48.7:1 and 32.4:1. (A•B)[4C] was used instead of A•B to ensure a tight seal with the membrane to control for the possibility of Ca^{2+} flux through the toroidal pore rather than the lumen of A•B. The results for the influx assay are summarised in Figure 72C.
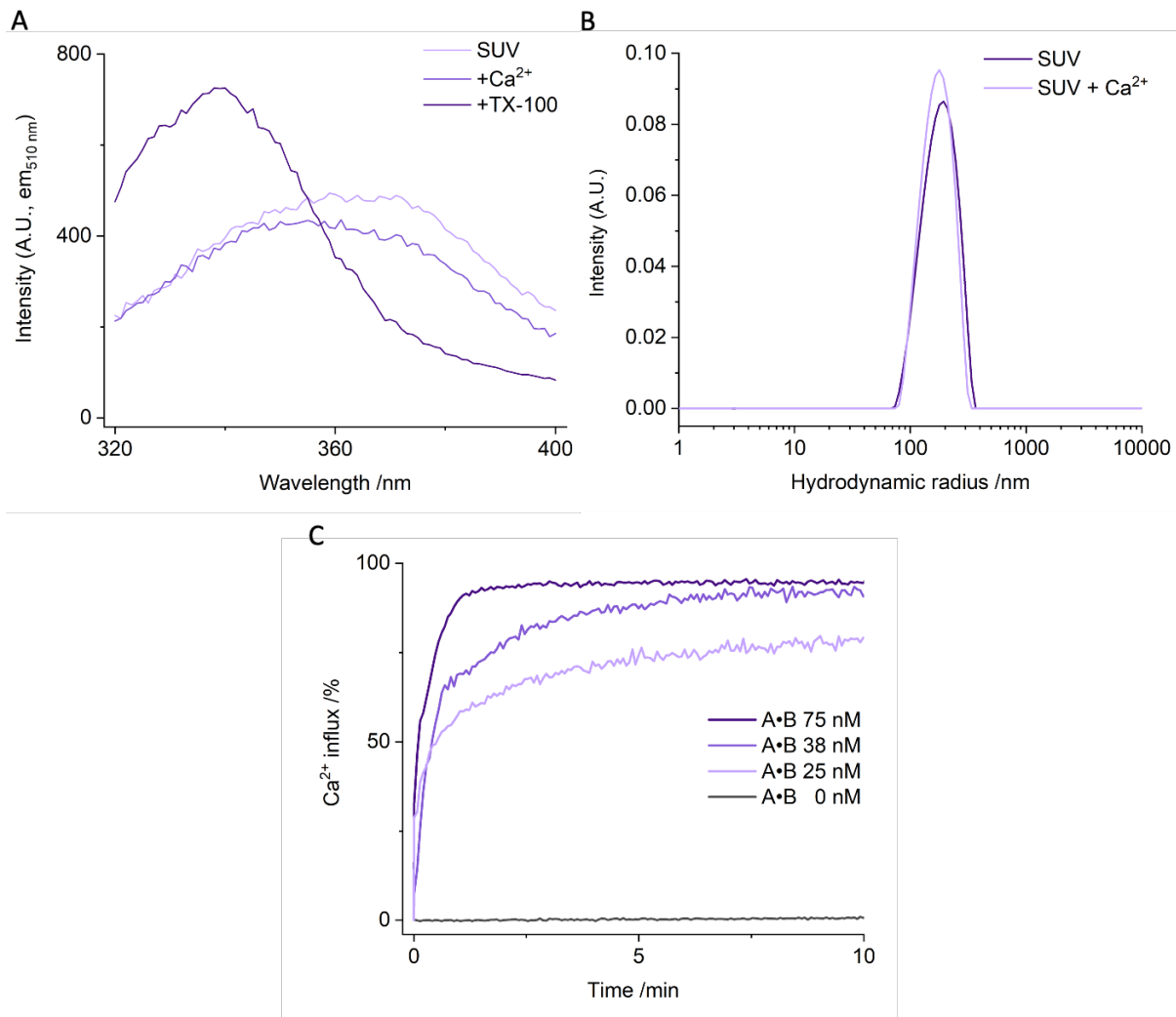
Figure 72. Ca^{2+} influx assay monitored via the ratiometric Ca^{2+} sensitive fluorophore, Fura-2. At low Ca^{2+} concentrations Fura-2 excites at 380 nm: however, as the concentration of Ca^{2+} increases, the excitation maximum shifts to 340 nm. The emission wavelength remains constant at 510 nm. Ca^{2+} binding can thus be assessed by monitoring the ratio of the excitation intensity at 340/380 nm. (A) Fluorescence scan of purified SUVs with encapsulated Fura-2 (100 μM) demonstrating the absence of Ca^{2+} in the vesicles and a low 340/380 ratio (0.95). Addition of 250 μM $CaCl_2$ results in a mild increase of the 340/380 ratio (1.13) consistent with some unpurified dye and confirms vesicles impermeability to both Fura-2 and Ca^{2+}. Upon addition of a detergent (Triton X-100), the vesicles are lysed removing the barrier between Fura-2 and Ca^{2+} and resulting in maximum binding indicated by a significant increase in the 340/380 ratio (5.62). (B) Dynamic light scattering analysis of vesicles formed from POPC with encapsulated Fura-2 (100 μM) in the absence and presence of Ca^{2+}. In the absence of Ca^{2+}, SUVs had an average diameter of 186 nm, while in the presence of Ca^{2+}, SUVs had an average diameter of 178 nm consistent with Ca^{2+} induced membrane compression. (C) Kinetic fluorescence traces of Ca^{2+} influx through $(A \cdot B)^{4C}$ to with Fura-2 encapsulated within SUVs. Efficient Ca^{2+} influx was observed at all three A•B concentrations: 75 nM (n=3), 38 nM (n=2), and 25 nM (n=1) indicating the pore is an effective ion channel even at low concentrations. Maximum

influx was recorded as the maximum amount of fluorescence observed following addition of detergent to rupture the vesicles.

The results demonstrated significant Ca^{2+} influx at all three concentrations of A•B. Indeed, 75 nM A•B achieved 90.3 ± 3.1% influx after only 70 seconds. Over the same period 38 nM achieved 70.0 ± 8.3% influx and 25 nM achieved 58.5%. After 10 min, 75, 38 and 25 nM achieved 95.0 ± 2.96%, 93.4 ± 2.17% and 79.2%, respectively. This was in stark contrast to the results from the SRB transport assays were, at 400 nM, A•B achieved 5.25 ± 1.03%, 3.57 ± 0.14% and 3.33 ± 0.26% release after 50 min for pre-folded A•B, A+B and AL^A+BL^B+keys, respectively. However, the two assays differed in two notable ways. SRB at 0.7 nm is 3x larger than Ca^{2+} at 0.23 nm.[339] Considering the simulations for the pore lumen (Fig. 28) indicated that the lumen could be as narrow as 0.2 nm, it was not surprising that SRB transport was slow and Ca^{2+} fast. In addition, transport of the negatively charged SRB through the highly negatively charged DNA lumen would be electrostatically unfavourable, which would only be exacerbated by the narrow lumen diameter. In contrast, Ca^{2+} is a divalent cation, which would interact favourably with the negatively charged phosphate backbone. Indeed, there was a risk of Ca^{2+} binding to the backbone; however, given the low concentration of Ca^{2+} compared to K^+, the Ca^{2+} would likely be displaced. However, in addition to the entropic favourability of SRB flux through the pore, SRB had a proximity advantage being encapsulated at 50 mM in SUVs, while Ca^{2+} was added at only 250 µM to pores that were 25-75 nM. Nevertheless, it was also likely that Ca^{2+} bound to the pores immediately upon A•B addition to the system and so were effectively transported to the vesicles, which would have a significant effect on the initial kinetics of transport considering that there are 200 negatively charged phosphates per A•B. However, addition of pores followed by Ca^{2+} resulted in nearly identical traces at 75 nM suggesting that this was likely not a significant effect on the observed timescale.

Unfortunately, due to COVID-19 restrictions, it was not possible to acquire the full dataset for the Ca^{2+} influx assay. It would have been of interest to assess Ca^{2+} influx from the pore assembled *in situ* from A+B as well as to gather the missing repeats for 38 nM (missing n=1) and 25 nM (missing n=2).

5.3. Conclusion

This chapter explored the design, assembly, characterisation and function of a four-helical bundle DNA nanopore (A•B) that can undergo triggered assembly from component monomers (A and B) in solution and on the surface of a membrane. A•B was based on the archetypal six-helix bundle (6HB) architecture form Burns *et al.,*[115] but with two of the duplexes removed and the nick shifted three nucleotides. A•B was split in half to generate two component monomers: A and B. A and B feature a central 21-bp DNA duplex, which is connected at the top and bottom by a 21-nt ssDNA

loop with a 4-nt poly-T spacer at either end. In addition, two ssDNA arms of 7- and 14-nt extend away from the top and bottom of the duplex, respectively. To assemble into the pore, the arms hybridise with the loop of the other component. For interactions with lipid bilayers, A and B can be functionalised with a cholesterol lipid anchor at the 3' end of strand A_2 or B_2, which is located two thirds of the way down the central helix. In addition, A and B can be fit with a 31-nt lock strand that hybridises with the arms of each component leaving a 10-nt toehold. The lock strands can be removed via a toehold strand displacement upon addition of a complementary 31-nt key.

The design of the monomer components and the folding and buffers conditions were optimised to achieve pore assembly in high yield from components A and B using gel electrophoresis. In addition, the locked components were successfully folded, and the locks successfully inhibited pore assembly, while the unlocking toehold mechanism was confirmed to function in high yield. Pore assembly over time monitored via PAGE indicated no difference in the rate of pore assembly from locked or unlocked components. UV thermal melts were also used to confirm structural stability and homogeneity between the pre-folded A•B and A•B assembled from component parts for $(A•B)^{\Delta C}$ in solution and A•B in the presence of SUVs. In addition, UV thermal melts indicated that A•B inserts into the lipid bilayer. Pore assembly on the membrane surface between a membrane tethered A and $B^{\Delta C}$ was confirmed using CLSM.

The biophysical properties of pore assembly were successfully derived. The binding properties of pore assembly were investigated using gel mobility shift assays and FRET fluorescence titrations. Very similar dissociation constants (K_d) in the nanomolar range were obtained for all the three conditions: $A^{\Delta C}$ vs $B^{\Delta C}$, A-SUV vs $B^{\Delta C}$, and A-SUV vs B. In addition, pore assembly between membrane tethered A and B was confirmed by investigation of the interaction between AL^A and BL^B on the membrane surface and by smFRET and single particle tracking. The kinetics of pore assembly were assessed using a pseudo-1st-order FRET assay and k_{on} successfully calculated for all three conditions. The dissociation rate constant, k_{off}, was derived for each of the three conditions using the determined K_d and k_{on}.

The FRET efficiency for each of the three conditions was calculated from the biophysical data. These values were used to confirm that pore assembly occurs in high yield whether in solution or on the surface of the membrane. In addition, the FRET efficiency was translated into a Cy3-Cy5 distance, which provided a good approximation for the difference in pore diameter in each of the three conditions. A difference in the Cy3-Cy5 distances between solution and membrane bound A•B indicated A•B insertion into the membrane. This was confirmed using linear dichroism.

Molecular dynamics (MD) simulations were performed to further probe the system and explore the biophysical data. The RMSF data for A and A•B in solution and on the membrane corroborated

the Cy3-Cy5 distances calculated from the experimentally derived FRET efficiencies and elucidated the effect of conformation and the membrane on the pore assembly. MD simulations also investigated the effect of the pore and monomer on the membrane. These simulations confirmed the formation of a toroidal lipid pore when A•B is inserted in the membrane and also that A has minimal effect on the membrane.

Molecular transport through A•B was confirmed using a sulforhodamine B (SRB) dye flux assay. In addition, comparable transport was achieved when A•B was assembled from A+B as well as from AL^A+BL^B+keys. Dye release from A•B assembled from monomers was lower than the pre-folded A•B at 400 nM, but comparable at 200 nM. The potential causes of difference were explored. In general, dye transport through A•B was low, which was in line with the small size of the pore.

The pore lumen was characterised using single-channel current recordings (SCCR) and MD simulations. SCCR confirmed the formation of stable pores in the membrane and confirmed a pore lumen of ~0.8 nm in diameter. The MD simulations of the channel lumen revealed a dynamic pore with a variable lumen that at its narrowest point contracts to yield a lumen of as small as 0.2 nm in diameter but can also expand to ~1 nm. A Ca^{2+} influx assay successfully demonstrated A•B ion channel activity by demonstrating significant influx at low concentrations. This result corroborated the findings from the MD lumen simulations and the SRB dye transport. The results indicate A•B is well suited for ion transport.

The DNA nanopore, A•B, demonstrated successful assembly from free component monomers as well as triggered assembly from locked components on the membrane surface. It was further demonstrated that A•B functions as a pore initiating molecular and ionic transport whether pre-folded or assembled from component parts.

5.4. Future Work

In the future, it would be of interest to complete the dataset for Ca^{2+} influx to demonstrate a larger concentration dependence as well as ion channel function following triggered assembly. The sensitivity of the Ca^{2+} influx assay was much better suited to studying the result of pore assembly on the membrane surface than the SRB dye flux assay. In addition, the sensitivity of this assay may allow partial deduction of the mechanism of insertion during or following assembly. Furthermore, it would be interesting to investigate the transport properties of different ions. This may be challenging to do as while there are fluorescent dyes that are sensitive to most ions, their K_d range significantly, which may impact the sensitivity of the technique.

In addition, it would be very interesting to thoroughly investigate the conformation of a DNA nanopore in a vesicle membrane using linear dichroism spectroscopy. Circular and linear dichroism spectroscopy are routinely employed to characterise protein and peptide pores in the membrane; however, they have never been used for DNA nanopores. The orientation of the pores in the membrane is key to their function and linear dichroism provides a relatively straightforward means of quickly assessing this. In the future, it would be useful to employ the sucrose technique deployed by Lundberg *et al.*[326] to reduce or eliminate vesicle scattering. Beyond characterizing the DNA nanopore, it would also be interesting the characterize the effect of the toroidal lipid pore on the LD spectra. This could be assessed by using two identical pores that differ only in the mode of insertion. One could carry a lipid anchor, which would cause a toroidal pore to form, while the other could use charge masking to mimic biological pore membrane insertion without disturbing the membrane structure.

In 2007, Kuzuya et al.[344] designed DNA nanotubes from half-tubes, which is conceptually similar to the work undertaken in this chapter. They postulate that one of the benefits would be to functionalise the interior of the half-tubes with therapeutic cargo. This is more realistic with the system designed here as assembly takes place on the membrane surface. This would be interesting to investigate as it could be designed so that the cargo is released upon pore assembly or bilayer spanning.

Furthermore, it would be interesting to impart an environmental control on pore assembly. It should be relatively straightforward to functionalise the lock strands with aptamer functionality so that the components are only unlocked at their target destination. This would be analogous to the adaptation of the lid functionality from the ligand-gated nanopore from Burns *et al.*[115] to the protein gated pore from Lanphere *et al.*[15] (explored in Chapter 6).

The pore could also be designed in a few different ways. For example, instead of assembly from two components to form an active pore, the pore could be formed by a barrel closing mechanism using a linear structure. It would also be of interest to explore a larger pore. A version for a 6HB could be fairly easily adapted A hybrid designed pore could also be very effective with a 6HB. Imparting more rigidity to the main backbone of the components would likely improve the kinetics of assembly.

Finally, the system as currently designed is unsuitable for use in a biological environment. The ssDNA regions make the components, in particular, very susceptible to exonuclease digestion. In addition, a larger pore would likely have better pharmacokinetic properties. However, this pore is well suited to use as part of a model system. It would be very interesting to use this pore as part of a synthetic model cell.

6. DNA nanopore with protein-gate featuring DNA aptamer functionality

6.1. Introduction

6.1.1. Thrombin binding aptamer

The thrombin binding aptamer (or TBA), which was reported by L. Bock, *et al.* in 1992,[167] is a short DNA aptamer composed of 15 nucleotides that binds to human thrombin with high affinity. This was also a landmark study as it was the first to use SELEX to investigate and develop an aptamer composed of single stranded DNA rather than of RNA. The TBA and has the following sequence (5' → 3'):

TBA: GGTTGGTGTGGTTGG

The structure of this guanine-rich oligonucleotide has been thoroughly explored and has been shown to self-assemble into an anti-parallel G-quadruplex[168,198,304,345–347] chair structure with two TT loops and one TGT loop in solution (see Fig. 73) when stabilized by monovalent cations.[345,348–350] In particular, the G-quadruplex structure of the TBA was shown to more stable in the presence of K^+ than Na^+, which resulted in melting temperatures (T_m) of ~53 °C,[345,346,351,352] and ~23 °C,[351] respectively. Indeed, circular dichroism (CD) has been used to show that in buffers without monovalent cations the TBA adopted a hairpin conformation and only switched a G-quadruplex upon addition of K^+.[145,195,353] Buffers with divalent cations, such as Mg^{2+}, appear to stabilize a B-form DNA hairpin. Despite this, Lin *et al.*,[195] further show that even in a buffer containing only Tris-HCl, titrating increasing concentrations of thrombin resulted in a change to the CD spectrum from that of a B-form DNA hairpin to the G-quadruplex suggesting that even in the absence of monovalent cations, thrombin will induce the G-quadruplex structure. This has also been demonstrated via Förster resonance energy transfer (FRET) using an aptamer beacon approach.[145] Measurements of the T_m also confirm this with the T_m of the TBA in the presence of thrombin in Na^+ and K^+ free buffer found to be very similar to the T_m of the TBA in K^+ buffer (51.3 °C[350], 58 °C[345]). When thrombin is added to the TBA in a buffer that contains either Na^+ or K^+, the T_m rises to 70 °C.[345] Taken together, this implies an induced fit binding mechanism.
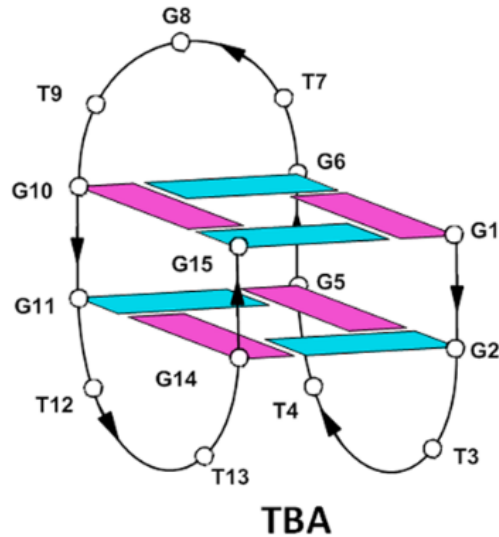
Figure 73. Schematic illustration of the G-quadruplex structure of the TBA. The bases are listed to indicate their role in the structure with the arrows indicating movement from the 5' to the 3' end of the DNA. The guanines that form the quadruplex structure are shown as rectangles to indicate their orientations and the directionality of the hydrogen bonding that stabilizes the structure. Adapted from T. Amato *et al.*.[218]

The structural binding properties of the TBA with thrombin have also been thoroughly investigated. Thrombin in a multifunctional serine protease with both pro- and anti-coagulation functions.[195,354] Furthermore, thrombin has four functional regions: the active catalytic site, an apolar binding site and two positively charged exosites.[195,354,355] Exosite I is known as the fibrinogen binding site and exosite II as the heparin binding site.[355] There is some disagreement surrounding the exact nature of the interaction between the TBA and thrombin. However, the consensus is that the TBA interacts with thrombin exosite I via the two TT loops via a predominantly electrostatic interaction in a 1:1 stoichiometry based on agreement between thrombin inhibition experiments,[167] NMR,[346,356] x-ray crystallography,[197,345] molecular dynamics simulations[352,357] and mass spectrometry.[198] Furthermore, it has been shown that the TBA is specific for human α-thrombin with negligible affinity for either β- or γ-thrombin, due to changes to exosite I.[170,345,358] Some studies have shown that the TBA can also interact with exosite II via a weaker electrostatic interaction at high TBA:thrombin ratios.[345,355,359]
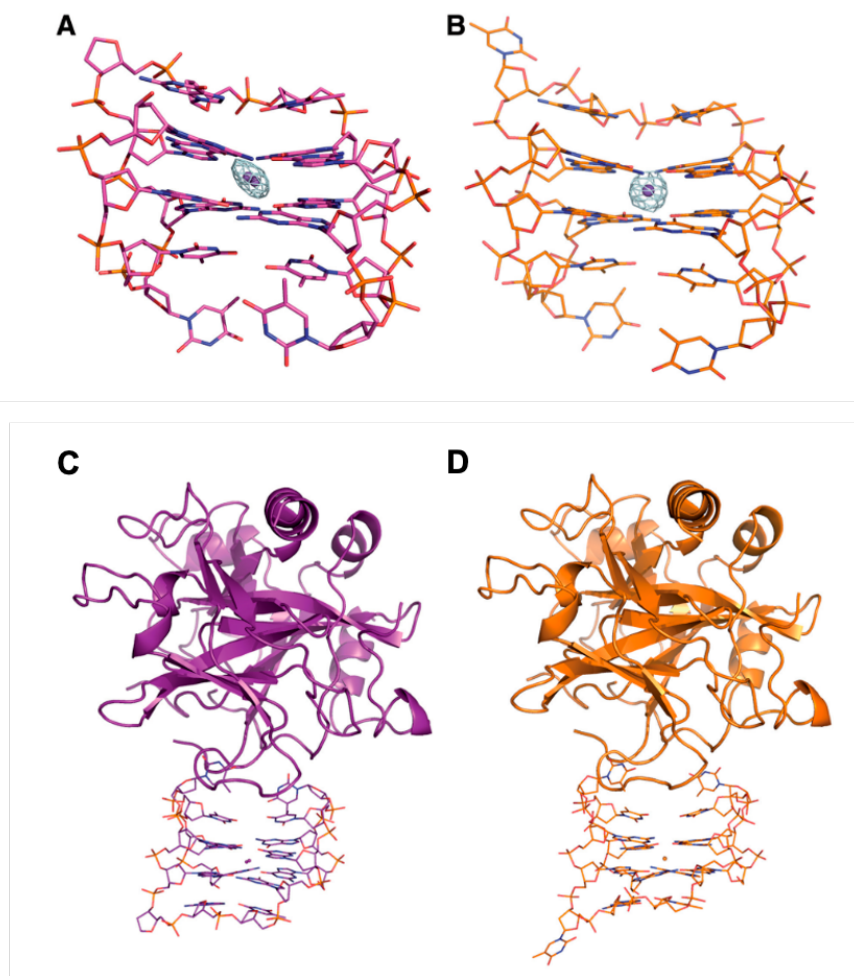
Figure 74. Crystal structures of the TBA stabilized by (A) Na^+ and (B) K^+ as well as the TBA bound to thrombin stabilized by (C) Na^+ and (D) K^+. In the Na^+ crystal structure (A and C), the T9 base (top left of A and bottom left of C, see Fig. 73) was not well resolved and is not shown. Adapted from Krauss *et al*,.[345]

The binding affinity of the TBA with thrombin has been well characterized using a variety of techniques demonstrating that the TBA binds to thrombin with a K_d that ranges between 0.5-450 nM (see Table 6).

Table 6: Selected rate and dissociation constants for the kinetics and thermodynamics of the association of thrombin and the TBA. Part adapted from Rotem *et al.*[272]

Method	k_{on} (M^{-1} s^{-1})	k_{off} (s^{-1})	K_d (M)	Reference
Competitive equilibrium binding			2.68×10^{-9}	Wu *et al.*[360]
			$7.5\text{-}10 \times 10^{-8}$	Tasset *et al.*[354]
Gel electrophoresis			1.00×10^{-7}	Macaya *et al.*[168]
Isothermal titration calorimetry			3.33×10^{-7}	Pagano *et al.*[355]
Surface plasmon resonance	1.89×10^5	3.83×10^{-3}	2.01×10^{-8}	Hasegawa *et al.*[361]
	2.27×10^4	9.54×10^{-3}	4.21×10^{-7}	Pinto *et al.*[362]
	1.40×10^7	0.55	3.92×10^{-7}	Ostatna *et al.*[363]
	5.19×10^6	8.90×10^{-2}	1.71×10^{-7}	Lin *et al.* [364]
Capillary electrophoresis	3.67×10^4	8.80×10^{-3}	2.40×10^{-7}	Berezonvski *et al.*[365]
	4.1×10^6	0.15	3.7×10^{-7}	Gong *et al.*[366]
	2.4×10^6	0.09	3.8×10^{-7}	
	2.7×10^6	0.12	4.6×10^{-7}	
	1.7×10^6	0.08	5.0×10^{-7}	
Single channel current recordings	1.97×10^7	1.5	7.7×10^{-8}	Rotem *et al.*[272]
	1.20×10^7	1.5	1.26×10^{-7}	
	1.98×10^6	2.57×10^{-2}	1.3×10^{-8}	Van Meervelt *et al.*[367]
	4.08×10^8	5.31		

6.2 Aims

The aim of this project was to design and build a synthetic DNA-based nanopore that was able to function as a biomimetic protein-gated channel (pNP, see Fig. 75). The gate was engineered to respond to the exogenous trigger of a specific protein. To achieve this, the DNA-based TBA was incorporated into the design of the nanopore's lid, which in the absence of the exogenous trigger: thrombin, no transport of molecular cargo would take place. However, addition of thrombin would result in binding with the aptamer and cause the lid to open by unzipping from the lid-docking

regions on the pore but remain bound to the pore at the hinge region. In this way the transport of molecular cargo across a lipid bilayer would only be possible upon addition of thrombin and actuation of the lid. The ability to control the transport of molecular cargo has applications for drug delivery as well as to function as a synthetic protein gate in larger systems. A final aim of this project was to incorporate the protein gate into a drug delivery system to increase the specificity and potency of the delivery of cytotoxic cargo to cancer cells.
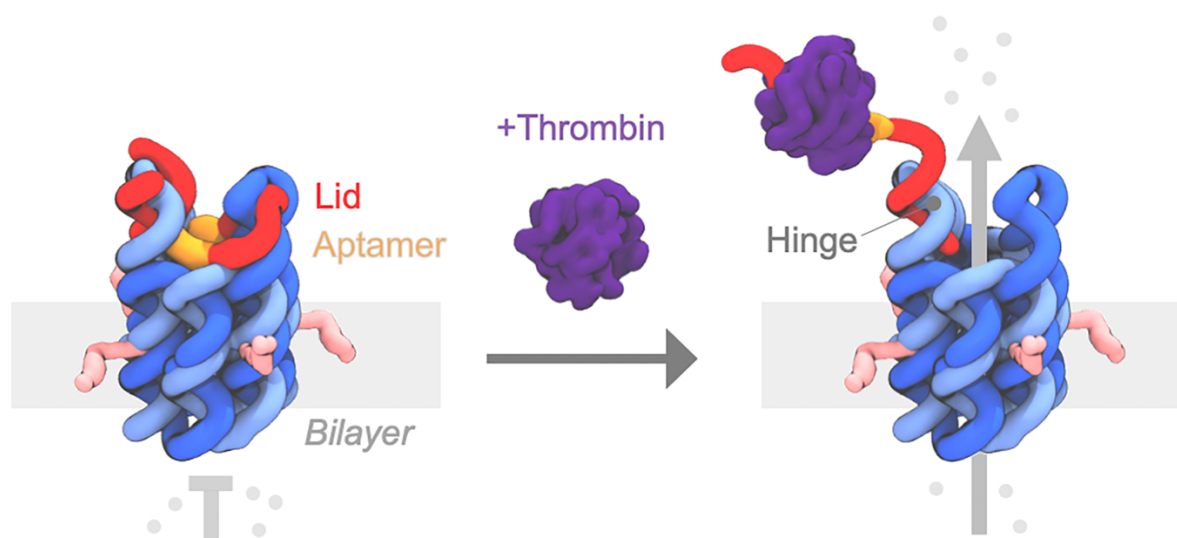
Figure 75. Schematic to illustrate the design and function of the membrane-spanning synthetic DNA-based biomimetic protein-gated nanopore. A DNA aptamer that binds to a specific protein, in this case thrombin, is placed within the nanopore lid sequence. The lid prevents passage of molecular cargo across the bilayer. Upon addition of thrombin, the protein-gate actuates at the hinge region and allows the transport of molecular cargo across the bilayer.

6.3. Results and Discussion

The majority of the results in this section were published in *Angew. Chem. Int. Ed.*, 2021, **60**, 1903-1908. The project was conceived by Dr. Patrick Arnott, Prof. Stefan Howorka and me. Dr. Patrick Arnott designed pNP2. The assessment of optimal folding conditions was conducted by me in consultation with Dr. Jonathan R. Burns. The initial stages of the project were performed by Katarina Korlova under the supervision of Dr. Patrick Arnott and me including TBA-thrombin binding, pore forming gels and CLSM GUV-binding experiments. pNP- and pNP2-thrombin binding and FRET lid-opening experiments were performed by me. SRB dye flux assays were performed by me in consultation with Dr. Patrick Arnott. The design of the DNA nanodevice and the cell-based assay experiment was undertaken in by Dr. Patrick Arnott, Sioned Fôn Jones and me. Dr. Patrick Arnott and Sioned Fôn Jones performed and analysed the results of the cell-based assay.

Apart from the cell-binding assay all other data analysis presented here was performed by me. Prof. Stefan Howorka supervised all stages of the project. All publications can be found reproduced in full in Appendix B (Section 10).

6.3.1. Aptamer design and thrombin binding

The thrombin binding aptamer (TBA) was chosen as it is a well characterized aptamer, has a relevant target and is very small (15-nucleotides in a compact G-quadruplex structure). Size was a critical aspect for the proof of concept as it was necessary to ensure the stability of the lid.

It was necessary to confirm that a gel-shift assay would be sufficient to measure binding between the TBA and thrombin as this was to be used later to determine the thrombin binding potential of the TBA when incorporated into the lid of the DNA nanopore (pNP) as a nanovalve. In order to improve visualization on the agarose gel a 26-nucleotide tail was added to the aptamer to increase ethidium bromide staining sensitivity. Shown below is the sequence of the TBA (red) with added 26 nt tail (black) from 5' → 3':

GGTTGGTGTGGTTGGTTTAAGTAGTTCAAGACCCCGTGACT

The TBA was titrated against increasing amounts of human α-thrombin from a ratio of 1:0.2 to 1:10 TBA:thrombin using an electrophoretic gel-shift assay (Fig. 76). Electrophoretic gel-shift assays are a common method used to ascertain the binding of nucleic acids to other structures[118] and have been used extensively to characterise aptamer-target binding.[184,225,236,243,259,272] This assay relies on the same principle as the gel-shift assays presented in the Chapter 4 (Section 4.2.2.).
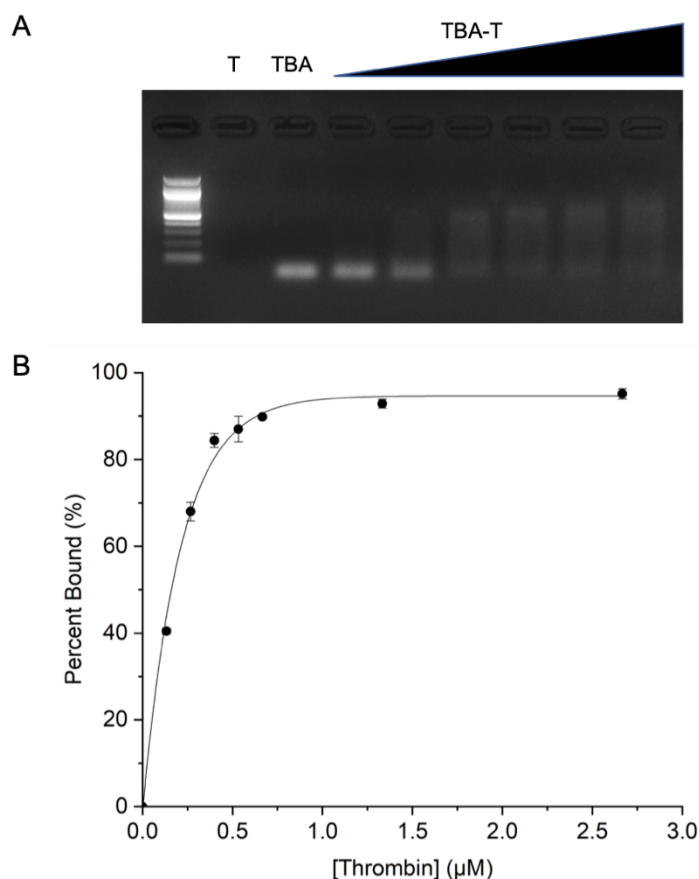
Figure 76: Binding of human α-thrombin (T) to the TBA aptamer with 26-nt tail: (A) Gel shift assay: increasing the concentration of thrombin results in the formation of a TBA-T complex, which is visualised by the formation of a band higher up the gel representing the larger complex. (B) Binding curve of TBA-T complexation displayed as percent bound with an average R^2 of 0.97. The data represent averages and standard deviations from 3 independent experiments. Adapted from C. Lanphere, *et al.*.[15]

The gel shift assay confirmed that the TBA complexed with human α-thrombin with a 1:1 stoichiometry. In addition, the Hill-Langmuir fit then yielded a dissociation constant (K_d) of $1.52 \pm 0.12 \times 10^{-7}$ M, which is in good agreement with the literature (see Table 6).

Successful complexation of the TBA with thrombin confirmed, the next step was to incorporate the TBA into the lid of the nanopore.

6.3.2. Design of the DNA nanopore with protein-gate, pNP

The design of the protein-gated nanopore (pNP) was adapted from the temperature-gated nanopore designed by Arnott *et al.*[125] and the ligand-gated nanopore by Burns *et al.*[115], which are based on the

archetypal six-helical bundle nanopore design.[118] Both of these pores have previously demonstrated the successful incorporation of a lid onto a nanopore and exhibited actuation from external stimuli. However, the design of temperature-gated pore was chosen over the very similar ligand-gated one because the slightly elongated loops of the docking strands in the temperature-gated nanopore provide added stability for the lid. This was an important factor considering that the unbound aptamer sequence must be included. This was also an advantage as it would allow for successful lid opening where the lid remained attached to the nanopore. This had several advantages such as limiting the amount of free exogenous DNA, ensuring that the nanopore remained close to the target, it gave the nanopore a dual modality by both binding and inhibiting the target. In addition, it ensures that the pore was not only actuated by the target, but that it remains at the target site. This also allowed for the future application of reversible actuation using a 'smart' aptamer. One final consideration was related to strand economy. The ligand-gated nanopore required 8 DNA oligonucleotides, while the temperature-gated nanopore required only 7.

The pNP features four lid docking regions, one on either side of each of the loops (Fig. 77). These four regions are then further divided into two distinct sections based on melting temperature: a hinge region where the lid is expected to remain attached to the body of the pore (hinge region, H, Fig. 77) and three docking regions (D_1-D_3, Fig. 8), which are expected to dissociate upon thrombin binding to reveal the open state of the pore. To achieve these conditions, the hinge region, H, and docking regions D_1-D_3 have duplex melting temperatures of 65, 45, 40, and 45 °C, respectively. The overall melting temperature of the pore is expected to be around 55 °C itself (based on the similar pores designed by Burn *et al.* and Arnott *et al.*) so the lid opening should not impact the overall stability of the pore and the lid should remain bound.
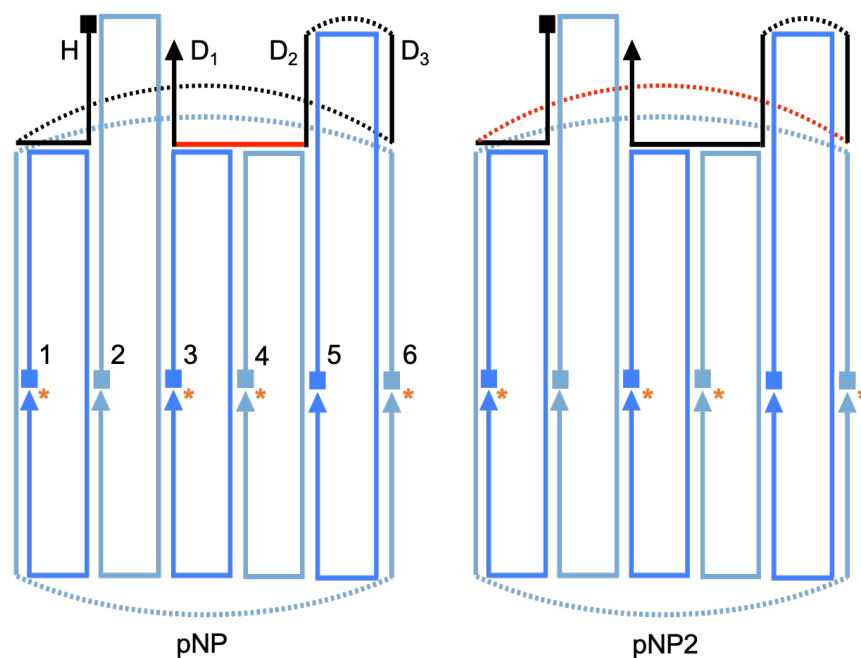
Figure 77. 2D maps of the pNP featuring the two different lid designs: pNP (left) and pNP2 (right). Orange asterisks indicate the position of cholesterol anchors, the lid is shown in black with the red coloured section representing the TBA sequence, the six oligonucleotides that comprise the six duplex-bundle are shown in light and dark blue, squares denote the 5' end of DNA and triangles the 3' end. The different lid binding regions are labelled at the top of pNP (right) with H, for hinge, and D_1-D_3 for the lid docking regions of the pore. Adapted from C. Lanphere, *et al.*.[15]

Two versions of the pNP were designed, each featuring a unique lid. In both of the lid designs, the TBA sequence was incorporated into the lumen spanning (and, therefore, blocking) sections of the lid. This was done to ensure that pore function was blocked in the closed state and was only restored by lid dissociation induced by aptamer complexation with thrombin. The two lid designs differ only in their placement of the TBA sequence. In Lid-1 (used for pNP) the TBA sequence was placed in the lumen spanning region near to the 3' end of the lid. This places the TBA between lid docking regions D_1 & D_2, which are regions expected to dissociate. It is expected that this will result in more facile aptamer formation and lid opening. In Lid-2 (used for pNP2) the TBA sequence was placed into the other lumen spanning region of the lid, near the 5' end of the lid between the hinge, H, and docking region D_3. This places the aptamer next to the hinge region of the pore which is not expected to dissociate and is expected to prevent non-actuated lid-dissociation. The sequences of the two lid designs are shown below (5' → 3') with the TBA sequence highlighted in red and the rest of the lid in black:

Lid-1:

148

AACCGCGCAGCGTTTTTTTTTTTATGACGTGCTTTTTTTTTTATCGTGACGGTTGGTGT GGTTGGCGTGATTACTTA

Lid-2:

AACCGCGCAGCGGGTTGGTGTGGTTGGTATGACGTGCTTTTTTTTTTATCGTGACTT TTTTTTTCGTGATTACTTA

3D illustrations of the pNP are shown below in Figure 78. The pNP is depicted top-down and side-on in both the closed state (with the lid bound to the docking regions, A & C) and the open, actuated state with thrombin (purple) bound to the TBA (B & D). The overall dimensions of the pore are approximately 13 nm x 5 nm with a 2 nm pore lumen.
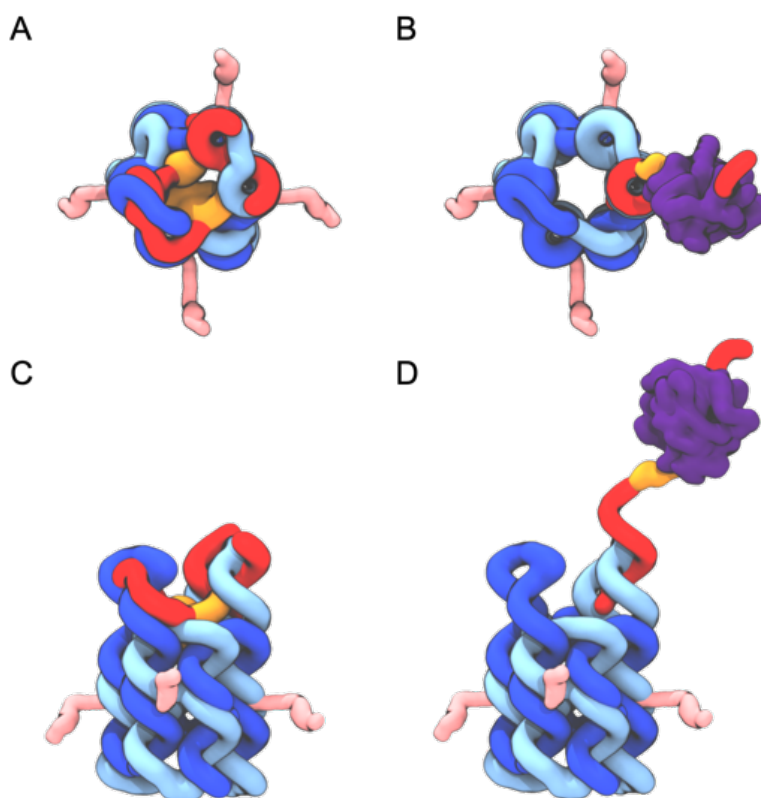
Figure 78. Top-down (A) and side-on view (C) of pNP in the closed state with bound lid. The six core oligonucleotides of the pNP barrel are shown in alternating colours of light and dark blue for clarity. The lid is shown in red with the TBA sequence highlighted in gold. In the closed state the lid traverses the pore lumen and blocks pore function. The cholesterol anchors, which are necessary to insert and anchor the pore in the hydrophobic interior of lipid bilayer membranes, are shown in pink. Top-down (B) and side-on view (D) of the pNP in its open, actuated state. Here the lid is shown bound to the pore only at docking region 1 and with thrombin (purple) bound to the TBA

(gold) section of the lid. The pore lumen is now unobstructed and pore function is restored. Adapted from Lanphere, *et al.*.[15]

6.3.3. pNP Assembly and Structural Confirmation

Following the design stages, it was necessary to fold (DNA structural assembly via thermal annealing) and characterise the pNP. The assembly of the pNP was achieved by mixing equimolar amounts of the six core oligonucleotides plus the lid in buffer and then heating this solution up to 95 °C before slowly cooling to 4 °C to allow the DNA nanostructure to assemble into its thermodynamically most stable structure. It is necessary to heat the oligonucleotides to above the melting temperature of any possible secondary structures to avoid misfolding. 95 °C is commonly used for this purpose as no secondary structures are expected at this temperature for any structure.[118]

The optimal conditions, including the folding buffer and folding protocol, for pNP assembly were then identified. These conditions were assayed using the native pore, pNP$^{\Delta C}$, without cholesterol modification. The two pores the pNP is based-on use different buffering and folding conditions. The ligand-gated pore from Burns *et al.,* was folded in 300 mM KCl, 15 mM Tris-HCl, pH 8 using a fast 20 min folding protocol.[115] The temperature-gated pore from Arnott *et al.*, was folded in 20 mM MgCl$_2$ using a slower 2 h folding protocol.[125] In light of this discrepancy, pNP$^{\Delta C}$ was folded in a range of different buffers to determine the optimal conditions. The buffers were: PBS; 300 mM KCl, 15 mM Tris-HCl, pH 7.6; 12 mM MgCl$_2$; 12 mM MgCl$_2$ 0.6 x TAE, pH 7.4; 16 mM MgCl$_2$; 16 mM MgCl$_2$ 0.8 x TAE, pH 7.4; 20 mM MgCl$_2$; and 20 mM MgCl$_2$ 1 x TAE, pH 7.4. As a control, the pNP$^{\Delta C}$-L (without the lid) was assayed first using a 15 h fold.

For the sequences of the oligonucleotides and detailed folding protocols, see Appendix A, Sections 9.5.1. and 9.2., respectively.

SDS polyacrylamide gel electrophoresis (PAGE) was used to probe the success of the pNP$^{\Delta C}$-L fold in each specified buffer.
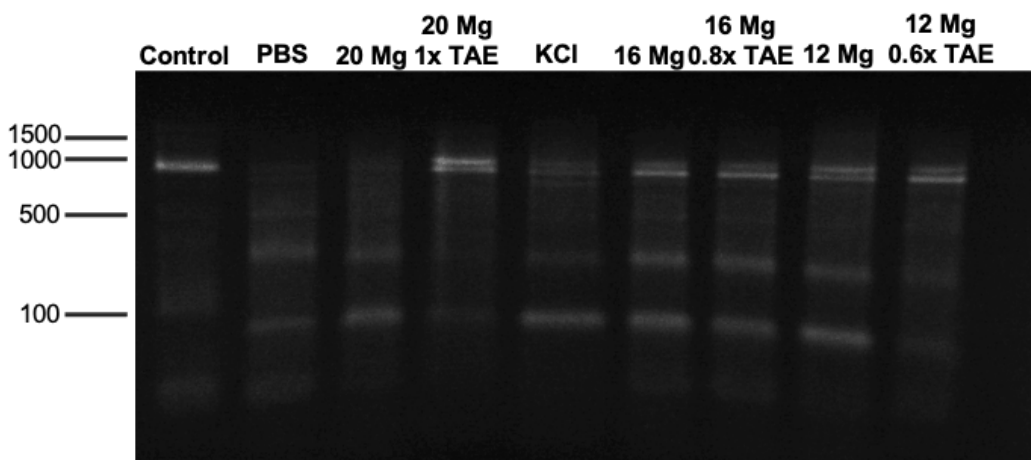
Figure 79. SDS PAGE gel of pNP$^{\Delta C}$-L folded in different buffer conditions using a 15 h fold to assess optimal folding conditions. The control is the NP from Burns et al.[115] folded in 1x PBS. In order, buffers are PBS (*PBS*); 20 Mg (*20 mM MgCl$_2$*); 20 Mg 1x TAE (*20 mM MgCl$_2$ 1 x TAE, pH 7.4*); KCl (*300 mM KCl, 15 mM Tris-HCl, pH 7.6*); 16 Mg (*16 mM MgCl$_2$*); 16 Mg 0.8xTAE (*16 mM MgCl$_2$ 0.8 x TAE, pH 7.4*); 12 Mg (*12 mM MgCl$_2$*); and 12 Mg 0.6 x TAE (*12 mM MgCl$_2$ 0.6 x TAE, pH 7.4*) folded using a 15 h folding protocol. 10% SDS PAGE (1x TGS buffer), 60 V, 60 min. Annotations to the left indicate the major bands in a 100 bp DNA ladder.

What is immediately apparent from the gel is none of the folding conditions have resulted in a single clean band for the pNP$^{\Delta C}$-L. Indeed, this gel was only obtained after SDS was used in the gel running buffer as native PAGE resulted in a very streaky gel that made analysis difficult, which indicates that the pNP$^{\Delta C}$-L is likely an unstable structure. It is probable that the long unhybridized ssDNA loops are the cause of the instability. The two conditions that appear to be the most successful were the folds in 12 mM MgCl$_2$ 0.6x TAE, pH 7.4 and 20 mM MgCl$_2$ 1x TAE, pH 7.4. KCl does not appear to be a suitable buffer for pNP$^{\Delta C}$-L. KCl shows more of the product band (as assessed from the control pore from Burns *et al.*) than PBS, but it remains faint with some faster migrating bands more prominent. Neither PBS nor unbuffered 20 mM MgCl$_2$ appear to have resulted in a product band at all. The others appear to have resulted in a product band, but also faster migrating bands of equal intensities.

pNP$^{\Delta C}$ was folded to see if the addition of the lid stabilized the structure. To compare the fully assembled structure to Burns *et al.* and Arnott *et al.*, pNP$^{\Delta C}$ was also folded using the 2.5 h folding protocol in addition to the 15 h protocol (Section 9.2.). However, unbuffered MgCl$_2$ was eliminated as a condition. It demonstrated no advantages over the other buffering conditions with the pNP$^{\Delta C}$-L and as future applications for the pore would necessitate biocompatibility, as close to physiological conditions as possible was desired. In addition, unbuffered MgCl$_2$ has been internally shown to cause aggregation of the pores, especially pores modified with cholesterol lipid anchors.

Native PAGE was used to probe the success of the folding of each condition.
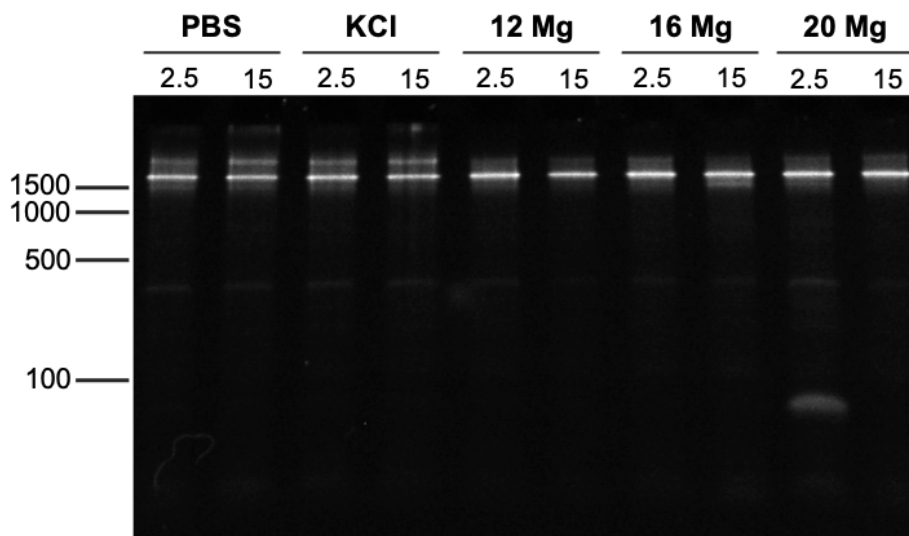
Figure 80. PAGE gel of pNP$^{\Delta C}$ folded in different buffers using two different folding protocols to assess optimal folding conditions. Buffers are PBS (*PBS*); KCl (*300 mM KCl, 15 mM Tris-HCl, pH 7.6*); 12 Mg (*12 mM MgCl$_2$ 0.6 x TAE, pH 7.4*); 16 Mg (*16 mM MgCl$_2$ 0.8 x TAE, pH 7.4*); 20 Mg (*20 mM MgCl$_2$ 1 x TAE, pH 7.4*) folded using either a 2.5 h (2.5) or 15 h (15) folding protocol. 10% PAGE (1x TGS buffer), 60 V, 60 min. Annotations to the left indicate the major bands in a 100 bp DNA ladder.

All 10 conditions demonstrated far superior folding compared to the pNP$^{\Delta C}$-L indicating that the lid significantly stabilizes the structure. All 10 conditions display an identical band just above the 1500 bp marker. This band corresponds to the nanopore band for both the ligand-gated nanopore from Burns *et al.* and the temperature-sensitive pore from Arnott *et al.*. Therefore, as this band is present in all conditions and matches similar pores from the literature, it can be concluded that this is the band for the pNP. Furthermore, with pNP$^{\Delta C}$, native PAGE was more than adequate to cleanly resolve the desired product band, unlike pNP$^{\Delta C}$-L, which indicates the structure is much more stable. However, a secondary band that runs just above the pNP$^{\Delta C}$ band is also evident in both the 2.5 h and 15 h folds in PBS and 300 mM KCl. In the 20 mM MgCl$_2$ 1 x TAE 2.5 h fold there is slight evidence of excess strands. This occurred in multiple gels after multiple folds, indicating this is not a suitable folding condition. Otherwise, all MgCl$_2$ folding conditions resulted in a very clean single product band, with 12 mM MgCl$_2$ using the 15 h protocol displaying a marginally sharper band.

To further assess the suitability of each folding condition, UV-thermal denaturing melts were used to calculate the T$_m$ (see Section 5.2.2). There are no desired applications for the pNP-L since the pNP has been designed so that the lid will remain attached to the pore following actuation, instead of being removed as was the case with the ligand-gated pore from Burns *et al.*, only the pNP was further investigated. Due to the similarities on the PAGE gel between PBS and KCl, only KCl will

be considered for a melt as this can be compared to Burns *et al.* Given the similarities in all of the MgCl$_2$, 16 mM MgCl$_2$ was also not assayed further. Therefore, pNP$^{\Delta C}$ folded in 300 mM KCl, 12 mM MgCl$_2$ and 20 mM MgCl$_2$ in both the 2.5 and 15 h folding protocols were assayed at 0.2 µM in 150 µL of the folding buffer using a UV-melt protocol, which includes a temperature ramp of 1 °C/min from 20-80 °C. The method is described in Section 9.5.5.

The processed melt profiles as well as the 1st derivative for each of the three buffers folded using the two folding protocols are shown below in Figure 81.
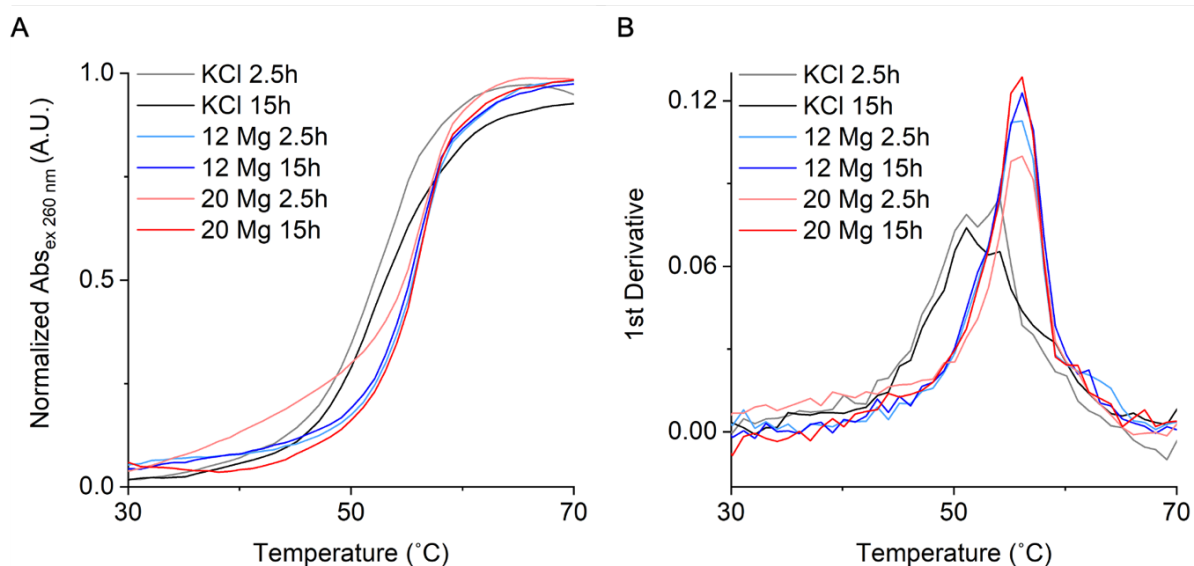
Figure 81. UV-melting profiles of the pNP$^{\Delta C}$ folded in different buffers using two different folding protocols to assess structural stability and optimal folding conditions. pNP$^{\Delta C}$ was assessed at 0.2 µM in 150 µL of the stated folding buffer. Samples were melted using a temperature ramp of 1 °C/min between 20 and 80 °C. Each trace represents an average from three independent repeats.

The derived T$_m$ (if multiple peaks were present, these are also listed) of the pNP$^{\Delta C}$ in each of the folding buffers and folding conditions are outlined in Table 7.

Table 7. The derived T_m of the pNP$^{\Delta C}$ in various buffers and folding conditions obtained from the 1st derivative taken from the UV-melt profiles shown in Figure 81.

Buffer	Folding Protocol	Avg. T_m (°C)
300 mM KCl	2.5 h	51.6 ± 0.8
		54.3 ± 0.3
	15 h	51.3 ± 0.3
		53.9 ± 0.6
12 mM MgCl$_2$	2.5 h	55.9 ± 0.5
	15 h	55.9 ± 0.2
20 mM MgCl$_2$	2.5 h	56.1 ± 0.1
	15 h	55.9 ± 0.2

It is apparent from the UV-melt profiles that pNP$^{\Delta C}$ folded in KCl has a lower T_m compared to when it is folded in a MgCl$_2$. Indeed, looking at the first derivate confirms this, but what is also apparent is that there are two peaks in the KCl folds, whereas the folds in MgCl$_2$ show a single peak. In the case of KCl, it is worth recalling that K^+ stabilizes the G-quadruplex of the TBA resulting in a T_m of ~53 °C compared to the TBA in the absence of K^+, which has a much lower T_m of approximately 23 °C. Indeed, in MgCl$_2$, the TBA has been observed to adopt a B-DNA hairpin rather than a G-quadruplex (see Section 6.1.1.) The formation of the G-quadruplex before the lid is fully annealed could impact the folding of the lid to the pNP$^{\Delta C}$. The two peaks could correspond to a correctly assembled pNP$^{\Delta C}$ as well as an incomplete state. This could be the cause of the two bands in the KCl folds in the gel in Figure 80 as well as the two peaks in the melting profile. Approximately 3 °C separates the two T_m in the KCl folds. This is very similar to the ~3.5 °C that separates the NP from the NP-O (NP-open – without the lid) from Burns *et al.* implying that this is the most likely state. However, an alternative explanation could be that two peaks simply correspond to the melting of the G-quadruplex and the pNP$^{\Delta C}$, respectively.

The T_m of the pNP folded using either folding protocol in MgCl$_2$ based buffers are nearly identical and all within error. The UV-melt profiles are also nearly identical. The only discrepancy is the 2.5 h fold in 20 mM MgCl$_2$, which shows an early and gentle rise that starts around 30 °C and continues before transforming into the same sharp transition as the other MgCl$_2$ folds.

Following this analysis, 12 mM MgCl$_2$ in 0.6x TAE using the 15 h folding protocol was chosen as the optimal folding condition for the pNP. This buffer also has the advantage of having the lowest salt conditions. Furthermore, the 15 h folding protocol was chosen over the 2.5 h protocol as it was found to be more reliable.

12 mM MgCl$_2$ in 0.6 x TAE and the 15 h folding protocol confirmed as the optimal folding conditions, gel electrophoresis was used to confirm the success of the folding of the pNPs. SDS PAGE was used to distinguish between the pNP$^{\Delta C}$ -L and pNP$^{\Delta C}$ for both pNP and pNP2 to confirm the successful folding of the pore and the successful incorporation of the lid (see Fig. 82). Both lid variants resulted in an identical band (both with and without the lid) as expected. pNP$^{\Delta C}$-L resulted in a faster migrating band, which is consistent with a slightly smaller structure and similar designs in the literature.[115,125] As they are critical for the pNP to function, it was also necessary to confirm the folding of the pore with cholesterol modifications. The pNP was modified with four cholesterol lipid anchors attached at the 3' end of strands 1, 3, 4, and 6 via a tri(ethylene glycol) (TEG) linker (see Fig. 77 and Fig. 78). The bands for the pNP and pNP2 displayed slightly slower band migration compared to the bands for the native pore (pNP$^{\Delta C}$) indicating a slightly larger structure consistent with the addition of the cholesterol lipid anchors. In addition, cholesterol modifications can interact with the gel matrix resulting in a slower migrating band.[118] This confirmed the successful folding of the pore with the cholesterol modified strands.
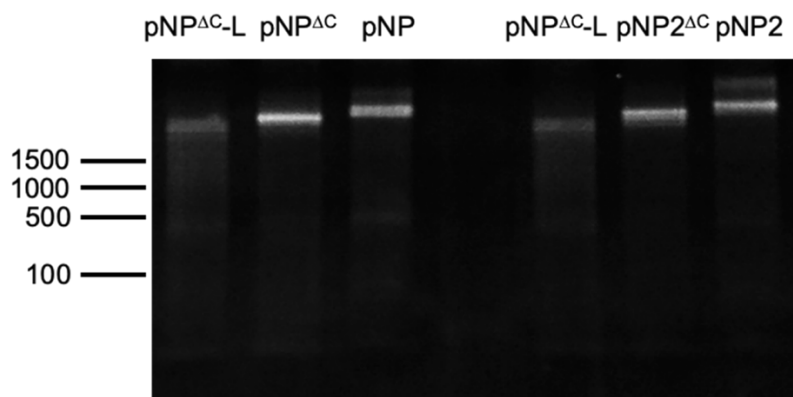
Figure 82. SDS PAGE gel of the pores: pNP and pNP2, to confirm assembly with and without the lid as well as successful incorporation of the four cholesterol lipid anchors. 12% PAGE (1x TGS buffer), 60 V, 60 min. Annotation to the left hand-side indicates the major ladder markers in a 100 bp DNA ladder. Lanes from left to right: pNP$^{\Delta C}$-L, pNP$^{\Delta C}$, pNP, pNP$^{\Delta C}$-L, pNP2$^{\Delta C}$, pNP2. Adapted from Lanphere, *et al.*.[15]

A change in band migration was a good indication that the cholesterols have been successfully incorporated; however, the gel gives no indication as to whether the lipid anchors have been successfully incorporated to the exterior of the pore, as expected, or if they have been turned inward. Therefore, confirmation of insertion into the lipid bilayer was required. To do this, a variant of pNP2 was designed called pNP^{TAMRA} (See Fig. 83A). This pore features a 14-nucleotide extension to the 3' end of Lid-2 (Lid-2-ext) to accommodate a short 15-nucleotide strand carrying a TAMRA dye (Fig. 83A, green). At the early stage of this project, adding a dye in this way was much more cost-effective than functionalising the lid itself with a dye due to the length of the lid sequence. To confirm membrane binding, the pNP^{TAMRA} with its 4-cholesterol lipid anchors was added to GUVs

and visualized under a confocal microscope. A bright ring around the GUVs confirms the successful anchoring of pNP^TAMRA to the lipid bilayer membrane and that the lid remains attached to the pore (Fig. 83B).
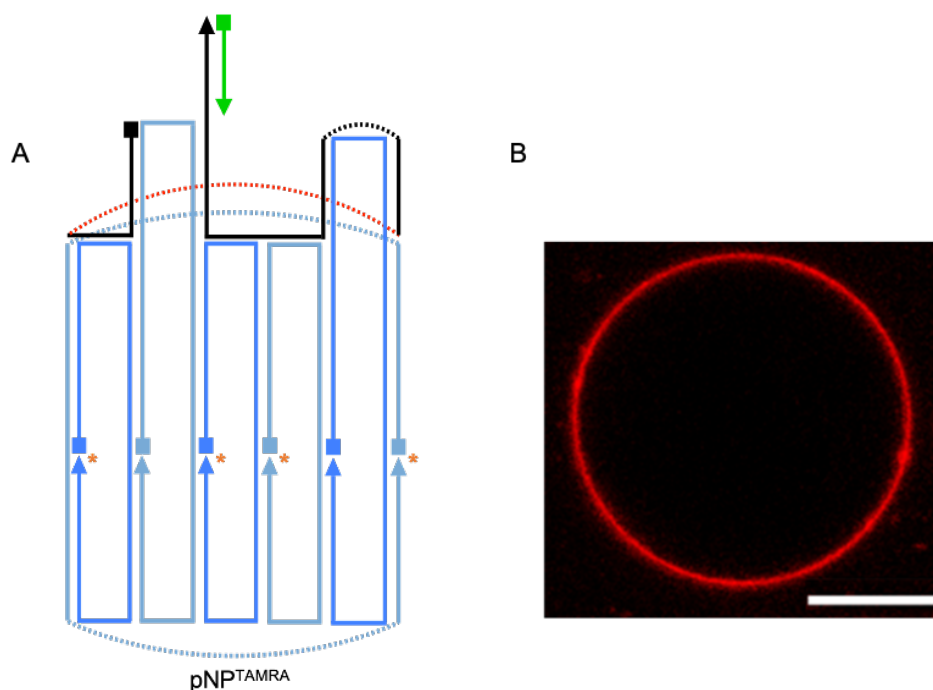
Figure 83. (A) 2D map of pNP^TAMRA. Orange asterisks indicate the position of cholesterol anchors, the lid, which features a 14-nucleotide extension to the 5' end of Lid-2 (Lid-2-ext) is shown in black with the red coloured section represents the TBA sequence, the green strand represents the short 15-nucleotide long strand carrying a TAMRA fluorophore, the six oligonucleotides that comprise the six duplex-bundle are shown in light and dark blue, squares denote the 5' end of DNA and triangles the 3' end. (B) Confocal laser scanning microscopy image of pNP^TAMRA bound to a giant unilamellar vesicle composed of POPC lipids. Scare bar represents 10 μm. Adapted from Lanphere, *et al.*.[15]

6.3.4. pNP-Thrombin Binding

Following confirmation of the successful folding of the pNP with TBA sequence incorporated into the lid, the next step was to probe the binding properties of the pNP with thrombin. It was important to investigate whether incorporation into the lid prevented TBA-thrombin binding and also to what degree the sterically hindered environment impacted TBA's affinity for thrombin.

pNP-thrombin binding was assayed using a gel-shift titration, just as TBA-thrombin binding was assayed in Section 6.3.1; however, as the pNP was much larger than the TBA, PAGE was used in

order to get better separation between the pNP and pNP-thrombin complex. pNP was titrated against increasing amounts of human α-thrombin from a ratio of 1:0.5 to 1:40 pNP:thrombin (Fig. 84).
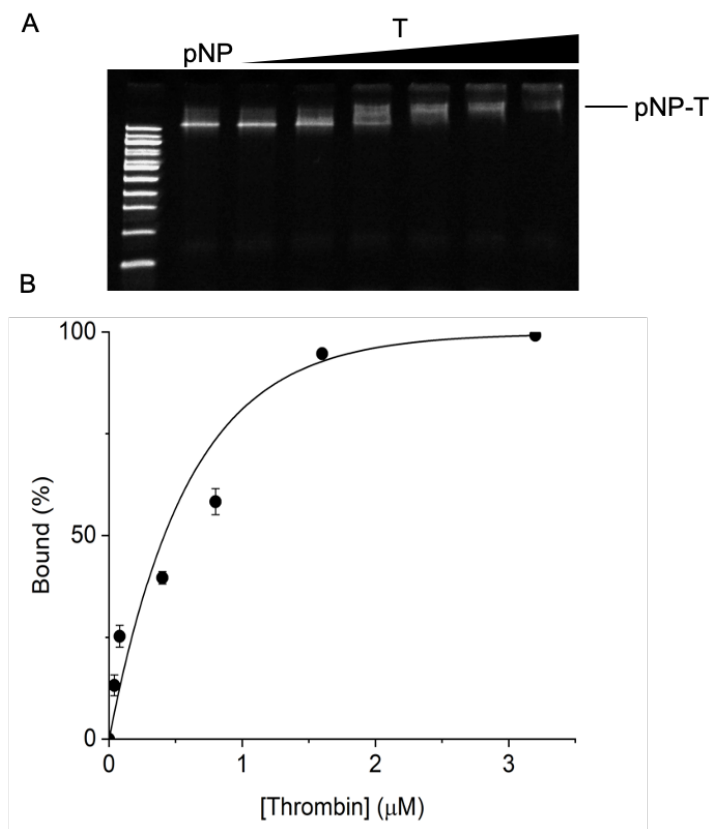
Figure 84. Binding of human α-thrombin (T) to pNP: (A) Gel shift assay: increasing the concentration of thrombin results in the formation of an pNP-T complex, which is visualised by the formation of a band higher up the gel representing the larger complex. 12% native PAGE (1xTBE buffer). 60 V for 90 min. L→R: 100 bp DNA ladder; pNP; pNP:T (1:0.5); pNP:T (1:1); pNP:T (1:5); pNP:T (1:10); pNP:T (1:20); pNP:T (1:40). (B) Binding curve of pNP-T complexation displayed as percent bound with an average R^2 of 0.96. The data represent averages and standard deviations from 3 independent experiments. Adapted from Lanphere, *et al.*.[15]

A definite band shift can be observed indicating the successful formation of the pNP-thrombin complex and also indicates that binding reaches saturation at a stoichiometry of approximately 1:20 pNP:thrombin. The saturation binding stoichiometry is significantly different for the pNP compared to the TBA (with 26-nt tail) on its own, which saturated at a 1:1 binding stoichiometry. The binding curve was generated using a Michaelis-Menten fit (as used in Section 4.2.2 and Section 5.2.3) with an R^2 of 0.96 and an implied K_d of 6.62 ± 0.93 x 10^{-7} M. Despite the much higher stoichiometry, the K_d was the same order of magnitude (only about 4.5 x higher) as that obtained for TBA-thrombin. The weaker K_d for the pNPs was expected considering the sterically hindered location of

the TBA sequence in the lid. The higher binding stoichiometry suggested that the formation of the aptamer was not as straightforward when incorporated into the lid.

To see how the location of the TBA sequence within the lid affected the binding to thrombin, pNP2 was titrated against human α-thrombin (Fig. 85).
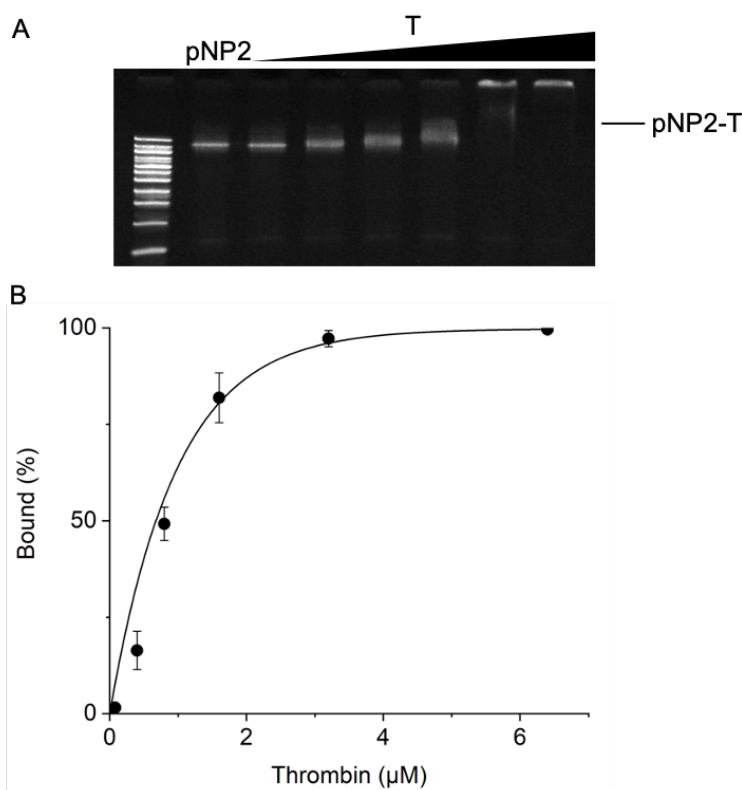
Figure 85. Binding of human α-thrombin (T) to pNP2: (A) Gel shift assay: increasing the concentration of thrombin results in the formation of an pNP2-T complex, which is visualised by the formation of a band higher up the gel representing the larger complex. 12% native PAGE (1xTBE buffer). 60 V for 90 min. L→R: 100 bp DNA ladder; pNP2; pNP2:T (1:1); pNP2:T (1:5); pNP2:T (1:10); pNP2:T (1:20); pNP2:T (1:40); pNP2:T (1:80). (B) Binding curve of pNP2-T complexation displayed as percent bound with an average R^2 of 0.96. The data represent averages and standard deviations from 3 independent experiments. Adapted from Lanphere, et al..[15]

pNP2 also demonstrated successful binding with thrombin, although it was weaker than pNP. In order to generate a successful binding curve, the pNP2:thrombin ratios had to be increased. Similarly, the indicated binding ratio appears to be 1:40. Although the stoichiometry of 1:20 pNP2 displayed 81.9 ± 6.5 % binding so the stoichiometry is likely somewhere in between 1:20 and 1:40. This resulted in a K_d of 13.12 ± 2.60 x 10^{-7} M, suggesting that the location of the TBA sequence in pNP2 is less favourable than in pNP.

In pNP2, and in some cases pNP, the titration was primarily driven by a more gradual upwards shift of the band rather than the formation of a true second band. It was hypothesized that this may be caused by non-specific interactions between thrombin and the nanopore or that the positive charges on thrombin result in an upwards shift.

Fortunately, this question was answered by an unsuccessful titration. One batch of pore appeared to fold unsuccessfully, or subsequently degraded after folding, resulting in the majority of the pore being formed without the lid. Two bands are apparent in this gel (see Fig. 86.): the major band being the pore without lid (pNP-L) and a faint, but still apparent pNP band. However, upon addition of thrombin, the pNP-L displayed no gradual upwards mobility even at the highest thrombin concentrations, while the fainter pNP band shows a gradual upshift as the thrombin concentration increases. This confirmed that the interaction between the pore and thrombin was limited to the lid. Therefore, the upwards mobility shift observed upon the addition of thrombin can be attributed to the formation of the pNP-thrombin complex only and not due to non-specific ionic interactions. A further simple, but equally important, conclusion can now also be drawn: the lid must remain attached to the pore upon complexation with thrombin or the band representing the pNP would not have shown any shift with increasing concentrations of thrombin.
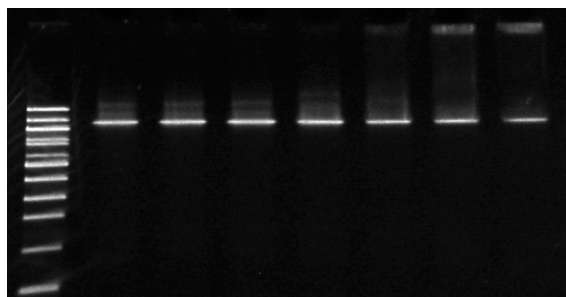
Figure 86. Unsuccessful PAGE titration with thrombin as the lid did not assemble correctly and pNP-L was the major species. No interaction between pNP-L and thrombin was observed.

6.3.5. pNP Lid Opening

Thrombin specific binding to the lid of the pNP now confirmed, the next step was to confirm that the formation of the aptamer and thrombin binding lead to actuation of the lid. To monitor thrombin induced lid opening FRET was used. FRET is a commonly employed technique for investigating mechanical processes in DNA nanotechnology, including the opening of lids[15,115,144], due to the special resolution on the order of nanometers[294]. Here, the 3' end of the lid was labelled with the donor fluorophore, Cy3, and the thymine loop of strand 3 with the acceptor fluorophore, Cy5 (the sequences can be found in Section 9.5.1). The thymine loop of strand 3 was selected for the location of the acceptor dye as this sits directly below D_1 and, therefore, the 3' end of the lid (see

Fig. 87). This placement will position the FRET pairs approximately 4 nm apart when the lid is bound to the pore in its closed state, well within the Förster distance (R_0) of 5.6-6 nm for the Cy3-Cy5 FRET pair[293,294]. This placement will also maximize the separation between the dyes in the open state, which is estimated to be between approximately 10-14 nm.
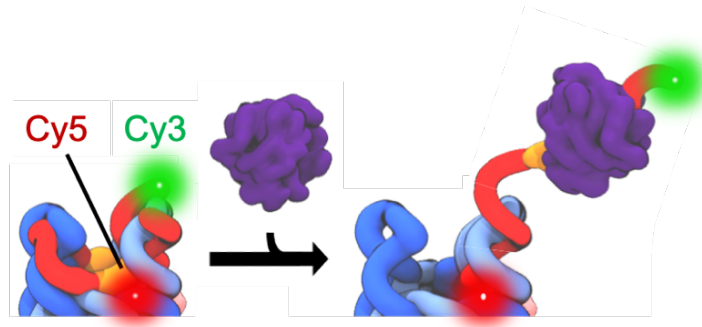
Figure 87. Schematic illustration of the FRET lid opening experiment. The left-hand side indicates the location of the FRET pair, Cy3 and Cy5, on the pNP in the closed state. The right-hand side indicates the change in proximity of the fluorophores following addition of thrombin and pore activation. The visualisation of lid opening presented in this schematic is for visualisation purposes only. In reality the lid opens downwards and away as the 5' end of the lid strand is inverted (see Fig. 77). However, this visualisation is sufficient for illustrative purposes. Adapted from Lanphere *et al.*.[15]

The validity of this approach was first probed using ensemble fluorescence in a fluorescence spectrophotometer. Initial scans were taken to confirm that FRET was indeed taking place by comparing the pNP in its closed state with both fluorophores compared to the pore with either the donor or the acceptor alone. FRET confirmed to be taking place, scans were repeated in the presence of thrombin. For best results, 100 nM pNP was incubated with 0.2 μM (a 1:2 molar ratio) or 2 μM thrombin (a 1:20 molar ratio) for 30 minutes at 30 °C before a scan was taken (see Fig. 88.). These ratios of pNP:thrombin were chosen based on the PAGE titrations (Fig. 84); 1:2 was expected to show weak opening, while 1:20 was expected to show near complete lid opening. This approach demonstrated a clear difference in the shape of the scans as more thrombin was added. Addition of thrombin lead to an increase in Cy3 emission and a decrease in Cy5 indicating decreasing FRET efficiency and increased distance between the FRET pairs implying lid opening (see Fig. 87 & Fig. 89.). However, it was difficult to ascertain the extent of lid opening as it was assumed that even in the open state FRET may still weakly occur; therefore, using the pNP with donor fluorophore only would not be an accurate control for maximal lid opening, as the lid is not expected to dissociate. To achieve maximum lid opening, the lid was artificially opened using the differential melting temperatures of the hinge and the docking regions on the pore. The pore was heated to 50 °C for 30 minutes to leave the lid bound only at the hinge region. In the absence of thrombin, it was considered that this may artificially overextend the lid compared to when bound to thrombin; however, as previously mentioned in Section 6.1. the melting temperature of the TBA has been reported to be ~53 °C,[345,346,351,352] in the presence of K$^+$ so this is expected to remain intact and

mirror the distance of the TBA-thrombin complex lid, making the heat-induced opening a good approximation. Following heating, the solution was then quickly added to a cuvette and scanned. This trace showed a slightly increased intensity for Cy3 emission and a slightly reduced Cy5 emission intensity compared to the trace for 2 μM thrombin implying that even at 2 μM, maximum lid opening has not been achieved. Based on this initial analysis, the extent of pNP lid opening was approximately 41% at 0.2 μM thrombin and 71% at 2 μM. The elevated temperature of the control must be considered as a factor as there is a possibility that at 50 °C (not far from the 56 °C pore or 53 °C TBA melting temperature) some of the pore has been destabilized leading to a greater increase compared to the 2 μM thrombin than is in fact the case. The elevated temperature could also affect the FRET signal. Nevertheless, the ensemble FRET analysis provided confirmation of a key result: the lid does in fact open upon thrombin binding.
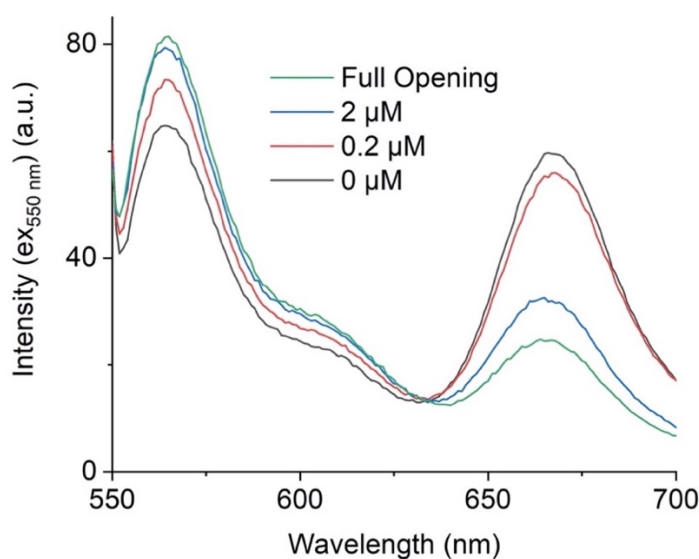
Figure 88. Ensemble fluorescence analysis of the thrombin-triggered opening of pNP. The pore carries a Cy3 tag (FRET donor) at the 3' end of the lid and a Cy5 tag (FRET acceptor) on the thymine loop of strand 3 at the pore opening. The close proximity of the two dyes leads to efficient Förster resonance energy transfer (FRET) manifested as a reduced Cy3 emission and elevated Cy5 emission in the pore's closed state. Addition of thrombin (final concentration of 0.2 μM (red) and 2 μM (blue)) to the pNP (0.1 μM) results in reduced FRET efficiency indicating an increased distance between the two fluorophores and implying successful thrombin-triggered opening of the pNP's lid. No change in FRET efficiency was observed in the absence of thrombin (black) while full opening (green) was observed after heating the pore to 50 °C to thermally open the lid. The corresponding increase in Cy3 and decrease in Cy5 emission indicates that thrombin binding leads to the lid's partial unzipping from the pore thereby separating the Cy3-lid from the Cy5 at the gate's barrel. Adapted from Lanphere *et al.*.[15]

The lid-opening process was then investigated kinetically. The conditions used for the scans was replicated. The pore was added to a cuvette at 100 nM and held for 5 min to allow the fluorescence signal to stabilise. Then, either buffer, 0.2 μM or 2 μM thrombin was rapidly added and the change in signal observed for 40 min. For ease of normalisation and comparison, only the trace for the Cy3 emission is shown. The Cy3 emission was selected over the Cy5 because it is on the lid and is therefore the species undergoing the change. The Cy5 emission was still measured and was used as an internal control for each run. The maximum extent of lid opening was again achieved by exploiting the differential melting temperatures between the lid and the hinge regions compared to docking sites D_1-D_3. Just as for the scans in Figure 88, the pore was incubated at 50 °C for 30 min to open the lid and then immediately placed into the fluorescence spectrophotometer. The emission intensity of the Cy3 and Cy5 in this control were observed to be tending back towards each other of the course of the 45 min run, which likely indicates that the lid began to close again as the temperature cooled (this was a prior observed phenomenon when assayed in gels). In light of this, the value chosen for the maximum extent of binding was that at 5 min when thrombin would have been added. Results were obtained for both pNP and pNP2 as well as a control pore, pNP3, the lid of which does not contain the TBA sequence. The results for pNP and pNP2 are shown below in Figure 89 and the results for pNP3 are shown in Figure 90.

In general, the FRET lid opening results mirror those obtained from the PAGE thrombin titrations. At both thrombin concentrations, pNP exhibited a greater extent of lid opening than pNP2, which was expected based on pNP's stronger affinity for thrombin. At 2 μM thrombin, pNP reached a maximum lid opening of 75.4 ± 12.5% vs 59.0 ± 8.53% for pNP2. There is a similar gap between the two pores at the same pore to thrombin ratio of 1:20 in the PAGE titrations, although the extent of lid opening is, in both cases, lower than the percent bound in the titrations. This discrepancy may indicate that not all binding leads to lid opening or it may imply that the control for maximum extend of lid opening provides too high a ceiling. Given the different temperature conditions for the control, this is a possibility. At 0.2 μM the two are more comparable with pNP reaching a maximum extent of opening at 36.4 ± 4.98% and pNP2 reaching 32.1 ± 1.65%. This is around what would be expected based on the titrations in both cases. Crucially, neither pNP nor pNP2 demonstrates any significant opening in the absence of thrombin (pNP: 2.25 ± 4.87%; pNP2: 4.85 ± 1.98%).
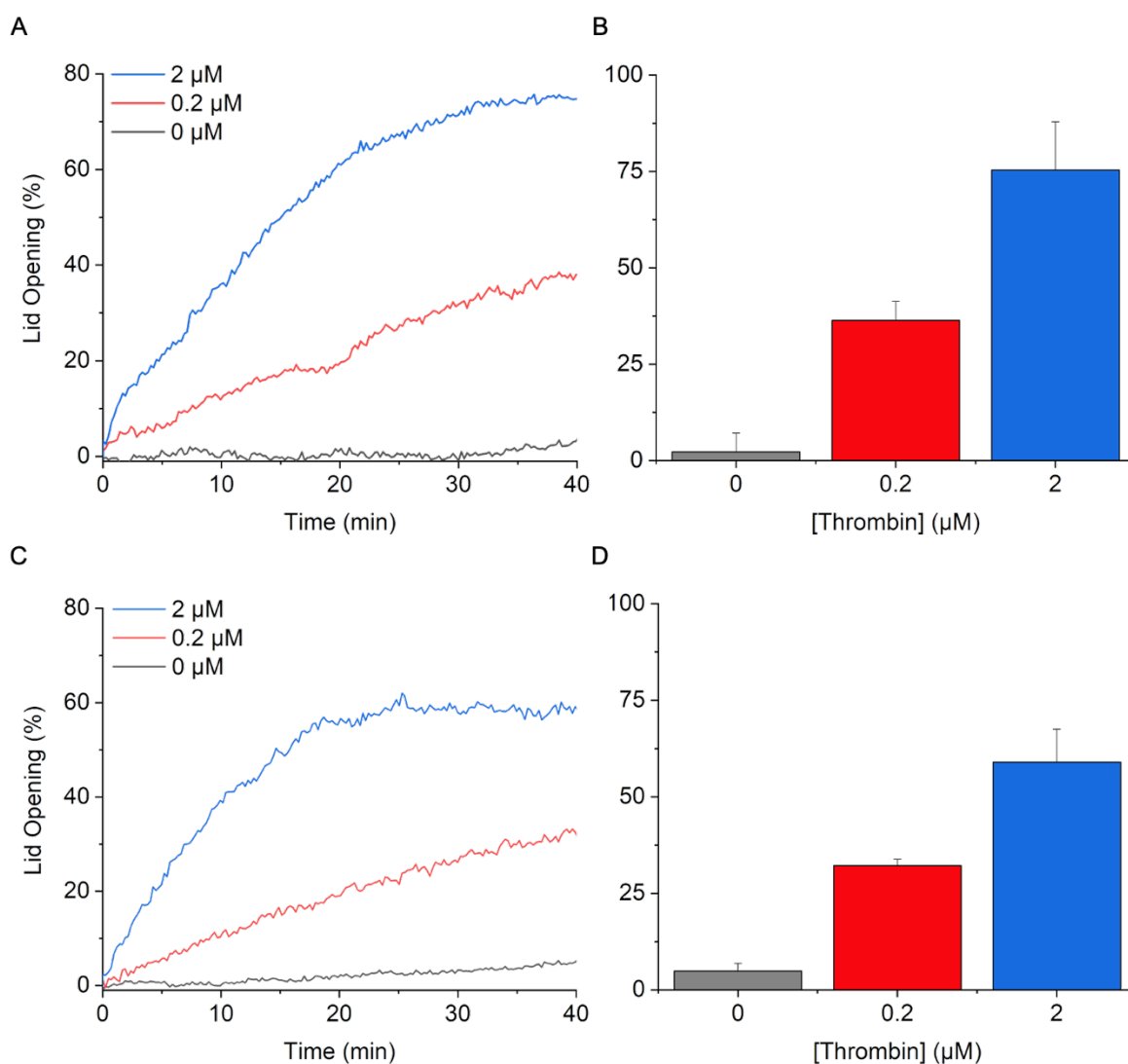
Figure 89. Kinetic fluorescence analysis of the thrombin-triggered opening of pNP. The opening of the lid is monitored as the change in FRET efficiency over-time as thrombin binding causes separation of the Cy3 dye (donor fluorophore) on the lid and the Cy5 dye (acceptor fluorophore) on the pore barrel. Lid opening results in separation of the dyes and a subsequent decrease in FRET efficiency manifest as an increase in Cy3 emission and a decrease in Cy5 emission when excited at 550 nm. For simplicity and ease of comparison, only the normalised Cy3 emission is shown. (A) Kinetic analysis of the Protein-gated lid opening of the pNP upon addition of 2 μM (blue), 0.2 μM (red) or 0 μM (black) thrombin monitored via FRET. (B) The maximum extent of pNP opening at each thrombin condition shown as a bar graph. (C) Kinetic analysis of pNP2 at each thrombin condition, the maximum extent of which is shown in (D) as a bar graph. Each trace is an average of three independent repeats, the standard deviation of which are shown by the error bars in the bar charts. Adapted from Lanphere *et al.*.[15]

The shape of the curves was then investigated. Looking first at the 2 μM traces, both curves exhibit the expected shape of logarithmic growth, especially considering the high thrombin to pore ratios

163

required to achieve binding saturation (see Fig. 84 and Fig. 86). Nevertheless, pNP2 undergoes an earlier and sharper levelling off than pNP. It is unclear why pNP2 levels off as sharply as it does. Investigating the PAGE band in Figure 85A for pNP2 at the 1:20 pore to thrombin ratio, a definite band shift is apparent, but it is not as clearly defined or upshifted as the corresponding band in Figure 84A for pNP. This may indicate that the less pronounced upshift is due to binding, but not complete lid opening or perhaps transient binding that does not lead to lid opening. Perhaps corroborating the weaker K_d this may suggest a higher barrier for lid actuation. It was hypothesized that the location of the TBA sequence in Lid-2 in pNP2 would lead to more hindered lid opening, which this does appear to corroborate. This may point to a complex equilibrium between thrombin concentration, binding and lid actuation. However, a detailed analysis of the thermodynamics of lid opening for both lid variants was beyond the scope of this project. In contrast to the 2 μM thrombin traces, which resemble a logarithmic growth curve, the traces for 0.2 μM are linear in shape. In addition, they both follow the same trend and there are no marked differences between the two, other than the pNP showing a slightly greater extent of lid opening. The point at which each individual trace levels off was calculated to determine the adequate amount of time to observe lid opening. The results are summarized in Table 8 below.

Table 8. Analysis of the average time required for maximum lid opening at different thrombin concentrations. Each time point was calculated as an average of three independent repeats.

	Time to achieve maximum lid opening (min)	
[Thrombin] (μM)	pNP	pNP2
0.2	37.5 ± 1.8	38.9 ± 1.4
2	31.2 ± 3.5	27.3 ± 3.8

As evident in Table 8, 30 min appeared to be an appropriate period of time for lid opening to occur for both pNP and pNP2 at 2 μM thrombin, but closer to 40 min was required for 0.2 μM thrombin. These results are consistent with the shapes of the respective curves at each thrombin concentration. It should be noted that these experiments were conducted at 22 °C. Incubation at 30 °C was expected to result in faster lid opening. In corroboration of this data, the results for the scans shown in Figure 88 for pNP – which were incubated at 30 °C for 30 min -- are within error of those obtained from the kinetic traces. That the values obtained from the scans and the kinetics were in agreement, despite the temperature difference, indicated that the maximum extent of lid opening had been met after 30 min. This also suggested that the narrow temperature window may have had a significant effect on the rate of lid opening.

The kinetics of lid opening were then investigated using an initial rates analysis. The initial rate for each condition was taken after 1 min. The results from each repeat were then averaged. The results are summarized below in in Table 9.

Table 9. Initial rates analysis of the thrombin mediated opening of the protein gate of pNP and pNP2. The initial rates were calculated as an average of three independent repeats.

[Thrombin] (µM)	Initial Rate (%.min^{-1})	
	pNP	pNP2
0.2	3.13 ± 1.2	2.05 ± 0.7
2	10.0 ± 1.9	8.01 ± 1.7

The initial rates follow the same trend as the maximum extent of release at each thrombin concentration for the two pores and pNP has a faster initial rate than pNP2 at both concentrations of thrombin. This supports the notion that the placement of the TBA sequence in pNP is more efficient than that of pNP2. While the initial rate of lid opening is slower in pNP2 it still does not readily explain the apparent ceiling experienced by pNP2. Not only that it appears earlier, but that the levelling off process appears to be faster than that of pNP (Fig. 89). Further investigation of the kinetics of lid opening suggests a complex mechanism. From the literature data summarised in Table 6, it is known that TBA-thrombin binding is a rapid process and exhibits strong binding. The literature also confirms that thrombin and TBA bind in a 1:1 stoichiometry (see Section 6.3.1.) as I have also shown (Fig. 76). Lid opening is, however, not such a simple process. Not only does TBA-thrombin binding need to occur, but the lid must also unzip from the three docking regions going from a largely duplexed state to a single stranded state – a thermodynamically unfavourable process. If the further relatively high binding saturation points for pNP and pNP2 to thrombin (in ratios of 1:20 and 1:40, respectively) are taken into account as well, this points to lid opening being governed by several mechanisms held in a complex equilibrium. As part of future work, it would be very interesting to perform detailed kinetic and mechanistic analysis to elucidate the complex lid opening mechanism.

Following this analysis and the differences between TBA-thrombin binding on its own compared to pNP- and pNP2-thrombin binding, a final control was necessary to prove that lid actuation is indeed linked to TBA-thrombin binding and not simply a result of thrombin addition to the pore. While the gel in Figure 86 confirmed that binding only occurs between the lid and thrombin, it doesn't prove that lid opening only occurs when thrombin-TBA binding occurs. To prove that the interaction between TBA and thrombin was required, a lid was designed, Lid-3, that does not contain the TBA sequence. The FRET lid opening experiment was repeated with this pore, noted pNP3, which is shown below in Figure 90.
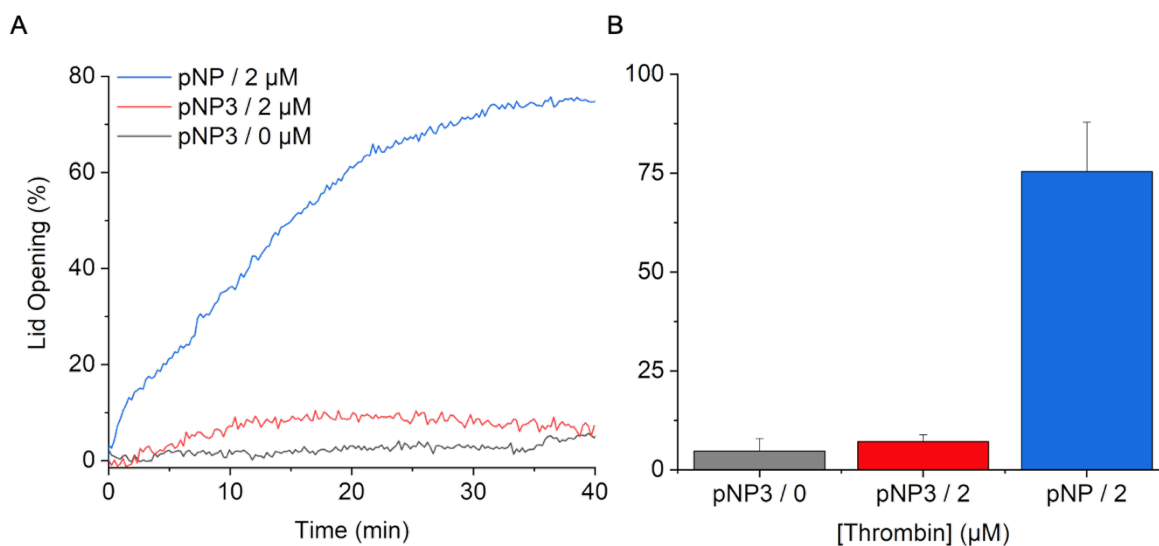
Figure 90. Kinetic fluorescence analysis to probe the specificity of lid actuation on the addition of thrombin using pNP3. pNP3 is a control pore that uses Lid-3, a lid that does not contain the TBA sequence. (A) Kinetic analysis of pNP3 and the pNP 2 μM thrombin trace shown for comparison. The lack of pNP3 opening even in the presence of a 20-fold excess of thrombin demonstrates the specificity of the aptamer and protein-gate. (B) Bar graph displaying the maximum extent of opening of the control pNP3 in the absence of thrombin (0 μM, black) and at 2 μM thrombin (blue) with the pNP 2 μM thrombin trace included for comparison. Each trace is an average of three independent repeats, the standard deviation of which are shown by the error bars in the bar charts. Adapted from Lanphere *et al.*.[15]

Upon addition of 2 μM thrombin, pNP3 did not demonstrate any significant opening over the 40 min compared to pNP3 when no thrombin was added, 7.12 ± 1.75% and 4.75 ± 3.18%, respectively. For comparison, the 2 μM thrombin induced lid opening of pNP from Figure 20 was included in the trace and bar graph in Figure 90 for comparison. This proves that lid opening is indeed driven by thrombin binding to the TBA in the lid.

6.3.6. Thrombin-Actuated Molecular Transport

Following the investigation into the lid and subsequent confirmation that thrombin was indeed required to actuate lid opening, it was necessary to investigate whether the protein-gate is able to control the transport of molecular cargo. To probe the transport properties of both the pNP and pNP2, a dye flux assay was used. Using a dye flux assay with a dye such as sulforhodamine B (SRB) is a powerful tool to monitor molecular transport only through the pore lumen as lipid bilayers are otherwise impermeable to SRB. Furthermore, SRB was a good choice of dye to assess transport, because it is small enough (~0.7 nm) to fit through the larger 6HB lumen (~2 nm), it carries a net charge of -1 so it was not expected to interact with the walls of the pore lumen and, in addition,

when SRB is encapsulated at high concentrations (> 20 mM) the dye is contact-quenched[115,118,368–371]. As the membrane was impermeable to SRB, fluorescence emission intensity was only restored following flux across the membrane or membrane lysis (Fig. 91). Therefore, any SRB flux across the membrane could be considered to have been transported across the membrane through the nanopore. In this way, the bulk transport properties of the nanopore could be assessed.

SRB (50 mM in 1 x PBS) was encapsulated in lipid vesicles formed from a 7:3 mole ratio of DOPC:DOPE. This lipid ratio has been well characterized for the dye flux assay.[15,115,118,125] These vesicles were then extruded through a 200 nm polycarbonate membrane to yield large unilamellar vesicles of ~200 nm in diameter (Figure 91). It has been previously reported that small nanopores with cholesterol lipid anchors insert more efficiently into lipid vesicles with a high degree of curvature.[11] External SRB was then removed and the buffer exchanged to 200 mM KCl, 10 mM Tris-HCl, pH 7.6. The external buffer was exchanged from PBS to this KCl buffer to better balance to interior and exterior osmoles in the absence of external SRB and so that during the assay secondary effects such as dye leakage are mitigated. Following purification, the vesicle suspension with encapsulated SRB was scanned using a fluorescence spectrometer to confirm successful encapsulation, contact quenching, and that a sufficient change in signal was observed upon lysis (Fig. 91).
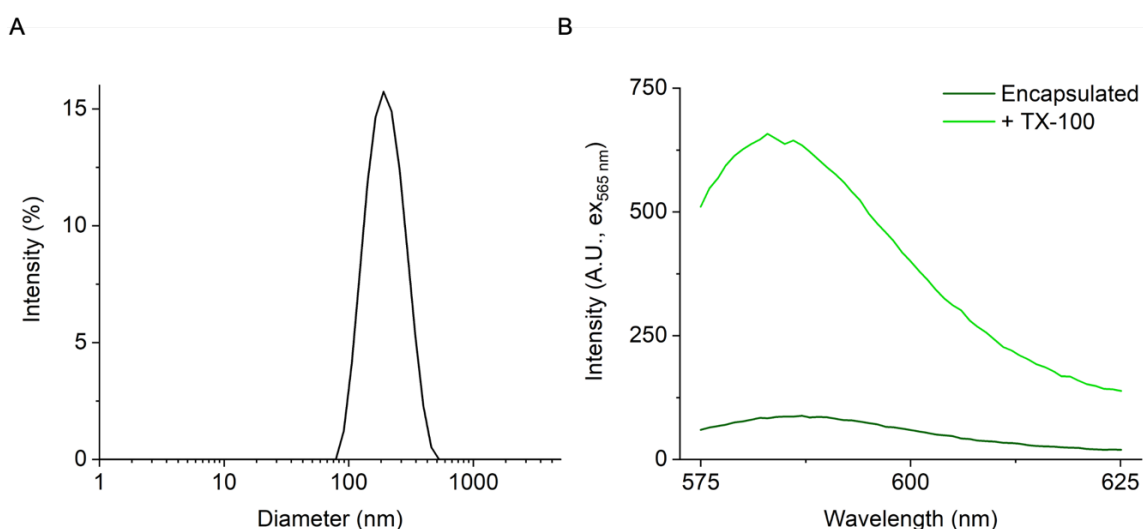
Figure 91. Characterization of vesicles used for the dye flux assay to probe the molecular transport properties of pNP and pNP2. (A) Dynamic light scattering analysis of vesicles formed from a 7:3 mole ratio of DOPC:DOPE with encapsulated 50 mM SRB. Analysis revealed LUVs with an average diameter of 216 ± 8 nm (n=3), which is consistent with extrusion 25 times through a 200 nm polycarbonate membrane. Adapted from Lanphere *et al.*.[15] (B) Fluorescence scan of purified LUVs with encapsulated SRB demonstrating that the fluorescence emission of SRB is quenched while encapsulated, but on addition of a detergent (Triton X-100) the vesicles are lysed releasing the SRB

into the external buffer, which ends contact-quenching and results in a strong increase in the intensity of SRB's fluorescence emission by ~ 7.5x.

The characterized LUVs with encapsulated SRB were then used to investigate the transport properties of the pNP and pNP2. Both Burns *et al.* and Arnott *et al.* have previously demonstrated that dye flux is possible with the base design of this pore; however, an important difference between the pNP and those pores is that thrombin, a 36 kDa protein, will remain bound to the lid, which is further tethered to the pore. Figure 77 shows that the lid has been designed such that it should be held down and away from the aperture upon opening. Nevertheless, there is the possibility, especially with pNP2 (that has the TBA located next to the hinge region), that thrombin may even transiently interact with the docking loops of the pore, which could block the lumen. Therefore, two of the primary concerns were whether (a) the lid opened sufficiently, while remaining bound to the pore, to permit molecular transport and (b) whether thrombin would block or in some other way prevent molecule transport. With this in mind, it was then of interest to see whether the location of the TBA in the lid affected the pore's ability to transport molecular cargo. A schematic for thrombin-actuation of the pNP gate allowing dye flux across a membrane is shown in Figure 92A.

Molecular transport was then probed using the SRB dye flux assay previously outlined in Chapter 5 (Section 5.2.7). Results were obtained for both pNP and pNP2 as well as the control pore, pNP3. This method was adapted from Lanphere *et al.*.[118] The results for both pNP and pNP2 are shown in Figure 92.
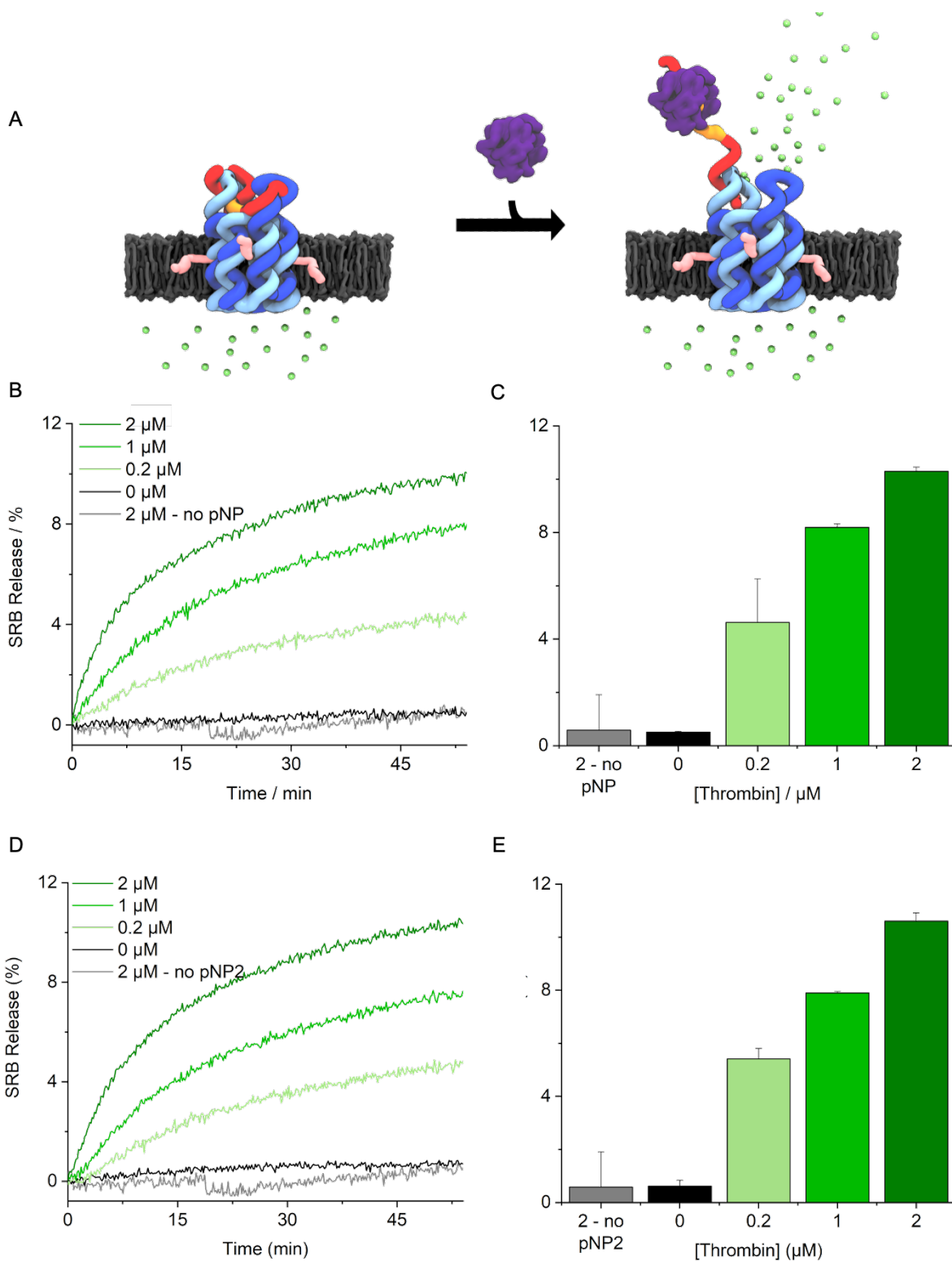
Figure 92. Thrombin-actuated opening of pNP controls transport of molecular cargo across a lipid bilayer. A) pNP is embedded in the lipid bilayer of LUVs with encapsulated SRB (green dots). At 50 mM, SRB is contact-quenched inside the vesicle and shows a muted fluorescence response. In the closed state of pNP, the encapsulated SRB cannot traverse the membrane. Addition of thrombin results in thrombin-TBA binding leading to the partial unzipping of the lid and the opening of the

gate to release SRB into the ambient buffer. The lower dye concentration abolishes contact-quenching and increases fluorescence. For visual clarity, a pore inserted in the membrane in the opposite orientation is not shown. The mixed orientations can lower the release to a degree of up to 50%. B) Kinetic traces of SRB fluorescence as a function of increasing thrombin concentration. 100% release is the total amount of fluorescence obtained upon rupturing vesicles with the detergent, Triton X-100. C) Bar chart of net fluorescence increase, summarizing data from (B). The data represent averages and standard deviations from at least 3 independent experiments. Adapted from Lanphere *et al.*.[15]

First and foremost, it was evident that both pNP and pNP2 successfully functioned as a membrane gate to control the transport of molecular cargo across the bilayer. In general, the results mirrored the results obtained from the FRET lid opening experiments outlined above in Section 6.3.5.. In the absence of thrombin, when the gate is closed, no significant molecular transport was observed through either pNP (0.51 ± 0.03%) or pNP2 (0.61 ± 0.23%). Indeed, what minimal change in fluorescence was observed may be attributed to background effects such as a few vesicles bursting or fusing or simply slight SRB leakage over the course of the experiment. Upon addition of thrombin, the protein-gate opens and allows dye flux across the membrane through the pore. As was observed with the FRET lid opening experiments, there is a thrombin concentration dependence to the extent of observed dye transport. Indeed, what is further striking is that a 10-fold increase in the concentration of thrombin (from 0.2 to 2 μM), which resulted in roughly a doubling of the extent of lid opening (Fig. 89), also results in a roughly 2-fold increase in the extend of dye release (pNP: 4.63 ± 1.63% at 0.2 μM and 10.30 ± 0.16% at 2 μM; pNP2: 5.41 ± 0.40% at 0.2 μM and 10.61 ± 0.31% at 2 μM; Fig. 92).
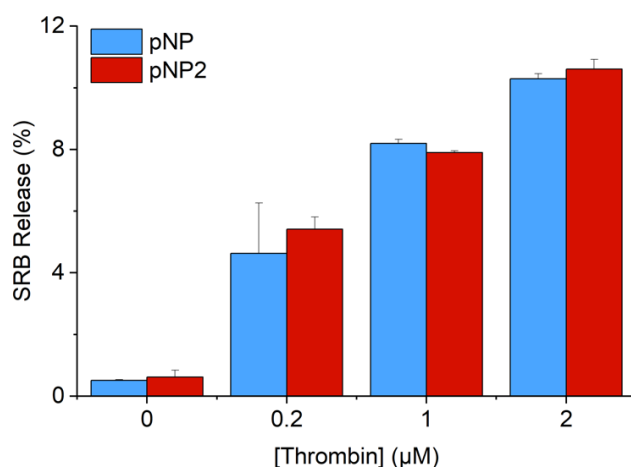
Figure 93. Comparison of the maximum extent of thrombin-mediated SRB release through pNP and pNP2 from LUVs demonstrating a thrombin-concentration dependence. Error bars represent the standard deviation from three independent repeats. Adapted from Lanphere *et al.*.[15]

In a marked divergence from both the gel binding assays and the FRET lid opening experiments, no significant difference in the extent of SRB release was observed between the two pores. This is shown more clearly by the comparative bar chart in Figure 93. This suggests that either the rate of transport was sufficiently slow compared to lid opening that the difference in thrombin binding affinity and the rate and extent of lid opening between the two pores became irrelevant or that the length of the dye-flux assay was sufficient for pNP2 to catch-up to pNP.

First, to rule out other effects, the experiment was repeated with pNP3, which, as discussed previously, has a lid that does not contain the TBA sequence and was shown not to exhibit lid opening upon addition of thrombin. As was the case with the FRET lid opening experiment, 2 μM thrombin was added to pNP3. The results for this experiment are shown below in Figure 94. Addition of 2 μM thrombin to pNP3 resulted in slightly noisy traces, but at 1.37 ± 0.81% demonstrated no significant transport. Indeed, it was similar to the thrombin control (0.58 ± 1.33%), which was 2 μM thrombin in the absence of any pores. Interestingly, this also resulted in noisy traces.
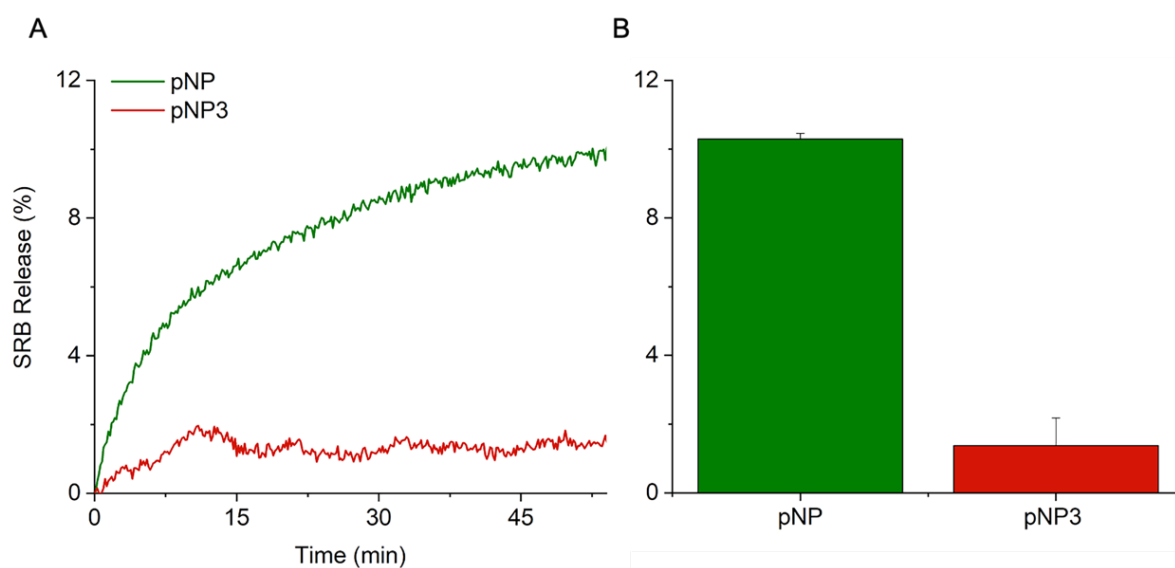
Figure 94. Comparison of SRB dye release from vesicles carrying pNP or pNP3.
The lid in pNP3 does not possess the TBA sequence making it unable to open in the presence of thrombin. pNP and pNP3 (30 μL, 1 μM) were added to vesicles containing 50 mM encapsulated SRB, which were then mixed with 2 μM thrombin. (A) Kinetic fluorescence traces of the dye release assay showing pNP (in green) pNP3 (red). (B) Bar chart of the net fluorescence increase after 50 min as illustrated in (A). The data represent averages and standard deviations from 3 independent experiments. Adapted from Lanphere et al..[15]

The lack of significant release from pNP3 indicated that the similar levels of release from pNP and pNP2 was not due to other effects but was indeed a result of thrombin-mediated lid opening and flux through the pore. Therefore, the discrepancy in the different activity shown in the gel-binding

assays and the FRET lid opening experiments compared to the dye flux assay must be related to the transport assay itself. This was first investigated using initial rates analysis. Compared to the traces for the FRET lid opening assay, the traces for the dye flux assay contained considerably more fluctuations. To overcome these fluctuations, the first 5 min of each trace was fit with a linear line and the initial rate calculated at 1, 1.5 and 2 min. These values were then averaged to reveal the initial rate for each trace. This was done to compensate for the fact that not all of the lines went through the origin. The results for the initial rate of release at each concentration of thrombin for pNP and pNP2 are summarized in Table 10.

Table 10. Initial rates analysis of the thrombin mediated transport of the fluorophore SRB through pNP and pNP2. The initial rates were calculated, and an average taken from three independent repeats.

	Initial Rate ($\%.min^{-1}$)	
[Thrombin] (μM)	pNP	pNP2
0.2	0.24 ± 0.04	0.07 ± 0.03
1	0.45 ± 0.10	0.22 ± 0.08
2	1.21 ± 0.17	0.67 ± 0.18

Before in depth analysis was conducted it was apparent that the initial rates for dye flux are an order of magnitude slower than the initial rates for lid opening. This suggests that the hypothesis proposed earlier was correct: compared to the rate of lid opening, the rate of dye flux through the pore is sufficiently slow that it is the rate limiting effect. However, in direct opposition to this hypothesis are the 50% lower initial rates of pNP2 compared to pNP and this ratio increases inversely with the concentration of thrombin. Looking at the traces in Figure 92, no stark visual difference is apparent between the rates of pNP and pNP2; however, pNP2 appears to have a slight lag at the beginning of the trace before the rate rapidly increases. It also appears that the duration of the lag is thrombin-concentration dependent. For comparison, this section of the traces was enlarged for both pNP and pNP2 in Figure 95.
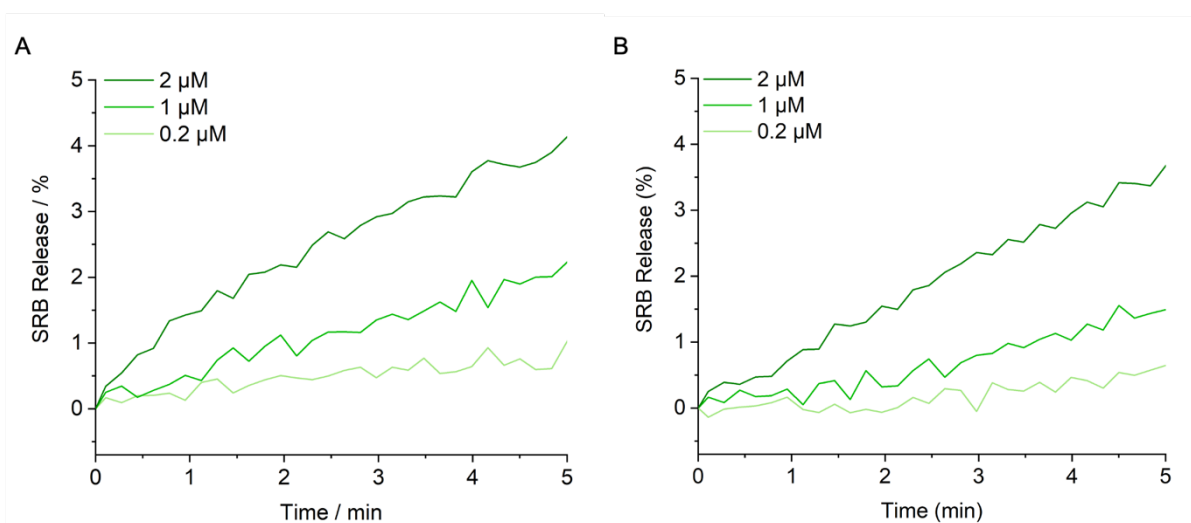
Figure 95. The first 5 min of the dye transport assay to investigate the difference in initial rates between pNP (A) and pNP2 (B). For clarity the pNP(2) only and thrombin only traces have been removed.

Comparing the two traces in Figure 95 above, the traces for pNP2 appear to show a period of very slow, if any, growth before the rate of release begins to rapidly increase. What is also interesting is that the length of time that this period of slow, if any, growth persists increases with decreasing thrombin concentration. It appears to last just under 1 min at 2 µM thrombin, around 2.5 min at 1 µM thrombin and between 3-4 min at 0.2 µM thrombin. This is interesting when compared to pNP, which does not exhibit a similar effect. This was determined not to be a processing error. Further analysis indicated that the extent of dye release produced by pNP at 5 min was only achieved by pNP2 at 6.5, 7.2 and 7.4 min at 2, 1 and 0.2 µM, respectively. Nevertheless, after the full 55 min, the maximum release from each of pNP and pNP2 was within error at all concentrations of thrombin.

As the pores are otherwise identical, this effect must necessarily be related to the placement of the TBA in the lid of each pore. While the initial rate of lid opening for pNP2 was slower than pNP, it was still substantially faster than the initial rate of transport. One explanation may be related to the location of the TBA in pNP2, which is attached to the end of the hinge region of the pore. It was previously speculated that this may cause thrombin to partially block the pore lumen for a brief period delaying transport. However, without detailed mechanistic studies, and perhaps molecular dynamics simulations, it will not be possible to say with any certainty. Needless to say, this effect does not appear to interfere with the overall ability of pNP2 to transport dye molecules over timescales that are more than adequate for future biotechnological or biomedical applications.

With future applications in mind, it was also of interest to investigate whether, in addition to a thrombin-concentration dependence, there was also a pore concentration dependence. For these experiments the previous conditions were replicated except that instead of a constant pore

concentration of 200 nM, the concentration was varied from 100 to 400 nM (Fig. 96). As the 1:10 ratio of pNP: thrombin had been successful in the previous set of experiments, this ratio was maintained for all pore concentration dependence experiments.
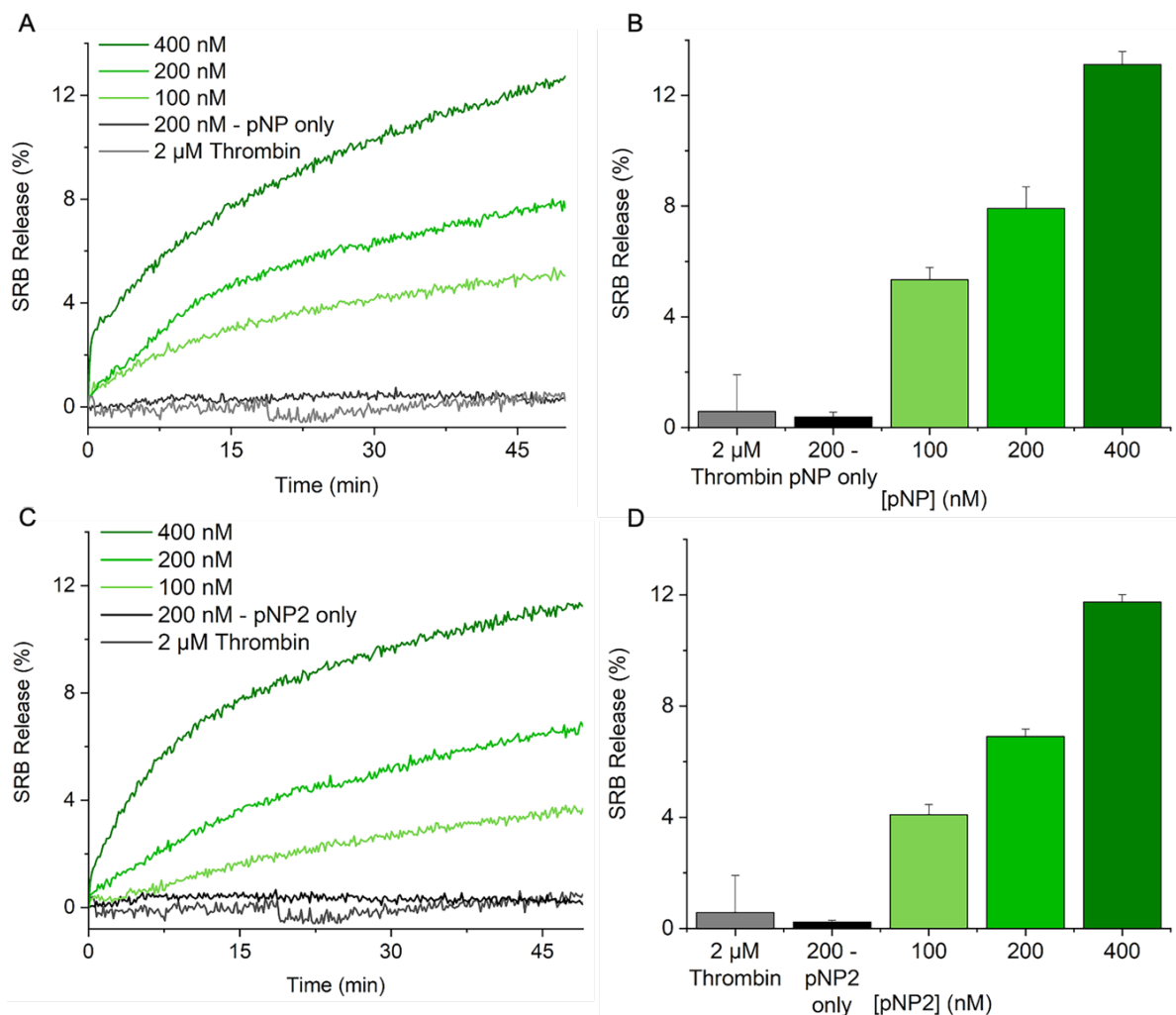
Figure 96. Dye transport assay investigating the thrombin-triggered fluorophore release as a function of pNP or pNP2 concentration. The experimental set-up is the same as the experiments to assay thrombin-concentration dependence. The ratio of thrombin:pore was held constant at 10:1 for all assays. (A) Kinetic traces of SRB fluorescence as a function of increasing pNP concentration. Release of 100% is the total amount of fluorescence obtained upon rupturing vesicles with detergent Triton-X-100. (B) Bar chart showing the percentage increase in SRB emission from (A). (C) Kinetic traces of SRB fluorescence as a function of increasing pNP2 concentration. Release of 100% is defined as above. (D) Bar chart showing the percentage increase in SRB emission from (C) The data represent averages and standard deviations from at least 3 independent experiments. Adapted from Lanphere *et al.*.[15]

As expected, a pore concentration-dependence was also observed for both pNP and pNP2. Looking at the bar charts in Figure 96B and D, it is interesting to note that, the shape of the increase in the maximum extent of SRB released at different pore concentrations appears to be exponential, whereas the shape of the increase for the thrombin-concentration dependence more closely resembled a logarithmic curve. That was not inherently surprising considering that addition of increasing amounts of thrombin to the same concentration of pore will yield increasingly diminished returns as once the lid is completely open that amount of transport done by a given pore will not change, while increasingly the concentration of the pore will result in a proportional increase in the amount of total SRB released.

Another interesting observation was that a difference between the amount of SRB released by pNP and pNP2 was now apparent. To highlight this observation, the bar graphs shown in Figures 96B and D were reproduced in Figure 97 for ease of comparison.
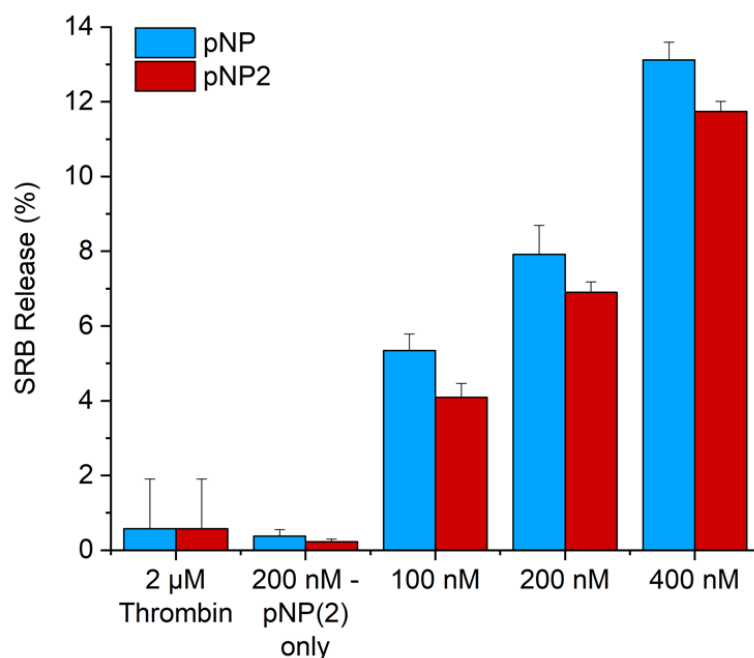
Figure 97. Comparison of the maximum extent of thrombin-mediated SRB release through pNP and pNP2 from LUVs demonstrating a pore-concentration dependence. Error bars represent the standard deviation from three independent repeats.

The first immediate observation is that pNP transported more SRB from LUVs at every concentration of pore assayed. An average difference of 1.2% release separates the two pore variants. This result was more in line with what was expected based on the gel-binding and FRET lid-opening experiments; however, it is now unclear why the previous set of results for the thrombin-concentration dependence showed that there was very little difference between pNP and pNP2 –

indeed, pNP2 even showed slightly higher release at 0.2 and 2 µM thrombin. To clarify, these experiments were repeated exactly as the previous set. The LUVs were prepared and left overnight before being purified in the morning the following day. They were then used within 48h of purification. 6 x 100 µL of 1 µM pNP and pNP2 were prepared, folded, combined and checked via PAGE before use. There were no discernible differences between any of the folds. All concentrations were done consecutively (pNP at a given concentration followed by pNP2 at the same concentration) to remove time as a potential variable.

One explanation for the difference in pNP vs pNP2 activity may be related to the temperature of the lab at the time the respective experiments were conducted. The pore concentration dependence experiments were conducted in late November when the temperature of the lab was around 18 °C, whereas the thrombin concentration dependence experiments were conducted in early August when the temperature in the lab was around 30 °C. This also likely explains the difference in the release at 200 nM, which for pNP was 10.30 ± 0.16% for the thrombin-concentration dependence and 7.92 ± 0.78% for the pore-concentration dependence: a difference of 2.38%. For pNP2 the difference is even more stark with a drop from 10.61 ± 0.31% for the thrombin-concentration dependence to 6.91 ± 0.27% for the pore-concentration dependence: a difference of 3.70%. While some difference in release between batches of vesicles is expected, this is unlikely to be the cause of both a substantial difference in release as well as a change in relative release between the two pores. The most likely explanation for the apparent parity in pNP and pNP2 activity at the higher temperature is that this mitigated an energetic barrier to pNP2 lid opening; most likely by improving the pNP2: thrombin binding ratio and increasing the extent of lid opening at a 1:10 pNP2: thrombin ratio. A temperature effect was previously suggested as a possible reason for the parity in results achieved between the scans and the kinetics for pNP lid opening at 0.2 µM thrombin, despite a difference of 10 min required to achieve the same level of release. However, as two different methods were used, this was not definitive. A more detailed mechanistic investigation would be required to confirm this.

Close inspection of the shape of the curves for pNP2 mediated release in Figure 96, reveals the same lag that was previously observed for pNP2 in the thrombin-concentration dependent experiment. This indicates that was not an artifact of the previous experiment. However, it does not appear to affect all conditions as it did in the previous thrombin-concentration experiment. Compared to pNP, all corresponding pNP2 curves show lower rates of release, which was expected given the lower overall maximum extend of release; however, the 400 nM appears to be unaffected, and the 200 nM only marginally affected, which is in line with the previous experiments. By contrast, the 100 nM pNP2 mediated release displays a particularly long lag (~5 min) before an increase is observed. As the pNP2:thrombin ratio was 1:10 as with the others, it is unlikely to be related to the ratio of thrombin. Nevertheless, the previously proposed hypothesis of partial thrombin blockage of the lumen following lid-opening based on the location of the TBA sequence in the lid likely also applies

here. As previously stated a better understanding would require a detailed mechanistic investigation of simulation.

The orientation of the pore likely also has an effect on the ability of the pNP to transport molecular cargo. If pNP were to insert in the opposite orientation – with the lid facing the interior of the LUVs – it would not be possible for dye flux to occur as the lid could not be unlocked. In theory, this could reduce the molecular transport capacity by up to 50%. However, the cholesterols were placed such that they are approximately 25% of the way up pNP in order to bias insertion in the correct orientation based on the proposed mechanism of nanopore insertion into lipid bilayers when modified with cholesterol lipid anchors by Birkholz *et al.*[131]. In addition to pore insertion in the lid-inwards orientation, it is possible that not all pNP will insert and that some will remain simply tethered to the surface. Indeed, Birkholz *et al.* further demonstrate that nanopores modified with 3-cholesterol lipid anchors can form clusters on the membrane surface due to interactions between the cholesterol anchors. The pNP has 4 cholesterol-lid anchors, which is expected to improve insertion into the highly curved membranes of the LUVs but may also leave pNP more open to cluster formation. If clusters do form, this will further reduce the transport capacity of the pNP.

6.3.7. A protein-gated nanodevice for targeted drug delivery

Having confirmed that thrombin-controlled transport through the pore was possible, the next step was to use the pNP to transport and deliver bio-relevant cargo. For this purpose, we wanted a cytotoxic drug that was small enough to fit through the 2 nm wide pore lumen and that was also clinically active against HeLa cervical cancer cell. It was also critical that the drug be water-soluble and be able to traverse the pNP. For this purpose, the clinically active ovarian and cervical cancer drug: topotecan[372] (marketed as Hycamtin by GlaxoSmithKline) was chosen (see Fig. 98).

Following on from the success of the dye flux assay, the same set-up was used here with topotecan in place of SRB to form a tri-component selective drug-delivery device. Topotecan was encapsulated at the therapeutically active concentration of 3 μM in LUVs composed of a 7:3 ratio of DOPC: DOPE in 300 mM KCl, 15 mM Tris-HCl, pH 7.4 to form two of the three components. The third component of the nanodevice being the pNP. Time and materials did not permit this assay to be performed for both pNP and pNP2 so only results for pNP2 were obtained. As the cell-based assay is run at 37 °C over the course of several days and given that pNP and pNP2 demonstrated comparable transport properties at higher temperatures and that time was not a factor, the two pores were considered interchangeable for this purpose. For the rest of this section, pNP will be a generic placeholder to refer to the pore, but pNP2, specifically, was used for this assay.

To form the tri-component nanodevice, pNP (1 µM) and topotecan filled LUVs (2.25 nM) were added in a 1:1 vol/vol ratio and well mixed. The tri-component nanodevice was then added to cells (final pNP and LUV concentrations of 100 nM and 0.225 nM). This was followed by addition of thrombin (16.5 µM final concentration). An excess of thrombin was used to ensure complete lid opening and maximise topotecan transport. A schematic for the cell-based assay is shown below in Figure 98. In addition to the functional nanodevice, the cells were also monitored with a range of controls including the nanodevice without thrombin, thrombin only, the topotecan only, topotecan loaded LUVs only and pNP only. Cells were monitored visually using a 20x air objective brightfield microscope after 1, 2 and 3 days (see Figure 99). After 3 d, cell viability was then ascertained using a WST-1 colorimetric assay.
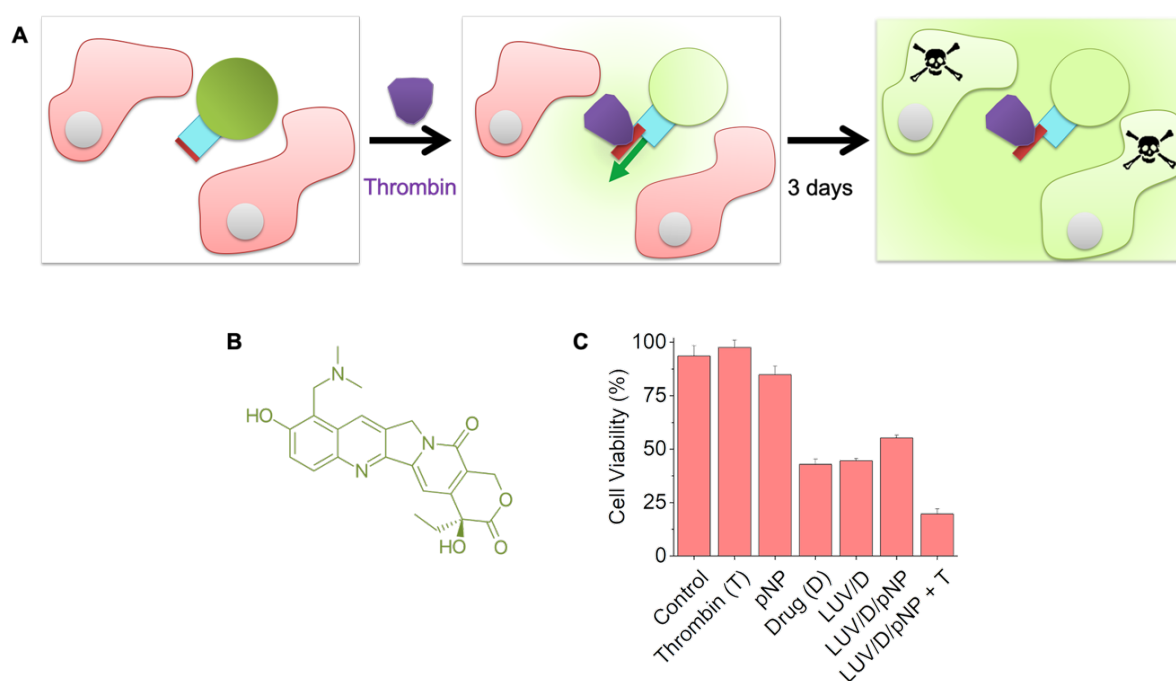
Figure 98. Protein-triggered opening of pNP releases a cytotoxic drug for controlled killing of cells. A) Scheme of the assay to demonstrate the controlled killing of HeLa cells (pink). The cells are exposed to pNP-functionalised-LUVs filled with the cytotoxic drug, topotecan (green), as well as thrombin (purple) to open pNP (blue, red), followed by incubation for 3 d to attain the cytotoxic effect of released topotecan. For visual clarity, a pore inserted in the membrane in the opposite orientation is not shown. The mixed orientations can lower the release to a degree of up to 50%. B) Chemical structure of topotecan. C) Graph displaying the viability of HeLa cells after 3 d incubation with either thrombin, pNP, topotecan, topotecan-filled LUVs with a lipid ratio of PC:PE (7:3), pNP-functionalised topotecan-filled LUVs, and the latter in combination with thrombin. The data represent averages and standard deviations collected from three independent repeats. The assay was carried out with pNP2 but is referred to as pNP for reasons of simplicity and because both variants

of the molecular gate have very similar transport properties. The cell viability was determined with the WST-1 colorimetric assay. Adapted from Lanphere *et al.*.[15]

The results of the cell-based assay demonstrate that the protein-gated nanodevice was more potent than topotecan alone or encapsulated in LUVs. Over the course of the three days, the viability of the HeLa cells in the presence of the nanodevice with added thrombin was reduced to 20 ± 2% compared to the cells incubated in buffer only, which had cell viability of 94 ± 5%. Topotecan showed itself to be a good choice of drug as, on its own, it resulted in a significant drop in cell viability to 43 ± 2%. Surprisingly, encapsulating topotecan in LUVs resulted in a very similar drop in cell viability (45 ± 1%) to the neat drug. This suggests that the LUVs can fuse with the cell membrane for intracellular drug delivery. What was also surprising was that if pNP was added to the LUVs with encapsulated topotecan, the drop in cell viability was reduced to 55 ± 1 %, perhaps suggesting that LUVs decoration with the negatively charged pNP reduces interaction or membrane fusion with the cell membrane. Therefore, this shows that the mode of action of the nanodevice is two-fold. 1) In the closed state, off-target effects are reduced compared to the neat drug (or drug encapsulated in LUVs) and 2) that upon addition of thrombin and the opening of the lid, the nanodevice results in a potent reduction in cell viability of 74% from the cells in buffer only. Neat topotecan, by comparison, results in only a 51% reduction in cell viability. Indeed, this reduction by the nanodevice even more potent when we consider than when thrombin is added on its own, there is actually an increase in cell viability to 98 ± 3% compared to the buffer control. Other studies have also found that addition of neat thrombin to HeLa cells results in an increase in cell viability compared to the control.[16] If we were to consider the reduction in cell viability from this point, the nanodevice would then have resulted in a reduction of 78% over the three days. The brightfield images of the cells at each timepoint for all conditions are shown in Figure 99 below.
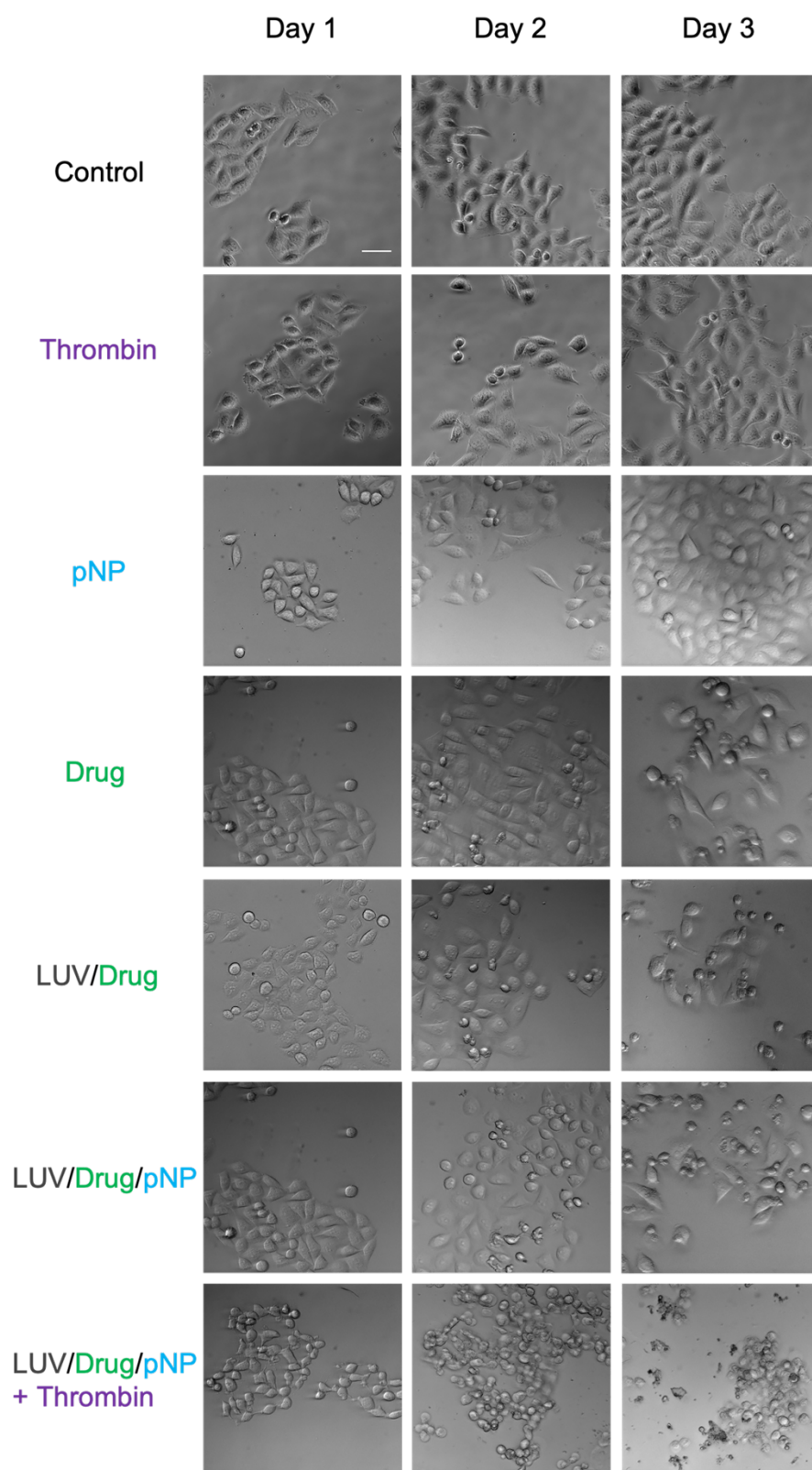
Figure 99. Brightfield images of HeLa cells, treated with different components of the nanodevice. Representative images from 3 independent experiments are shown. Images were captured using a 20x air objective at timepoints of 1, 2 and 3 days. pNP in this illustration refers specifically to pNP2. Scale bar, 50 μm. Adapted from Lanphere *et al.*.[15]

6.4. Conclusion

This chapter explored the design, assembly, characterization and function of a DNA nanopore that is able to function as a synthetic biomimetic protein-gated nanopore (pNP). The pore is based on an archetypal six-helical bundle DNA architecture,[118] but features two looped extensions from the top of the pore to accommodate a lid. These loops comprise three docking regions, which have a low T_m, and a hinge region, which has a high T_m, allowing the lid to open and yet remain bound to the pore. The lid features a 15-nucleotide long aptamer sequence that folds into a G-quadruplex with a high affinity for thrombin. The aptamer is known as the "thrombin binding aptamer" or TBA. The affinity of the TBA for thrombin was successfully assayed and a dissociation constant consistent with the literature was generated. Two variants of the pNP were designed with the TBA sequence in alternative lumen-spanning regions of the lid: one between a docking region and the hinge region (pNP) and one between two docking regions (pNP2).

The appropriate folding conditions were ascertained and both pNP and pNP2 were shown to have successfully folded with and without the lids as well as with and without four cholesterol lipid anchors using gel electrophoresis. UV thermal melts were also used to confirm structural stability and explore structural characteristics. Furthermore, a variant of the pNP that carries a TAMRA fluorophore (pNP^{TAMRA}) was shown to insert into the lipid bilayer of a giant unilamellar vesicle using confocal laser scanning microscopy.

The effect on TBA-thrombin binding of the placement of the TBA within the lid of the nanopore was investigated. Both pNP and pNP2 successfully demonstrated binding to thrombin using gel shift assays; however, their binding affinities were 5x and 10x weaker, respectively, compared to the TBA alone. In addition, the apparent ratio of pNP to thrombin required for full binding was shown to be 1:20 for pNP and 1:40 for pNP2 compared to 1:1 for the TBA alone. Furthermore, it was confirmed that the pNP only interacts with thrombin via the TBA in the lid.

Thrombin actuation of the lid was explored using a FRET lid opening assay. Crucially, thrombin was shown to actuate the lid of both pNP and pNP2 and, as indicated by the gel shift assay, there was a thrombin concentration dependence to lid opening. The differences in the rate and extent of lid opening as well as the time required to achieve maximum lid opening were investigated at different thrombin concentrations for both pNP and pNP2. Significantly, no lid opening was observed in the absence of either thrombin or the TBA in the lid.

Following confirmation of thrombin-induced lid actuation, the capacity of the pNP for molecular transport was investigated using a dye flux assay. The dye flux assay successfully demonstrated that both pNP and pNP2 were able to control the transport of a fluorescent dye from large unilamellar

vesicles. In the absence of thrombin or the TBA sequence no dye flux was observed. Furthermore, both a thrombin and a pore concentration dependence were established. The effect of TBA placement in the lid as well as the effect of temperature on the extent of dye released were also explored.

The ability of the pNP to function as part of a therapeutic nanodevice to selectively deliver cytotoxic cargo to HeLa cells was investigated using a cell-viability assay. Upon addition of thrombin the pNP successfully delivered the cervical and ovarian cancer drug, topotecan, from LUVs to HeLa cells resulting in a >50% reduction in cell viability compared to the neat drug and a 78% reduction compared to the control. In addition, the nanodevice also reduced off-target effects compared to the neat drug. In the absence of thrombin, the nanodevice resulted in a drop in cell viability of only 39% compared to the 51% of the neat drug compared to the control.

6.5 Future Work

In the future, it would be of interest to engineer the lid to be reversible. It has already been shown that TBA on its own has a stronger binding affinity to thrombin so this could be exploited to remove thrombin from the lid. Beyond simply removing the target, it would also be interesting to develop a smart lid that opened in the presence of a target analyte but closed in the presence of another. This would prevent pore function at non-target sites as well as allow activity to be tailored. It would also be of interest to conduct a detailed mechanistic study of lid opening using molecular dynamics. This could allow such a smart lid to be designed with precisely controlled function.

The logical next step would also be to replace the TBA with other aptamers. The design of the nanopore is very modular so only the lid would need to be replaced making the design very versatile. The TBA has a very short sequence, and the G-quadruplex is a very compact structure, which are advantageous when it comes to lid stability. Longer aptamer sequences and/or larger secondary structures may pose a challenge. The loops of the pore could be extended to add more stability, but this will have to be balanced as this may make the pore too unstable once the lid is opened. This may not be a factor once the pore is inserted into a membrane, but it would need to be considered. Using this design on a larger pore could also help accommodate a larger aptamer, but it may not prevent leaks as well.,

A further step would be to try to use the pore as a synthetic gate in a cellular membrane. Alternatively, this technology could be used to make model synthetic cells by functioning as the cellular membrane machinery. The ease with which the aptamer could be changed makes this design well suited for this type of application.

7. Conclusion

This thesis presented two methods to control the activity of small barrel-like DNA nanopores: (1) pore assembly that can be triggered from inactive components on the membrane surface to yield an active pore and (2) inclusion of a protein-gate to modulate transport activity unless in the presence of a trigger protein. Both methods proved effective to prevent activity in their inactive or closed states. Furthermore, the specificity of the trigger mechanism was demonstrated in each case. In each case, activity was demonstrated: activity as a synthetic ion channel and the ability to function as part of a nanodevice for targeted drug delivery. Both of these methods fulfil the aim of this thesis by advancing the capability of small barrel-like DNA nanopores.

In addition, both methods have successfully replicated the function of biological proteins. Pore assembly on the membrane surface replicates protein and peptide pore formation, which has not been previously demonstrated. Protein and peptide pore monomers tend to be compact structures that have well defined interactions with the lipid bilayer and each other. DNA tends to have a looser structure and the effect of the membrane on the assembly of two tethered components was not well understood. With the addition of the insight gained from DNA hybridisation under steric constraints from the model system, this thesis provides insight on both pore assembly as well as the interaction of DNA nanostructures on the membrane surface.

The modulation of channel activity by addition of a specific analyte, or class of analyte, is a common motif for biological surface pores. Synthetic DNA-based gates have been previously demonstrated using a ligand and temperature gate, but this work advances on those by using a biologically relevant trigger. Two different placements of the aptamer sequence within the lid were explored to provide insight into the gate-design and the mechanism of gate-function. Both of these methods represent advances in the use of DNA nanotechnology, and more specifically DNA nanopores, to replicate natural functions.

Both pores were designed to be modular in design to allow for straightforward adaptation and application. The design of the components was fairly straightforward and should be able easily accommodate additional duplexes, which may even improve stability, to be applicable for larger diameter nanopores. Similarly, the locking mechanism could be easily adapted to function in analogy to the protein-gate or via some other exogenous trigger. The location of the aptamer sequence within the lid of the protein-gated pore allows it to be easily swapped for an aptamer for any desired target without significantly impacting the overall design. It is expected that both methods for the control over assembly and pore function will be widely applicable for biomedicine and as research tools within DNA nanotechnology, and chemical and synthetic biology.

Finally, the work produced in this thesis was used to develop a unified set of protocols for the design, assembly and characterisation of membrane-spanning DNA nanopores.[118] The field of DNA nanopores is rapidly evolving and garnering increased interest from the scientific community. However, despite this general interest, no unified protocol for the design, assembly and characterisation of DNA nanopores existed. The few protocols that were available were typically produced for protein or peptide nanopores, which were not always relevant or applicable. This set of protocols was recently published in Nature Protocols[118] and is expected to further aid the development of the field of DNA nanopores and their application in DNA nanotechnology and chemical and synthetic biology.

8. Bibliography

1   B. Alberts, A. Johnson, J. Lewis, M. Raff, K. Roberts and P. Walter, *Molecular Biology of the Cell, 4th Edition*, Garland Science, New York, 4th edn., 2002.

2   M. Langecker, V. Arnaut, J. List and F. C. Simmel, *Acc. Chem. Res.*, 2014, **47**, 1807–1815.

3   H. I. Petrache, S. W. Dodd and M. F. Brown, *Biophys. J.*, 2000, **79**, 3172–3192.

4   H. H. G. Tsai, J. Bin Lee, H. S. Li, T. Y. Hou, W. Y. Chu, P. C. Shen, Y. Y. Chen, C. J. Tan, J. C. Hu and C. C. Chiu, *Biochim. Biophys. Acta - Biomembr.*, 2015, **1848**, 1234–1247.

5   D. Offenbartl-Stiegert, UCL (University College London), 2020.

6   M. M. Lapinski, A. Castro-Forero, A. J. Greiner, R. Y. Ofoli and G. J. Blanchard, *Langmuir*, 2007, **23**, 11677–11683.

7   V. Nele, M. N. Holme, U. Kauscher, M. R. Thomas, J. J. Doutch and M. M. Stevens, *Langmuir*, 2019, **35**, 6064–6074.

8   A. Akbarzadeh, R. Rezaei-Sadabady, S. Davaran, S. W. Joo, N. Zarghami, Y. Hanifehpour, M. Samiei, M. Kouhi and K. Nejati-Koshki, *Nanoscale Res. Lett.*, 2013, **8**, 1–8.

9   K. M. Scherer, J.-H. Spille, H.-G. Sahl, F. Grein and U. Kubitscheck, *Biophys. J.*, 2015, **108**, 1114–1124.

10   P. M. Arnott, H. Joshi, A. Aksimentiev and S. Howorka, *Langmuir*, 2018, **34**, 15084–15092.

11   J. R. Burns and S. Howorka, *ACS Nano*, 2018, **12**, 3263–3271.

12   L. Blau and G. Weissmann, *Biochemistry*, 1988, **27**, 5661–5666.

13   P. C. A. Barreleiro, R. P. May and B. Lindman, in *Faraday Discussions*, 2002, vol. 122, pp. 191–201.

14   Y. Okumura and Y. Iwata, *Membranes (Basel).*, 2011, **1**, 109–118.

15   C. Lanphere, P. M. Arnott, S. F. Jones, K. Korlova and S. Howorka, *Angew. Chemie Int. Ed.*, 2021, **60**, 1903–1908.

16   L. Gao, Y. Cui, Q. He, Y. Yang, J. Fei and J. Li, *Chem. - A Eur. J.*, 2011, **17**, 13170–13174.

17   R. D. Hills and N. McGlinchey, *J. Comput. Chem.*, 2016, **37**, 1112–1118.

18   W. Chen, F. Duša, J. Witos, S.-K. Ruokonen and S. K. Wiedmer, *Sci. Rep.*, 2018, **8**, 14815.

19   D. Papahadjopoulos and J. C. Watkins, *BBA - Biomembr.*, 1967, **135**, 639–652.

20   A. Kessel, N. Ben-Tal and S. May, *Biophys. J.*, 2001, **81**, 643–658.

21   S.-T. Yang, A. J. B. Kreutzberger, J. Lee, V. Kiessling and L. K. Tamm, *Chem. Phys. Lipids*, 2016, **199**, 136–143.

22   S. J. Singer and G. L. Nicolson, *Science*, 1972, **175**, 720–731.

23   G. L. Nicolson, *Biochim. Biophys. Acta - Biomembr.*, 2014, **1838**, 1451–1466.

24   membrane | Definition, Structure, & Functions | Britannica, https://www.britannica.com/science/membrane-biology, (accessed 28 March 2021).

25   S. Howorka, *Curr. Opin. Biotechnol.*, 2011, 22, 485–491.

26   C. Strambio-De-Castillia, M. Niepel and M. P. Rout, *Nat. Rev. Mol. Cell Biol.*, 2010, **11**, 490–

501.

27   C. Dekker, *Nat. Nanotechnol.*, 2007, **2**, 209–215.

28   S. Bhakdil and J. Tranum-Jensen, *Microbiol. Mol. Biol. Rev*, 1991, **55**, 733–751.

29   I. Iacovache, F. G. van der Goot and L. Pernot, *Biochim. Biophys. Acta - Biomembr.*, 2008, 1778, 1611–1623.

30   R. A. Hirst, A. Kadioglu, C. O'Callaghan and P. W. Andrew, *Clin. Exp. Immunol.*, 2004, 138, 195–201.

31   S. P. Hardy, T. Lund and P. E. Granum, *FEMS Microbiol. Lett.*, 2001, **197**, 47–51.

32   J. T. Buckley, S. P. Howard, A. K. Chopra and C. W. Houston, *Infect. Immun.*, 1999, 67, 466–467.

33   J. A. T. Young and R. J. Collier, *Annu. Rev. Biochem.*, 2007, **76**, 243–265.

34   W. Shi, A. K. Friedman and L. A. Baker, *Anal. Chem.*, 2017, **89**, 157–188.

35   S. Howorka, *Nat. Nanotechnol.*, 2017, 12, 619–630.

36   J. J. Kasianowicz, E. Brandin, D. Branton and D. W. Deamer, *Proc. Natl. Acad. Sci.*, 1996, **93**, 13770–13773.

37   O. Braha, L. Q. Gu, L. Zhou, X. Lu, S. Cheley and H. Bayley, *Nat. Biotechnol.*, 2000, **18**, 1005–1007.

38   L. Q. Gu, O. Braha, S. Conlan, S. Cheley and H. Bayley, *Nature*, 1999, **398**, 686–690.

39   J. Ettedgui, J. J. Kasianowicz and A. Balijepalli, *J. Am. Chem. Soc.*, 2016, **138**, 7228–7231.

40   M. Kukwikila and S. Howorka, *Anal. Chem.*, 2015, **87**, 9149–9154.

41   L. Harrington, S. Cheley, L. T. Alexander, S. Knapp and H. Bayley, *Proc. Natl. Acad. Sci. U. S. A.*, 2013, **110**, E4417-26.

42   K. Göpfrich, C. Y. Li, M. Ricci, S. P. Bhamidimarri, J. Yoo, B. Gyenes, A. Ohmann, M. Winterhalter, A. Aksimentiev and U. F. Keyser, *ACS Nano*, 2016, **10**, 8207–8214.

43   J. Clarke, H.-C. Wu, L. Jayasinghe, A. Patel, S. Reid and H. Bayley, *Nat. Nanotechnol.*, 2009, **4**, 265–270.

44   C. Yang, F. Sesterhenn, J. Bonet, E. A. van Aalen, L. Scheller, L. A. Abriata, J. T. Cramer, X. Wen, S. Rosset, S. Georgeon, T. Jardetzky, T. Krey, M. Fussenegger, M. Merkx and B. E. Correia, *Nat. Chem. Biol.*, 2021, **17**, 492–500.

45   G. A. Khoury, J. Smadbeck, C. A. Kieslich and C. A. Floudas, *Trends Biotechnol.*, 2014, **32**, 99–109.

46   D. Setiawan, J. Brender and Y. Zhang, *Expert Opin. Drug Discov.*, 2018, **13**, 587–604.

47   B. N. Miles, A. P. Ivanov, K. A. Wilson, F. Doğan, D. Japrung and J. B. Edel, *Chem. Soc. Rev.*, 2013, **42**, 15–28.

48   N. Li, S. Yu, C. C. Harrell and C. R. Martin, *Anal. Chem.*, 2004, **76**, 2025–2030.

49   J. H. Yuan, F. Y. He, D. C. Sun and X. H. Xia, *Chem. Mater.*, 2004, **16**, 1841–1844.

50   N. Fertig, C. Meyer, R. H. Blick, C. Trautmann and J. C. Behrends, *Phys. Rev. E - Stat. Nonlinear, Soft Matter Phys.*, 2001, **64**, 409011–409014.

51   J. Li, D. Stein, C. McMullan, D. Branton, M. J. Aziz and J. a Golovchenko, *Nature*, 2001, **412**, 166–169.

52   A. Siwy, Zuzanna, Fuliński, *Phys. Rev. Lett.*, 2002, **89**, 198103.

53   A. J. Storm, J. H. Chen, X. S. Ling, H. W. Zandbergen and C. Dekker, *Nat. Mater.*, 2003, **2**, 537–540.

54   S. R. Park, H. Peng and X. S. Ling, *Small*, 2007, **3**, 116–119.

55   C. C. Harrell, S. B. Lee and C. R. Martin, *Anal. Chem.*, 2003, **75**, 6861–6867.

56   J. A. Rodríguez-Manzo, M. Puster, A. Nicolaï, V. Meunier and M. Drndic, *ACS Nano*, 2015, **9**, 6555–6564.

57   N. A. W. Bell, M. Muthukumar and U. F. Keyser, *Phys. Rev. E - Stat. Nonlinear, Soft Matter Phys.*, 2016, **93**, 022401.

58   W. Li, N. A. W. Bell, S. Hernández-Ainsa, V. V Thacker, A. M. Thackray, R. Bujdoso and U. F. Keyser, *ACS Nano*, 2013, **7**, 4129–4134.

59   C. Plesa, J. W. Ruitenberg, M. J. Witteveen and C. Dekker, *Nano Lett.*, 2015, **15**, 3153–3158.

60   M. M. Marshall, J. Ruzicka, O. K. Zahid, V. C. Henrich, E. W. Taylor and A. R. Hall, *Langmuir*, 2015, **31**, 4582–4588.

61   H. W. Ch Postma, *Nano Lett.*, 2010, **10**, 420–425.

62   Z. Siwy, P. Apel, D. Baur, D. D. Dobrev, Y. E. Korchev, R. Neumann, R. Spohr, C. Trautmann and K. O. Voss, in *Surface Science*, 2003, vol. 532–535, pp. 1061–1066.

63   A. R. Hall, A. Scott, D. Rotem, K. K. Mehta, H. Bayley and C. Dekker, *Nat. Nanotechnol.*, 2010, **5**, 874–877.

64   M. G. Blackburn, M. Gait, D. Loakes and D. M. Williams, *Nucleic Acids in Chemistry and Biology*, Royal Society of Chemistry, Cambridge, 2007.

65   N. C. Seeman and P. S. Lukeman, *Rep. Prog. Phys*, 2005, **68**, 237–270.

66   J. D. Watson and F. H. C. Crick, *Nature*, 1953, **171**, 737–738.

67   N. C. Seeman, *Sci. Am.*, 2004, **290**, 64–75.

68   N. C. Seeman, *Nature*, 2003, **421**, 427–431.

69   S. Naz and A. Fatima, *Mol. Biotechnol.*, 2013, **53**, 345–350.

70   A. Vainrub and B. M. Pettitt, *Biopolymers*, 2003, **68**, 265–270.

71   J. C. García-Ramos, R. Galindo-Murillo, F. Cortés-Guzmán and L. Ruiz-Azuara, *J. Mex. Chem. Soc.*, 2017, **57**, 245–259.

72   J. M. Berg, J. L. Tymoczko and L. Stryer, *Biochemistry*, W H Freeman, New York, 5th edn., 2002.

73   R. Holliday, *Genet. Res., Camb*, 1964, **5**, 282–304.

74   L. Martino, A. Virno, A. Randazzo, A. Virgilio, V. Esposito, C. Giancola, M. Bucci, G. Cirino and L. Mayol, *Nucleic Acids Res.*, 2006, **34**, 6653–6662.

75   M. Guéron and J. L. Leroy, *Curr. Opin. Struct. Biol.*, 2000, 10, 326–331.

76   N. C. Seeman, *J. Theor. Biol.*, 1982, **99**, 237–247.

77   N. R. Kallenbach, R.-I. Ma and N. C. Seeman, *Nature*, 1983, **305**, 829–831.

78   J. Chen and N. C. Seeman, *Nature*, 1991, **350**, 631–633.

79   Y. W. Zhang and N. C. Seeman, *J. Am. Chem. Soc.*, 1994, **116**, 1661–1669.

80   P. W. K. Rothemund, *Nature*, 2006, **440**, 297–302.

81   E. Benson, A. Mohammed, J. Gardell, S. Masich, E. Czeizler, P. Orponen and B. Högberg, *Nature*, 2015, **523**, 441–444.

82   N. E. C. Haley, T. E. Ouldridge, I. Mullor Ruiz, A. Geraldini, A. A. Louis, J. Bath and A. J. Turberfield, *Nat. Commun.*, 2020, **11**, 2562.

83   B. Yurke, A. J. Turberfield, A. P. Mills, F. C. Simmel and J. L. Neumann, *Nature*, 2000, **406**, 605–608.

84   D. Y. Zhang and E. Winfree, *J. Am. Chem. Soc.*, 2009, **131**, 17303–17314.

85   J. Li, A. Johnson-Buck, Y. R. Yang, W. M. Shih, H. Yan and N. G. Walter, *Nat. Nanotechnol.*, 2018, **13**, 723–729.

86   A. J. Thubagere, W. Li, R. F. Johnson, Z. Chen, S. Doroudi, Y. L. Lee, G. Izatt, S. Wittman, N. Srinivas, D. Woods, E. Winfree and L. Qian, *Science*, 2017, **357**, eaan6558.

87   L. Yang, Y. Zhao, X. Xu, K. Xu, M. Zhang, K. Huang, H. Kang, H. Lin, Y. Yang and D. Han, *Angew. Chemie Int. Ed.*, 2020, **59**, 17697–17704.

88   H. Pei, X. Zuo, D. Zhu, Q. Huang and C. Fan, *Accounts Chem Res*, 2014, **47**, 550–559.

89   T. Omabegho, R. Sha and N. C. Seeman, *Science*, 2009, **324**, 67–71.

90   S. Li, Q. Jiang, S. Liu, Y. Zhang, Y. Tian, C. Song, J. Wang, Y. Zou, G. J. Anderson, J.-Y. Han, Y. Chang, Y. Liu, C. Zhang, L. Chen, G. Zhou, G. Nie, H. Yan, B. Ding and Y. Zhao, *Nat. Biotechnol.*, 2018, **36**, 258–264.

91   A. S. Walsh, H. Yin, C. M. Erben, M. J. A. Wood and A. J. Turberfield, *ACS Nano*, 2011, **5**, 5427–5432.

92   J. O. McNamara, E. R. Andrechek, Y. Wang, K. D. Viles, R. E. Rempel, E. Gilboa, B. A. Sullenger and P. H. Giangrande, *Nat. Biotechnol.*, 2006, **24**, 1005–1015.

93   H. Lee, A. K. R. Lytton-Jean, Y. Chen, K. T. Love, A. I. Park, E. D. Karagiannis, A. Sehgal, W. Querbes, C. S. Zurenko, M. Jayaraman, C. G. Peng, K. Charisse, A. Borodovsky, M. Manoharan, J. S. Donahoe, J. Truelove, M. Nahrendorf, R. Langer and D. G. Anderson, *Nat. Nanotechnol.*, 2012, **7**, 389–393.

94   R. Hu, X. Zhang, Z. Zhao, G. Zhu, T. Chen, T. Fu and W. Tan, *Angew. Chemie Int. Ed.*, 2014, **53**, 5821–5826.

95   P. Wang, M. A. Rahman, Z. Zhao, K. Weiss, C. Zhang, Z. Chen, S. J. Hurwitz, Z. G. Chen, D. M. Shin and Y. Ke, *J. Am. Chem. Soc.*, 2018, **140**, 2478–2484.

96   D. Bhatia, S. Surana, S. Chakraborty, S. P. Koushika and Y. Krishnan, *Nat. Commun.*, , DOI:10.1038/ncomms1337.

97   N. Arulkumaran, C. Lanphere, C. Gaupp, J. R. Burns, M. Singer and S. Howorka, *ACS Nano*, 2021, **15**, 4394–4404.

98   G. Zhu, R. Hu, Z. Zhao, Z. Chen, X. Zhang and W. Tan, *J. Am. Chem. Soc.*, 2013, **135**, 16438–16445.

99   D. Jiang, Z. Ge, H. J. Im, C. G. England, D. Ni, J. Hou, L. Zhang, C. J. Kutyreff, Y. Yan, Y. Liu, S. Y. Cho, J. W. Engle, J. Shi, P. Huang, C. Fan, H. Yan and W. Cai, *Nat. Biomed. Eng.*, 2018, **2**, 865–877.

100   D. Zboralski, K. Hoehlig, D. Eulberg, A. Frömming and A. Vater, *Cancer Immunol. Res.*, 2017, **5**, 950–956.

101   J. R. Burns, N. Al-Juffali, S. M. Janes and S. Howorka, *Angew. Chemie Int. Ed.*, 2014, **53**, 12466–12470.

102   T. Diederichs, G. Pugh, A. Dorey, Y. Xing, J. R. Burns, Q. Hung Nguyen, M. Tornow, R. Tampé and S. Howorka, *Nat. Commun.*, 2019, **10**, 1–11.

103   N. A. W. Bell, C. R. Engst, M. Ablay, G. Divitini, C. Ducati, T. Liedl and U. F. Keyser, *Nano Lett.*, 2012, **12**, 512–517.

104   S. Hernández-Ainsa, N. A. W. Bell, V. V. Thacker, K. Göpfrich, K. Misiunas, M. E. Fuentes-Perez, F. Moreno-Herrero and U. F. Keyser, *ACS Nano*, 2013, **7**, 6024–6030.

105   Y.-S. Borghei, M. Hosseini, M. Dadmehr, S. Hosseinkhani, M. R. Ganjali and R. Sheikhnejad, *Anal. Chim. Acta*, 2016, **904**, 92–97.

106   K. M. Flavier and S. G. Boxer, *Biophys. J.*, 2017, **113**, 1260–1268.

107   G. Stengel, R. Zahn and F. Höök, *J. Am. Chem. Soc.*, 2007, **129**, 9584–9585.

108   Y. Yang, M. A. Goetzfried, K. Hidaka, M. You, W. Tan, H. Sugiyama and M. Endo, *Nano Lett.*, 2015, **15**, 6672–6676.

109   S. F. J. Wickham, J. Bath, Y. Katsuda, M. Endo, K. Hidaka, H. Sugiyama and A. J. Turberfield, *Nat. Nanotechnol.*, 2012, **7**, 169–173.

110   O. I. Wilner, Y. Weizmann, R. Gill, O. Lioubashevski, R. Freeman and I. Willner, *Nat. Nanotechnol.*, 2009, **4**, 249–254.

111   J. Nangreave, H. Yan and Y. Liu, *J. Am. Chem. Soc.*, 2011, **133**, 4490–4497.

112   S. M. Shamah, J. M. Healy and S. T. Cload, *Acc. Chem. Res.*, 2008, **41**, 130–138.

113   D. H. J. Bunka and P. G. Stockley, *Nat. Rev. Microbiol.*, 2006, **4**, 588–596.

114   J. R. Burns, E. Stulz and S. Howorka, *Nano Lett.*, 2013, **13**, 2351–2356.

115   J. R. Burns, A. Seifert, N. Fertig and S. Howorka, *Nat. Nanotechnol.*, 2016, **11**, 152–158.

116   M. Langecker, V. Arnaut, T. G. Martin, J. List, S. Renner, M. Mayer, H. Dietz and F. C. Simmel, *Science*, 2012, **338**, 932–936.

117   S. Howorka, *Science*, 2016, 352, 890–891.

118   C. Lanphere, D. Offenbartl-Stiegert, A. Dorey, G. Pugh, E. Georgiou, Y. Xing, J. R. Burns and S. Howorka, *Nat. Protoc.*, 2021, **16**, 86–130.

119   K. Göpfrich, C. Y. Li, I. Mames, S. P. Bhamidimarri, M. Ricci, J. Yoo, A. Mames, A. Ohmann, M. Winterhalter, E. Stulz, A. Aksimentiev and U. F. Keyser, *Nano Lett.*, 2016, **16**, 4665–4669.

120   S. M. Douglas, A. H. Marblestone, S. Teerapittayanon, A. Vazquez, G. M. Church and W. M.

Shih, *Nucleic Acids Res.*, 2009, **37**, 5001–5006.

121 H. Jun, F. Zhang, T. Shepherd, S. Ratanalert, X. Qi, H. Yan and M. Bathe, *Sci. Adv.*, 2019, **5**, eaav0655.

122 E. de Llano, H. Miao, Y. Ahmadi, A. J. Wilson, M. Beeby, I. Viola and I. Barisic, *Nucleic Acids Res.*, 2020, **48**, 8269–8275.

123 A. Seifert, K. Göpfrich, J. R. Burns, N. Fertig, U. F. Keyser and S. Howorka, *ACS Nano*, 2015, **9**, 1117–1126.

124 V. Maingi, J. R. Burns, J. J. Uusitalo, S. Howorka, S. J. Marrink and M. S. P. Sansom, *Nat. Commun.*, 2017, **8**, 14784.

125 P. M. Arnott and S. Howorka, *ACS Nano*, 2019, **13**, 3334–3340.

126 A. Ohmann, C.-Y. Li, C. Maffeo, K. Al Nahas, K. N. Baumann, K. Göpfrich, J. Yoo, U. F. Keyser and A. Aksimentiev, *Nat. Commun.*, 2018, **9**, 2426.

127 K. Göpfrich, T. Zettl, A. E. C. Meijering, S. Hernández-Ainsa, S. Kocabey, T. Liedl and U. F. Keyser, *Nano Lett.*, 2015, **15**, 3134–3138.

128 H. Joshi and P. K. Maiti, *Nucleic Acids Res.*, 2018, **46**, 2234–2242.

129 S. Krishnan, D. Ziegler, V. Arnaut, T. G. Martin, K. Kapsner, K. Henneberg, A. R. Bausch, H. Dietz and F. C. Simmel, *Nat. Commun.*, 2016, **7**, 12787.

130 J. R. Burns, K. Göpfrich, J. W. Wood, V. V. Thacker, E. Stulz, U. F. Keyser and S. Howorka, *Angew. Chemie Int. Ed.*, 2013, **52**, 12069–12072.

131 O. Birkholz, J. R. Burns, C. P. Richter, O. E. Psathaki, S. Howorka and J. Piehler, *Nat. Commun.*, 2018, **9**, 1521.

132 M. D. E. Jepsen, R. S. Sørensen, C. Maffeo, A. Aksimentiev, J. Kjems and V. Birkedal, *Nanoscale*, 2019, **11**, 18475–18482.

133 P. Chidchob, D. Offenbartl-Stiegert, D. McCarthy, X. Luo, J. Li, S. Howorka and H. F. Sleiman, *J. Am. Chem. Soc.*, 2019, **141**, 1100–1108.

134 M. Banchelli, F. Gambinossi, A. Durand, G. Caminati, T. Brown, D. Berti and P. Baglioni, *J. Phys. Chem. B*, 2010, **114**, 7348–7358.

135 M. Banchelli, F. Betti, D. Berti, G. Caminati, F. B. Bombelli, T. Brown, L. M. Wilhelmsson, B. Nordén and P. Baglioni, *J. Phys. Chem. B*, 2008, **112**, 10942–10952.

136 F. Gambinossi, M. Banchelli, A. Durand, D. Berti, T. Brown, G. Caminati and P. Baglioni, *J. Phys. Chem. B*, 2010, **114**, 7338–7347.

137 M. E. Haberland and J. A. Reynolds, *Proc. Natl. Acad. Sci. U. S. A.*, 1973, **70**, 2313–2316.

138 J. Burns and S. Howorka, *Nanomaterials*, 2019, **9**, 490.

139 S. Krishnan, D. Ziegler, V. Arnaut, T. G. Martin, K. Kapsner, K. Henneberg, A. R. Bausch, H. Dietz and F. C. Simmel, *Nat. Commun.*, , DOI:10.1038/ncomms12787.

140 J. R. Thompson, B. Cronin, H. Bayley and M. I. Wallace, *Biophys. J.*, 2011, **101**, 2679–2683.

141 S. Bhakdi, H. Bayley, A. Valeva, I. Walev, B. Walker, U. Weller, M. Kehoe and M. Palmer, *Arch. Microbiol.*, 1996, 165, 73–79.

142   C. D. Fjell, J. A. Hiss, R. E. W. Hancock and G. Schneider, *Nat. Rev. Drug Discov.*, 2011, **11**, 37–51.

143   L. Messager, J. R. Burns, J. Kim, D. Cecchin, J. Hindley, A. L. B. Pyne, J. Gaitzsch, G. Battaglia and S. Howorka, *Angew. Chemie - Int. Ed.*, 2016, **55**, 11106–11109.

144   E. S. Andersen, M. Dong, M. M. Nielsen, K. Jahn, R. Subramani, W. Mamdouh, M. M. Golas, B. Sander, H. Stark, C. L. P. Oliveira, J. S. Pedersen, V. Birkedal, F. Besenbacher, K. V. Gothelf and J. Kjems, *Nature*, 2009, **459**, 73–76.

145   N. Hamaguchi, A. Ellington and M. Stanton, *Anal. Biochem.*, 2001, **294**, 126–131.

146   G. Mayer, *Angew. Chemie - Int. Ed.*, 2009, **48**, 2672–2689.

147   P. R. Bouchard, R. M. Hutabarat and K. M. Thompson, *Annu. Rev. Pharmacol. Toxicol.*, 2010, **50**, 237–257.

148   G. Zhu and X. Chen, *Adv. Drug Deliv. Rev.*, 2018, 134, 65–78.

149   A. V Lakhin, V. Z. Tarantul and L. V Gening, *Acta Naturae*, 2013, 5, 34–43.

150   A. D. Ellington and J. W. Szostak, *Nature*, 1990, **346**, 818–822.

151   W. Zhou, R. Saran and J. Liu, *Chem. Rev.*, 2017, **117**, 8272–8325.

152   M. Rajendran and A. D. Ellington, *Anal. Bioanal. Chem.*, 2008, **390**, 1067–1075.

153   H. Qu, A. T. Csordas, J. Wang, S. S. Oh, M. S. Eisenstein and H. T. Soh, *ACS Nano*, 2016, **10**, 7558–7565.

154   R. D. Jenison, S. C. Gill, A. Pardi and B. Polisky, *Science*, 1994, **263**, 1425–1429.

155   M. A. D. Neves, O. Reinstein, M. Saad and P. E. Johnson, *Biophys. Chem.*, 2010, **153**, 9–16.

156   A. Ruscito and M. C. DeRosa, *Front. Chem.*, , DOI:10.3389/fchem.2016.00014.

157   C.-H. Kim, L.-P. Lee, J.-R. Min, M.-W. Lim and S.-H. Jeong, *Biosens. Bioelectron.*, 2014, **51**, 426–430.

158   D. E. Huizenga and J. W. Szostak, *Biochemistry*, 1995, **34**, 656–665.

159   C. H. Lin and D. J. Patel, *Nat. Struct. Biol.*, 1996, **3**, 1046–1050.

160   R. Chinnappan, R. AlZabn, A. K. Fataftah, A. Alhoshani and M. Zourob, *Anal. Bioanal. Chem.*, 2020, **412**, 4691–4701.

161   C. Tuerk and L. Gold, *Science*, 1990, **249**, 505–510.

162   P. Mallikaratchy, R. V. Stahelin, Z. Cao, W. Cho and W. Tan, *Chem. Commun.*, 2006, 3229.

163   D. A. Daniels, H. Chen, B. J. Hicke, K. M. Swiderek and L. Gold, *Proc. Natl. Acad. Sci.*, 2003, **100**, 15416–15421.

164   J. Hu, J. Wu, C. Li, L. Zhu, W. Y. Zhang, G. Kong, Z. Lu and C. J. Yang, *ChemBioChem*, 2011, **12**, 424–430.

165   C. B. Chen, G. A. Chernis, V. Q. Hoang and R. Landgraf, *Proc. Natl. Acad. Sci.*, 2003, **100**, 9226–9231.

166   M. Liu, J. Wang, Y. Chang, Q. Zhang, D. Chang, C. Y. Hui, J. D. Brennan and Y. Li, *Angew. Chemie - Int. Ed.*, 2020, **59**, 7706–7710.

167   L. C. Bock, L. C. Griffin, J. A. Latham, E. H. Vermaas and J. J. Toole, *Nature*, 1992, **355**, 564–

566.

168   R. F. Macaya, J. A. Waldron, B. A. Beutel, H. Gao, M. E. Joesten, M. Yang, R. Patel, A. H. Bertelsen and A. F. Cook, *Biochemistry*, 1995, **34**, 4478–4492.

169   A. Pasternak, F. J. Hernandez, L. M. Rasmussen, B. Vester and J. Wengel, *Nucleic Acids Res.*, 2011, **39**, 1155–1164.

170   Y. Bai, Y. Li, D. Zhang, H. Wang and Q. Zhao, *Anal. Chem.*, 2017, **89**, 9467–9473.

171   H. Ulrich Goringer, M. Zacharias, M. Engstler, M. Homann and M. Lorger, *Comb. Chem. High Throughput Screen.*, 2006, **9**, 491–499.

172   W. Pan, R. C. Craven, Q. Qiu, C. B. Wilson, J. W. Wills, S. Golovine and J. F. Wang, *Proc. Natl. Acad. Sci.*, 1995, **92**, 11509–11513.

173   P. Parekh, Z. Tang, P. C. Turner, R. W. Moyer and W. Tan, *Anal. Chem.*, 2010, **82**, 8642–8649.

174   X. Zou, J. Wu, J. Gu, L. Shen and L. Mao, *Front. Microbiol.*, 2019, **10**, 1462.

175   I. Lebars, P. Legrand, A. Aimé, N. Pinaud, S. Fribourg and C. Di Primo, *Nucleic Acids Res.*, 2008, **36**, 7146–7156.

176   S. Yamazaki and M. Famulok, in *Methods in Molecular Biology*, Humana Press, Totowa, NJ, 2009, vol. 535, pp. 187–199.

177   S. Yamazaki, L. Tan, G. Mayer, J. S. Hartig, J.-N. Song, S. Reuter, T. Restle, S. D. Laufer, D. Grohmann, H.-G. Kräusslich, J. Bajorath and M. Famulok, *Chem. Biol.*, 2007, **14**, 804–812.

178   M. A. Ditzler, D. Bose, N. Shkriabai, B. Marchand, S. G. Sarafianos, M. Kvaratskhelia and D. H. Burke, *Nucleic Acids Res.*, 2011, **39**, 8237–8247.

179   J. G. Bruno and J. L. Kiel, *Biosens. Bioelectron.*, 1999, **14**, 457–464.

180   F. Chen, X. L. Zhang, J. Zhou, S. Liu and J. Liu, *Mol. Biol. Rep.*, 2012, **39**, 2157–2162.

181   C. A. Kellenberger, C. Chen, A. T. Whiteley, D. A. Portnoy and M. C. Hammond, *J. Am. Chem. Soc.*, 2015, **137**, 6432–6435.

182   W. Song, R. L. Strack and S. R. Jaffrey, *Nat. Methods*, 2013, **10**, 873–875.

183   J. Mi, Y. Liu, Z. N. Rabbani, Z. Yang, J. H. Urban, B. A. Sullenger and B. M. Clary, *Nat. Chem. Biol.*, 2010, **6**, 22–24.

184   P. J. Bates, J. B. Kahlon, S. D. Thomas, J. O. Trent and D. M. Miller, *J. Biol. Chem.*, 1999, **274**, 26369–26377.

185   P. J. Bates, D. A. Laber, D. M. Miller, S. D. Thomas and J. O. Trent, *Exp. Mol. Pathol.*, 2009, **86**, 151–164.

186   D. Shangguan, Z. C. Cao, Y. Li and W. Tan, *Clin. Chem.*, 2007, **53**, 1153–1155.

187   Y. Xu, J. A. Phillips, J. Yan, Q. Li, Z. H. Fan and W. Tan, *Anal. Chem.*, 2009, **81**, 7436–7442.

188   H. Liu, Z. Zhu, H. Kang, Y. Wu, K. Sefan and W. Tan, *Chem. - A Eur. J.*, 2010, **16**, 3791–3797.

189   Z. Tang, D. Shangguan, K. Wang, H. Shi, K. Sefah, P. Mallikratchy, H. W. Chen, Y. Li and W. Tan, *Anal. Chem.*, 2007, **79**, 4900–4907.

190   Z. Tang, P. Parekh, P. Turner, R. W. Moyer and W. Tan, *Clin. Chem.*, 2009, **55**, 813–822.

191 J. J. Trausch, M. Shank-Retzlaff and T. Verch, *Vaccine*, 2017, **35**, 5495–5502.

192 W. Rowe, M. Platt and P. J. R. Day, *Integr. Biol.*, 2009, **1**, 53–58.

193 L. Li, X. Chen, C. Cui, X. Pan, X. Li, H. S. Yazd, Q. Wu, L. Qiu, J. Li and W. Tan, *J. Am. Chem. Soc.*, 2019, **141**, 17174–17179.

194 T. Hermann and D. J. Patel, *Science*, 2000, 287, 820–825.

195 P.-H. Lin, R.-H. Chen, C.-H. Lee, Y. Chang, C.-S. Chen and W.-Y. Chen, *Colloids Surfaces B Biointerfaces*, 2011, **88**, 552–558.

196 P. H. Lin, S. L. Yen, M. S. Lin, Y. Chang, S. R. Louis, A. Higuchi and W. Y. Chen, *J. Phys. Chem. B*, 2008, **112**, 6665–6673.

197 I. R. Krauss, A. Pica, A. Merlino, L. Mazzarella and F. Sica, *Acta Crystallogr. Sect. D Biol. Crystallogr.*, 2013, **69**, 2403–2411.

198 J. Zhang, R. R. O. Loo and J. A. Loo, *J. Am. Soc. Mass Spectrom.*, 2017, **28**, 1815–1822.

199 J. E. Smith, C. D. Medley, Z. Tang, D. Shangguan, C. Lofton and W. Tan, *Anal. Chem.*, 2007, **79**, 3075–3082.

200 M. Kimoto, R. Yamashige, K. I. Matsunaga, S. Yokoyama and I. Hirao, *Nat. Biotechnol.*, 2013, **31**, 453–457.

201 J. C. Cox, P. Rudolph and A. D. Ellington, *Biotechnol. Prog.*, 1998, **14**, 845–850.

202 L. S. Green, C. Bell and N. Janjic, *Biotechniques*, 2001, **30**, 1094–1110.

203 M. A. Dellafiore, J. M. Montserrat and A. M. Iribarren, *Front. Chem.*, 2016, 4, 18.

204 A. Davydova, M. Vorobjeva, D. Pyshnyi, S. Altman, V. Vlassov and A. Venyaminova, *Crit. Rev. Microbiol.*, 2016, **42**, 847–865.

205 A. Cibiel, C. Pestourie and F. Ducongé, *Biochimie*, 2012, **94**, 1595–1606.

206 D. Han, Z. Zhu, C. Wu, L. Peng, L. Zhou, B. Gulbakan, G. Zhu, K. R. Williams and W. Tan, *J. Am. Chem. Soc.*, 2012, **134**, 20797–20804.

207 C. R. Ireson and L. R. Kelland, *Mol. Cancer Ther.*, 2006, **5**, 2957–2962.

208 J. Zhou and J. Rossi, *Nat. Rev. Drug Discov.*, 2017, **16**, 181–202.

209 K. Sefah, Z. W. Tang, D. H. Shangguan, H. Chen, D. Lopez-Colon, Y. Li, P. Parekh, J. Martin, L. Meng, J. A. Phillips, Y. M. Kim and W. H. Tan, *Leukemia*, 2009, **23**, 235–244.

210 T. Iwagawa, S. P. Ohuchi, S. Watanabe and Y. Nakamura, *Biochimie*, 2012, **94**, 250–257.

211 K. Sefah, D. Shangguan, X. Xiong, M. B. O'Donoghue and W. Tan, *Nat. Protoc.*, 2010, **5**, 1169–1185.

212 Y.-A. Shieh, S.-J. Yang, M.-F. Wei and M.-J. Shieh, *ACS Nano*, 2010, **4**, 1433–1442.

213 Y. Liu, C.-T. Kuan, J. Mi, X. Zhang, B. M. Clary, D. D. Bigner and B. A. Sullenger, *Biol. Chem.*, 2009, **390**, 137–144.

214 A. A. Haller and P. Sarnow, *Proc. Natl. Acad. Sci.*, 1997, **94**, 8521–8526.

215 L. Cerchia and V. de Franciscis, *Trends Biotechnol.*, 2010, **28**, 517–525.

216 L. Civit, I. Theodorou, F. Frey, H. Weber, A. Lingnau, C. Gröber, M. Blank, C. Dambrune, J. Stunden, M. Beyer, J. Schultze, E. Latz, F. Ducongé, M. H. G. Kubbutat and G. Mayer, *Sci.*

Rep., 2019, **9**, 4976.

217   G. Zhu, H. Zhang, O. Jacobson, Z. Wang, H. Chen, X. Yang, G. Niu and X. Chen, *Bioconjug. Chem.*, 2017, **28**, 1068–1075.

218   T. Amato, A. Virgilio, L. Pirone, V. Vellecco, M. Bucci, E. Pedone, V. Esposito and A. Galeone, *Sci. Rep.*, 2019, **9**, 9184.

219   B. Niebel, C. Lentz, M. Pofahl, G. Mayer, A. Hoerauf, K. M. Pfarr and M. Famulok, *Chem. - A Eur. J.*, 2010, **16**, 11100–11107.

220   M. Hafner, E. Vianini, B. Albertoni, L. Marchetti, I. Grüne, C. Gloeckner and M. Famulok, *Nat. Protoc.*, 2008, **3**, 579–587.

221   G. Pasut and F. M. Veronese, *J. Control. Release*, 2012, **161**, 461–472.

222   S. Schwartz and W. M. Amoaku, *Drugs*, 2005, **65**, 1578.

223   D. Maberley, *Issues Emerg. Health Technol.*, 2005, 1–4.

224   C. P. Rusconi, J. D. Roberts, G. A. Pitoc, S. M. Nimjee, R. R. White, G. Quick, E. Scardino, W. P. Fay and B. A. Sullenger, *Nat. Biotechnol.*, 2004, **22**, 1423–1428.

225   M. C. Willis, B. Collins, T. Zhang, L. S. Green, D. P. Sebesta, C. Bell, E. Kellogg, S. C. Gill, A. Magallanez, S. Knauer, R. A. Bendele, P. S. Gill and N. Janjić, *Bioconjug. Chem.*, 1998, **9**, 573–582.

226   K. Heo, S.-W. Min, H. J. Sung, H. G. Kim, H. J. Kim, Y. H. Kim, B. K. Choi, S. Han, S. Chung, E. S. Lee, J. Chung and I.-H. Kim, *J. Control. Release*, 2016, **229**, 1–9.

227   H. Dougan, D. M. Lyster, C. V. Vo, A. Stafford, J. I. Weitz and J. B. Hobbs, *Nucl. Med. Biol.*, 2000, **27**, 289–297.

228   S. Ni, Z. Zhuo, Y. Pan, Y. Yu, F. Li, J. Liu, L. Wang, X. Wu, D. Li, Y. Wan, L. Zhang, Z. Yang, B.-T. Zhang, A. Lu and G. Zhang, *ACS Appl. Mater. Interfaces*, 2020, acsami.0c05750.

229   J. C. Rohloff, A. D. Gelinas, T. C. Jarvis, U. A. Ochsner, D. J. Schneider, L. Gold and N. Janjic, *Mol. Ther. - Nucleic Acids*, 2014, **3**, e201.

230   M. C. R. Buff, F. Schäfer, B. Wulffen, J. Müller, B. Pötzsch, A. Heckel and G. Mayer, *Nucleic Acids Res.*, 2010, **38**, 2111–2118.

231   C. Feng, S. Dai and L. Wang, *Biosens. Bioelectron.*, 2014, **59**, 64–74.

232   J. Huang, Z. Zhu, S. Bamrungsap, G. Zhu, M. You, X. He, K. Wang and W. Tan, *Anal. Chem.*, 2010, **82**, 10158–10163.

233   J.-L. He, Z.-S. Wu, H. Zhou, H.-Q. Wang, J.-H. Jiang, G.-L. Shen and R.-Q. Yu, *Anal. Chem.*, 2010, **82**, 1358–1364.

234   H. Ozaki, A. Nishihira, M. Wakabayashi, M. Kuwahara and H. Sawai, *Bioorg. Med. Chem. Lett.*, 2006, **16**, 4381–4384.

235   N. Saraf, M. Villegas, B. J. Willenberg and S. Seal, *ACS Omega*, 2019, **4**, 2234–2240.

236   S. Shubham, J. Hoinka, S. Banerjee, E. Swanson, J. A. Dillard, N. J. Lennemann, T. M. Przytycka, W. Maury and M. Nilsen-Hamilton, *Sci. Rep.*, 2018, **8**, 12373.

237   H.-L. Chen, W.-H. Hsiao, H.-C. Lee, S.-C. Wu and J.-W. Cheng, *PLoS One*, 2015, **10**,

e0131240.

238   C. Bai, Z. Lu, H. Jiang, Z. Yang, X. Liu, H. Ding, H. Li, J. Dong, A. Huang, T. Fang, Y. Jiang, L. Zhu, X. Lou, S. Li and N. Shao, *Biosens. Bioelectron.*, 2018, **110**, 162–167.

239   C. Bayraç, F. Eyidoğan and H. Avni Öktem, *Biosens. Bioelectron.*, 2017, **98**, 22–28.

240   N. Duan, S. Wu, C. Zhu, X. Ma, Z. Wang, Y. Yu and Y. Jiang, *Anal. Chim. Acta*, 2012, **723**, 1–6.

241   S. Wu, N. Duan, Y. Qiu, J. Li and Z. Wang, *Int. J. Food Microbiol.*, 2017, **261**, 42–48.

242   J. Tan, N. Yang, Z. Hu, J. Su, J. Zhong, Y. Yang, Y. Yu, J. Zhu, D. Xue, Y. Huang, Z. Lai, Y. Huang, X. Lu and Y. Zhao, *Nanoscale Res. Lett.*, 2016, **11**, 298.

243   D. Porciani, L. N. Cardwell, K. D. Tawiah, K. K. Alam, M. J. Lange, M. A. Daniels and D. H. Burke, *Nat. Commun.*, 2018, **9**, 2283.

244   M. Beltrán-Gastélum, B. Esteban-Fernández de Ávila, H. Gong, P. L. Venugopalan, T. Hianik, J. Wang and V. Subjakova, *ChemPhysChem*, 2019, **20**, 3177–3180.

245   Q. Pan, C. O. K. Law, M. M. H. Yung, K. C. Han, Y. L. Pon and T. C. K. Lau, *PLoS One*, 2018, **13**, e0198980.

246   S. M. Khoshfetrat and M. A. Mehrgardi, *Bioelectrochemistry*, 2017, **114**, 24–32.

247   M. V. Berezovski, M. Lechmann, M. U. Musheev, T. W. Mak and S. N. Krylov, *J. Am. Chem. Soc.*, 2008, **130**, 9137–9143.

248   H. Shi, X. He, K. Wang, X. Wu, X. Ye, Q. Guo, W. Tan, Z. Qing, X. Yang and B. Zhou, *Proc. Natl. Acad. Sci.*, 2011, **108**, 3900–3905.

249   J. Zhang, L. P. Smaga, N. S. R. Satyavolu, J. Chan and Y. Lu, *J. Am. Chem. Soc.*, 2017, **139**, 17225–17228.

250   J. S. Paige, T. Nguyen-Duc, W. Song and S. R. Jaffrey, *Science*, 2012, **335**, 1194–1194.

251   X. Chang, C. Zhang, C. Lv, Y. Sun, M. Zhang, Y. Zhao, L. Yang, D. Han and W. Tan, *J. Am. Chem. Soc.*, 2019, **141**, 12738–12743.

252   C. P. Rusconi, E. Scardino, J. Layzer, G. A. Pitoc, T. L. Ortel, D. Monroe and B. A. Sullenger, *Nature*, 2002, **419**, 90–94.

253   K. M. Bompiani, D. M. Monroe, F. C. Church and B. A. Sullenger, *J. Thromb. Haemost.*, 2012, **10**, 870–880.

254   S. Oney, R. T. S. Lam, K. M. Bompiani, C. M. Blake, G. Quick, J. D. Heidel, J. Y. C. Liu, B. C. MacK, M. E. Davis, K. W. Leong and B. A. Sullenger, *Nat. Med.*, 2009, **15**, 1224–1228.

255   D. L. Staudacher, V. Putz, L. Heger, J. Reinöhl, M. Hortmann, S. L. Zelenkofske, R. C. Becker, C. P. Rusconi, C. Bode and I. Ahrens, *Eur. Hear. J. Acute Cardiovasc. Care*, 2019, **8**, 520–526.

256   E. S. Gragoudas, A. P. Adamis, E. T. Cunningham, M. Feinsod and D. R. Guyer, *N. Engl. J. Med.*, 2004, **351**, 2805–2816.

257   E. W. M. Ng, D. T. Shima, P. Calias, E. T. Cunningham, D. R. Guyer and A. P. Adamis, *Nat. Rev. Drug Discov.*, 2006, **5**, 123–132.

258   Y. Cheng, G. Zhao, S. Zhang, F. Nigim, G. Zhou, Z. Yu, Y. Song, Y. Chen and Y. Li, *PLoS*

One, 2016, **11**, e0167094.

259   S. Soundararajan, W. Chen, E. K. Spicer, N. Courtenay-Luck and D. J. Fernandes, *Cancer Res.*, 2008, **68**, 2358–2365.

260   F. Schwoebel, L. T. van Eijk, D. Zboralski, S. Sell, K. Buchner, C. Maasch, W. G. Purschke, M. Humphrey, S. Zöllner, D. Eulberg, F. Morich, P. Pickkers and S. Klussmann, *Blood*, 2013, **121**, 2311–2315.

261   D. Oberthür, J. Achenbach, A. Gabdulkhakov, K. Buchner, C. Maasch, S. Falke, D. Rehders, S. Klussmann and C. Betzel, *Nat. Commun.*, 2015, **6**, 6923.

262   C. Maasch, K. Buchner, D. Eulberg, S. Vonhoff and S. Klussmann, *Nucleic Acids Symp. Ser.*, 2008, **52**, 61–62.

263   E. Zavyalova, V. Legatova, R. Alieva, A. Zalevsky, V. Tashlitsky, A. Arutyunyan and A. Kopylov, *Biomolecules*, 2019, **9**, 41.

264   B. Cosmi, *Curr. Opin. Mol. Ther.*, 2009, 11, 322–328.

265   S. M. Nimjee, J. D. Lohrmann, H. Wang, D. J. Snyder, T. J. Cummings, R. C. Becker, S. Oney and B. A. Sullenger, *Mol. Ther.*, 2012, **20**, 391–397.

266   G. Biesecker, L. Dihel, K. Enney and R. . Bendele, *Immunopharmacology*, 1999, **42**, 219–230.

267   E. K. Waters, R. M. Genga, M. C. Schwartz, J. A. Nelson, R. G. Schaub, K. A. Olson, J. C. Kurz and K. E. McGinness, *Blood*, 2011, **117**, 5514–5522.

268   J. P. Vavalle and M. G. Cohen, *Future Cardiol.*, 2012, **8**, 371–382.

269   G. J. Jaffe, D. Eliott, J. A. Wells, J. L. Prenner, A. Papp and S. Patel, *Ophthalmology*, 2016, **123**, 78–85.

270   A. M. Lincoff, R. Mehran, T. J. Povsic, S. L. Zelenkofske, Z. Huang, P. W. Armstrong, P. G. Steg, C. Bode, M. G. Cohen, C. Buller, P. Laanmets, M. Valgimigli, T. Marandi, V. Fridrich, W. J. Cantor, B. Merkely, J. Lopez-Sendon, J. H. Cornel, J. D. Kasprzak, M. Aschermann, V. Guetta, J. Morais, P. R. Sinnaeve, K. Huber, R. Stables, M. A. Sellers, M. Borgman, L. Glenn, A. I. Levinson, R. D. Lopes, V. Hasselblad, R. C. Becker and J. H. Alexander, *Lancet*, 2016, **387**, 349–356.

271   N. J. Ganson, T. J. Povsic, B. A. Sullenger, J. H. Alexander, S. L. Zelenkofske, J. M. Sailstad, C. P. Rusconi and M. S. Hershfield, *J. Allergy Clin. Immunol.*, 2016, **137**, 1610-1613.e7.

272   D. Rotem, L. Jayasinghe, M. Salichou and H. Bayley, *J. Am. Chem. Soc.*, 2012, **134**, 2781–2787.

273   M. R. Henry, P. Wilkins Stevens, J. Sun and D. M. Kelso, *Anal. Biochem.*, 1999, **276**, 204–214.

274   C. Yoshina-Ishii and S. G. Boxer, *J. Am. Chem. Soc.*, 2003, **125**, 3696–3697.

275   Y. Gao, L. K. Wolf and R. M. Georgiadis, *Nucleic Acids Res.*, 2006, **34**, 3370–3377.

276   K. Pappaert, P. Van Hummelen, J. Vanderhoeven, G. V. Baron and G. Desmet, *Chem. Eng. Sci.*, 2003, **58**, 4921–4930.

277   W. Michel, T. Mai, T. Naiser and A. Ott, *Biophys. J.*, 2007, **92**, 999–1004.

278   F. Baldelli Bombelli, F. Betti, F. Gambinossi, G. Caminati, T. Brown, P. Baglioni, D. Berti, Y. Sun, T. J. Yang, T. Brown, B. Norden, T. Brown and B. Norden, *Soft Matter*, 2009, **5**, 1639.

279   S. J. Cooper and J. M. Stubbs, *Chem. Phys. Lett.*, 2015, **634**, 230–235.

280   G. Tulzer and C. Heitzinger, *Nanotechnology*, 2016, **27**, 1–9.

281   J. Ma, M. G. Wang, A. H. Mao, J. Y. Zeng, Y. Q. Liu, X. Q. Wang, J. Ma, Y. J. Tian, N. Ma, N. Yang, L. Wang and S. Q. Liao, *Genet. Mol. Res.*, 2013, **12**, 1399–1410.

282   S. Howorka, L. Movileanu, O. Braha and H. Bayley, *Proc. Natl. Acad. Sci.*, 2001, **98**, 12996–13001.

283   I. Pfeiffer and F. Höök, *J. Am. Chem. Soc.*, 2004, **126**, 10224–10225.

284   K. Bielec, K. Sozanski, M. Seynen, Z. Dziekan, P. R. ten Wolde and R. Holyst, *Phys. Chem. Chem. Phys.*, 2019, **21**, 10798–10807.

285   J. X. Zhang, J. Z. Fang, W. Duan, L. R. Wu, A. W. Zhang, N. Dalchau, B. Yordanov, R. Petersen, A. Phillips and D. Y. Zhang, *Nat. Chem.*, 2018, **10**, 91–98.

286   K. Castelino, B. Kannan and A. Majumdar, *Langmuir*, 2005, **21**, 1956–1961.

287   M. Chung and S. G. Boxer, *Langmuir*, 2011, **27**, 5492–5497.

288   F. B. Bombelli, F. Betti, F. Gambinossi, G. Caminati, T. Brown, P. Baglioni and D. Berti, *Soft Matter*, 2009, **5**, 1639–1645.

289   H. Ravan, S. Kashanian, N. Sanadgol, A. Badoei-Dalfard and Z. Karami, *Anal. Biochem.*, 2014, 444, 41–46.

290   A. Czogalla, H. G. Franquelim and P. Schwille, *Biophys. J.*, 2016, **110**, 1698–1707.

291   A. W. Peterson, R. J. Heaton and R. M. Georgiadis, *Nucleic Acids Res.*, 2001, **29**, 5163–5168.

292   J. Ambia-Garrido, A. Vainrub and B. M. Pettitt, *Comput. Phys. Commun.*, 2010, **181**, 2001–2007.

293   S. Hohng, C. Joo and T. Ha, *Biophys. J.*, 2004, **87**, 1328–1337.

294   Y. Sun, C. Rombola, V. Jyothikumar and A. Periasamy, *Cytom. Part A*, 2013, **83**, 780–793.

295   K. M. Parkhurst and L. J. Parburst, *Biochemistry*, 1995, **34**, 285–292.

296   J. F. Corbett, *J. Chem. Educ.*, 1972, **49**, 663.

297   A. Tsourkas, M. A. Behlke, S. D. Rose and G. Bao, *Nucleic Acids Res.*, 2003, **31**, 1319–1330.

298   A. J. Genot, D. Y. Zhang, J. Bath and A. J. Turberfield, *J. Am. Chem. Soc.*, 2011, **133**, 2177–2182.

299   J. A. Wyer, M. B. Kristensen, N. C. Jones, S. V. Hoffmann and S. B. Nielsen, *Phys. Chem. Chem. Phys.*, 2014, **16**, 18827–18839.

300   E. Carrillo-Nava, L. Busch, Y. Mejía-Radillo, K. Boehm and H.-J. Hinz, *J. Phys. Chem. B*, 2010, **114**, 16087–16098.

301   J. Nangreave, H. Yan and Y. Liu, *Biophys. J.*, 2009, **97**, 563–571.

302   B. Yurke and A. P. Mills, *Genet. Program. Evolvable Mach.*, 2003, **4**, 111–122.

303   V. Maingi, M. Lelimousin, S. Howorka and M. S. P. Sansom, *ACS Nano*, 2015, **9**, 11209–11217.

304   J. Zhou, H. Tateishi-Karimata, J.-L. Mergny, M. Cheng, Z. Feng, D. Miyoshi, N. Sugimoto and C. Li, *Biochimie*, 2016, **121**, 204–208.

305   R. J. Schwarz and C. Richert, *Nanoscale*, 2017, **9**, 7047–7054.

306   A. Rangnekar, K. V Gothelf and T. H. LaBean, *Nanotechnology*, 2011, **22**, 235601.

307   M. M. Ackerman, C. Ricciardi, D. Weiss, A. Chant and C. M. Kraemer-Chant, *J. Chem. Educ.*, 2016, **93**, 2089–2095.

308   J. H.-S. Kim, A. Marafie, X.-Y. Jia, J. V. Zoval and M. J. Madou, *Sensors Actuators B Chem.*, 2006, **113**, 281–289.

309   D. Mocanu, A. Kolesnychenko, S. Aarts, A. Troost-Dejong, A. Pierik, E. Vossenaar and H. Stapert, *J. Biotechnol.*, 2009, **139**, 179–185.

310   C. Gadgil, A. Yeckel, J. J. Derby and W.-S. Hu, *J. Biotechnol.*, 2004, **114**, 31–45.

311   A. Wang, C. Chan Miller and J. W. Szostak, *Biophys. J.*, 2019, **116**, 659–669.

312   G. Dorrington, N. P. Chmel, S. R. Norton, A. M. Wemyss, K. Lloyd, D. Praveen Amarasinghe and A. Rodger, *Biophys. Rev.*, 2018, **10**, 1385–1399.

313   H. Niroomand, G. A. Venkatesan, S. A. Sarles, D. Mukherjee and B. Khomami, *J. Membr. Biol.*, 2016, **249**, 523–538.

314   W. C. Hung, F. Y. Chen and H. W. Huang, *Biochim. Biophys. Acta - Biomembr.*, 2000, **1467**, 198–206.

315   S. Kara, S. Afonin, O. Babii, A. N. Tkachenko, I. V. Komarov and A. S. Ulrich, *Biochim. Biophys. Acta - Biomembr.*, 2017, **1859**, 1828–1837.

316   W. M. Howell, in *Fluorescent Energy Transfer Nucleic Acid Probes*, Humana Press, New Jersey, 2006, vol. 335, pp. 33–42.

317   S. A. E. Marras, *Methods Mol. Biol.*, 2006, 335, 3–16.

318   H. Son, W. Mo, J. Park, J. W. Lee and S. Lee, *Biosensors*, 2020, **10**, 3–9.

319   A. S. Walsh, H. Yin, C. M. Erben, M. J. A. Wood and A. J. Turberfield, *ACS Nano*, 2011, **5**, 5427–5432.

320   S. Lee, J. Lee and S. Hohng, *PLoS One*, 2010, **5**, e12270.

321   L. Olejko and I. Bald, *RSC Adv.*, 2017, **7**, 23924–23934.

322   S. A. E. Marras and M. K. Johansson, in *Methods in Molecular Biology: Fluorescent Energy Transfer Nucleic Acid Probes: Designs and Protocols*, ed. V. V. Didenko, Humana Press Inc., Totowa, New Jersey, 2006, pp. 3–17.

323   M. Ardhammar, P. Lincoln and B. Norden, *Proc. Natl. Acad. Sci.*, 2002, **99**, 15313–15317.

324   A. Rodger, G. Dorrington and D. L. Ang, *Analyst*, 2016, **141**, 6490–6498.

325   B. Norden, A. Rodger and T. Dafforn, *Linear Dichroism and Circular Dichroism*, 2010, vol. 212.

326   E. P. Lundberg, B. Feng, A. Saeid Mohammadi, L. M. Wilhelmsson and B. Nordén, *Langmuir*, 2013, **29**, 285–293.

327   Z. Zhang, Y. Yang, F. Pincet, M. C. Llaguno and C. Lin, *Nat. Chem.*, 2017, **9**, 653–659.

328   O. Mendoza, P. Calmet, I. Alves, S. Lecomte, M. Raoux, C. Cullin and J. Elezgaray, *Nanoscale*, 2017, **9**, 9762–9769.

329   T. M. Fyles, *Chem. Soc. Rev.*, 2007, **36**, 335–347.

330   A. Patel, R. A. Hirst, C. Harrison, K. Hirota and D. G. Lambert, in *Calcium Signaling Protocols*,

eds. D. G. Lambert and R. D. Rainbow, Humana Press, Totowa, NJ, 2013, pp. 37–47.

331   C. Vorndran, A. Minta and M. Poenie, *Biophys. J.*, 1995, **69**, 2112–2124.

332   L. Hugonin, V. Vukojević, G. Bakalkin and A. Gräslund, *Biochim. Biophys. Acta - Biomembr.*, 2008, **1778**, 1267–1273.

333   G. Grynkiewicz, M. Poenie and R. Y. Tsien, *J. Biol. Chem.*, 1985, 260, 3440–3450.

334   R. Godbout, S. Légaré, M. Auger, C. Carpentier, F. Otis, M. Auger, P. Lagüe and N. Voyer, *PLoS One*, 2016, **11**, e0166587.

335   M. F. M. Sciacca, S. A. Kotler, J. R. Brender, J. Chen, D.-K. Lee and A. Ramamoorthy, *Biophys. J.*, 2012, **103**, 702–710.

336   M. D. Bootman, K. Rietdorf, T. Collins, S. Walker and M. Sanderson, *Cold Spring Harb. Protoc.*, 2013, **8**, 83–99.

337   K. Scott Brimble and V. S. Ananthanarayanan, *Biochim. Biophys. Acta - Biomembr.*, 1992, **1105**, 319–327.

338   R. Berendes, A. Burger, D. Voges, P. Demange and R. Huber, *FEBS Lett.*, 1993, **317**, 131–134.

339   R. D. Shannon, *Acta Crystallogr. Sect. A*, 1976, **32**, 751–767.

340   D. Larsson, B. Larsson, T. Lundgren and K. Sundell, *Anal. Biochem.*, 1999, **273**, 60–65.

341   A. Melcrová, S. Pokorna, M. Vošahlíková, J. Sýkora, P. Svoboda, M. Hof, L. Cwiklik and P. Jurkiewicz, *Langmuir*, 2019, **35**, 11358–11368.

342   M. Javanainen, A. Melcrová, A. Magarkar, P. Jurkiewicz, M. Hof, P. Jungwirth and H. Martinez-Seara, *Chem. Commun.*, 2017, **53**, 5380–5383.

343   A. Melcrová, S. Pokorna, S. Pullanchery, M. Kohagen, P. Jurkiewicz, M. Hof, P. Jungwirth, P. S. Cremer and L. Cwiklik, *Sci. Rep.*, 2016, **6**, 38035.

344   A. Kuzuya, R. Wang, R. Sha and N. C. Seeman, *Nano Lett.*, 2007, **7**, 1757–1763.

345   I. Russo Krauss, A. Merlino, A. Randazzo, E. Novellino, L. Mazzarella and F. Sica, *Nucleic Acids Res.*, 2012, **40**, 8119–8128.

346   R. F. Macaya, P. Schultze, F. W. Smith, J. A. Roe and J. Feigon, *Proc. Natl. Acad. Sci.*, 1993, **90**, 3745–3749.

347   K. Y. Wang, S. McCurdy, R. G. Shea, S. Swaminathan and P. H. Bolton, *Biochemistry*, 1993, **32**, 1899–1904.

348   D. Sen and W. Gilbert, *Curr. Opin. Struct. Biol.*, 1991, **1**, 435–438.

349   W. Liu, Y. Fu, B. Zheng, S. Cheng, W. Li, T. C. Lau and H. Liang, *J. Phys. Chem. B*, 2011, **115**, 13051–13056.

350   S. Nagatoishi, N. Isono, K. Tsumoto and N. Sugimoto, *Biochimie*, 2011, **93**, 1231–1238.

351   S. Nagatoishi, Y. Tanaka and K. Tsumoto, *Biochem. Biophys. Res. Commun.*, 2007, **352**, 812–817.

352   B. Pagano, L. Martino, A. Randazzo and C. Giancola, *Biophys. J.*, 2008, **94**, 562–569.

353   I. Smirnov and R. H. Shafer, *J. Mol. Biol.*, 2000, **296**, 1–5.

354   D. M. Tasset, M. F. Kubik and W. Steiner, *J. Mol. Biol.*, 1997, **272**, 688–698.

355 B. Pagano, L. Martino, A. Randazzo and C. Giancola, *Biophys. J.*, 2008, **94**, 562–569.

356 K. Padmanabhan, K. P. Padmanabhan, J. D. Ferrara, J. E. Sadler and A. Tulinsky, *J. Biol. Chem.*, 1993, **268**, 17651–17654.

357 R. Reshetnikov, A. Golovin, V. Spiridonova, A. Kopylov and J. Šponer, *J. Chem. Theory Comput.*, 2010, **6**, 3003–3014.

358 L. R. Paborsky, S. N. McCurdy, L. C. Griffin, J. J. Toole and L. L. K. Leung, *J. Biol. Chem.*, 1993, **268**, 20808–20811.

359 S. Nagatoishi, Y. Tanaka and K. Tsumoto, *Biochem. Biophys. Res. Commun.*, 2007, **352**, 812–817.

360 Q. Wu, M. Tsiang and J. E. Sadler, *J. Biol. Chem.*, 1992, **267**, 24408–24412.

361 H. Hasegawa, K. I. Taira, K. Sode and K. Ikebukuro, *Sensors*, 2008, **8**, 1090–1098.

362 A. Pinto, M. C. Bermudo Redondo, V. C. Ozalp and C. K. O'Sullivan, *Mol. Biosyst.*, 2009, **5**, 548–553.

363 V. Ostatná, H. Vaisocherová, J. Homola and T. Hianik, *Anal. Bioanal. Chem.*, 2008, **391**, 1861–1869.

364 P. H. Lin, R. H. Chen, C. H. Lee, Y. Chang, C. S. Chen and W. Y. Chen, *Colloids Surfaces B Biointerfaces*, 2011, **88**, 552–558.

365 M. Berezovski, R. Nutiu, Y. Li and S. N. Krylov, *Anal. Chem.*, 2003, **75**, 1382–1386.

366 M. Gong, I. Nikcevic, K. R. Wehmeyer, P. A. Limbach and W. R. Heineman, *Electrophoresis*, 2008, **29**, 1415–1422.

367 V. Van Meervelt, M. Soskine and G. Maglia, *ACS Nano*, 2014, **8**, 12826–12835.

368 R. F. Chen and J. R. Knutson, *Anal. Biochem.*, 1988, **172**, 61–77.

369 R. El Jastimi and M. Lafleur, *Biospectroscopy*, 1999, **5**, 133–140.

370 P. M. G. Löffler, O. Ries, A. Rabe, A. H. Okholm, R. P. Thomsen, J. Kjems and S. Vogel, *Angew. Chemie - Int. Ed.*, 2017, **56**, 13228–13231.

371 P. M. G. Löffler, O. Ries and S. Vogel, in *Methods in Molecular Biology*, Humana Press Inc., 2020, vol. 2063, pp. 101–118.

372 D. Lorusso, A. Pietragalla, S. Mainenti, V. Masciullo, G. Di Vagno and G. Scambia, *Crit. Rev. Oncol. Hematol.*, 2010, **74**, 163–174.

373 Y. Jejoong, S. A. N, L. Chen-Yu and A. Aleksei, cadnano to PDB File Converter, https://nanohub.org/resources/cadnanocvrt, (accessed 30 March 2021).

374 R. Abagyan, M. Totrov and D. Kuznetsov, *J. Comput. Chem.*, 1994, **15**, 488–506.

375 K. Vanommeslaeghe, E. Hatcher, C. Acharya, S. Kundu, S. Zhong, J. Shim, E. Darian, O. Guvench, P. Lopes, I. Vorobyov and A. D. Mackerell, *J. Comput. Chem.*, 2009, **31**, 671–690.

376 W. L. DeLano, PyMOL | pymol.org, https://pymol.org/2/, (accessed 30 March 2021).

377 J. Ao, V. Ribeiro, B. Radak, J. Stone, J. Gullingsrud, J. Saam and J. Phillips, *psfgen User's Guide*, 2020.

378 J. Yoo, C.-Y. Li, S. M. Slone, C. Maffeo and A. Aksimentiev, in *Methods in Molecular Biology*, Humana Press Inc., 2018, vol. 1811, pp. 209–229.

379   C. Maffeo, J. Yoo and A. Aksimentiev, *Nucleic Acids Res.*, 2016, **44**, 3013–3019.

380   W. Humphrey, A. Dalke and K. Schulten, *J. Mol. Graph.*, 1996, **14**, 33–38.

381   A. Aksimentiev, M. Sotomayor, D. Wells and Z. Huang, *Theor. Comput. Biophys. Group, Univ. Illinois Urbana-Champaign.*

382   R. L. Davidchack, R. Handel and M. V. Tretyakov, *J. Chem. Phys.*, 2009, **130**, 234101.

383   S. E. Feller, Y. Zhang, R. W. Pastor and B. R. Brooks, *J. Chem. Phys.*, 1995, **103**, 4613–4621.

384   J. C. Phillips, R. Braun, W. Wang, J. Gumbart, E. Tajkhorshid, E. Villa, C. Chipot, R. D. Skeel, L. Kalé and K. Schulten, *J. Comput. Chem.*, 2005, **26**, 1781–1802.

385   U. Essmann, L. Perera, M. L. Berkowitz, T. Darden, H. Lee and L. G. Pedersen, *J. Chem. Phys.*, 1995, **103**, 8577–8593.

386   S. Miyamoto and P. A. Kollman, *J. Comput. Chem.*, 1992, **13**, 952–962.

387   T. Darden, D. York and L. Pedersen, *J. Chem. Phys.*, 1993, **98**, 10089–10092.

388   G. Makov and M. C. Payne, *Phys. Rev. B*, 1995, **51**, 4014–4022.

389   D. Van Der Spoel, E. Lindahl, B. Hess, G. Groenhof, A. E. Mark and H. J. C. Berendsen, *J. Comput. Chem.*, 2005, **26**, 1701–1718.

390   C. Ginestet, *J. R. Stat. Soc. Ser. A (Statistics Soc.)*, 2011, **174**, 245–246.

391   J. S. Racine, *J. Appl. Econom.*, 2012, **27**, 167–172.

392   A. Ramanathan and P. K. Agarwal, *J. Phys. Chem. B*, 2009, **113**, 16669–16680.

393   X. Daura, K. Gademann, B. Jaun, D. Seebach, W. F. van Gunsteren and A. E. Mark, *Angew. Chemie Int. Ed.*, 1999, **38**, 236–240.

394   O. S. Smart, J. G. Neduvelil, X. Wang, B. A. Wallace and M. S. P. Sansom, *J. Mol. Graph.*, 1996, **14**, 354–360.

395   T. Giorgino, *Comput. Phys. Commun.*, 2014, **185**, 317–322.

396   R. Guixà-González, I. Rodriguez-Espigares, J. M. Ramírez-Anguita, P. Carrió-Gaspar, H. Martinez-Seara, T. Giorgino and J. Selent, *Bioinformatics*, 2014, **30**, 1478–1480.

9. Appendix A: Experimental

9.1. Materials

Unmodified, fluorophore-labelled and cholesterol-modified DNA oligonucleotides were procured from Integrated DNA Technologies (Belgium or US) or ATD Bio (UK) on a 100 or 200 nmol scale with HPLC purification. 1,2-dioleoyl-sn-glycero-3-phosphocholine (DOPC), 1,2-dioleoyl-sn-glycero-3-phosphoethanolamine (DOPE), 1-palmitoyl-2-oleoyl-sn-glycero-3-phosphocholine (POPC) and 1,2-diphytanoyl-sn-glycero-3-phosphocholine (DPhPC) were procured from Avanti Polar Lipids (US). Human alpha-thrombin was purchased from Haematologic Technologies on a 100 μg scale in 50% glycerol/water (v/v). All other reagents and solvents were purchased from Merck (UK) unless specified.

9.2. Folding Protocols

9.2.1. Fast Fold

Samples were folded at 1 μM in 100-1000 μL in an Eppendorf tube. Assembly was achieved using an Eppendorf ThermoMixer Comfort (UK). The ThermoMixer was heated to 95 °C and held for 5 min. The ThermoMixer was then turned off and allowed to cool to r.t. over the course of 30 min. After 30 min, samples were removed and stored at 4 °C.

9.2.2. 2.5 h Fold

Samples were folded at 1 μM in 100 μL. Assembly was achieved using a BioRad T100 Thermocycler (UK) using a programme involving heating to 95 °C and holding for 0.5 min, then cooling to 75°C within 5 min and holding for 1 min, before cooling to 4 °C at a rate of 0.5 °C per 1 min.

9.2.3. 15 h Fold

Samples were folded at 1 μM in 100 μL. Assembly was achieved using a BioRad T100 thermocycler (UK) using a programme including heating to 85°C for 10 min, cooling to 65°C within 5 min, cooling to 25 °C at a rate of 0.1 °C per 2 min, and cooling to 10 °C at a rate of 0.2 °C per min.

9.3. Model System

9.3.1. Sequences and structural composition of the Model System

Table 11. Names, modifications and sequences of DNA oligonucleotides used for folding R, S and S$_{NP}$

ID	Sequence 5' → 3'
R$^{\Delta C}$	TAGTCGATTTTATCCATGCA
R	Sequence of R$^{\Delta C}$ carrying a cholesterol *via* a tri(ethylene glycol) (TEG) linker at the 3' terminus
^{Cy3}R$^{\Delta C}$	^{Cy3}TAGTCGATTTTATCCATGCA
^{Cy3}R	Sequence of ^{Cy3}R$^{\Delta C}$ carrying a cholesterol *via* a TEG linker at the 3' terminus
S	TGCATGGATAAAATCGACTA
^{Cy5}S	TGCATGGATAAAATCGACTATTTTT^{Cy5}
1	ACA GGA TTT TCG CCT GCT GGG GCA AAC CAG CGT GGA CCG CTT TTT TGG CTA TTC TTT TGA TTT ATA AGG GAT TTT GCC GAT TTC GGA A
2	CAA CTC TCT CAG GGC CAG GCG GTG AAG GGC AAT CAG CTG TTG TTT TCA ACA GCA TCC TGT TTC CGA AAT CGG CAT TAA AGA CCA GCT G
3	TCT CAC TGG TGA AAA GAA AAA CCA CCC TGG CGC CCA ATA CGC TTT TTC CCC GCG CGT TGG CCG ATT CAT TAA TGC AGC TGG CAC GAC A
4	GGC GAA ATG ATT GCT TTC ACC AGT GAG ATG TCG TGA CGT GGA TTT TTC CAC GTT CTT TAA TAG TGG ACT CTT GTT CCA AAC TGG AAC A
5	TGT TCC AAA TAG CCA AGC GGT CCA CGC TCC CTG AGG GGC GCC
6	CAT TAA TTT TTT CTC CTT CAC CGC CTG GGG TTT GCT TAT AAA
7	AGG GTG GGA ATC GGA CAA GAG TCC ACT AAA ATC CCC CCA GCA

8	TCA AAA GGT TTG GAC CAA CGC GCG GGG AGC GTA TTA GAG TTG
1-ext	TGC ATG GAT AAA ATC GAC TAT TTT ACA GGA TTT TCG CCT GCT GGG GCA AAC CAG CGT GGA CCG CTT TTT TGG CTA TTC TTT TGA TTT ATA AGG GAT TTT GCC GAT TTC GGA A
2-ext	TGC ATG GAT AAA ATC GAC TAT TTT CAA CTC TCT CAG GGC CAG GCG GTG AAG GGC AAT CAG CTG TTG TTT TCA ACA GCA TCC TGT TTC CGA AAT CGG CAT TAA AGA CCA GCT G
5-ext	TGC ATG GAT AAA ATC GAC TAT TTT TGT TCC AAA TAG CCA AGC GGT CCA CGC TCC CTG AGG GGC GCC
^{Cy5}5-ext	TGCATGGATAAAATCGACTATTTTT^{Cy5}GTTCCAAATAGCCAAGCGGTCC ACGCTCCCTGAGGGGCGCC

X^{Cy3} = Cy3 fluorophore; X^{Cy5} = Cy5 fluorophore

Table 12. Names and strand compositions of structures used for the DNA nanopore with biomimetic triggered assembly

Nanopore	Composition
NP	1, 2, 3, 4, 5, 6, 7, 8
$S_{NP}1$	1-ext, 2, 3, 4, 5, 6, 7, 8
$S_{NP}2$	1, 2-ext, 3, 4, 5, 6, 7, 8
S_{NP}	1, 2, 3, 4, 5-ext, 6, 7, 8
$^{Cy5}S_{NP}$	1, 2, 3, 4, ^{Cy5}5-ext, 6, 7, 8
$R^{ΔC}•S$	$R^{ΔC}$, S
R•S	R, S
$R^{ΔC}•S_{NP}$	$R^{ΔC}$, 1, 2, 3, 4, 5-ext, 6, 7, 8
$R•S_{NP}$	R, 1, 2, 3, 4, 5-ext, 6, 7, 8
$^{Cy3}R^{ΔC}•S^{Cy5}$	$^{Cy3}R^{ΔC}$, S^{Cy5}
R•S	^{Cy3}R, S^{Cy5}

$R^{\Delta C} \bullet S_{NP}$	$^{Cy3}R^{\Delta C}$, 1, 2, 3, 4, ^{Cy5}5-ext, 6, 7, 8
$R \bullet S_{NP}$	^{Cy3}R, 1, 2, 3, 4, ^{Cy5}5-ext, 6, 7, 8

9.3.2. Agarose Gel Electrophoresis

The assembled DNA nanostructures and component DNA oligonucleotides were analysed with 2-3% agarose (Invitrogen, UK) gels in 1x TAE buffer (40 mM Tris, 20 mM acetic acid, 1 mM EDTA, pH 8.3). For gel loading, a solution of the DNA nanostructure (2 µL, 1 µM) was mixed with folding buffer (13 µL) and 6x gel loading dye (5 µL, New England Biolabs, UK). The gel was run at 60 V for 60 min at 4 °C unless specified. The gel bands were visualised by staining with ethidium bromide and UV illumination. A 100 bp marker (New England Biolabs, UK) was used as a reference standard.

9.3.3. Transition Electron Microscopy (TEM)

DNA nanopores (6 µL, 1 µM) were added onto glow discharge-treated TEM grids. After 30 s the excess liquid was removed with filter paper. The sample was then stained with 2% uranyl formate solution. After 10 s, the excess liquid was removed with filter paper and the grid was air-dried (approx. 2 min). TEM analysis was performed on a JEM-2100 electron microscope (JEOL) operated at 200 kV and images were acquired with an Orius SC200 camera.

9.3.4. Giant Unilamellar Vesicles (GUV) Preparation

A solution of POPC lipids (5 µL, 10 mM in chloroform) was added to an ITO coated glass slide. Within 5 minutes the solvent evaporated, and a dried lipid film was formed. The glass slide was then inserted in a vesicle prep device (Nanion). An O-ring was added around the patch. Sucrose 10 solution (300 µL, 1 M in water) was added to the lipid film patches confined by the O-ring. Finally, another ITO glass slide was applied from the top, resulting in a sealed chamber. An alternating electric field was applied between the two slides according to the following protocol: 3 V, 5 Hz for 120 minutes. The solution was collected and stored at 4 °C.

9.3.5. Confocal Microscopy

Confocal laser scanning microscopy was performed using a Leica TCS SPE High-Resolution Spectral Confocal microscope (Leica, Germany). GUVs (10 µL, 130 µM lipid concentration) were added to a FluoroDish (World Precision Instruments) with buffer (500 µL, 1x TAE, 500 mM NaCl, pH 8.1) and the solution gently mixed. R (10 µL, 1 µM) was added to the dish, mixed and left for 10 minutes to ensure insertion into the GUVs. S_{NP} (10 µL, 1 µM) was then added and thoroughly mixed.

The mixture was left for 5 min to let the GUVs sink to the bottom of the dish. GUVs were visualized under two wavelengths 570 nm (for Cy3) and 670 nm (for Cy5). The data was then recorded.

9.3.6. Preparation of small unilamellar vesicles (SUVs)

DOPC (70 μL, 10 mM) and DOPE (30 μL, 10 mM) in chloroform were added to a 5 mL round bottom flask. The solvent was removed using a rotary evaporator (Buchi) to yield a thin film, which was further dried under high vacuum (Buchi) for 1 h. The lipid was re-suspended in 1 mL of buffer containing: 1 M KCl, 50 mM Tris-HCl, pH 8. The solution was sonicated for 20 min at 30 °C and then equilibrated for 1 h before being extruded 25 times through a 0.1 μm polycarbonate membrane (Avanti Polar Lipids, US) using the extruder kit (Avanti Polar Lipids, US). SUVs were then stored at 4 °C and used within 48 h.

9.3.7. Agarose gel electrophoretic mobility shift assay

R (5 μL, 1 μM) was mixed with S (1 μM stock) in 1 M KCl, 50 mM Tris, pH 8 yielding concentrations of 0 to 0.5 μM in a final volume of 20 μL. Following incubation for 30 min at 30 °C, 6x gel loading dye (5 μL, New England Biolabs) was added, the samples were mixed and loaded onto a thermally equilibrated 3% agarose gel. The gel was run in 1x TAE buffer, pH 8.3 at 60 V for 60 min at 4 °C. The gel bands were visualised by staining with ethidium bromide and UV illumination. A 100 bp marker (New England Biolabs, UK) was used as a reference standard. In the case of R_{SUV} vs S or S_{NP}, R (5 μL, 1 μM) was first added to SUVs (5 μL, 100 nm, 16.7 nM). Instead of a 3% agarose gel, a 2% gel was used. All other conditions were the same. Band intensities were analysed using ImageJ and normalised as $(1-(I_{DNA}-I_{background}))$. The normalised intensities were then fit to a Michaelis-Menten curve to determine the K_d.

9.3.8. Fluorescence Studies Monitoring FRET Pair Interactions Over Time

Solution: the hybridisation of R with S or S_{NP} was investigated by monitoring Cy3 emission (ex_{550nm}, em_{570nm}) using a fluorescence spectrophotometer (Cary Eclipse, Agilent, UK). To a 10 mm quartz cuvette (Hellma Analytics), R (1.5 μL, 100 nM) to buffer (103.5 μL; 1M KCl, 50 mM Tris-HCl, pH 8.0) and the signal left to stabilize for 5 min. Then, S or S_{NP} (15 μL, 1 μM) was rapidly added and mixed. Hybridisation was monitored for 800 s.

On the surface of SUVs: the hybridisation of R_{SUV} with S or S_{NP} was investigated by monitoring Cy3 emission (ex_{550nm}, em_{570nm}) using a fluorescence spectrophotometer (Cary Eclipse, Agilent, UK). To a 10 mm quartz cuvette (Hellma Analytics), R (1.5 μL, 1 μM) and SUVs (0.375 μL, 100 nm, 16.67 nM) were added, mixed and left to bind for 10 min. R (1.5 μL, 100 nM) to buffer (127.5 μL; 1M

KCl, 50 mM Tris-HCl, pH 8.0) and the signal left to stabilize for 5 min. Then, S or S_{NP} (15 μL, 1 μM) was rapidly added and mixed. Hybridisation was monitored for 800 s.

9.4. DNA Nanopore with Biomimetic Triggered Assembly

9.4.1. Sequences and composition of the structures used Chapter 5.

Table 13. Names, modifications and sequences of DNA oligonucleotides used for folding A, B, A•B and variants.

ID	Sequence 5' → 3'
A_1	ATT AGC GAA CGT GGA TTT TGT CCG ACA TCG GCA AGC TCA CTT TTT CGA CT
A_2	TTG CCG ATG TCG GAC TTT TGA ACG ATC TTC GCC TGC TGC GTT TTG TGA GC
B_1	AGG CGA AGA TCG TTC TTT TCC TGC ACG TCC AAC TGG TCA GTT TTC GCA GC
B_2	AGT TGG ACG TGC AGG TTT TTC CAC GTT CGC TAA TAG TCG ATT TTC TGA CC
L^A	GGA CCA TGG TTC CAC GTT CGC TAA TAG TCG A
L^B	CCTGGTACGACATTTTTCCACGTTCGCTAATAGTCGATTTTATCC ATGCA
K^A	TCG ACT ATT AGC GAA CGT GGA ACC ATG GTC C
K^B	CGC AGC AGG CGA AGA TCG TTC TAG CTT GAC C
A_1 (chol)	Sequence of A_1 carrying a cholesterol *via* tri(ethylene glycol) TEG linker at the 3' terminus
A_2 (chol)	Sequence of A_2 carrying a cholesterol *via* a TEG linker at the 3' terminus
B_1 (chol)	Sequence of B_1 carrying a cholesterol *via* a TEG linker at the 3' terminus
B_2 (chol)	Sequence of B_2 carrying a cholesterol *via* a TEG linker at the 3' terminus
$^{Cy3}A_1$	^{Cy3}ATT AGC GAA CGT GGA TTT TGT CCG ACA TCG GCA AGC TCA CTT TTT CGA CT

$^{Cy5}B_1$	^{Cy5}AGG CGA AGA TCG TTC TTT TCC TGC ACG TCC AAC TGG TCA GTT TTC GCA GC

X^{Cy3} = base labelled with Cy3 fluorophore; X^{Cy5} = base labelled with Cy5 fluorophore

Table 14. Names and strand compositions of structures used in Chapter 5.

Nanopore	Composition
$A^{\Delta C}$	A_1, A_2
$B^{\Delta C}$	B_1, B_2
A	A_1, A_2 (chol)
B	B_1, B_2 (chol)
$^{Cy3}A^{\Delta C}$	$^{Cy3}A_1$, A_2
^{Cy3}A	$^{Cy3}A_1$, A_2 (chol)
$^{Cy5}B^{\Delta C}$	$^{Cy5}B_1$, B_2
^{Cy5}B	$^{Cy5}B_1$, B_2 (chol)
$A^{\Delta C}L^A$	A_1, A_2, L^A
$B^{\Delta C}L^B$	B_1, B_2, L^B
AL^A	A_1, A_2 (chol), L^A
BL^B	B_1, B_2 (chol), L^B
$^{Cy3}AL^A$	$^{Cy3}A_1$, A_2 (chol), L^A
$^{Cy5}BL^B$	$^{Cy5}B_1$, B_2 (chol), L^B
$(A{\bullet}B)^{\Delta C}$	A_1, A_2, B_1, B_2
$(A{\bullet}B)^{1C}$	A_1, A_2 (chol), B_1, B_2
$A{\bullet}B$	A_1, A_2 (chol), B_1, B_2 (chol)
$(A{\bullet}B)^{4C}$	A_1 (chol), A_2 (chol), B_1 (chol), B_2 (chol)

9.4.2. Nanopore assembly

Equimolar mixtures of DNA oligonucleotides (1 µL each, stock concentration of 100 µM) were dissolved at 1 µM in a buffer solution of either buffer A (1x PBS: (137 mM NaCl, 2.7 mM KCl, 10 mM Na_2HPO_4, 1.8 mM KH_2PO_4, pH 7.4), buffer B (300 mM KCl, 15 mM Tris-HCl, pH 7.4) or buffer C (12 mM $MgCl_2$ in 0.6x TAE (40 mM Tris, 20 mM acetic acid), pH 7.4) to a final volume of 100 µL. Folding was achieved using the 2.5 h folding protocol. Samples were stored at 4 °C for up to 1 week.

9.4.3. PAGE

The assembled DNA nanostructure and component DNA oligonucleotides were analysed with commercial 10% polyacrylamide gels (BioRad, UK) in 1x TBE buffer (100 mM Tris, 90 mM boric acid, 1 mM EDTA, pH 8.3). For gel loading, a solution of the DNA nanopores (2 µL, 1 µM) was mixed with folding buffer (13 µL, 2 mM $MgCl_2$ in 0.6x TAE, pH 7.4) and 6x gel loading dye (5 µL, New England Biolabs, UK). Gels were run at 115 V for 90 min at 4 °C. The gel bands were visualised by staining with ethidium bromide and UV illumination. A 100 bp marker (New England Biolabs, UK) was used as a reference standard.

9.4.4. Agarose gel electrophoresis

The assembled DNA nanostructures and component DNA oligonucleotides were analysed with 2-3% agarose (Invitrogen, UK) gels in 1x TAE buffer (40 mM Tris, 20 mM acetic acid, 1 mM EDTA, pH 8.3). For gel loading, a solution of the DNA nanostructure (2 µL, 1 µM) was mixed with folding buffer (13 µL) and 6x gel loading dye (5 µL, New England Biolabs, UK). The gel was run at 60 V for 60 min at 4 °C. The gel bands were visualised by staining with ethidium bromide and UV illumination. A 100 bp marker (New England Biolabs, UK) was used as a reference standard.

9.4.5. Preparation of small unilamellar vesicles (SUVs)

DPhPC (100 µL, 10 mM) or POPC (100 µL, 10 mM) in chloroform was added to a 5 mL round bottom flask. The solvent was removed using a rotary evaporator (Buchi) to yield a thin film, which was further dried under high vacuum (Buchi) for 1 h. The lipid was re-suspended in 1 mL of either buffer A or buffer B. The solution was sonicated for 20 min at 30 °C and then equilibrated for 1 h before being extruded 25 times through a 0.1 µm polycarbonate membrane (Avanti Polar Lipids, US) using the extruder kit (Avanti Polar Lipids, US). SUVs were then stored at 4 °C and used within 48 h.

9.4.6. Melting temperature (T_m) analysis using UV-vis spectroscopy

UV melting profiles were obtained using a 10 mm quartz cuvette (Hellma Analytics) in a Varian Cary 300 Bio UV–vis spectrophotometer (Agilent, UK) equipped with a Peltier element (Agilent, UK). Samples were analysed at 200 nM and SUVs composed of DPhPC at 200 µM lipid concentration. Samples were analysed by monitoring the change in absorbance at 260 nm as the temperature was increased from 20 to 80 °C at a rate of 1 °C/min. Melting profiles were then background corrected, and the 1st derivative calculated to identify the T_m.

9.4.7. Electrophoretic mobility shift assay

For binding titrations: A (5 µL, 1 µM) was mixed with B (1 µM stock) in buffer A yielding concentrations of 0 to 0.5 µM in a final volume of 20 µL. After incubation for 30 min at 30 °C, and 6x gel loading dye (5 µL, New England Biolabs) was added, and the samples were loaded onto a thermally equilibrated 3% agarose gel. The gel was run in 1x TAE buffer, pH 8.3 at 60 V for 60 min at 4 °C. The gel bands were visualised by staining with ethidium bromide and UV illumination. A 100 bp marker (New England Biolabs, UK) was used as a reference standard. In the case of A-SUV vs B, A (5 µL, 1 µM) was first added to SUVs (5 µL, 100 nm, 16.7 nM). Instead of a 3% agarose gel, a 2% gel was used. All other conditions were the same. Band intensities were analysed using ImageJ and normalised as $(1-(I_A-I_{background}))$. The normalised intensities were then fit to a Michaelis-Menten curve to determine the K_d.

For kinetic assembly: $A^{\Delta C}$ (5 µL, 1 µM) was mixed with $B^{\Delta C}$ (5 µL, 1 µM) in buffer A to a final volume of 20 µL. Samples were incubated at 30 °C for 0, 1, 5, 10, 15, 20, 25 and 30 min while shaking at 500 rpm. Samples were prepared in reverse time order and after all samples were prepared, samples were crashed in ice water to arrest pore formation. Samples were mixed with 6x gel loading dye (5 µL) and then samples were loaded onto thermally equilibrated 10% PAGE. The gel was run in 1x TBE buffer at 115 V for 90 min at 4 °C. Staining and molecular markers were as described above. For $A^{\Delta C}L^A$ vs $B^{\Delta C}L^B$ conditions were exactly the same except that the keys, K^A and K^B (1 µL, pre-mixed, 5 µM) were also added to each timepoint.

9.4.8. Preparation of giant unilamellar vesicles (GUVs)

A solution of POPC lipids (5 µL, 10 mM in chloroform) was added to an ITO coated glass slide. Within 5 minutes the solvent evaporated, and a dried lipid film was formed. The glass slide was then inserted in a vesicle prep device (Nanion). An O-ring was added around the patch. Sucrose 10 solution (300 µL, 1 M in water) was added to the lipid film patches confined by the O-ring. Finally, another ITO glass slide was applied from the top, resulting in a sealed chamber. An alternating

electric field was applied between the two slides according to the following protocol: 3 V, 5 Hz for 120 minutes. The solution was collected and stored at 4 °C.

9.4.9. Confocal laser scanning microscopy

Confocal laser scanning microscopy was performed using a Leica TCS SPE High-Resolution Spectral Confocal microscope (Leica, Germany). GUVs (10 μL, 130 μM lipid concentration) were added to a FluoroDish (World Precision Instruments) with buffer (500 μL, 1x TAE, 500 mM NaCl, pH 8.1) and the solution gently mixed. A (10 μL, 1 μM) was added to the dish, the solution was mixed thoroughly and left for 10 minutes to ensure insertion into the GUVs. $B^{\Delta C}$ (10 μL, 1 μM) was then added and the solution thoroughly mixed. The mixture was left for 5 min to let the GUVs sink to the bottom of the dish. The FluorDish was placed under the microscope set to 96x zoom and visualised through the microscope until clear GUVs were found. The sample was then viewed through the brightfield and two wavelengths: 570 nm (for A: Cy3) and 670 nm (for B: Cy5). Images were was then recorded.

9.4.10. FRET assay to monitor pore assembly

For binding titrations: The assembly of A•B was investigated using a fluorescence spectrophotometer (Cary Eclipse, Agilent, UK). To a plastic Eppendorf tube was added $A^{\Delta C}$ or A (12 μL, 1 μM), $B^{\Delta C}$ or B (0 μL, 1.2 μL, 2.4 μL, 6 μL, 12 μL; 1 μM), SUVs (0 μL, 6 μL; 1 mM lipid, 7.22 nM SUV) and buffer B to a final volume of 120 μL. The tube was then incubated at 30 °C for 30 min while shaking at 750 rpm. The combined solution was then added to a 10 mm quartz cuvette (Hellma Analytics) and placed in the fluorescence spectrophotometer and scanned (ex$_{545\ nm}$, em$_{555\text{-}725\ nm}$). AB was used as a control for maximum assembly. Where SUVs were used, A and SUVs were mixed and left to bind for 10 min prior to addition of $B^{\Delta C}$ or B.

For kinetic assembly: The assembly of A•B was investigated by monitoring Cy3 emission (ex$_{550nm}$, em$_{570nm}$) using a fluorescence spectrophotometer (Cary Eclipse, Agilent, UK). To a 10 mm quartz cuvette (Hellma Analytics), $A^{\Delta C}$ or A (2.5 μL, 1 μM) was added to SUVs (0 μL, 1.25 μL; 1 mM lipid, 7.22 nM SUV) and buffer B (97.5, 96.25 μL) and the signal left to stabilize for 5 min. Then, $B^{\Delta C}$ or B (50 μL, 1 μM) was rapidly added and mixed. Pore formation was monitored for 1 h. Where SUVs were used, A and SUVs were mixed and left to bind for 10 min prior to the start of the run.

9.4.11. Preparation of planar lipid bilayers on a glass slide and smFRET and single particle tracking

Planar lipid bilayers were formed on glow discharged glass slides provided by ONI (UK). SUVs composed of DPhPC in buffer A (15 μL, 1 mM) were placed onto the support and left for 15 min.

Some solution (~ 5 μL) was then supplanted with d.H$_2$O and left for 1-2 min. This was repeated 3 times. After the 3rd wash with d.H$_2$O, the solution was washed with buffer A. Slides were used within 1 h and topped up with buffer A as necessary. smFRET and single particle tracking was performed using a NanoImager S (ONI, UK) by Jon Shewring from ONI. Structures were added (1 μL, 1 nM in buffer A) to planar lipid bilayers composed of DPhPC on glass slides.

9.4.12. Linear dichroism

Solution-phase flow linear dichroism spectroscopy was performed on a Jasco-810 spectropolarimeter using a photo elastic modulator 1/2 wave plate. A micro-volume quartz Couette flow cell with ~0.5 mm annular gap and quartz capillaries were used (all from Kromatec Ltd, UK). Molecular alignment was achieved by applying the constant flow of the sample solution between two coaxial cylinders, a stationary quartz rod and a rotating cylindrical capillary. LD spectra were acquired with laminar flow obtained by maintaining the rotation speed at 3000 rpm and processed by subtracting non-rotating baseline spectra. DNA nanopores were assayed at 1.4 μM and SUVs composed of POPC at 500 μM lipid concentration.

9.4.13. Preparation of fluorophore-filled SUVs and dye release assay

A solution of the lipid DPhPC (100 μL, 10 mM) in chloroform was added to a 5 mL round bottom flask. The solvent was removed using a rotary evaporator (Buchi) to yield a thin film, which was further dried under high vacuum (Buchi) for 1 h. The lipid was re-suspended in buffer A containing SRB (50 mM). The solution was sonicated for 20 min at 30 °C and then equilibrated for 3 h. SUVs were extruded 25 times through a 100 nm polycarbonate membrane (Avanti Polar Lipids, US) using the extruder kit (Avanti Polar Lipids, US). The non-encapsulated dye was removed using a NAP-25 column (Cytivia, UK), and SUVs were exchanged into buffer D (0.2 M KCl, 10 mM Tris pH 7.4). Purified SUVs were used within 48 h and gently resuspended immediately prior to use.

For the release assays, A•B and all components were folded in buffer C using the 15 h folding protocol. Components were folded at 2 μM to control for volume effects. The SUV suspension with encapsulated SRB (10 μL) and buffer D (110 μL, 80 μL) was added to a 10 mm quartz cuvette (Hellma Analytics). Fluorescence was monitored using a Varian Cary Eclipse fluorescence spectrophotometer (Agilent, UK) at 586 nm and excited at 565 nm. After 5 min, A, A+B, A•B, AL+BL or AL+BL+keys (30 μL, or 60 μL; 1 μM in buffer C) were added to a final volume of 150 μL. After 55 min of monitoring fluorescence, samples were mixed with a 1% (v/v) solution of Triton X-100 (10 μL) to lyse all vesicles to identify maximum SRB release. Maximum fluorescence emission and the fluorescence prior to addition of the nanopore (or components) were used to calculate the extent of release as %. Components (and keys, where applicable) were incubated together for 30 min at r.t. prior to addition.

9.4.14. Preparation of Fura-2-filled SUVs and Ca²⁺ influx assay

A solution of the lipid POPC (100 μL, 10 mM) in chloroform was added to a 5 mL round bottom flask. The solvent was removed using a rotary evaporator (Buchi) to yield a thin film, which was further dried under high vacuum (Buchi) for 1 h. The lipid was re-suspended in buffer E (500 mM NaCl, 100 mM HEPES, pH 7.4) containing the fluorophore fura-2 (100 μM). The solution was sonicated for 20 min at 30°C and then equilibrated for 3 h. SUVs were extruded 25 times through a 100 nm polycarbonate membrane (Avanti Polar Lipids, US) using the extruder kit (Avanti Polar Lipids, US). The non-encapsulated dye was removed using Illustra MicroSpin S-400 spin columns (Cytivia, UK). SUVs were then subjected to dynamic light scattering with a Malvern Zetasizer Nano S (UK) to confirm the vesicles' diameter. Purified SUVs were used within 48 h and gently resuspended immediately prior to use. For Ca²⁺ influx assays, the SUV suspension with encapsulated Fura-2 (30 μL) and buffer E (138.33 μL, 145.83 μL, 148.33 μL) were added to a 10 mm quartz cuvette (Hellma Analytics). Fluorescence was monitored using a Varian Cary Eclipse fluorescence spectrophotometer (Agilent, UK) at 510 nm and excited at 340 and 380 nm. After 2.5 min, $CaCl_2$ (16.67 μL, 3 mM in H_2O) was added and allowed to stabilise for a further 2.5 min. At 5 min, $(A•B)^{\Delta C}$ (15 μL, 7.5 μL, 5 μL, 1 μM in buffer B) was added to a final volume of 200 μL. After 30 min of monitoring fluorescence, samples were mixed with a 1% solution (v/v) of Triton X-100 (10 μL) to lyse all vesicles to identify maximum Ca²⁺ influx. Ca²⁺ influx was monitored as the ratio of the change in emission at each excitation wavelength as a ratio of 340/380 nm. The maximum 340/380 nm ratio following addition of Triton-X-100 was used to normalize all traces.

9.4.15. Nanopore current recordings

Single-channel current measurements were carried out as in5. Briefly, an integrated chip-based, parallel bilayer recording setup was used (Orbit Mini, Nanion Technologies, Munich, Germany) with multielectrode-cavity-array (MECA) chips (IONERA, Freiburg, Germany). Bilayers were formed of DPhPC dissolved in octane (10 mg/mL). The electrolyte solution was 1 M KCl and 10 mM HEPES, pH 7.4. For pore insertion, a 2:1 mixture of cholesterol-anchored DNA nanopores and 0.5% OPOE (n-octyloligooxyethylene, in 1 M KCl, 10 mM HEPES, pH 7.4) was added to the cis side of the bilayer. Successful incorporation was observed by detecting current steps. The current traces were not Bessel-filtered and acquired at 10 kHz using Element Data Recorder software (Element s.r.l., Italy). Single-channel analysis was performed using Clampfit software (Molecular Devices, Sunnyvale, CA, USA).

9.4.16. Simulation Preparation

DNA nanostructures were designed in caDNAno, then translated to all atom models in python.[373] The poly-thymine linker regions at the pore termini were then constructed using the MolSoft ICM software suite.[374] TEG-Cholesterol lipid anchors were parametrised using cgenff,[375] attached using pyMol[376] and CHARMM36 compatible topology files were generated using psfgen.[377] Initial structures were minimised in a vacuum for 10,000 steps (2 fs), then simulated for 100,000 steps (2 ns) using an elastic restraint network[378] derived from the ENRG webserer.[379]

DNA Nanostructures A and A•B were simulated in a 1 M KCl solution with TIP3 water prepared in VMD.[380] The component A was simulated in a box of 16 x 14 x 19 nm, with a total of 6.5k atoms. Nanopore A•B was simulated in 13 x 11 x 15 nm box, totalling 437k atoms. A 1 ns NpT equilibration was run to equilibrate box size and pressure before a 50 ns NvT equilibration to further relax the DNA structures. Production simulations were then run in in the NpT ensemble.

For the membrane tethered and transmembrane simulations, VMD was used to generated membranes and orient the DNA nanostructures, informed by linear dichroism experimental data and maintaining favourable cholesterol orientations.[20] The membrane tethered component A was simulated in a 15 x 15 x 16 nm box of 1 M KCl, bisected by a 1-palmitoyl-2-oleoyl-sn-glycero-3-phosphocholine (*POPC*) bilayer, totalling 303k atoms. While the membrane spanning A•B nanopore was simulated in a 12 x 12 x 12 nm box totalling 141k atoms. Fixed atom restraints were placed on all atoms except those belonging to the lipid tails, which were then melted over 0.5 ns of dynamics in the NvT ensemble, as the temperature was bought up to 301 K.[381] Fixed atom restraints were replaced with harmonic restraints, with a spring constant of 1 kcal/mol/Å², on the heavy atoms of the DNA phosphate backbones. Simulation box size and pressure were equilibrated in the NpT ensemble for 3.5 ns, with harmonic restraints being lowered by 0.5 kcal/mol/Å² every 0.5 ns. Unrestrained dynamics in the NvT ensemble allowed the system to fully equilibrate, and production simulations were performed in the NpT ensemble.

Production simulations were performed at 301K and 1.013 bar pressure, maintained with the Langevin thermostat[382] and the Nosé-Hoover Langevin piston method.[383] Simulations were performed in NAMD,[384] a smooth switching algorithm[385] with a switch distance of 8 Å, a cut off of 10 Å and a pair list distance of 12 Å was implemented for van der Waals interactions. A 2 fs time step was used and hydrogen bond lengths were constrained using the SETTLE and SHAKE algorithms.[386] Particle Mesh Ewald electrostatics were computed over a cubic grid with a 1.0 Å spacing[387] and periodic boundary conditions.[388] Equilibration simulations were performed on a on a single GPU 1080Ti workstation and production runs were performed in parallel on 850 CPU cores of the UCL Grace HPC facility.

9.4.17. Simulation Analysis

Analysis was performed using GROMACs[389] and VMD tools on the production simulations, after discarding the initial 10 ns, graphs were prepared using *ggplot*[390] and *RStudio*.[391]

9.4.17.1. RMSF$_{10}$.

gmx_covar and gmx_aneig were used to investigate the ten top quasi-harmonic modes[392] of root mean squared fluctuations (RMSF) of the DNA backbone heavy atoms, averaged per-residue, to interrogate structural dynamics of the DNA nanostructures while accounting for thermal noise and stochastic motion.

9.4.17.2. Clustering.

gmx_cluster was used to prepare snapshots of the membrane spanning A•B DNA nanostructure trajectory. Clustering was performed with a cut-off of 0.35 nm using the gromos method.[393]

9.4.17.3 Lumen Analysis.

Clustered coordinates were analysed using HOLE,[394] with a channel-end radius of 0.8 nm and a sampling distance of 0.25 nm. To account for asymmetry of the DNA nanostructure, coordinates were then rotated and analysed again.

9.4.17.4. Lipid Analysis.

gmx_gangle was used to measure the angle of phosphate and nitrogen atoms in the lipid head groups, split by lipid leaflet, compared to the bilayer normal, over the initial equilibration simulations. Production simulations were analysed using gmx_rms, and the VMD plugins density_profile_tool[395] and MEMBPLUGIM[396] to determine lipid RMSF, average lipid density and area-per-lipid, respectively.

9.5. DNA nanopore with protein-gate featuring DNA aptamer functionality

9.5.1. Design and Sequences of the Protein-Gated Nanopore.

Table 15. Names, modifications and sequences of DNA oligonucleotides used for folding protein-gated nanopore (pNP) and variants.

ID	Sequence 5' → 3'
TBA	GGTTGGTGTGGTTGGTTTAAGTAGTTCAAGACCCCGTGACT
1	AGCGAACGTGGATTTTGTCCGACATCGGCAAGCTCCCTTTTTCGACTATT
2	CCGATGTCGGACATTCGCTGCGCGGTTTTTTTAAGTAATCACGTTCACGATCTTCGCCTGCTGGGTTTTGGGAGCTTG
3	CGAAGATCGTGTTTTTCCACAGTTGATTGCCCTTCACTTTTCCCAGCAGG
4	AATCAACTGTGGTTTTTCTCACTGGTGATTAGAATGCTTTTGTGAAGGGC
5	TCACCAGTGAGATAGTCACGATATTTTGCACGTCATATTATGTCGTACCAGGTGCATGGATTTTTGCATTCTAA
6	CCTGGTACGACATTTTTCCACGTTCGCTAATAGTCGATTTTATCCATGCA
1(chol)	Sequence of 1 carrying a cholesterol *via* tri(ethylene glycol) TEG linker at the 3' terminus
3(chol)	Sequence of 3 carrying a cholesterol *via* a TEG linker at the 3' terminus
4(chol)	Sequence of 5 carrying a cholesterol *via* a TEG linker at the 3' terminus
6(chol)	Sequence of 5 carrying a cholesterol *via* a TEG linker at the 3' terminus
lid	AACCGCGCAGCGTTTTTTTTTTATGACGTGCTTTTTTTTTATCGTGACGGTTGGTGTGGTTGGCGTGATTACTTA

lid(Cy3)	AACCGCGCAGCGTTTTTTTTTTTATGACGTGCTTTTTTTTTTATCGT GACGGTTGGTGTGGTTGGCGTGATTACTTA^{Cy3}
3(Cy5)	CGAAGATCGTGTT^{Cy5}TTTCCACAGTTGATTGCCCTTCACTTTTCCC AGCAGG
lid-II	AACCGCGCAGCGGGTTGGTGTGGTTGGTATGACGTGCTTTTTTT TTATCGTGACTTTTTTTTTCGTGATTACTTA
lid-II(Cy3)	ACCGCGCAGCGGGTTGGTGTGGTTGGT^{Cy3}ATGACGTGCTTTTTTT TTTATCGTGACTTTTTTTTTCGTGATTACTTA
lid-control	AACCGCGCAGCGTTTTTTTTTTTATGACGTGCTTTTTTTTTTATCGT GACTTTTTTTTTCGTGATTACTTA
lid-control(Cy3)	AACCGCGCAGCGTTTTTTTTTTTATGACGTGCTTTTTTTTTTATCGT GACTTTTTTTTTCGTGATTACTTA^{Cy3}
lid-II-ext	AACCGCGCAGCGGGTTGGTGTGGTTGGTATGACGTGCTTTTTTT TTATCGTGACTTTTTTTTTCGTGATTACTTACACCGATCAAGAAG
dye-ext	CTTCT^{T}TTGATCGGTG

X^{Cy3} = base labelled with Cy3 fluorophore; X^{Cy5} = base labelled with Cy5 fluorophore; X^{T} = base labelled with TAMRA fluorophore.

Table 16. Names and strand compositions of pNP and variants.

Nanopore	Composition
pNP$^{\Delta C}$	1, 2, 3, 4, 5, 6, lid
pNP2$^{\Delta C}$	1, 2, 3, 4, 5, 6, lid-II
pNP3$^{\Delta C}$	1, 2, 3, 4, 5, 6, lid-control
pNP	1(chol), 2, 3(chol), 4(chol), 5, 6(chol), lid
pNP2	1(chol), 2, 3(chol), 4(chol), 5, 6(chol), lid-II
pNP3	1(chol), 2, 3(chol), 4(chol), 5, 6(chol), lid-control

pNP$^{\Delta C}$-L	1, 2, 3, 4, 5, 6
pNP^{TAMRA}	1(chol), 2, 3(chol), 4(chol), 5, 6(chol), lid-II-ext, dye-ext
pNP$^{\Delta C,Cy3,Cy5}$	1, 2, 3(Cy5), 4, 5, 6, lid(Cy3)
pNP2$^{\Delta C,Cy3,Cy5}$	1, 2, 3(Cy5), 4, 5, 6, lid-II(Cy3)
pNP3$^{\Delta C,Cy3,Cy5}$	1, 2, 3(Cy5), 4, 5, 6, lid-control(Cy3)

9.5.2. DNA assembly

Equimolar mixtures of DNA oligonucleotides (1 µL each, stock concentration of 100 µM) were dissolved at 1 µM in a buffer solution of 12 mM MgCl2 in 0.6x TAE (40 mM Tris, 20 mM acetic acid), pH 7.4 to a final volume of 100 µL. Folding was achieved using the 15 h folding protocol. Samples were stored at 4 °C.

9.5.3. SDS PAGE

The assembled DNA nanostructure and component DNA oligonucleotides were analysed with commercial 10% polyacrylamide gels (BioRad, UK) in 1x TGS (25 mM Tris, 192 mM glycine and 0.1% SDS, pH 8.6). For gel loading, a solution of the DNA nanopores (2 µL, 1 µM) was mixed with folding buffer (13 µL, 2 mM MgCl$_2$ in 0.6x TAE, pH 7.4) and 6x gel loading dye (5 µL, New England Biolabs, UK). The gel was run at 60 V for 60 min at 4°C. The gel bands were visualised by staining with ethidium bromide and UV illumination. A 100 bp marker (New England Biolabs, UK) was used as a reference standard.

9.5.4. Thrombin-TBA electrophoretic mobility shift assay

TBA (10 µL, 4 µM) were mixed with thrombin (10 µM stock) in buffer A (0.3 M KCl, 15 mM Tris pH 7.4) yielding concentrations of 0 to 2.67 µM in a final volume of 50 µL. After incubation for 30 min at 30°C, and 6x gel loading dye (10 µL, New England Biolabs) was added, and the samples were loaded onto a thermally equilibrated 2% agarose gel. The gel was run in 1x TAE buffer, pH 8.3 at 60 V for 60 min at 4°C. Staining and molecular markers were as described above.

9.5.5. Melting temperature (T$_m$) analysis using UV-vis spectroscopy

UV melting profiles were obtained using a 10 mm quartz cuvette (Hellma Analytics) in a Varian Cary 300 Bio UV–vis spectrophotometer (Agilent, UK) equipped with a Peltier element (Agilent, UK). Samples (200 nM) were analysed by monitoring the change in absorbance at 260 nm as the temperature was increased from 20 to 80 °C at a rate of 1 °C/min. Melting profiles were then background corrected, and the 1st derivative calculated to identify the T$_m$.

9.5.6. Preparation of giant unilamellar vesicles (GUVs)

A solution of DOPC lipids (3 µL, 10 mM in chloroform) and DOPE lipids (2 µL, 10 mM in chloroform) was added to an ITO coated glass slide. Within 5 minutes the solvent evaporated, and a dried lipid film was formed. The glass slide was then inserted in a vesicle prep device (Nanion). An O-ring was added around the patch. Sucrose 10 solution (300 µL, 1 M in water) was added to the lipid film patches confined by the O-ring. Finally, another ITO glass slide was applied from the top, resulting in a sealed chamber. An alternating electric field was applied between the two slides according to the following protocol: 3 V, 5 Hz for 120 minutes. The solution was collected and stored at 4 °C.

9.5.7. Confocal laser scanning microscopy

Confocal laser scanning microscopy was performed using a Leica TCS SPE High-Resolution Spectral Confocal microscope (Leica, Germany). GUVs (10 µL, 130 µM lipid concentration) were added to a FluoroDish (World Precision Instruments) with buffer (500 µL, 1x TAE, 500 mM NaCl, pH 8.1) and the solution gently mixed. Then, pNP^{TAMRA} (10 µL, 1 µM) was added to the dish, the solution was mixed thoroughly and left for 10 minutes to ensure insertion into the GUVs and to let the GUVs sink to the bottom of the dish. The FluorDish was placed under the microscope set to 96x zoom and visualised through the microscope until clear GUVs were found. The sample was then viewed through the brightfield and using the 570 nm laser. Images were was then recorded.

9.5.8. Thrombin-pNP electrophoretic mobility shift assay

pNP (2 µL, 1 µM) was mixed with thrombin (10 µM) in buffer A yielding concentrations of 0 to 3.2 µM in a final volume of 20 µL. After incubation for 30 min at 30°C, 6x gel loading dye

(5 µL) was added, and the samples were loaded onto thermally equilibrated 10% PAGE. The gel was run in 1x TBE buffer (89 mM Tris-borate and 2 mM EDTA, pH 8.3) at 60 V for 90 min at 4°C. Staining and molecular markers were as described above.

9.5.9. Lid-opening FRET assay

The extent of the protein-gated lid opening of pNP was determined by monitoring Cy3 emission (ex540nm, em570nm) using a fluorescence spectrophotometer (Cary Eclipse, Agilent, UK). To a quartz cuvette (Hellma Analytics), pNP (11 µL, 1 µM) were added to buffer A (108.5 µL or 93.5 µL) and, after 5 min incubation, thrombin in buffer A (40 µM) was added (1.5 µL or 7.5 µL) yielding the final concentrations of 0.2 or 2 µM equivalent to pNP:thrombin ratios of 1:2 or 1:20, respectively. Lid opening was monitored for 40 min.

9.5.10. Preparation of fluorophore-filled LUVs and dye release assay

Solutions of the lipids DOPC (70 µL, 10 mM) and DOPE (30 µL, 10 mM) in chloroform were added to a 5 mL round bottom flask. The solvent was removed using a rotary evaporator (Buchi) to yield a thin film, which was further dried under high vacuum (Buchi) for 1 h. The lipid was re-suspended in PBS (137 mM NaCl, 2.7 mM KCl, 10 mM Na_2HPO_4, 1.8 mM KH_2PO_4, pH 7.4) containing SRB (50 mM). The solution was sonicated for 20 min at 30°C and then equilibrated for 3 h. LUVs were extruded 25 times through a 200 nm polycarbonate membrane (Avanti Polar Lipids, US) using the extruder kit (Avanti Polar Lipids, US). The non-encapsulated dye was removed using a NAP-25 column (GE Healthcare, UK), and LUVs were exchanged into buffer B (0.2 M KCl, 10 mM Tris pH 7.4). LUVs were then subjected to dynamic light scattering with a Malvern Zetasizer Nano S (UK) to confirm the vesicles' diameter. Purified LUVs were used within 48 h and gently resuspended immediately prior to use. For release assays, the LUV suspension with encapsulated SRB (10 µL), pNP (30 µL, 1 µM) and buffer B (95 µL, 102.5 µL, 108.5 µL) were added to a 10 mm quartz cuvette (Hellma Analytics). Fluorescence was monitored at 586 nm and excited at 565 nm. After 5 min, thrombin (15 µL, 7.5 µL, 1.5 µL; 20 µM in buffer A) was added to give a ratio of 1:1, 1:5 or 1:10 (pNP:thrombin) in final volume of 150 µL. After 60 min of monitoring fluorescence, samples were mixed with a 1% solution of Triton X-100 (10 µL) to lyse all vesicles to identify maximum SRB release. Maximum fluorescence emission and the fluorescence prior to addition of thrombin were used to calculate the kinetics of release as %. For the kinetic analysis of efflux, the first 5 min of three 2 µM thrombin-mediated release traces were fitted with a linear line-of-best-fit. For the 0 µM thrombin-mediated release trace (baseline), the first 10

min of seven traces obtained from different batches of fluorophore-filled LUVs were averaged to one trace which was fitted to the line-of-best-fit. From these lines-of-best-fits, the initial rate at 1 min, 1.5 min, and 2 min were calculated and averaged to minimize fluctuations in the data.

9.5.11. Cell culture

HeLa cells were a gift from Dr Jeremy Carlton, King's college London. Cells were cultured at 37 °C and 5% CO_2 in Dulbecco's Modified Eagle Medium (DMEM) GlutaMAX™ (Gibco; Life Technologies) supplemented with 10% heat-inactivated Fetal Bovine Serum (FBS) (Gibco; Life Technologies) and 1% Penicillin – Streptomycin solution (Gibco; Life Technologies).

9.5.12. Cell-based assay

On day 0, HeLa cells were plated at a density of 10,000 cells per well in a 96-well plate and left to grow overnight. The next day (day 1), cells were supplanted with fresh culture medium and treated with either: thrombin (10 µL, 165 µM) in buffer A, pNP2 (10 µL, 1 µM); topotecan (10 µL, 3 µM), LUVs filled with 3 µM topotecan (10 µL, 0.1 mM, PC:PE 7:3 lipid ratio), pNP2 functionalized topotecan-filled LUVs (20 µL), and the latter in combination with thrombin (10 µL, 165 µM in buffer A). All wells were made up to final volume of 100 µL. The treated cells were maintained in a humidified atmosphere, containing 5% CO_2 at 37°C, for 3 d. Brightfield images were captured at day 1, 2 and 3 using an inverted Nikon Eclipse microscope, 20x air objective. Images were processed using ImageJ. On day 3, a WST-1 colorimetric assay was used to quantify cell viability. WST-1 (10 µL) was added to the culture medium in each well (100 µL) and incubated for 3 h. The absorbance was determined at 450 nm using a microplate reader (VICTOR multilabel plate reader, PerkinElmer), and the absorbance reading at 620 nm was used as a reference. The experiment was performed in triplicate.

10. Appendix B: Publications